Studies of Incoherent Effects for the Upgrade of the Large Hadron Collider and Detector Applications

Konstantinos Paraschou

A dissertation submitted for the degree of
Doctor of Philosophy (PhD)

Department of Physics
Faculty of Sciences
Aristotle University of Thessaloniki
Thessaloniki, Greece
June 2023

Μελέτες Μη-Συνεκτικών Φαινομένων για την Αναβάθμιση του Μεγάλου Επιταχυντή Αδρονίων (LHC) και Οργανολογικές Εφαρμογές

Κωνσταντίνος Παράσχου

ΔΙΔΑΚΤΟΡΙΚΗ ΔΙΑΤΡΙΒΗ

Τμήμα Φυσικής
Σχολή Θετικών Επιστημών
Αριστοτέλειο Πανεπιστήμιο Θεσσαλονίκης
Θεσσαλονίκη, Ελλάδα
Ιούνιος 2023

Επταμελής Εξεταστική Επιτροπή:

1. Τζαμαρίας Σπυρίδων, Καθηγητής Τμ. Φυσικής ΑΠΘ (επιβλέπων).
2. Κορδάς Κωνσταντίνος, Καθηγητής Τμ. Φυσικής ΑΠΘ (μέλος).
3. Παπαφιλίππου Ιωάννης, Διευθυντής Έρευνας CERN (μέλος).
4. Πετρίδου Χαρίκλεια, Ομ. Καθηγήτρια Τμ. Φυσικής ΑΠΘ.
5. Σαμψωνίδης Δημήτριος, Καθηγητής Τμ. Φύσικης ΑΠΘ.
6. Iadarola Giovanni, Κύριος Ερευνητής CERN.
7. Αργυρόπουλος Θεόδωρος, Κύριος Ερευνητής CERN.

Abstract

Operation of the Large Hadron Collider (LHC) with protons has revealed that different bunches evolve differently mostly due to the interaction between the two colliding beams and due to electron clouds that form inside the vacuum chamber. This thesis studies these effects through modelling with numerical simulations and analysis of the available experimental data. The analysis of the beam loss rates measured during Run 2 of the LHC, and identifies that electron clouds forming in the common beam chamber of the quadrupole magnets near the high-luminosity interaction points are the main cause of beam losses. Moreover, the evolution of the beam observables (beam loss rate and emittance growth) is slow enough that it can only be observed over a timescale that lasts multiple hours. The simulation of such timescales is typically very time-consuming and can become impractical to simulate. In this work, Graphics Processing Units are employed to simulate distributions of particles in parallel for longer timescales (in the order of several tens of minutes). Simulations of the long-term effect of the beam-beam interaction done in the context of this thesis show that under the weak-strong approximation, the qualitative behavior of the beam loss rate evolution is reproduced. Additionally, they showed that the beam-beam interaction by itself does not contribute to emittance growth or to the development of tails in the transverse beam profile distributions. Simulation of the effect of the electron cloud on the slow beam degradation is much more challenging than for the beam-beam interaction. In fact, due to the complex electron distributions that form in the electron cloud, simulations of such effects need special care. Here, a framework for the simulation of slow beam degradation due to electron cloud effects is developed. In this framework, the weak-strong approximation is used to apply the map that describes the interaction with an electron cloud distribution that is at its typical dynamic equilibrium. The electron distribution is calculated with Particle-In-Cell simulations during pre-processing and the scalar potential that describes the interaction is interpolated with a tricubic interpolation scheme in order to preserve the symplectic structure of the map. Moreover, a method is developed to refine the potential in order to combat the limitations of the interpolation scheme. The simulations performed in this work show a clear slow beam degradation due to electron clouds through Frequency Map Analysis, calculation of dynamic aperture, as well as through the estimation of beam loss rates and of slow emittance growth from simulations with particle distributions. In addition, a stochastic and non-linear model for the response of the PICOSEC Micromegas detector is developed in the context of research and development for particle detectors. The presented model is constructed in order to gain insight on the main physical mechanisms causing the previously observed behavior in the response of the detector, found both in measurements and detailed simulations. The model is based on a simple mechanism of "time-gain per interaction" and employs a statistical description of the evolution of the electron avalanche that forms. It describes quantitatively the dynamical and statistical properties of the microscopic quantities, which determine the PICOSEC timing characteristics, in excellent agreement with the simulations. In parallel, it offers phenomenological explanations for the behavior of these microscopic variables. The formulae expressing this model can be used as a tool for fast and reliable predictions, provided that the input parameter values (e.g. drift velocities) are known for the considered operating conditions. Overall, this thesis identifies the main mechanisms for beam losses in the LHC and develops a practical approach for modelling such long-term effects in numerical simulations of beam-beam and electron cloud interactions, which are critical for the success of high-luminosity particle colliders. Furthermore, it proposes a simple model to explain the behavior of the PICOSEC Micromegas detector which can be used to optimize its performance. The developed methods, tools and simulation results provide critical input for the high-luminosity upgrade of the Large Hadron Collider and upgrade of detectors.

Acknowledgements

I am sincerely grateful to all the people who took part in my journey leading all the way to end of this thesis. Their support and the interactions with them was what made this possible, and most importantly, enjoyable.

Professor Spyros Tzamarias encouraged me to pursue this topic for my thesis and to this point, I cannot imagine a topic that would suit me and my interests more. In addition to advising me in matters regarding my thesis, he would always help me to try and see the bigger picture in science and in life. For these things, the always interesting conversations, the jokes, the coffees and all of the support I will be eternally grateful.

I had the luck of also being advised by Dr. Yannis Papaphilippou who welcomed me to join his group at CERN. I could always count on his knowledge of non-linear beam dynamics to steer me in the right direction when I would be in doubt. Moreover, it was because of Yannis that I had the opportunity to work with Dr. Gianni Iadarola and for that I couldn't be more thankful.

Gianni's support was enormous and invaluable to my research. He helped me with great patience and always inspired me with his vast knowledge across the different topics in accelerator physics. By spending half a day in the control room with Gianni, (performing a beam experiment at the Large Hadron Collider) I would learn much more than by following a full course of accelerator physics.

I am also indebted to the rest of the people taking part in the examining committee of my thesis: Prof. Kostas Kordas, Dr. Theodoros Argyropoulos, Prof. Dimos Sampsonidis, Prof. Chara Petridou, who all provided a critical view to my thesis. I especially thank Elias Métral, Giovanni Rumolo, Hannes Bartosik and Gianluigi Arduini for welcoming me be to part of their section/group at CERN. There are many more colleagues which I cannot thank enough for their help, questions and comments, among which include Lotta, Benoit, Riccardo, Martin, Rogelio, Fanouria, Nicolas, Xavier, Carlo, Guido, Ilias, Ewen, Tobias, Luca, Bjorn, Elle, Michele, Sebastien, Mael, Thomas, Eraldo, Nikos, Sofia, Vera, Michael, Joschua, Felix, Elena, Julie, Josephine, Veronika, Giulia and Giulia.

I hold special gratitude to the other people who gave me inspiration. Some of them are colleagues, some of them are close friends, but they are all very important to me and helped me grow as a person. Those include Alina, Natalia, Jamie, Alessandro, Adam, Lily, David, Laurens, Eszter, Tirsi, Thenia, Tiona, Lorenzo, Frederik, Christina, Stergios, Mihai, Diana and Gertrud.

However, the most important people to this journey are my family: my father Vasilis, my mother Maria and my brother Nikos. They always supported me and I knew I could count on them whenever I needed them.

Εκτεταμένη Περίληψη

Η λειτουργία του Μεγάλου Επιταχυντή Αδρονίων (LHC) με πρωτόνια αποκάλυψε ότι διαφορετικές υποδέσμες εξελίσσονται διαφορετικά κυρίως λόγω της αλληλεπίδρασης μεταξύ των δύο συγκρουόμενων δεσμών και λόγω των νεφών ηλεκτρονίων που σχηματίζονται μέσα στο θάλαμο κενού. Η παρούσα διατριβή αναλύει τους ρυθμούς απώλειας δέσμης που μετρήθηκαν κατά τη διάρκεια της δεύτερου κύκλου λειτουργίας του LHC και προσδιορίζει ότι τα νέφη ηλεκτρονίων που σχηματίζονται στον κοινό θάλαμο δέσμης των τετραπολικών μαγνητώνν κοντά στα σημεία αλληλεπίδρασης υψηλής φωτεινότητας είναι η κύρια αιτία για τις αργές απώλειες δέσμης. Επιπλέον, η εξέλιξη των παρατηρήσιμων μεγεθών της δέσμης (ρυθμός απώλειας δέσμης και αύξηση της εκπεμπτικότητας) είναι αρκετά αργή ώστε να μπορεί να παρατηρηθεί μόνο σε μια χρονική κλίμακα που διαρκεί αρκετές ώρες. Η προσομοίωση τέτοιων χρονικών κλιμάκων είναι συνήθως πολύ χρονοβόρα και η προσομοίωσή της μπορεί να καταστεί ανέφικτη. Στην παρούσα εργασία, χρησιμοποιούνται μονάδες επεξεργασίας γραφικών για την προσομοίωση κατανομών σωματιδίων παράλληλα για μεγαλύτερες χρονικές κλίμακες (της τάξης μερικών δεκάδων λεπτών). Οι προσομοιώσεις της μακροπρόθεσμης επίδρασης της αλληλεπίδρασης δέσμης-δέσμης που έγιναν στο πλαίσιο αυτής της διατριβής δείχνουν ότι υπό την ασθενή-ισχυρή προσέγγιση, η ποιοτική συμπεριφορά της εξέλιξης του ρυθμού απώλειας της δέσμης αναπαράγεται. Επιπλέον, έδειξαν ότι η αλληλεπίδραση δέσμης-δέσμης από μόνη της δεν συμβάλλει στην αύξηση της εκπεμπτικότητας ή στην ανάπτυξη ουρών στις κατανομές των σωματιδίων της δέσμης στο εγκάρσιο επίπεδο. Από την άλλη πλευρά, οι προσομοιώσεις της επίδρασης του νέφους ηλεκτρονίων στην αργή υποβάθμιση της δέσμης δεν έχει μελετηθεί τόσο λεπτομερώς όσο η αλληλεπίδραση δέσμης-δέσμης στη βιβλιογραφία. Εξ αιτίας των πολύπλοκων κατανομών ηλεκτρονίων που σχηματίζονται στο νέφος ηλεκτρονίων, οι προσομοιώσεις τέτοιων επιδράσεων χρειάζονται ιδιαίτερη προσοχή. Στην παρούσα εργασία παρουσιάζεται και αναπτύσσεται ένα πλαίσιο για την προσομοίωση της αργής υποβάθμισης της δέσμης λόγω νέφους ηλεκτρονίων. Σε αυτό το πλαίσιο, χρησιμοποιείται η ασθενής-ισχυρή προσέγγιση για την εφαρμογή της απεικόνισης που περιγράφει την αλληλεπίδραση με μια κατανομή νέφους ηλεκτρονίων που βρίσκεται στην τυπική της δυναμική ισορροπία. Η κατανομή ηλεκτρονίων υπολογίζεται με προσομοιώσεις Particle-In-Cell κατά το στάδιο της προεπεξεργασίας και το βαθμωτό δυναμικό που περιγράφει την αλληλεπίδραση παρεμβάλλεται με ένα τρισδιάστοτο κυβικό σχήμα παρεμβολής προκειμένου να διατηρηθεί η συμπλεκτική δομή της απεικόνισης. Επιπλέον, αναπτύσσεται μια μέθοδος για τη βελτίωση του δυναμικού προκειμένου να καταπολεμηθούν οι περιορισμοί του σχήματος παρεμβολής. Οι προσομοιώσεις που πραγματοποιήθηκαν σε αυτή την εργασία δείχνουν μια σαφή αργή υποβάθμιση της δέσμης λόγω των νεφών ηλεκτρονίων μέσω της ανάλυσης απεικόνισης συχνοτήτων, του υπολογισμού του δυναμικού εύρους, καθώς και μέσω της εκτίμησης των ρυθμών απώλειας δέσμης και της αργής αύξησης της εκπεμπτικότητας από προσομοιώσεις με κατανομές σωματιδίων.

Στην προσπάθειά τους να περιγράψουν τους θεμελιώδεις νόμους της φυσικής, οι φυσικοί έχουν στραφεί στη χρήση επιταχυντών σωματιδίων προκειμένου να εκτελέσουν ελεγχόμενα πειράματα με σωματίδια υψηλής ενέργειας. Ο σχεδιασμός ενός επιταχυντή επικεντρώνεται συνήθως γύρω από την 'οπτική' του. Η οπτική συνίσταται ουσιαστικά στη συγκεκριμένη τροφοδοσία ρεύματος κάθε μαγνήτη προκειμένου να επιτευχθεί ένας συγκεκριμένος στόχος. Για παράδειγμα, οι κύριοι τετραπολικοί μαγνήτες τροφοδοτούνται έτσι ώστε οι ταλαντώσεις των των πρωτονίων να μην υπερβαίνουν το διαθέσιμο άνοιγμα μέσα στο θάλαμο κενού. Σε ένα άλλο τρόπο, ισχυρά τετράπολα τοποθετούνται γύρω από τα σημεία σύγκρουσης σωματιδίων στον επιταχυντή, τα οποία τροφοδοτούνται με τέτοιο τρόπο ώστε το μέγεθος της δέσμης να είναι ελάχιστο στο σημείο αλληλεπίδρασης των δύο δεσμών, αυξάνοντας έτσι την πυκνότητα των πρωτονίων και συνεπώς τον αριθμό των συγκρούσεων. Από την άποψη της φυσικής της δέσμης, πρέπει να δοθεί ιδιαίτερη προσοχή προκειμένου να αποφευχθούν φαινόμενα που είναι επιζήμια για τη σταθερή κίνηση των πρωτονίων μέσα σε έναν κυκλικό επιταχυντή υψηλής ενέργειας. Μια σημαντική κατηγορία τέτοιων επιζήμιων φαινομένων είναι αυτά που ονομάζονται μονό-σωματιδιακά μη-γραμμικά φαινόμενα και συνήθως σχετίζονται με μη-γραμμικά μαγνητικά πεδία στη διάταξη του επιταχυντή. Οι μαγνήτες υψηλής τάξης (εξαπολικοί, οκταπολικοί, δεκαπολικοί, κ.λπ.) χρησιμοποιούνται για τη διόρθωση των πιθανών μη-γραμμικών ατελειών στα πεδία των μαγνητών. Επιπλέον, οι εξαπολικοί και οκταπολικοί μαγνήτες χρησιμοποιούνται συνήθως για να προκαλέσουν μια συσχέτιση μεταξύ της συχνότητας ταλάντωσης ενός πρωτονίου με την ενέργειά του ή το πλάτος της ταλάντωσής του. Ο έλεγχος αυτής της σχέσης είναι απαραίτητος για την αποφυγή σύμφωνης ασταθής κίνησης της δέσμης, ένα φαινόμενο που ανήκει στην κατηγορία των συλλογικών φαινομένων. Εξ ορισμού, τα συλλογικά φαινόμενα είναι εκείνα τα οποία οφείλονται στο γεγονός ότι πολλαπλά σωματίδια είναι παρόντα στο εσωτερικό του επιταχυντή. Ακολουθούν ορισμένα παραδείγματα τέτοιων φαινομένων. Η αλληλεπίδραση μεταξύ διαφόρων σωματιδίων στην ίδια δέσμη αναφέρεται συνήθως ως "φαινόμενο άμεσου χωρικού φορτίου". Η άμεση αλληλεπίδραση μεταξύ δύο διαφορετικών δεσμών (στο σημείο όπου οι δέσμες συγκρούονται) ονομάζονται "φαινόμενα δέσμης-δέσμης". Τα πρωτόνια μπορούν επίσης να αλληλεπιδρούν έμμεσα. Για παράδειγμα, τα γεωμετρικά όρια του θάλαμου κενού (υποθέτοντας τέλεια αγωγιμότητα) εισάγουν το φαινόμενο του "έμμεσου χωρικού φορτίου", τα οποία συνήθως περιγράφονται από εικονικά φορτία. Επιπλέον, οι θάλαμοι των οποίων τα τοιχώματα φέρουν ηλεκτρική αντίσταση ή απότομες μεταβάσεις στη γεωμετρία τους μπορούν να προκαλέσουν ηλεκτρομαγνητικά πεδία που επάγονται από τη δέσμη και καθυστερούν αυτής. Ένα άλλο είδος έμμεσης αλληλεπίδρασης είναι αυτό των φαινομένων νέφους ηλεκτρονίων. Η ίδια η δέσμη μπορεί να ευνοήσει τη συσσώρευση παγιδευμένων ηλεκτρονίων εντός των τοιχωμάτων του θαλάμου δέσμης, αν το υλικό του τοιχώματος του θαλάμου δέσμης πληροί ορισμένες προϋποθέσεις και επιτρέπει τον πολλαπλασιασμό των ηλεκτρονίων. Στην παρουσία φαινομένων νέφους ηλεκτρονίων, τα σωματίδια της δέσμης και το νέφος ηλεκτρονίων αλληλεπιδρούν μεταξύ τους. Όλα τα παραπάνω φαινόμενα μπορούν να επηρεάσουν τη ευστάθεια της δέσμης, όπου τα σωματίδια της δέσμης εκτελούν συμφασικές ταλαντώσεις οι οποίες επηρεάζουν τα σωματίδια της δέσμης, αυξάνοντας κάθε φορά το πλάτος των ταλαντώσεων.

Ωστόσο, ακόμη και όταν οι αστάθειες της συνεκτικής δέσμης ελέγχονται, τα επαγόμενα ηλεκτρομαγνητικά πεδία από αυτά τα φαινόμενα είναι συνήθως μη-γραμμικά. Αυτά τα μη-γραμμικά ηλεκτρομαγνητικά πεδία προκαλούν μη-γραμμικότητα στις τροχιές των μεμονωμένων σωματιδίων της δέσμης, παρόμοια με τα προαναφερθέντα φαινόμενα μεμονωμένων σωματιδίων. Σε αυτή την περίπτωση, ονομάζονται μη-συμφασικά φαινόμενα (δηλαδή κάθε σωματίδιο εκτελεί ταλαντώσεις που έχουν διαφορετική φάση απο τα υπόλοιπα σωματίδια). Τα περισσότερα μη-συνεκτικά φαινόμενα οδηγούν σε πολύ αργή αύξηση της εκπεμπτικότητας της δέσμης και σε μείωση του χρόνου ημιζωής της δέσμης. Τα μη-συνεκτικά φαινόμενα έχουν συνήθως πολύπλοκη περιγραφή και το αποτέλεσμά τους είναι παρατηρήσιμα μόνο σε μεγάλες χρονικές κλίμακες, οι οποίες είναι συνήθως απρόσιτες σε προσομοιώσεις. Στην παρούσα διατριβή, τα μη-συμφασικά φαινόμενα που παρατηρούνται στον Μεγάλο Επιταχυντή Αδρονίων (LHC)[1] μελετώνται. Ο LHC είναι ο μεγαλύτερος μέχρι σήμερα επιταχυντής με την υψηλότερη ενέργεια κέντρου μάζας. Πρόκειται για ένα σύγχροτρον, με διάταξη επαναλαμβανόμενων FODO (Εστίασης-Απόκλισης) κελιών που αποτελούν τη συντριπτική πλειοψηφία της διάταξής του, η οποία χωρίζεται σε 8 τόξα και 8 περιοχές εισαγωγής. Ενώ τα 8 τόξα αποτελούνται σχεδόν εξ ολοκλήρου από κελιά FODO, μια ποικιλία εξοπλισμού περιλαμβάνεται στις περιοχές εισαγωγής (Insertion Regions). Ιδιαίτερης σημασίας είναι η περιοχή εισαγωγής 1 (IR1), η περιοχή εισαγωγής 2 (IR2), η περιοχή εισαγωγής 5 (IR5) και η περιοχή εισαγωγής 8 (IR8), όπου τοποθετούνται οι ανιχνευτές ATLAS[2], ALICE[3], CMS[4] και LHCb[5] αντίστοιχα. Ο στόχος του LHC είναι να συγκρούονται πρωτόνια (ή άλλα αδρόνια) στο κέντρο καθενός από τους ανιχνευτές. Ένα μέγεθος που είναι ανεξάρτητο από το σύστημα αναφοράς και σχετίζεται σε μεγάλο βαθμό με τον αριθμό των συγκρούσεων είναι η φωτεινότητα.

Οι κύριοι παράγοντες που επηρεάζουν τη φωτεινότητα είναι πληθυσμοί των υποδέσμων, ο αριθμός των υποδεσμών και η (r.m.s.) έκταση των δέσμων στο εγκάρσιο επίπεδο, στο σημείο της σύγκρουσης. Άλλοι παράγοντες επηρεάζουν τη φωτεινότητα είναι οι γωνίες διασταύρωσης μεταξύ των δύο δεσμών, οι μη-μετωπικές συγκρούσεις, οι μη-γκαουσιανές κατανομές σωματιδίων των δεσμών, μεταξύ άλλων. Ένα μικρότερο μέγεθος δέσμης και ένας υψηλότερος πληθυσμός δέσμης αυξάνουν την παραγόμενη φωτεινότητα. Με την ελαχιστοποίηση της αύξησης της εκπεμπτικότητας, η οποία σχετίζεται άμεσα με το μέγεθος της δέσμης, και μεγιστοποιώντας το χρόνο ημιζωής της δέσμης, η φωτεινότητα και επομένως η 'παραγωγή συγκρούσεων' αυξάνεται. Η μελέτη που παρουσιάζεται εδώ αφορά τα μη-συνεκτικά συλλογικά φαινόμενα τα οποία υποβαθμίζουν το χρόνο ημιζωής της δέσμης και προκαλούν αύξηση της εκπομπτικότητας στις δέσμες πρωτονίων στον LHC. Τα δύο πιο σημαντικά φαινόμενα αυτού του τύπου βρέθηκαν να είναι η αλληλεπίδραση δέσμης-δέσμης και τα φαινόμενα νέφους ηλεκτρονίων. Οι προσομοιώσεις των μη-συνεκτικών φαινομένων δέσμης-δέσμης έχουν μακρά ιστορία με βάση τον φορμαλισμό που αναπτύχθηκε στην αναφορά [6] και χρησιμοποιώντας την ασθενή-ισχυρή προσέγγιση. Η ασθενής-ισχυρή προσέγγιση αναφέρεται σε προσομοιώσεις όπου ένα 'ασθενές' σωματίδιο μελετάται υπό την επίδραση μιας 'ισχυρής" δύναμης η οποία δεν μπορεί να επηρεαστεί από το 'ασθενές' σωματίδιο. Πρόκειται για μια προσέγγιση που είναι κατάλληλη για αργά μη-συνεκτικά φαινόμενα λόγω του ότι προκαλούν μόνο μικρές αλλαγές στα προφίλ της δέσμης. Με αυτόν τον τρόπο, τα ηλεκτρομαγνητικά πεδία που παράγονται από μια άλλη δέσμη (σε αλληλεπιδράσεις δέσμης-δέσμης) ή από ένα νέφος ηλεκτρονίων μπορεί να υπολογιστεί μία φορά και να χρησιμοποιηθεί για την επίλυση πολλαπλών φορών των εξισώσεων κίνησης του ‛ασθενούς” σωματιδίου υπό την επίδρασή τους.

Η ιστορία των μη-συνεκτικών φαινομένων του νέφους ηλεκτρονίων χρονολογείται κατά τις τελευταίες δύο δεκαετίες. Τα πρώιμα αποτελέσματα προσομοίωσης αποτελούνται από υπολογισμούς της διασποράς των συχνωτήτων ταλάντωσης, των στρεβλώσεων των βητατρονικών συναρτήσεων και της διασποράς, καθώς και της σύζευξης συγχροτρονικών-βητατρονικών ταλαντώσεων[7, 8, 9]. Ορισμένες προσπάθειες έγιναν για την περιγραφή της εξέλιξης του νέφους ηλεκτρονίων με τη χρήση απλοποιημένων μοντέλων[10] και να υπολογιστούν αναλυτικά οι δυνάμεις που προκαλούνται στα σωματίδια της δέσμης. Αυτές οι προσεγγίσεις βρέθηκαν βολικές από άποψη χρόνου υπολογισμού, αλλά δεν μπορούσαν να περιγράψουν ρεαλιστικές κατανομές του νέφους ηλεκτρονίων κατά την παρουσία κλίσεων στο μαγνητικό πεδίο της μη συνεκτικής επίδρασης του νέφους ηλεκτρονίων μέσω αυτοσυνεπών προσομοιώσεων σωματιδίων Particle-In-Cell[11]. Η προσέγγιση αυτή διαπιστώθηκε ότι είναι εξαιρετικά απαιτητική σε υπολογιστικό χρόνο και δεν μπορούσε να επιτρέψει την προσομοίωση μεγάλων χρονικών κλιμάκων που απαιτούνται για την μελέτη αυτών των φαινομένων σε ρεαλιστικές διαμορφώσεις. Επιχειρήθηκε η ασθενής-ισχυρή προσέγγιση στις αναφορές[12, 13], όπου οι δυνάμεις του νέφους ηλεκτρονίων προ-καταγράφηκαν σε ένα διακριτό πλέγμα με βάση προσομοιώσεις της δυναμικής των ηλεκτρονίων Particle-In-Cell. Αν και πολύ ταχύτερα από άποψη από πλευράς χρόνου υπολογισμού, απαιτείται η χρήση ενός σχήματος παρεμβολής για τον υπολογισμό των δυνάμεων σε οποιαδήποτε θέση του σωματιδίου της δέσμης. Σε αυτές τις εργασίες, το ζήτημα της συμπλεκτικότητας δεν είχε αντιμετωπιστεί.

Η μελέτη που παρουσιάζεται στην παρούσα διατριβή προτείνει τη χρήση μιας παρόμοιας προσέγγισης που βασίζεται στην ασθενή-ισχυρή προσέγγιση. Ωστόσο, το σχήμα παρεμβολής επιλέγεται έτσι ώστε να διατηρείται η συμπλεκτική δομή των εξισώσεων κίνησης, προκειμένου να βελτιωθεί η αριθμητική ακρίβεια. Η χρήση συμλεκτικών απεικονίσεων είναι επίσης γνωστό ότι καταστέλλουν την τεχνητή ανάπτυξη ή απόσβεση στις ταλαντώσεις (βητατρονίων και συγχρότρων) των σωματιδίων σε έναν επιταχυντή όπου η κίνηση των σωματιδίων μπορεί να θεωρηθεί Χαμιλτονιανή[14]. Σύμφωνα με την ασθενή-ισχυρή προσέγγιση, το ζήτημα του θορύβου λόγω του διακριτού αριθμού των μακροσωματιδίων που εκφράζουν την κατανομή του ηλεκτρονιακού νέφους ξεπερνιέται με τη μέση τιμή πολλαπλών προσομοιώσεων. Επίσης, ένα σχήμα για τη βελτίωση του δυναμικού που περιγράφει την αλληλεπίδραση του νέφους ηλεκτρονίων αναπτύσσεται προκειμένου να να καταπολεμηθούν οι περιορισμοί του σχήματος παρεμβολής. Με αυτά τα εργαλεία, η δυναμική των πρωτονίων υπό την επίδραση ρεαλιστικών κατανομών νέφους ηλεκτρονίων προσομοιώνεται ενώ χρησιμοποιείται ένα μη-γραμμικό μοντέλο της πολύπλοκης διάταξης του LHC. Οι χρονικές κλίμακες προσομοίωσης εκτείνονται έως και αρκετά λεπτά αποθήκευσης δέσμης στον LHC, παρέχοντας με αυτόν τον τρόπο ποσότητες που μπορούν να παρατηρηθούν στις συνθήκες του πειράματος. Τέλος, η ισχύς από μοντέρνες κάρτες γραφικών (Graphics Processing Units) αξιοποιείται για την παράλληλη προσομοίωση μεγάλου αριθμού πρωτονίων. Ως αποτέλεσμα, προσομοιώνονται ρεαλιστικές κατανομές σωματιδίων μέσω μεγάλης ακρίβειας και συμπλεκτικών μοντέλων τόσο της διάταξης του LHC όσο και των αλληλεπιδράσεων του νέφους ηλεκτρονίων, για ρεαλιστικές χρονικές κλίμακες. Στο πρώτο κεφάλαιο αυτής της διατριβής, δίνεται μια γρήγορη ανασκόπηση της σχετικής δυναμικής των μεμονωμένων σωματιδίων. Αναπτύσσεται ο φορμαλισμός της ιχνηλάτησης σωματιδίων με τη χρήση συμπλεκτικών απεικονίσεων καθώς και το πλαίσιο ανάλυσης της κίνησης αυθαίρετα συζευγμένων σωματιδίων με τη χρήση γραμμικών κανονικών μορφών. Επιπλέον, οι εξισώσεις κίνησης για σωματίδια που εκτελούν συγχρονικές ταλαντώσεις εκφράζονται με τη χρήση ελλειπτικών συναρτήσεων Jacobi, προκειμένου να οριστούν κατανομές σωματιδίων ταιριαστές με την διάταξη του επιταχυντή με τα επιθυμητά χαρακτηριστικά. Στο δεύτερο κεφάλαιο, ο μηχανισμός του νέφους ηλεκτρονίων περιγράφεται και σημειώνονται οι σημαντικότερες παράμετροι για το σχηματισμό του. Παραδείγματα σχηματισμού νεφών ηλεκτρονίων σε διάφορα μαγνητικά πεδία παρουσιάζονται και αναπτύσσεται ο φορμαλισμός των δυνάμεων που ασκούνται στα σωματίδια της δέσμης από το νέφος ηλεκτρονίων. Επίσης παρουσιάζεται μια σύντομη ανασκόπηση των τελευταίων αποτελεσμάτων σχετικά με τα μη-συνεκτικά φαινόμενα των νεφών ηλεκτρονίων. Στο τρίτο κεφάλαιο, μετρήσεις των αργών απωλειών της δέσμης για συγκρουόμενες δέσμες πρωτονίων στον LHC παρουσιάζονται. Η ανάλυση των απωλειών αυτών ανά υποδέσμη αποκαλύπτει ότι το νέφος ηλεκτρονίων είναι ένας σημαντικός παράγοντας που καθορίζει αυτές τις απώλειες. Το τέταρτο κεφάλαιο ασχολείται με μακροχρόνιες προσομοιώσεις συγκρουόμενων δεσμών, την εκτίμηση των απωλειών καθώς και την εξέλιξη των εγκάρσιων κατανομών της δέσμης. Στο πέμπτο κεφάλαιο, το πλαίσιο των προσομοιώσεων με φαινόμενα νέφους ηλεκτρονίων υπό την ασθενής-ισχυρή προσέγγιση αναπτύσσεται και εφαρμόζεται στην περίπτωση πρωτονίων στον LHC σε ενέργεια 450 GeV.

Με την αύξηση της φωτεινότητας που παράγεται σε έναν επιταχυντή σωματιδίων, ο ρυθμός των συγκρούσεων αυξάνεται αναγκαστικά. Προκειμένου να αναλυθούν σωστά οι συγκρούσεις σωματιδίων, οι ανιχνευτές σωματιδίων πρέπει να είναι σε θέση να διακρίνουν μεταξύ διαφορετικών συγκρούσεων. Η παρούσα μελέτη παρουσιάζει ένα στοχαστικό και μη-γραμμικό φαινομενολογικό μοντέλο των χρονικών χαρακτηριστικών των σημάτων που παράγονται στους ανιχνευτές αερίου γεμίσματος. Ειδικότερα, μοντελοποιεί τις αναδυόμενες ιδιότητες του σήματος, οι οποίες οφείλονται στη μετάδοση/ολίσθηση και, ταυτόχρονα, στον πολλαπλασιασμό (καταιονισμό) των ηλεκτρονίων υπό την επίδραση ενός ηλεκτρικού πεδίου. Το μοντέλο αυτό αναπτύσσεται στο πλαίσιο του ανιχνευτή PICOSEC-Micromegas, ο οποίος στοχεύει σε καλύτερη χρονική διακριτική ικανότητα (της τάξης μερικών πικοδευτερολέπτων) στον εντοπισμό της άφιξης των σωματιδίων.

Η διατριβή χωρίζεται σε δύο μέρη. Το πρώτο μέρος είναι αφιερωμένο στη μελέτη των μη-συνεκτικών φαινομένων στον LHC. Στο πρώτο κεφάλαιο του πρώτου μέρους αυτής της διατριβής, γίνεται μια σύντομη ανασκόπηση της σχετικής δυναμικής των μεμονωμένων σωματιδίων. Ο φορμαλισμός της ιχνηλάτησης σωματιδίων με τη χρήση συμπλεκτικών απεικονίσεων αναπτύσσεται καθώς και το πλαίσιο ανάλυσης της κίνησης αυθαίρετα συζευγμένων σωματιδίων με τη χρήση γραμμικών κανονικών μορφών. Επιπλέον, οι εξισώσεις κίνησης για σωματίδια που εκτελούν συγχροτρονικές ταλαντώσεις εκφράζονται με τη χρήση ελλειπτικών συναρτήσεων Jacobi, προκειμένου να οριστούν ταιριαστές κατανομές σωματιδίων με τα επιθυμητά χαρακτηριστικά. Στο δεύτερο κεφάλαιο, ο μηχανισμός της δημιουργίας νέφους ηλεκτρονίων περιγράφεται και σημειώνονται οι σημαντικότερες παράμετροι για το σχηματισμό του. Παραδείγματα σχηματισμού νεφών ηλεκτρονίων σε διάφορα μαγνητικά πεδία παρουσιάζονται και αναπτύσσεται ο φορμαλισμός των δυνάμεων που οδηγούνται από το νέφος ηλεκτρονίων και δρουν στα σωματίδια της δέσμης. Παρουσιάζεται επίσης μια σύντομη ανασκόπηση των πιο πρόσφατων αποτελεσμάτων σχετικά με τα μη-συνεκτικά φαινόμενα που προκαλούνται από νέφη ηλεκτρονίων. Στο τρίτο κεφάλαιο, παρουσιάζονται μετρήσεις των αργών απωλειών της δέσμης για συγκρουόμενες δέσμες πρωτονίων στον LHC. Η ανάλυση των απωλειών αυτών ανά υποδέσμη αποκαλύπτει ότι το νέφος ηλεκτρονίων είναι ένας σημαντικός παράγοντας που καθορίζει αυτές τις απώλειες. Το τέταρτο κεφάλαιο ασχολείται με μακροχρόνιες προσομοιώσεις συγκρουόμενων δεσμών για την εκτίμηση των απωλειών καθώς και την εξέλιξη των κατανομών σωματιδίων στη δέσμη. Στο πέμπτο κεφάλαιο αναπτύσσεται το πλαίσιο προσομοιώσεων με φαινόμενα νέφους ηλεκτρονίων υπό την ασθενή-ισχυρή προσέγγιση και εφαρμόζεται στην περίπτωση των πρωτονίων στον LHC ενέργειας 450 GeV.

Το δεύτερο μέρος της διατριβής εξετάζει το φαινομενολογικό μοντέλο που αναπτύχθηκε για να εξηγήσει τα χαρακτηριστικά χρονισμού της απόκρισης του ανιχνευτή PICOSEC Micromegas. Στο έκτο κεφάλαιο (πρώτο κεφάλαιο του δεύτερου μέρους), δίνεται μια σύντομη επισκόπηση για τον ανιχνευτή PICOSEC Micromegas, συμπεριλαμβανομένης της προηγούμενης επιτυχίας της αναπαραγωγής των χαρακτηριστικών χρονισμού του με λεπτομερείς προσομοιώσεις, και συζητούνται οι βασικές παραδοχές που έγιναν στο μοντέλο. Στο έβδομο κεφάλαιο, μοντελοποιούνται οι μέσοι χρόνοι μετάδοσης των ηλεκτρονίων, όταν εκφράζονται ως συναρτήσεις του μήκους του καταιονισμού ηλεκτρονίων και ως συναρτήσεις του του αριθμού των ηλεκτρονίων στον καταιονισμό. Στο όγδοο κεφάλαιο, μοντελοποιείται η χρονική διακριτική ικανότητα όταν εκφράζεται ως συνάρτηση των δύο προαναφερθέντων μεταβλητών και της επίδρασης των ηλεκτρονίων που διατρέχουν το πλέγμα Micromegas ενσωματώνονται στο μοντέλο. Στο ένατο κεφάλαιο, συζητούνται οι κατανομές που εκφράζουν τα χρονικά χαρακτηριστικά των χρόνων μετάδοσης.

Τέλος, παρουσιάζεται μια σύνοψη των προηγούμενων κεφαλαίων και συζητούνται οι επιπτώσεις για τις μελλοντικές αναβαθμίσεις του LHC καθώς και ο τρόπος με τον οποίο το μοντέλο μπορεί να χρησιμοποιηθεί για την αναβάθμιση του ανιχνευτή PICOSEC Micromegas. Στο Παράρτημα A, το πλεονέκτημα της χρήσης τρικυβικής παρεμβολής απεικονίζεται με την αριθμητική επίλυση των εξισώσεων κίνησης ενός πλέγματος Toda[15], χρησιμοποιώντας απεικονίσεις που βασίζονται σε σχήματα κυβικής και γραμμικής παρεμβολής. Οι αριθμητικές λύσεις συγκρίνονται στη συνέχεια με τις αναλυτικές για να δείξουν ότι η τρικυβική παρεμβολή αποδίδει πολύ καλύτερα στη διατήρηση των ολοκληρωμάτων της κίνησης. Στο Παράρτημα B, αναφέρονται οι συγκλίσεις των μελετών με νέφη ηλεκτρονίων, που δείχνουν ότι οι προσομοιώσεις συγκλίνουν με την επιλογή των αριθμητικών παραμέτρων. Στο προσάρτημα C περιλαμβάνονται πίνακες παραμέτρων για τις μεταβλητές που χρησιμοποιούνται από το αναπτυγμένο φαινομενολογικό μοντέλο του ανιχνευτή PICOSEC Micromegas. Τέλος, στο Παράρτημα D, παρατίθεται ο φορμαλισμός του τρόπου υπολογισμού της διακύμανσης μιας μεταβλητής που εξαρτάται από μια άλλη μεταβλητή.

Η ανάλυση των αργών απωλειών ανά υποδέσμη αποκάλυψε ότι τα μη-συνεκτικα συλλογικά φαινόμενα που προέρχονται από τις αλληλεπιδράσεις δέσμης-δέσμης και τα νέφη ηλεκτρονίων είναι οι κύριες πηγές των απωλειών αργής δέσμης στον LHC. Ειδικότερα, η εισαγωγή της μετωπικής αλληλεπίδρασης δέσμης-δέσμης όταν οι δέσμες τίθενται σε σύγκρουση προκαλεί μια απότομη προσωρινή αύξηση των απωλειών αργής δέσμης, η οποία μειώνεται μέσα στην επόμενη ώρα. Δέσμες στην ουρά των κατανομών της δέσμης φαίνεται να υποφέρουν συστηματικά από υποβαθμισμένη διάρκεια ζωής της δέσμης. Αυτό αποδίδεται σε φαινόμενα νέφους ηλεκτρονίων στις περιοχές εισαγωγής γύρω από τα σημεία αλληλεπίδρασης 1 και 5, όπου στεγάζονται τα πειράματα ATLAS και CMS. Αυτό συνάδει με μια σημαντική πυκνότητα ηλεκτρονίων στην εσωτερική τριπλέτα τετραπόλων (Inner Triplet), η οποία επίσης ενισχύεται σημαντικά από την παρουσία των δύο δέσμων στον ίδιο θάλαμο κενού. Χρησιμοποιήθηκαν προσομοιώσεις ιχνηλάτησης προκειμένου να προβλεφθεί η υποβάθμιση από τέτοιου είδους μη-συνεκτικές συλλογικές επιδράσεις. Λόγω της πρόσφατης προόδου στην ανάπτυξη λογισμικού προσομοίωσης ιχνηλάτησης, οι κάρτες γραφικών μπορούσαν να χρησιμοποιηθούν ώστε να επιτευχθεί σημαντική αύξηση της ταχύτητας υπολογισμού, όπου τα σωματίδια παρακολουθούνται παράλληλα σε όλη τη διάταξη του LHC και συμπεριλαμβανομένου των σχετικών συλλογικών φαινομένων (αλληλεπιδράσεις δέσμης- δέσμης ή φαινόμενα νέφους ηλεκτρονίων). Μια πρώτη προσπάθεια στη χρήση προσομοιώσεων παρακολούθησης σωματιδίων ήταν η αναπαραγωγή της συμπεριφοράς στις αργές απώλειες δέσμης όταν οι δύο δέσμες συγκρούονται. Η μελέτη έδειξε ότι, μέσω της αύξησης στην υπολογιστική ισχύ, οι παρατηρήσιμες ποσότητες όπως ο ρυθμός αργών απωλειών της δέσμης και η αύξηση της εκπεμπτικότητας μπορούν να προσομοιωθούν με προσομοιώσεις ιχνηλάτησης σωματιδίων σε ρεαλιστικές χρονικές κλίμακες, της τάξης αρκετών λεπτών, έως και μισής ώρας. Επιπλέον, η συμπεριφορά των αργών απωλειών της δέσμης λόγω της εισαγωγής της μετωπικής αλληλεπίδρασης δέσμης-δέσμης, αναπαράχθηκε με επιτυχία στις προσομοιώσεις. Ένας σημαντικός περιορισμός στην ποσοτική πρόβλεψη των αργών απωλειών της δέσμης διαπιστώθηκε ότι είναι η αβεβαιότητα στον πληθυσμό των ουρών των εγκάρσιων κατανομών σωματιδίων της δέσμης, για την οποία δεν υπάρχει ακριβής και συστηματική μέτρηση. Σημαντικό βήμα προόδου έγινε στις προσομοιώσεις των μη-συνεκτικών φαινομένων του νέφους ηλεκτρονιων. Οι μετρήσεις των απωλειών της αργής δέσμης καθώς και της αύξησης της εκπεμπτικότητας αποκάλυψαν ότι το μέγεθος αυτών των φαινομένων είναι αρκετά μικρό ώστε να επιτρέπεται η χρήση της ασθενούς-ισχυρής προσέγγισης. Επιπλέον, διαπιστώθηκε ότι η χρήση καρτών γραφικών παρέχει το κατάλληλο υπολογιστικό περιβάλλον για την εκτέλεση προσομοιώσεων λόγω της μαζικά παράλληλης αρχιτεκτονικής τους με σχετικά μεγάλη μνήμη (σε σύγκριση με τη διαθέσιμη μνήμη σε έναν τυπικό μονο- πύρηνο κόμβο CPU ενός υπολογιστικού συμπλέγματος). Η σχετικά μεγάλη μνήμη απαιτείται λόγω του μεγάλου αποτυπώματος μνήμης (της τάξης των αρκετών GB) της απεικόνισης που περιγράφει μια αλληλεπίδραση με ένα νέφος ηλεκτρονίων. Η απαιτούμενη μνήμη είναι τόσο μεγάλη επειδή η δυναμική των ηλεκτρονίων στο εσωτερικό της κατανομής ενός νέφους ηλεκτρονίων δημιουργεί πολύπλοκα ηλεκτρομαγνητικά πεδία που εξαρτώνται από τον χρόνο. Μια αναλυτική προσέγγιση αυτών των πεδίων γίνεται όλο και πιο δύσκολη, ιδίως σε παρουσία κλίσεων μαγνητικού πεδίου. Κατά συνέπεια, προσομοιώσεις Particle-In-Cell χρησιμοποιούνται για την εύρεση αυτών των χρονοεξαρτώμενων ηλεκτρομαγνητικών πεδίων σε ένα διακριτό πλέγμα. Το γεγονός ότι τα πεδία είναι γνωστά μόνο σε ένα διακριτό πλέγμα απαιτεί ιδιαίτερη προσοχή εάν η δυναμική της δέσμης πρέπει να προσομοιωθεί με την παρουσία τους. Η Χαμιλτονιάνη δομή της δυναμικής των πρωτονίων της δέσμης υποδηλώνει ότι η χρήση συμπλεκτικών απεικονίσεων μπορεί να αυξήσει σημαντικά την ακρίβεια στην αριθμητική επίλυση των εξισώσεων κίνησης των πρωτονίων που ταξιδεύουν στη διάταξη του LHC. Για το σκοπό αυτό, αναπτύχθηκε μια μέθοδος που χρησιμοποιεί ένα σχήμα τρικυβικής παρεμβολής στα διακριτά σημεία των πεδίων του νέφους ηλεκτρονίου, προκειμένου να διατηρηθεί η συμπλεκτική δομή της απεικόνισης που περιγράφει την αλληλεπίδραση με το νέφος ηλεκτρονίου. Επίσης, αναπτύσσεται μια αριθμητική μέθοδος που μπορεί και καταστέλλει αποτελεσματικά συστηματικά αριθμητικά σφάλματα που εισάγονται κατά το στάδιο της παρεμβολής. Χρησιμοποιώντας την αναπτυχθείσα μέθοδο, πραγματοποιήθηκαν προσομοιώσεις ιχνηλάτησης σωματιδίων για πρωτόνια σε ενέργεια 450 GeV στο πλέγμα του LHC, υπό την επίδραση μη-συνεκτικών φαινομένων από νέφη ηλεκτρονίων στα τόξα της διάταξης του LHC. Τα αποτελέσματα έδειξαν ότι οι δείκτες μη-γραμμικής δυναμικής της δέσμης όπως το δυναμικό εύρος και η ανάλυση απεικόνισης συχνοτήτων μπορούν να επηρεαστούν σημαντικά από την επίδραση του νέφους ηλεκτρονίων. Επιπλέον, παρατηρήθηκε υποβάθμιση του χρόνου ημιζωής της δέσμης αν και η ποσοτική πρόβλεψη περιορίστηκε και πάλι από την αβεβαιότητα στις ουρές των των εγκάρσιων κατανομών της δέσμης. Από την άλλη πλευρά, οι προσομοιώσεις έδειξαν μια συνεχή αύξηση της εκπεμπτικότητας της ίδιας τάξης μεγέθους με εκείνη που παρατηρήθηκε σε προηγούμενες μετρήσεις που αναφέρονται στο βιβλιογραφία. Αυτή είναι η πρώτη φορά που λεπτομερείς προσομοιώσεις του μη-συνεκτικού φαινομένου των νεφών ηλεκτρονίων έχουν πραγματοποιηθεί παρουσία του μη-γραμμικού μοντέλου του πλέγματος του LHC, για μεγάλες και παρατηρήσιμες χρονικές κλίμακες, και παρουσία πολλαπλών πηγών νέφους ηλεκτρονίων, δηλαδή νέφη ηλεκτρονίων που σχηματίζονται σε διπολικά και τετραπολικά μαγνητικά πεδία. Οι μελέτες αυτές αποκτούν όλο και μεγαλύτερη σημασία λόγω της αυξημένης ανησυχίας από την επίδραση νέφων ηλεκτρονίων στην λειτουργία του LHC. Σε κάθε μια από τις συντηρήσεις μακράς διακοπής λειτουργίας του LHC, η απόδοση στη δευτερογενή εκπομπή ηλεκτρονίων του θαλάμου κενού παρατηρείται ότι υφίσταται μη-αναστρέψιμη υποβάθμιση. Η μεγαλύτερη απόδοση δευτερογενούς εκπομπής ηλεκτρονίων έχει ως αποτέλεσμα ισχυρότερα νέφη ηλεκτρονίων τα οποία μπορούν γρήγορα να οδηγήσουν σε μείωση του δυναμικού εύρους. Επιπλέον, ισχυρότερα νέφη ηλεκτρονίων απαιτούν ισχυρότερες μη-γραμμικότητες στα μαγνητικά πεδία της διάταξης του LHC (χρωματικότητα και εύρος στην συχνότητα ταλαντώσεων σωματιδίων) προκειμένου να ελεγχθούν οι συνεκτικές αστάθειες της δέσμης που προκαλούνται από το ίδιο το νέφος ηλεκτρονίων. Αυτές οι ισχυρότερες μη-γραμμικότητες μπορούν να υποβαθμίσουν ακόμη περισσότερο το δυναμικό εύρος. Κατά τη διάρκεια αυτής της μελέτης, τα νέφη ηλεκτρονίων στα τετράπολα της εσωτερικής τριπλέτας έχουν εντοπιστεί ως η κύρια πηγή σημαντικής υποβάθμισης του χρόνου ημιζωής της δέσμης κατά τη λειτουργία του LHC. Στο πλαίσιο της αναβάθμισης του LHC υψηλής φωτεινότητας, τα τετράπολα της εσωτερικής τριπλέτας σχεδιάζεται να αντικατασταθούν. Οι επιφάνειες του θαλάμου κενού των νέων τετραπόλων της εσωτερικής τριπλέτας θα επικαλυφθούν με άμορφο άνθρακα, ώστε να περιοριστεί ο σχηματισμός νεφών ηλεκτρονίων.

Στο πλαίσιο της μοντελοποίησης των χαρακτηριστικών χρονισμού του ανιχνευτή PICOSEC Micromegas, η παρούσα εργασία χρησιμοποιεί τη σύγκριση πειραματικών δεδομένων με λεπτομερείς προσομοιώσεις, βασισμένες στο λογισμικό GARFIELD++, και συμπληρωμένες με μια στατιστική περιγραφή του σχηματισμού του ηλεκτρονικού σήματος, για τον προσδιορισμό των μικροσκοπικών μεγεθών που καθορίζουν τα χαρακτηριστικά χρονισμού του PICOSEC. Στη συνέχεια, αναπτύσσεται ένα στοχαστικό μοντέλο που περιγράφει τις ιδιότητες των παραπάνω ποσοτήτων, προσφέροντας μια φαινομενολογική, μικροσκοπική ερμηνεία των παρατηρούμενων ιδιοτήτων χρονισμού του ανιχνευτή. Το μοντέλο βασίζεται σε:

1. Το γεγονός ότι ένα ηλεκτρόνιο που ολισθαίνει σε ένα αέριο υπό την επίδραση ενός ομογενούς ηλεκτρικού πεδίου επιτυγχάνει μεγαλύτερη ταχύτητα ολίσθησης όταν, εκτός από την ελαστική σκέδαση, υφίσταται και ανελαστικές αλληλεπιδράσεις,
2. Την υπόθεση ότι ένα νεοπαραγόμενο ηλεκτρόνιο μέσω ιονισμού αποκτά ένα ορισμένο χρονικό κέρδος σε σχέση με τον γονέα του και στη συνέχεια παρασύρεται με την ίδια ταχύτητα με το γονέα ηλεκτρόνιο.

Οι παράμετροι εισόδου του μοντέλου είναι κοινώς χρησιμοποιούμενες στατιστικές μεταβλητές, με εξαίρεση την παράμετρο του χρονικού κέρδους που έχει εισαχθεί εδώ, και έχουν προσδιοριστεί με την ανάλυση των αποτελεσμάτων προσομοίωσης του GARFIELD++. Οι ποσοτικές προβλέψεις του μοντέλου συγκρίθηκαν εκτενώς με τα σχετικά αποτελέσματα προσομοίωσης GARFIELD++ και διαπιστώθηκε ότι βρίσκονται σε εξαιρετική συμφωνία σε όλες τις συνθήκες λειτουργίας του PICOSEC που εξετάστηκαν στην παρούσα μελέτη, αποδεικνύοντας την επιτυχία αυτής της στοχαστικής ερμηνείας. Όπως επιδεικνύεται μέσω της παρούσας εργασίας, το μοντέλο που αναπτύχθηκε είναι πολύ επιτυχημένο στην παροχή πληροφοριών για τους κύριους μικροσκοπικούς μηχανισμούς που καθορίζουν τα χαρακτηριστικά του χρονισμού του ανιχνευτή, και στην συνεκτική εξήγηση της απροσδόκητης συμπεριφοράς μικροσκοπικών μεγεθών, τα οποία έχουν ήδη παρατηρήθηκαν στις προσομοιώσεις GARFIELD++. Λόγω της πολύ καλής συμφωνίας των προβλέψεων του μοντέλου με το GARFIELD++, οι τύποι που αναπτύχθηκαν εδώ μπορούν να χρησιμοποιηθούν ως εργαλείο για γρήγορες προβλέψεις, υπό την προϋπόθεση ότι οι τιμές των παραμέτρων εισόδου του μοντέλου είναι γνωστές για τις εξεταζόμενες συνθήκες λειτουργίας. Αυτό περιορίζει την εφαρμογή του μοντέλου που αναπτύχθηκε ως αυτόνομο εργαλείο. Ωστόσο, με διαθέσιμες τιμές των παραμέτρων εισόδου για ορισμένες λειτουργικές ρυθμίσεις, είναι δυνατόν να παραμετροποιηθούν εμπειρικά, ώστε να χρησιμοποιηθούν για να παρέχουν δεδομένα εισόδου στο μοντέλο για μια ευρύτερη περιοχή λειτουργικών ρυθμίσεων που καλύπτονται από την ανωτέρω παραμετροποίηση.

Contents

List of Tables

List of Figures

Introduction

In the quest for describing the fundamental laws of physics that describe nature, physicists have turned to the usage of particle accelerators in order to perform controlled experiments with high energy particles.

The design of the accelerator is typically centered around its “optics”. The optics consist essentially in the specific powering of each magnet in order to achieve a certain aim. For example, the main quadrupole magnets are powered such that the oscillations of the protons do not exceed the available aperture inside the vacuum chamber. In another fashion, strong quadrupoles are placed around the colliding points in the accelerator, which are powered in such a way that the beam size is small in the interaction point of the two beams, hence increasing the proton density and therefore the number of collisions.

From the beam physics point of view, special care has to be taken in order to avoid effects that are deleterious to the stable motion of the protons inside a high-energy circular accelerator. An important category of such deleterious effects are those called single-particle non-linear effects and are typically related to non-linear magnetic fields in the lattice of the accelerator. High-order magnets (sextupole, octupole, decapole, e.t.c.) are employed to correct the possible non-linear imperfections in the fields of the magnets. Moreover, sextupole and octupole magnets are typically used to induce a relation between the oscillation frequency of a proton with its energy or its amplitude of oscillation. The control of this relation is essential in order to prevent coherent beam instabilities, an effect which belongs in the category of collective effects.

By definition, collective effects are those which are driven by the fact that multiple particles are present inside the accelerator. Some examples of such effects follow. The direct interaction between the different particles in the same beam is typically referred to as “direct space-charge effect[27]”. The direct interaction between different particles of different beams (at the point where the beams collide) are called “beam-beam effects[28]”. The protons can also interact indirectly. For example, the geometric boundaries of the beam chamber (assuming perfect conductivity) introduce the effect of “indirect space-charge effects[27]”, which are typically described by image currents. Moreover, chambers with resistive walls or sudden transitions in their geometry can induce effects of “beam-induced wakefields[29]”. Another kind of indirect interaction is that of electron cloud effects[30]. The beam itself can favor the accumulation of trapped electrons within the walls of the beam chamber, if the material of the beam chamber wall meets certain conditions and allows the multiplication of electrons. In the presence of electron cloud effects, the particle beam and the cloud of electrons interact with each other.

All of the above effects can influence the coherent stability of the beam, where the beam particles perform coherent oscillations which feed back into the beam particles, increasing each time the amplitude of the oscillations[31]. However, even when the coherent beam instabilities are controlled, the induced electromagnetic fields from these effects are typically non-linear. These non-linear electromagnetic fields induce non-linearities in the trajectories of the individual beam particles, similar to the aforementioned single-particle effects. In this case, they are called incoherent effects.

Most incoherent effects lead to a very slow increase of the beam emittances and a decrease of the beam lifetime. Incoherent effects have a typically complex description and their outcome is only observable on long time scales, which are usually out of reach in simulations.

In this thesis, incoherent effects observed at the Large Hadron Collider (LHC)[1] are studied. The LHC is the largest collider to date with the highest centre-of-mass energy reach. It is a synchrotron, with an arrangement of repeating FODO (Focusing-Defocusing) cells consisting the vast majority of its layout, which is split into 8 arcs and 8 insertion regions (IR). While the 8 arcs consist almost entirely of FODO cells, a variety of equipment is included in the IR regions. Of particular importance are the Insertion Region 1 (IR1), Insertion Region 2 (IR2), Insertion Region 5 (IR5) and the Insertion Region 8 (IR8), where the detectors ATLAS[2], ALICE[3], CMS[4] and LHCb[5] are positioned, respectively. The aim of the LHC is to collide protons (or other hadrons) at the center of each of these detectors. A quantity that is independent of the frame of reference and is very much related to the number of collisions is the luminosity L, which for two head-on colliding beams with Gaussian profiles can be calculated by the overlapping integral between the density of protons in the two colliding bunched beams [32]:

$$L = \frac{N_1 N_2 f N_b}{4\pi\sigma_x\sigma_y}, \tag{1}$$

where N_1 and N_2 are the two bunch populations, f is the revolution frequency of the particles, N_b is the number of bunches in the beam, while σ_x and σ_y are the horizontal and vertical r.m.s. beam sizes. Several other factors affect the luminosity like crossing angles between the two beams, collision offsets, non-Gaussian beam profiles, among others. However, it is clear that a smaller beam size and a higher bunch population increase the luminosity produced. By minimizing the emittance growth, which is directly related to the beam size, and maximizing the beam lifetime, luminosity and therefore "physics production" is increased.

The study presented here concerns the incoherent collective effects which are degrading the beam lifetime and causing an increase of the emittance in the proton beams at the LHC. The two most important effects of this type are found to be beam-beam interactions and electron cloud effects. Simulations of incoherent beam-beam effects have a long history based on the formalism developed in Ref. [6] and using a weak-strong approximation. The weak-strong approximation refers to simulations where a "weak" particle is studied under the influence of a "strong" force which cannot be influenced by the "weak" particle. This is an approximation that is well suited to slow incoherent effects due to the fact that they cause only small changes in beam profiles. In this way, the electromagnetic fields produced by another beam (in beam-beam interactions) or by an electron cloud can be calculated once, and used to solve multiple times the equations of motion of the "weak" particle under their influence.

The history of incoherent electron cloud effects dates back to the last two decades. Early simulation results consist of calculations of tune spreads, distortions of betatron functions and dispersion as well as synchro-betatron coupling[7, 8, 9]. Some attempts were made to describe the evolution of the electron cloud using simplified models [10] and compute the forces induced on the beam particles analytically. These approaches were found convenient in terms of computation time but they could not describe realistic electron cloud distributions in the presence of magnetic field gradients. Attempts to study the incoherent effect of electron cloud through self-consistent Particle-In-Cell (PIC) simulations of particles[11] were also made. This approach was found to be extremely demanding in computational time and could not allow the simulation of long time scales required for the study of these effects in realistic configurations. The weak-strong approach was attempted in Refs. [12, 13] where the electron cloud forces were pre-recorded on a discrete grid based on Particle-In-Cell electron dynamics simulations. Although, much faster in terms of computation time, an interpolation scheme was required to compute the forces on an arbitrary location of the beam particle. In those works, the issue of symplecticity was not addressed.

The study that is presented in this thesis proposes the use of a similar approach based on the weak-strong approximation. However, the interpolation scheme is chosen such that the symplectic structure of the equations of motion is preserved in order to improve the numerical accuracy. The usage of a symplectic map is also known to suppress artificial growth or damping in the (betatron and synchrotron) oscillations of particles in an accelerator where particle motion can be considered Hamiltonian [14]. Under the weak-strong approximation, the issue of noise due to the discrete number of macroparticles expressing the electron cloud distribution is overcome by averaging multiple simulations. A scheme to refine the potential describing the electron cloud interaction is also developed in order to combat the limitations of the interpolation scheme. With these tools in hand, the proton dynamics under the influence of realistic electron cloud distributions is simulated while employing a non-linear model of the complex LHC lattice. The simulation time-scales extend up to several minutes of beam storage in the LHC, providing this way quantities that can be observed in the experiment conditions. Finally, the power of Graphics Processing Units is leveraged in order to simulate a large number of protons in parallel. As an outcome, realistic particle distributions are simulated through accurate and symplectic models of both the LHC lattice and the electron cloud interactions, for realistic timescales.

By increasing the luminosity produced in a particle collider, the rate of events necessarily increases. In order to properly analyse the particle collisions, particle detectors need to be able to distinguish between different collisions. This study presents a stochastic and non-linear phenomenological model of the timing characteristics of signals produced in gas-based detectors. In particular, it models the emerging properties of the signal, which are due to the transmission/drift and, at the same time, multiplication (avalanche) of the electrons under the influence of an applied electric field. This model is developed in the context of the PICOSEC-Micromegas detector which aims at a better timing resolution (in the order of several picoseconds) in pinpointing the arrival of particles.

The thesis is split into two major parts. The first part is devoted to the study of incoherent effects in the LHC. In the first chapter of the first part of this thesis, a quick review of the relevant single-particle dynamics is given. The formalism of particle tracking using symplectic maps is developed as well as the framework of analysing arbitrarily coupled particle motion using linear normal forms. Moreover, the equations of motion for particles performing synchrotron oscillations are expressed using Jacobi elliptic functions in order to define matched particle distributions with the desired characteristics. In the second chapter, the mechanism of electron cloud buildup is described and the most relevant parameters to its formation are noted. Examples of electron clouds forming in various magnetic field are shown and the formalism of electron cloud-driven forces acting on beam particles is laid out. A short review is also presented on the latest results concerning incoherent electron clouds effects. In the third chapter, measurements of slow beam losses for colliding proton beams in the LHC are presented. The bunch-by-bunch analysis of these losses reveals that electron cloud is a significant factor determining these losses. The fourth chapter is concerned with long-term simulations of colliding beams and the estimation of losses as well as the evolution of the beam profiles. In the fifth chapter, the framework of simulations with electron cloud effects under the weak-strong approximation is developed and applied to the case of protons in the LHC at injection energy.

The second part of the thesis discusses the phenomenological model that is developed to explain the timing characteristics of the PICOSEC Micromegas detector response. In the sixth chapter (first chapter of the second part), a quick overview is given about the PICOSEC Micromegas detector including the previous success of reproducing its timing characteristics with detailed microscopic simulations, and discusses the basic assumptions made in the model. In the seventh chapter, the mean transmission times of the electrons are modelled, when expressed as functions of the length of the electron avalanche and as functions of the number of electrons in the avalanche. In the eighth chapter, the timing resolution is modelled when expressed as the function of the two aforementioned variables and the effect of the electrons traversing through the Micromegas mesh are incorporated in the model. In the ninth chapter, the distributions that express the timing characteristics of the transmission times are discussed.

Finally, the conclusion presents a summary of the previous chapters and discusses implications for the future upgrades in the LHC and how the model can be used to upgrade the PICOSEC Micromegas detector. In Appendix A, the advantage of using tricubic interpolation is illustrated by solving numerically the equations of motion of a Toda lattice[15], using maps based on cubic and linear interpolation schemes. The numerical solutions are then compared to the analytical ones to show that tricubic interpolation performs much better in preserving the integrals of motion. In Appendix B, the convergence of studies with electron clouds are reported, showing that the simulations are converged with the choice of the numerical parameters. In Appendix C, parameter tables are included for the variables used by the developed phenomenological model. Finally, Appendix D, lays out the formalism of how the variance of a variable dependent on another variable can be calculated.

Part I

Incoherent effects in the Large Hadron Collider

Chapter 1

Single-particle dynamics

1.1 Relativistic particles in electromagnetic fields

A relativistic particle of mass m, charge q and with momentum $\mathbf{p} = (p_x, p_y, p_z)$ in an electromagnetic field associated to a scalar potential $\mathbf{\Phi}$ and vector potential $\mathbf{A} = (A_x, A_y, A_z)$ moves according to the Hamiltonian[33, 34]

$$H = c\sqrt{(\mathbf{P} - q\mathbf{A})^2 + m^2c^2} + q\Phi, \tag{1.1}$$

where c is the speed of light and $\mathbf{P} = (P_x, P_y, P_z)$ is the canonical momentum [1] defined as:

$$P_x = p_x + qA_x, \tag{1.2}$$

$$P_y = p_y + qA_y, \tag{1.3}$$

$$P_z = p_z + qA_z. \tag{1.4}$$

The Hamiltonian H expresses the total energy of the particle with:

$$H = \mathcal{E} + q\Phi, \tag{1.5}$$

with $\mathcal{E} = \gamma mc^2$ and $\gamma = (1 - \beta^2)^{1/2}$, where β is the ratio of the particle's speed to the speed of light. The differential equations that govern the particle's motion are:

$$\frac{\mathrm{d}X}{\mathrm{d}t} = \frac{\partial H}{\partial P_x}, \tag{1.6}$$

$$\frac{\mathrm{d}P_x}{\mathrm{d}t} = -\frac{\partial H}{\partial X}, \tag{1.7}$$

$$\frac{\mathrm{d}Y}{\mathrm{d}t} = \frac{\partial H}{\partial P_y}, \tag{1.8}$$

$$\frac{\mathrm{d}P_y}{\mathrm{d}t} = -\frac{\partial H}{\partial Y}, \tag{1.9}$$

$$\frac{\mathrm{d}Z}{\mathrm{d}t} = \frac{\partial H}{\partial P_z}, \tag{1.10}$$

$$\frac{\mathrm{d}P_z}{\mathrm{d}t} = -\frac{\partial H}{\partial Z}, \tag{1.11}$$

---

[1] It is reminded that the canonical variables are those variables for which the equations of motion can be derived from the Hamiltonian in the form of Eqs. (1.6)-(1.11).

where the time t is the independent variable and X, Y, Z are the physical cartesian coordinates.

In an accelerator beam line, the electromagnetic fields come from dedicated static components, e.g. magnets. If an accelerator beam line is considered such that the components are aligned along the Z coordinate, it is convenient to make a change of variable such that Z is the independent variable. This way the equations of motion can be integrated from one accelerator component to another.

The change of independent variable can be done by recalling the stationary-action principle, which states that a system's equations of motion are defined such that the action is stationary along the system's trajectory. Instead of considering the action that is defined by the path integral in time from t_A to t_B of the corresponding Lagrangian:

$$S = \int_{t_A}^{t_B} L \, \mathrm{d}t = \int_{t_A}^{t_B} P_x \frac{\mathrm{d}X}{\mathrm{d}t} + P_y \frac{\mathrm{d}Y}{\mathrm{d}t} + P_z \frac{\mathrm{d}Z}{\mathrm{d}t} - H \, \mathrm{d}t, \tag{1.12}$$

a change of variable is made to express the action as path integral in the coordinate Z from Z_A to Z_B:

$$S = \int_{Z_A}^{Z_B} L \frac{\mathrm{d}t}{\mathrm{d}Z} \, \mathrm{d}Z = \int_{Z_A}^{Z_B} P_x \frac{\mathrm{d}X}{\mathrm{d}Z} + P_y \frac{\mathrm{d}Y}{\mathrm{d}Z} + H \frac{\mathrm{d}(-t)}{\mathrm{d}Z} - (-P_z) \, \mathrm{d}Z. \tag{1.13}$$

By comparing Eqs. 1.12 and 1.13, the change of independent variable is accomplished by considering $-P_z$ as the new Hamiltonian. In the comparison, it also possible to see that the new pair of canonical conjugate variables is the $(-t, H)$ pair. By rearranging Eq. 1.1 and renaming H as E, it follows that

$$-P_z = -\sqrt{\frac{(E - q\Phi)^2}{c^2} - (P_x - qA_x)^2 - \left(P_y - qA_y\right)^2 - m^2c^2} - qA_z. \tag{1.14}$$

Typically the involved magnetic fields are complex, and analytical solutions for the equations of motion are difficult to find. In fact, in the most general case, the equations of motion are non-integrable, *i.e.* their analytical solutions do not even exist, and can lead to chaotic dynamics. It is therefore necessary to employ numerical methods to solve the equations of motion. To assist the numerical integration process, new variables can be defined such that they remain small as the particle propagates along the beam line. Initially the Hamiltonian is divided by a reference momentum P_0 to define a new Hamiltonian:

$$H_1 = \frac{-P_z}{P_0} \tag{1.15}$$

Although, the reference momentum can take any value, it is convenient to have it be equal to the momentum of the ideal particle for which the accelerator is designed. Equation 1.14 becomes

$$H_1 = -\sqrt{\frac{(E - q\Phi)^2}{P_0^2c^2} - \frac{(P_x - qA_x)^2}{P_0^2} - \frac{\left(P_y - qA_y\right)^2}{P_0^2} - \frac{m^2c^2}{P_0^2}} - \frac{qA_z}{P_0}. \tag{1.16}$$

After this scaling, Hamilton's equations will hold for the following pairs of canonical conjugate pairs.

$$X,\;\; \tilde{P}_x = \frac{P_X}{P_0}, \tag{1.17}$$

$$Y,\;\; \tilde{P}_y = \frac{P_y}{P_0}, \tag{1.18}$$

$$-t,\;\; \tilde{E} = \frac{E}{P_0}. \tag{1.19}$$

To ease notation, scaled potentials can be defined as:

$$\phi = \frac{q\Phi}{P_0 c}, \tag{1.20}$$

$$a_x = \frac{qA_x}{P_0}, \tag{1.21}$$

$$a_y = \frac{qA_y}{P_0}, \tag{1.22}$$

$$a_z = \frac{qA_z}{P_0}. \tag{1.23}$$

The Hamiltonian of Eq. (1.16) expressed in the newly defined variables becomes:

$$H_1 = -\sqrt{\left(\frac{\tilde{E}}{c} - \phi\right)^2 - \left(\tilde{P}_x - a_x\right)^2 - \left(\tilde{P}_y - a_y\right)^2 - \frac{m^2c^2}{P_0^2}} - a_z. \tag{1.24}$$

The coordinate that is related to time is rather inconvenient as it will be constantly increasing. An additional transformation is made to use instead a variable related to time that also expresses the longitudinal distance of a particle with respect to the ideal reference particle. In order to ensure that the canonical form for the equations of motion is preserved, a generating function of the second kind is employed. These kind of functions are of the form

$$F_2 = F_2(q_i, P_i; s), \tag{1.25}$$

where the pairs of the old canonical variables (q_i, p_i) are related to the pairs of the new canonical variables (Q_i, P_i) and where s is the independent variable. The old and new variables are defined from the relations:

$$p_i = \frac{\partial F_2}{\partial q_i}, \tag{1.26}$$

$$Q_i = \frac{\partial F_2}{\partial P_i}, \tag{1.27}$$

$$K = H + \frac{\partial F_2}{\partial s},. \tag{1.28}$$

Here Eq. (1.28) relates the old Hamiltonian H to the new Hamiltonian K. The particular generating function of the second kind that is interesting in this case is:

$$F_2(q_1, P_1, q_2, P_2, q_3, P_3; s) = q_1P_1 + q_2P_2 + \left(\frac{s}{\beta_0} + cq_3\right)\left(\frac{1}{\beta_0} + P_3\right), \tag{1.29}$$

where β_0 is a constant equal to the β factor of the ideal reference particle. By substituting this F_2 in Eqs. (1.26)-(1.28), we obtain:

$$p_1 = P_1, \tag{1.30}$$

$$p_2 = P_2, \tag{1.31}$$

$$p_3 = c\left(\frac{1}{\beta_0} + P_3\right), \tag{1.32}$$

$$Q_1 = q_1, \tag{1.33}$$

$$Q_2 = q_2, \tag{1.34}$$

$$Q_3 = \frac{s}{\beta_0} + cq_3, \tag{1.35}$$

$$K = H + \frac{1}{\beta_0^2} + \frac{P_3}{\beta_0}. \tag{1.36}$$

Replacing the old variables, the Hamiltonian and renaming the independent variable from z to s, the system of equations becomes:

$$P_1 = \tilde{P}_x, \tag{1.37}$$

$$P_2 = \tilde{P}_y, \tag{1.38}$$

$$P_3 = \frac{\tilde{E}}{c} - \frac{1}{\beta_0}, \tag{1.39}$$

$$Q_1 = x, \tag{1.40}$$

$$Q_2 = y, \tag{1.41}$$

$$Q_3 = \frac{s}{\beta_0} - ct, \tag{1.42}$$

$$K = H_1 + \frac{1}{\beta_0^2} + \frac{P_3}{\beta_0}. \tag{1.43}$$

To ease notation once more, the new variables are renamed as:

$$p_x = \tilde{P}_x, \tag{1.44}$$

$$p_y = \tilde{P}_y, \tag{1.45}$$

$$p_\tau = \frac{\tilde{E}}{c} - \frac{1}{\beta_0}, \tag{1.46}$$

$$\tau = \frac{s}{\beta_0} - ct, \tag{1.47}$$

$$K = H_1 + \frac{1}{\beta_0^2} + \frac{p_\tau}{\beta_0}. \tag{1.48}$$

Finally, the Hamiltonian is renamed to H, the longitudinal component of the vector potential a_z is renamed to match the independent variable s and the constant term $1/\beta_0^2$ is dropped as it does not contribute to the dynamics of the particle. The Hamiltonian is finally written as:

$$H = \frac{p_\tau}{\beta_0} - \sqrt{\left(p_\tau + \frac{1}{\beta_0} - \phi\right)^2 - (p_x - a_x)^2 - \left(p_y - a_y\right)^2 - \frac{1}{\beta_0^2\gamma_0^2}} - a_s \tag{1.49}$$

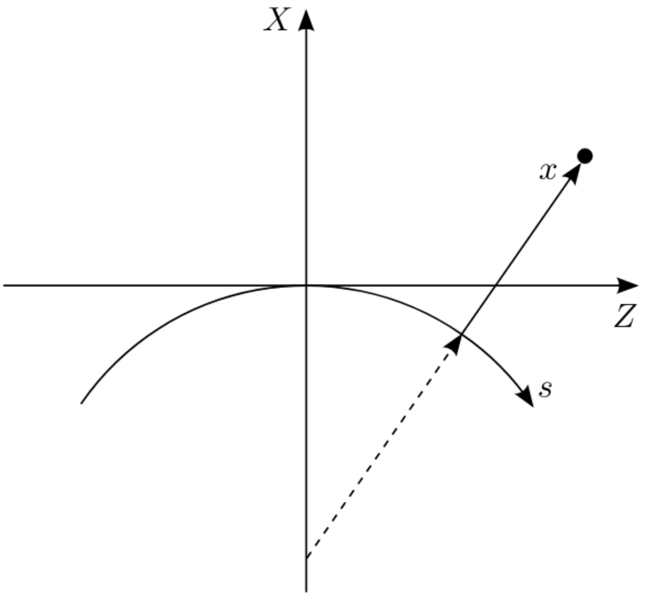

Figure 1.1: Curved coordinates system with respect to the Cartesian coordinate system. Figure adapted from Ref. [14].

1.1.1 Curved coordinate system

So far the beam line has been assumed to be straight. Instead, circular accelerators have, by definition, components that bend the trajectory of particles. It is therefore important that the independent variable s measures the distance in the curved path that an ideal particle would follow when moving through such components. For simplicity only a curvature in the horizontal plane is assumed here and we call ρ the curvature radius of the trajectory. The cartesian coordinates (X, Y, Z) are related to the curved coordinates (x, y, s) through the relations:

$$X = (x + \rho) \cos\left(\frac{s}{\rho}\right) - \rho, \tag{1.50}$$

$$Y = y, \tag{1.51}$$

$$Z = (x + \rho) \sin\left(\frac{s}{\rho}\right). \tag{1.52}$$

To properly transform the coordinate system and preserve the Hamiltonian structure of the equations, a mixed-variable generating function of the third kind is used:

$$F_3 = F_3(p_i, Q_i; t) \tag{1.53}$$

where the old variables, the new variables and the new Hamiltonian are defined through the relations:

$$q_i = -\frac{\partial F_3}{\partial p_i}, \tag{1.54}$$

$$P_i = -\frac{\partial F_3}{\partial Q_i}, \tag{1.55}$$

$$K = H + \frac{\partial F_3}{\partial t}. \tag{1.56}$$

The generating function that produces the transformation in Eqs. (1.50)-(1.51) is:

$$F_3 = -\left((Q_1 + \rho)\cos\left(\frac{Q_3}{\rho}\right) - \rho\right) p_1 - Q_2 p_2 - (Q_1 + \rho)\sin\left(\frac{Q_3}{\rho}\right) p_3. \tag{1.57}$$

Applying the transformation from the Cartesian coordinate system (old) to the curved coordinate system (new) the momenta are transformed as:

$$P'_x = P_X \cos\left(\frac{s}{\rho}\right) + P_Z \sin\left(\frac{s}{\rho}\right), \tag{1.58}$$

$$P'_y = P_Y, \tag{1.59}$$

$$P'_s = P_Z\left(1 + \frac{x}{\rho}\right)\cos\left(\frac{s}{\rho}\right) + P_X\left(1 + \frac{x}{\rho}\right)\sin\left(\frac{s}{\rho}\right),. \tag{1.60}$$

Finally, the vector potential should be transformed as well to match the components in the new coordinate system, where the vector potential becomes:

$$A_x = A_X \cos\left(\frac{s}{\rho}\right) + A_Z \sin\left(\frac{s}{\rho}\right), \tag{1.61}$$

$$A_y = A_Y, \tag{1.62}$$

$$A_s = A_Z \cos\left(\frac{s}{\rho}\right) + A_X \sin\left(\frac{s}{\rho}\right). \tag{1.63}$$

Following the same steps as in the previous section, we consider $-P'_s$ as the new Hamiltonian and we apply the appropriate canonical transformations, obtaining the Hamiltonian in a curved coordinate system:

$$H = \frac{p_\tau}{\beta_0} - (1 + hx)\sqrt{\left(p_\tau + \frac{1}{\beta_0} - \phi\right)^2 - (p_x - a_x)^2 - \left(p_y - a_y\right)^2 - \frac{1}{\beta_0^2\gamma_0^2}} \\ - (1 + hx)\, a_s, \tag{1.64}$$

where the scalar ϕ and vector (a_x, a_y, a_s) potentials have been scaled as before.

In practice, accelerators are usually composed of multiple components, *e.g.* dipole magnets or quadrupole magnets, with each one occupying a region in s. The scalar and vector potentials therefore will be functions of s. The particle can be propagated from the entrance of an accelerator component to its exit by solving the equations of motion according to the Hamiltonian. This is repeated for all the accelerator components, each one with a different Hamiltonian, until the particle completes a full turn around the accelerator. This defines one turn for a particle and, of course, multiple turns can be simulated as required.

1.1.2 Symplectic integration of motion in an accelerator lattice

It quickly becomes apparent when inspecting Eq. (1.64) that the equations of motion are difficult to solve for arbitrary potentials ϕ, a_x, a_y, a_s which are generally functions of x, y and, in some cases, also functions of τ. Often, numerical integration is the only practical way to study the particle motion.

When simulating the dynamics of particles in an accelerator, it is of particular importance to choose a numerical integration scheme that preserves the symplectic structure of the equations of motion. If the numerical model is not symplectic, artificial growth or damping can be introduced in the amplitude of the particle trajectories[35]. As an example, the well-known Runge-Kutta scheme is not symplectic[35].

It is important to note that the combination of two symplectic maps applied successively is also a symplectic map. The most widely used scheme is based on the splitting of the Hamiltonian H in two integrable Hamiltonians with known solutions. The simplest case is having one dependent on the coordinates H_1 and one on the generalized momenta H_2, in which case the solution to the equations of motion becomes trivial:

$$H(x, p_x, y, p_y, \tau, p_\tau; s) = H_1(x, y, \tau; s) + H_2(p_x, p_y, p_\tau; s). \tag{1.65}$$

Using Lie algebra notation[35], the solution to the equations of motion according to a Hamiltonian H can be written as:

$$\vec{X}(s_0 + L) = e^{-L\,:H:}\vec{X}(s_0), \tag{1.66}$$

where $:H:$ is the operator of the Poisson bracket:

$$:H: = [H, \quad] = \sum_i \frac{\partial H}{\partial x_i}\frac{\partial}{\partial p_i} - \frac{\partial H}{\partial p_i}\frac{\partial}{\partial x_i}. \tag{1.67}$$

By solving the equations of motion for the Hamiltonians H_1, H_2 the following maps are known:

$$e^{-L_1\,:H_1:}, \quad e^{-L_2\,:H_2:}, \tag{1.68}$$

where the exponential operator is defined as:

$$e^{:f:} = \sum_{k=0}^{\infty} \frac{1}{k!}\,(:f:)^k\,. \tag{1.69}$$

The Baker-Campbell-Hausdorff (BCH) formula can be used to concatenate such maps. The BCH formula reads:

$$e^{:f:}e^{:g:} = e^{:h:}, \tag{1.70}$$

where f and g are arbitrary functions of the dynamical variables and

$$h = f + g + \frac{1}{2}:f:g + \frac{1}{12}\left(:f:^2 g + :g:^2 f\right) + O\left((f,g)^4\right). \tag{1.71}$$

This shows that the successive iteration of the two maps in Eq. (1.68) produces a map, which corresponds to a Hamiltonian that is approximately equal to the original one. Several schemes exist to arrange the successive multiple iteration of the maps in Eq. (1.68) in order to approximate the original Hamiltonian to higher orders. The most popular schemes include the Leapfrog integrator, the Yoshida-Forest-Ruth integrators [36, 37], while most recent developments include the CSABA$_\mathrm{m}$ integrators [38]. For example, the Leapfrog scheme approximates the solution of the Hamiltonian in Eq. (1.65) with the following arrangement of maps:

$$e^{-L:H:} \approx e^{-(L/2):H_2:} e^{-L:H_1:} e^{-(L/2):H_2:}. \tag{1.72}$$

We note that the square root in the Hamiltonian of Eq. (1.64) cannot be split and typically produces equations of motion that cannot be solved. For this reason, the square root is typically Taylor-expanded around the origin.

The maps for the most popular high energy accelerator components are reported in the following subsections [39, 40].

Straight drift space

The Hamiltonian in a straight ($h = 0$) and field-free ($\phi = a_x = a_y = a_s = 0$) region of length L is:

$$H = \frac{p_\tau}{\beta_0} - \sqrt{\left(p_\tau + \frac{1}{\beta_0}\right)^2 - p_x^2 - p_y^2 - \frac{1}{\beta_0^2\gamma_0^2}}. \tag{1.73}$$

The map resulting from this Hamiltonian is:

$$x \mapsto x + \frac{p_x}{p_z} L, \tag{1.74}$$

$$y \mapsto y + \frac{p_y}{p_z} L, \tag{1.75}$$

$$\tau \mapsto \tau + \left(\frac{1}{\beta_0} - \frac{p_\tau + 1/\beta_0}{p_z}\right) L, \tag{1.76}$$

with

$$p_z = \sqrt{\left(p_\tau + \frac{1}{\beta_0}\right)^2 - p_x^2 - p_y^2 - \frac{1}{\beta_0^2\gamma_0^2}}. \tag{1.77}$$

The expanded Hamiltonian in a straight, field-free region of length L is:

$$H = \frac{p_\tau}{\beta_0} - \delta + \frac{p_x^2 + p_y^2}{2\,(1+\delta)}, \tag{1.78}$$

with

$$\delta = \sqrt{p_\tau^2 + 2\frac{p_\tau}{\beta_0} + 1} - 1. \tag{1.79}$$

The corresponding map is:

$$x \mapsto x + \frac{p_x}{1+\delta}L, \tag{1.80}$$

$$y \mapsto y + \frac{p_y}{1+\delta}L, \tag{1.81}$$

$$\tau \mapsto \tau + \left(\frac{\delta}{\beta_0} - \frac{p_\tau}{1+\delta} - \frac{p_x^2+p_y^2}{2\beta(1+\delta)^2}\right)L, \tag{1.82}$$

with

$$\frac{1}{\beta} = \frac{p_\tau + 1/\beta_0}{1+\delta}. \tag{1.83}$$

Dipole magnet

The Hamiltonian describing the particle motion in a dipole magnet of length L in a curvilinear reference system of constant curvature h in the horizontal plane and with a uniform magnetic field B_y can be found from the vector potential:

$$a_x = 0, \quad a_y = 0, \quad a_s = \frac{qB_y}{P_0}\left(x - \frac{hx^2}{2\,(1+hx)}\right). \tag{1.84}$$

The expanded Hamiltonian for the dipole magnet becomes:

$$H = \frac{p_\tau}{\beta_0} + \frac{1}{2}\frac{p_x^2+p_y^2}{1+\delta} - (1+hx)(1+\delta) + k_0\left(x + \frac{hx^2}{2}\right), \tag{1.85}$$

where $k_0 = \frac{qB_y}{P_0}$. The Hamiltionian can be split in two terms:

$$H_{\text{drift}} = \frac{p_\tau}{\beta_0} + \frac{1}{2}\frac{p_x^2+p_y^2}{1+\delta} - \delta, \tag{1.86}$$

which is the expanded Hamiltonian for a straight drift, and:

$$H_{\text{dipole}} = -hx(1+\delta) + k_0\left(x + \frac{hx^2}{2}\right), \tag{1.87}$$

which can be considered as the Hamiltonian of a "thin" dipole and produces the following map:

$$p_x \mapsto p_x + (h - k_0 + h\delta - k_0 hx)\,L, \tag{1.88}$$

$$\tau \mapsto \tau - \frac{hx}{\beta}L. \tag{1.89}$$

Multipolar fields

The Hamiltonian expressing a "thin" multipolar field is:

$$H = a_s = L \cdot \mathcal{R}\left[\sum_{n=0}\left(k_n + i\hat{k}_n\right)(x+iy)^{n+1}\right], \tag{1.90}$$

where $\Re$ is the real part of the complex number and the normalized normal components k_n and normalized skew components $\hat{k}_n$ are defined as:

$$k_n = n!\frac{q}{P_0}\frac{B_{n+1}}{r_0^n}, \tag{1.91}$$

$$\hat{k}_n = n!\frac{q}{P_0}\frac{A_{n+1}}{r_0^n}, \tag{1.92}$$

with B_n, A_n being the normal and skew magnetic fields defined with an arbitrary reference radius r_0.

The map produced by this Hamiltonian is:

$$p_x \mapsto p_x - L\cdot\Re\left[\sum_{n=0}\frac{1}{n!}\left(k_n + i\hat{k}_n\right)(x+iy)^n\right], \tag{1.93}$$

$$p_y \mapsto p_y + L\cdot\Im\left[\sum_{n=0}\frac{1}{n!}\left(k_n + i\hat{k}_n\right)(x+iy)^n\right], \tag{1.94}$$

where $\Im$ is the imaginary part of the complex number.

RF cavity

The scaled vector potential for an idealized RF cavity is equal to:

$$a_s = -\frac{qV}{P_0 c}\cos\left(\phi_0 - k\tau\right), \tag{1.95}$$

where V is the cavity's voltage, ϕ_0 is a constant phase and k is proportional to the frequency f of the RF field:

$$k = \frac{2\pi f}{c} = \frac{\omega}{c}. \tag{1.96}$$

The map of this "thin" ideal RF cavity is:

$$p_\tau \mapsto p_\tau + \frac{qV}{P_0 c}\sin\left(\phi - k\tau\right). \tag{1.97}$$

In this convention, the RF cavity is phase-locked to the reference particle.

1.2 Normalized phase space

Due to the large number of dimensions in the phase space (6D) and due to the fact that there is intrinsic coupling between oscillations in one plane and another, it is helpful to make an eigenvector analysis of the motion in order to find the uncoupled modes of oscillation (uncoupled to first order in the dynamical variables).

This is achieved by analyzing the one-turn map linearized around the closed orbit. If the closed orbit is defined by the vector $z_0 = (x_0, p_{x,0}, y_0, p_{y,0}, \tau_0, p_{\tau,0})^T$ then the application of the linearized one-turn map M brings the vector $z = (x, p_x, y, p_y, \tau, p_\tau)^T$ from the turn s_0 to the next turn $s_0 + C$ as:

$$z(s_0 + C) - z_0 = M\left(z(s_0) - z_0\right). \tag{1.98}$$

Evaluation of the one-turn map

The components of the linearized one-turn map M_{ij} are equal to:

$$M_{ij} = \left. \frac{\partial z_i\left(s_0 + C\right)}{\partial z_j\left(s_0\right)} \right|_{z_0}, \tag{1.99}$$

i.e. each component is equal to the partial derivative of the i-th component of the final 6D position with respect to the j-th component of the initial 6D position, evaluated at the position of the closed orbit. This one-turn map can either be found at machine precision by using automatic differentiation[41] or a finite difference method can be applied to approximate it.

Symplectification of the one-turn map

The one-turn map must be symplectic since it is the result of the concatenation of multiple symplectic maps. However, especially if the finite difference method is used, the map will be found to be only approximately symplectic due to the precision of the method. The map can be symplectified (made symplectic) by constructing a matrix that is approximately equal to a non-symplectic matrix M but is symplectic. This can be obtained by using Healy's symplectification algorithm [42]:

$$M_s = \left(\mathbf{I} + \mathbf{SW}\right)\left(\mathbf{I} - \mathbf{SW}\right)^{-1}, \tag{1.100}$$

where

$$\mathbf{W} = \frac{\mathbf{V} + \mathbf{V}^T}{2}, \tag{1.101}$$

$$\mathbf{V} = \mathbf{S}\left(\mathbf{I} - \mathbf{M}\right)\left(\mathbf{I} + \mathbf{M}\right)^{-1}, \tag{1.102}$$

with $\mathbf{I}$ being the identity matrix and

$$\mathbf{S} = \begin{pmatrix} 0 & 1 & 0 & 0 & 0 & 0 \\ -1 & 0 & 0 & 0 & 0 & 0 \\ 0 & 0 & 0 & 1 & 0 & 0 \\ 0 & 0 & -1 & 0 & 0 & 0 \\ 0 & 0 & 0 & 0 & 0 & 1 \\ 0 & 0 & 0 & 0 & -1 & 0 \end{pmatrix}. \tag{1.103}$$

Diagonalization

After M has been symplectified, its six complex eigenvalues λ_i and six complex eigenvectors $\vec{v}_i$ can be calculated. Since M is a real and symplectic matrix, the eigenvalues and eigenvectors form complex conjugate pairs, $\lambda_k^{\pm}$ and $v_k^{\pm}$, respectively, with $k = 1, 2, 3$ and

$$v_k^{\pm} = a_k \pm i b_k, \tag{1.104}$$

$$\lambda_k^{\pm} = \cos\mu_k \pm i \sin\mu_k, \tag{1.105}$$

where μ_k are real numbers and a_k, b_k are real vectors. The matrix $\mathbf{M}$ can be written in the form:

$$\mathbf{M} = \mathbf{WRW}^{-1}, \tag{1.106}$$

with

$$\mathbf{R} = \begin{pmatrix} \cos\mu_1 & \sin\mu_1 & 0 & 0 & 0 & 0 \\ -\sin\mu_1 & \cos\mu_1 & 0 & 0 & 0 & 0 \\ 0 & 0 & \cos\mu_2 & \sin\mu_2 & 0 & 0 \\ 0 & 0 & -\sin\mu_2 & \cos\mu_2 & 0 & 0 \\ 0 & 0 & 0 & 0 & \cos\mu_3 & \sin\mu_3 \\ 0 & 0 & 0 & 0 & -\sin\mu_3 & \cos\mu_3 \end{pmatrix}, \tag{1.107}$$

and

$$\mathbf{W} = \begin{pmatrix} a_{1,1} & b_{1,1} & a_{2,1} & b_{2,1} & a_{3,1} & b_{3,1} \\ a_{1,2} & b_{1,2} & a_{2,2} & b_{2,2} & a_{3,2} & b_{3,2} \\ a_{1,3} & b_{1,3} & a_{2,3} & b_{2,3} & a_{3,3} & b_{3,3} \\ a_{1,4} & b_{1,4} & a_{2,4} & b_{2,4} & a_{3,4} & b_{3,4} \\ a_{1,5} & b_{1,5} & a_{2,5} & b_{2,5} & a_{3,5} & b_{3,5} \\ a_{1,6} & b_{1,6} & a_{2,6} & b_{2,6} & a_{3,6} & b_{3,6} \end{pmatrix}. \tag{1.108}$$

Rescaling of the eigenvectors

The columns b_1, b_2 and b_3 in Eq. (1.104) are rescaled to have the symplecticity condition on W:

$$\mathbf{W}^T\mathbf{S}\mathbf{W} = \mathbf{S}, \tag{1.109}$$

which imply

$$a_k^T\,\mathbf{S}\,b_k = 1, \tag{1.110}$$

with which three of the six eigenvalues and eigenvectors are selected.

Ordering of eigenvectors

The ordering of the eigenvectors and eigenvalues is done such that mode 1 is associated to the horizontal plane, mode 2 is associated to the vertical plane and mode 3 to the longitudinal plane. This is achieved by ordering them such that the following conditions hold

$$\left|a_{1,1} \pm ib_{1,1}\right| > \left|a_{1,3} \pm ib_{1,3}\right|, \left|a_{1,5} \pm ib_{1,5}\right|, \tag{1.111}$$

$$\left|a_{2,3} \pm ib_{2,3}\right| > \left|a_{2,1} \pm ib_{2,1}\right|, \left|a_{2,5} \pm ib_{2,5}\right|, \tag{1.112}$$

$$\left|a_{3,5} \pm ib_{3,5}\right| > \left|a_{3,1} \pm ib_{3,1}\right|, \left|a_{3,3} \pm ib_{3,3}\right|. \tag{1.113}$$

Courant-Snyder parameterization

Finally, each eigenvector is rephased such that

$$b_{j,2j-1} = 0, \quad j = 1, 2, 3. \tag{1.114}$$

This choice is frequently referred to as the Courant-Snyder parameterization.

Normalized coordinates

The coordinates in the normalized phase space can be defined as:

$$\hat{z} = W^{-1}\left(z - z_0\right) = \left(\hat{x}, \hat{p}_x, \hat{y}, \hat{p}_y, \hat{\tau}, \hat{p}_\tau\right). \tag{1.115}$$

The "linearized" action and angle variables can also be defined:

$$J_1 = \frac{\hat{z}_1^2 + \hat{z}_2^2}{2} = \frac{\hat{x}^2 + \hat{p}_x^2}{2}, \tag{1.116}$$

$$\tan\phi_1 = -\frac{\hat{z}_2}{\hat{z}_1} = -\frac{\hat{p}_x}{\hat{x}}, \tag{1.117}$$

$$J_2 = \frac{\hat{z}_3^2 + \hat{z}_4^2}{2} = \frac{\hat{y}^2 + \hat{p}_y^2}{2}, \tag{1.118}$$

$$\tan\phi_2 = -\frac{\hat{z}_4}{\hat{z}_3} = -\frac{\hat{p}_y}{\hat{y}}, \tag{1.119}$$

$$J_3 = \frac{\hat{z}_5^2 + \hat{z}_6^2}{2} = \frac{\hat{\tau}^2 + \hat{p}_\tau^2}{2}, \tag{1.120}$$

$$\tan\phi_3 = -\frac{\hat{z}_6}{\hat{z}_5} = -\frac{\hat{p}_\tau}{\hat{\tau}}. \tag{1.121}$$

1.3 Synchrotron motion in action-angle variables

Although synchrotron motion of particles inside a bunched beam is non-linear, it is integrable when it is driven by an RF cavity of a frequency. It is directly equivalent to the pendulum problem [43], one of the most studied non-linear problems.

Above the transition energy[14] and without acceleration, the synchronous phase is equal to π and the Hamiltonian H describing the synchrotron motion is:

$$H = \frac{qV_{RF}}{2\pi f_{RF} P_0 C_0}\cos\left(\frac{2\pi f_{RF}}{c}\tau\right) - \frac{\eta_p}{2\beta_0^2}p_\tau^2, \tag{1.122}$$

where q is the charge of the particle, V_{RF} is the amplitude of the voltage powering the Radio-Frequency (RF) cavity, f_{RF} is the frequency of the RF cavity, C_0 is the accelerator's circumference and η_p is the phase slip factor equal to:

$$\eta_p = \alpha_p - \frac{1}{\gamma_0^2}, \tag{1.123}$$

with α_p being the momentum compaction factor defined by the beam optics[14]. To make notation easier, the following variables are introduced:

$$A = \frac{qV_{RF}}{2\pi f_{RF} P_0 C_0}, \tag{1.124}$$

$$B = \frac{2\pi f_{RF}}{c}, \tag{1.125}$$

$$C = \frac{\eta_p}{2\beta_0^2}. \tag{1.126}$$

Using Eqs. (1.124), (1.125) and (1.126) the Hamiltonian becomes

$$H = A\cos\left(B\tau\right) - Cp_{\tau}^{2}. \tag{1.127}$$

For the "libration" case, i.e. for stable motion inside the "RF bucket", the value of H ranges in the interval $[0, A]$. $H = 0$ corresponds to the separatrix line separating "libration" and "rotation" of the pendulum, while $H = A$ corresponds the value for the synchronous particle, which is the hypothetical particle that always passses through the RF cavity at the same phase. Using the trigonometric identity

$$\cos\left(\theta\right) = 1 - 2\sin^{2}\left(\frac{\theta}{2}\right), \tag{1.128}$$

Eq. (1.127) is rewritten as

$$H = A\left(1 - 2\sin^{2}\left(\frac{B}{2}\tau\right)\right) - Cp_{\tau}^{2}, \tag{1.129}$$

$$-H + A = 2A\sin^{2}\left(\frac{B}{2}\tau\right) + Cp_{\tau}^{2}, \tag{1.130}$$

$$\frac{-H + A}{2A} = \sin^{2}\left(\frac{B}{2}\tau\right) + \frac{C}{2A}p_{\tau}^{2}. \tag{1.131}$$

Introducing the variable

$$m = \frac{-H + A}{2A}, \tag{1.132}$$

Eq. (1.131) becomes

$$m = \sin^{2}\left(\frac{B}{2}\tau\right) + \frac{C}{2A}p_{\tau}^{2}. \tag{1.133}$$

The value of m ranges in the interval $[0, 1]$ with $m = 0$ corresponding to the synchronous particle and with $m = 1$ corresponding to the separatrix. The stable fixed point is located at $\tau = 0$ while the unstable fixed points are located at $\tau = \pm\frac{\pi}{B}$

The action variable is defined as:

$$J = \frac{1}{2\pi}\oint p_{\tau}\mathrm{d}\tau \tag{1.134}$$

$$= \frac{1}{2\pi}4\int_{0}^{\frac{\pi}{B}} p_{\tau}\mathrm{d}\tau \tag{1.135}$$

$$= \frac{2\sqrt{2A}}{\pi\sqrt{C}}\int_{0}^{\frac{\pi}{B}}\sqrt{m - \sin^{2}\left(\frac{B}{2}\tau\right)}\mathrm{d}\tau, \tag{1.136}$$

Through a change of variables with

$$\sqrt{m}\sin\phi = \sin\left(\frac{B}{2}\tau\right), \tag{1.137}$$

and

$$\frac{2\sqrt{m}}{B}\frac{\cos\phi}{\sqrt{1 - m\sin^{2}\phi}}\mathrm{d}\phi = \mathrm{d}\tau, \tag{1.138}$$

the action becomes

$$J = \frac{2\sqrt{2A}}{\pi\sqrt{C}}\int_0^{\frac{\pi}{B}} \sqrt{m - m\sin^2\phi}\mathrm{d}\tau \tag{1.139}$$

$$= \frac{2\sqrt{2A}}{\pi\sqrt{C}}\int_0^{\frac{\pi}{B}} \sqrt{m}\sqrt{1 - \sin^2\phi}\mathrm{d}\tau \tag{1.140}$$

$$= \frac{2\sqrt{2A}}{\pi\sqrt{C}}\int_0^{\frac{\pi}{B}} \sqrt{m}\cos\phi\mathrm{d}\tau \tag{1.141}$$

$$= \frac{4\sqrt{2A}}{\pi B\sqrt{C}}\int_0^{\frac{\pi}{2}} \frac{m\cos^2\phi}{\sqrt{1 - m\sin^2\phi}}\mathrm{d}\phi \tag{1.142}$$

$$= \frac{4\sqrt{2A}}{\pi B\sqrt{C}}\int_0^{\frac{\pi}{2}} \frac{m\cos^2\phi}{\sqrt{1 - m\sin^2\phi}}\mathrm{d}\phi \tag{1.143}$$

$$= \frac{4\sqrt{2A}}{\pi B\sqrt{C}}\int_0^{\frac{\pi}{2}} \frac{m - m\sin^2\phi}{\sqrt{1 - m\sin^2\phi}}\mathrm{d}\phi \tag{1.144}$$

$$= \frac{4\sqrt{2A}}{\pi B\sqrt{C}}\int_0^{\frac{\pi}{2}} \frac{m - 1 + 1 - m\sin^2\phi}{\sqrt{1 - m\sin^2\phi}}\mathrm{d}\phi \tag{1.145}$$

$$= \frac{4\sqrt{2A}}{\pi B\sqrt{C}}\left((m-1)\int_0^{\frac{\pi}{2}} \frac{1}{\sqrt{1 - m\sin^2\phi}}\mathrm{d}\phi + \int_0^{\frac{\pi}{2}} \frac{1 - m\sin^2\phi}{\sqrt{1 - m\sin^2\phi}}\mathrm{d}\phi\right). \tag{1.146}$$

$$\tag{1.147}$$

From this one can write:

$$J = \frac{4\sqrt{2A}}{\pi B\sqrt{C}}\left(\int_0^{\frac{\pi}{2}} \sqrt{1 - m\sin^2\phi}\,\mathrm{d}\phi - (1-m)\int_0^{\frac{\pi}{2}} \frac{1}{\sqrt{1 - m\sin^2\phi}}\mathrm{d}\phi\right). \tag{1.148}$$

In this expression it is possible to recognize the complete elliptic integral of the first kind:

$$K(m) = \int_0^{\frac{\pi}{2}} \frac{1}{\sqrt{1 - m\sin^2\phi}}\mathrm{d}\phi, \tag{1.149}$$

and the complete elliptic integral of the second kind:

$$E(m) = \int_0^{\frac{\pi}{2}} \sqrt{1 - m\sin^2\phi}\,\mathrm{d}\phi. \tag{1.150}$$

By substituting Eqs. (1.149), (1.150) into Eq. (1.148):

$$J = \frac{4\sqrt{2A}}{\pi B\sqrt{C}}\left(E(m) - (1-m)K(m)\right). \tag{1.151}$$

The frequency of the synchrotron oscillations is:

$$
\begin{aligned}
\nu(J) &= \frac{\partial H}{\partial J} && (1.152)\\
&= \frac{\partial H}{\partial m}\left(\frac{\partial J}{\partial m}\right)^{-1} && (1.153)\\
&= -2Am\left(\frac{\partial J}{\partial m}\right)^{-1} && (1.154)\\
&= -\frac{\pi B\sqrt{2AC}}{4}\left(\frac{\partial}{\partial m}\left(E(m)-(1-m)\,K(m)\right)\right)^{-1} && (1.155)\\
&= -\frac{\pi B\sqrt{2AC}}{4}\left(\frac{2}{K(m)}\right) && (1.156)\\
&= -\frac{\pi B\sqrt{2AC}}{2K(m)}, && (1.157)\\
& && (1.158)
\end{aligned}
$$

or

$$\nu(J) = -\frac{\pi\sqrt{\pi f_{RF} q V_{RF} \eta_p}}{c\sqrt{P_0 C_0} K(m(J))}, \tag{1.159}$$

where m can be found by inverting Eq. (1.151). The angle variable is then defined as:

$$\phi = \nu(J)t + a, \tag{1.160}$$

with a being an integration constant.

The original variables are related to the normalized coordinates by the following relations:

$$
\begin{aligned}
\tau &= \frac{2}{B}\sin^{-1}\left(\sqrt{m}\cdot sn\left(4K(m)\nu(m)t\,|\,m\right)\right), && (1.161)\\
p_\tau &= \sqrt{\frac{2Am}{C}}\cdot cn\left(4K(m)\nu(m)t\,|\,m\right), && (1.162)
\end{aligned}
$$

where the Jacobi elliptic functions sn and cn have been used, which are given by:

$$
\begin{aligned}
sn\left(u|\,m\right) &= \sin\varphi, && (1.163)\\
cn\left(u|\,m\right) &= \cos\varphi, && (1.164)
\end{aligned}
$$

with ϕ defined as the inverse of the function:

$$u = \int_0^{\phi}\frac{\mathrm{d}\theta}{\sqrt{1-m\sin^2\theta}} = F(\varphi|m). \tag{1.165}$$

This means that in order to evaluate the sn and cn functions for a variable u and a given parameter m, the above equation must be inverted:

$$\varphi = F^{-1}(u|m). \tag{1.166}$$

After φ has been determined, the Jacobi elliptic functions can be evaluated by using Eqs. (1.163) and (1.164).

For a given value in the action variable, the τ and p_τ coordinates can be sampled by choosing a random $\nu(m)t \in (0, 1)$ to have a "matched" distribution. A matched distribution is one that does not depend on time. Although each particle is moving according the equations of motion, their distribution remains unchanged at the limit of an infinite number of particles.

In the case where all particles are "captured" by the RF system and there is no particle executing "rotating" motion, synchrotron motion is bounded for any value of the action, or equivalently of m. A result of this is that for a given projection, a distribution $\rho_\tau(\tau)$ or $\rho_{p_\tau}(p_\tau)$, there exists a unique distribution of the action $\rho_J(J)$ or of the normalized Hamiltonian $\rho_m(m)$. The projection can be decomposed as:

$$\rho_x(x) = \sum_{i=1}^{N} g(x|m_i) \cdot \rho_m(m_i)\Delta m_i. \tag{1.167}$$

where x can be either τ or p_τ, and $g(x|m_i)$ is the projection of matched distribution given a single value m_i. This distribution can be evaluated with randomly sampling pairs of τ, p_τ by choosing uniformly in ϕ from 0 to 2π, and taking the projection to x. Because synchrotron motion is bounded, a recursive relation can be used to compute $\rho_m(m)$:

$$\begin{aligned}
\rho_x(x_N) &= g(x_N|m_N) \cdot \rho_m(m_N)\Delta m_N, \\
\rho_x(x_{N-1}) &= \rho_x(x_N) + g(x_{N-1}|m_{N-1}) \cdot \rho_m(m_{N-1})\Delta m_{N-1}, \\
\rho_x(x_{N-2}) &= \rho_x(x_{N-1}) + g(x_{N-2}|m_{N-2}) \cdot \rho_m(m_{N-2})\Delta m_{N-2}, \\
&\dots \\
\rho_x(x_0) &= \rho_x(x_1) + g(x_0|m_0) \cdot \rho_m(m_0)\Delta m_0,
\end{aligned}$$

where the given projection $\rho_x(x_i)$ has been discretized in the samples $x_i = i \cdot \Delta x$. The variable m_i is found by using Eq. (1.133) and setting the conjugate variable of x to 0. For example, if $x = \tau$, then:

$$m_i = \sin^2\left(\frac{B}{2}x_i\right). \tag{1.168}$$

The term Δm_i comes from the fact that the coordinate change from x to m_i is a non-linear transformation. If $x = \tau$, it can be approximated as:

$$\Delta m_i \approx \sin^2\left[\frac{B}{2}\left(x_i + \frac{\Delta x}{2}\right)\right] - \sin^2\left[\frac{B}{2}\left(x_i - \frac{\Delta x}{2}\right)\right]. \tag{1.169}$$

After ρ_m has been found, a matched 2D distribution (with a given projection in either τ or p_τ) can be acquired by randomly sampling m (according to $\rho_m(m)$ and $\nu(m)t$ (uniformly in $[0, 1]$), and finally transforming the pairs $(m, \nu(m)t)$ to (τ, p_τ).

1.4 Large Hadron Collider

The Large Hadron Collider (LHC) [1] is the largest collider to date and holds the record for the highest center-of-mass energy in collisions between protons. It is a synchrotron, mostly composed of repeating FODO (Focusing-Defocusing) cells. A structure of FODO cells is a repeating structure of quadrupole magnets with alternating polarity. A quadrupole that focuses on one plane, defocuses on the other. By alternating the polarity of the quadrupole magnets it is possible to contain the particle trajectories inside the aperture of the vacuum chamber. Dipole magnets are inserted between the quadrupole magnets to bend the trajectories of the particles in order to form a periodic "storage ring" that closes on itself.

The layout of the LHC is split into 8 arcs and 8 Insertion Regions (IR) also referred to as long straight sections. The 8 arcs consist almost entirely of FODO cells composed of dipole, quadrupole, sextupole and octupole magnets. Next to each of the dipole magnets, there are spool-pieces correctors attached to them that allow them to induce high-order multipolar fields (up to decapolar fields) in order to compensate for the multipolar fields induced by magnet imperfections. The source of the magnet imperfections is the discrete nature of coils that induce the magnetic fields in the superconducting magnets of the LHC. Although their design is optimized to minimize such imperfections, they cannot be eliminated completely. Moreover, small deviations in the manufacturing process can also contribute to such effects.

The main dipole magnets each sit inside their own cryostat which enables them to reach low temperature and achieve a superconducting state. Each arc is made from 23 regular cells, each consisting in 6 dipole magnets of length equal to 14.3 meters. This makes 1168 dipole magnets in the LHC arcs regular cells. Each arc and insertion region is connected by a "dispersion suppressor region", whose primary aim is to cancel the horizontal dispersion that is generated by the dipole magnets. Each dispersion suppressor region consists of an additional 8 main dipole magnets, thus bringing the total of the main dipole magnets in the LHC to 1232.

Each of the main quadrupole magnet (of length equal to 3.1 meters) in the arc regular cells sits in a "short straight section" cryostat. The main sextupole (of length equal to 0.369 meters) and main octupole (of length equal to 0.32 meters) magnets sit inside the same cryostat that defines the short straight section.

The different IRs include a variety of equipment. Most notably,

1. The detector of the "A Large Toroidal Apparatus" (ATLAS) experiment is hosted in IR1.

2. The detector of the ALICE experiment and the injection point of the beam rotating clockwise are hosted in IR2.

3. The momentum cleaning collimators are hosted in IR3, where a large dispersion function is set in order to intercept particles with large longitudinal amplitude oscillations.

4. Most beam instrumentation is hosted in IR4, e.g. the Beam Current Transformers used to measure the intensity of the beam, the Wirescanners used to measure the size of the beam, together with the RF cavities used to accelerate the protons and to perform phase focusing to preserve the bunched structure of the beam.

5. Insertion region 5 hosts the detector of the Compact Muon Solenoid (CMS) experiment.

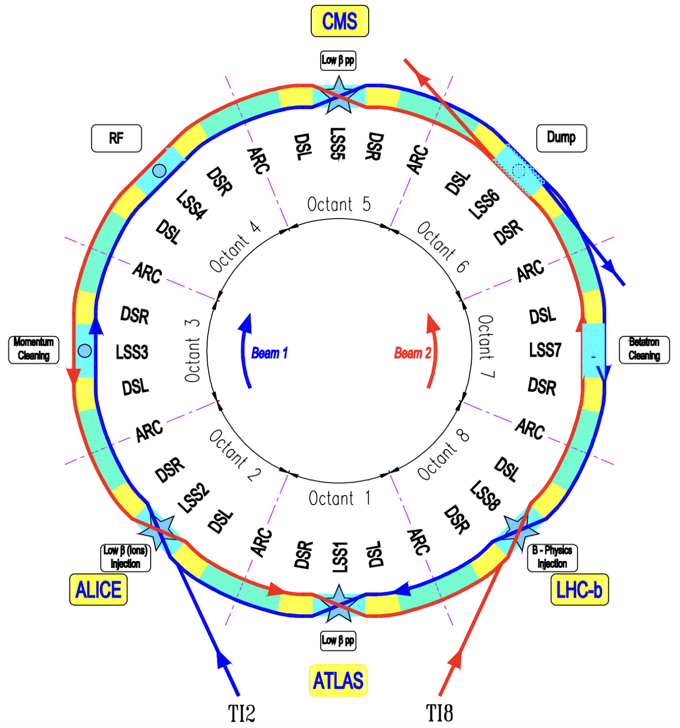

Figure 1.2: Schematic layout of the LHC. Beam 1 circulates clockwise and Beam 2 counter-clockwise. Figure adapted from Ref. [1].

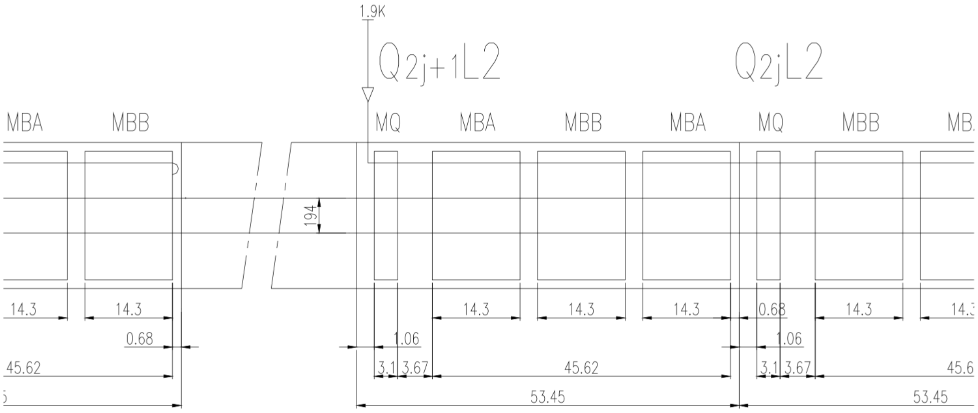

Figure 1.3: Schematic layout of an LHC FODO half-cell. Figure adapted from Ref. [1].

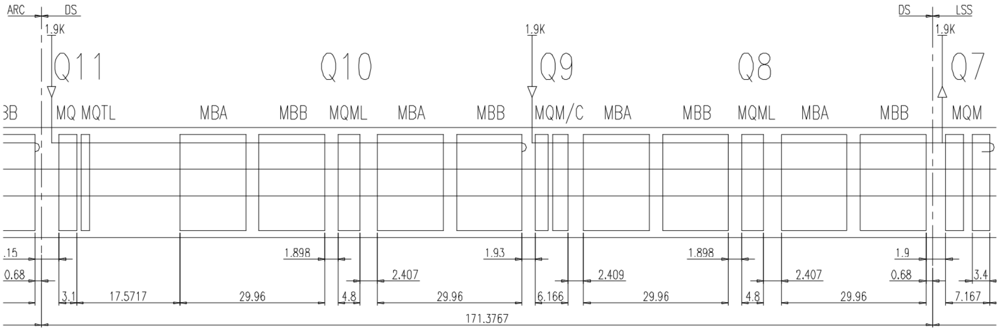

Figure 1.4: Schematic layout of an LHC dispersion suppressor region next to IR2. Figure adapted from Ref. [1].

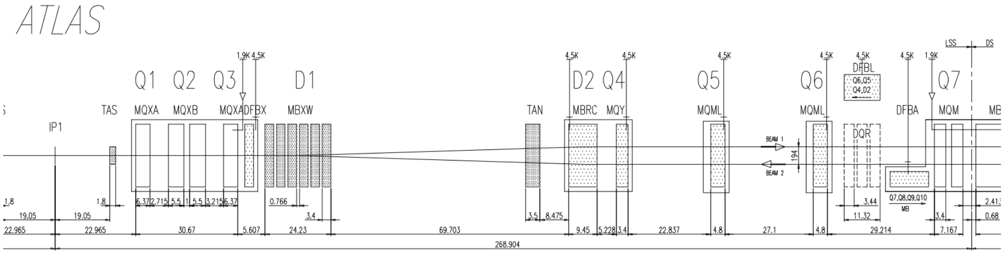

Figure 1.5: Schematic layout of the right side of IR1. Figure adapted from Ref. [1].

6. Insertion region 6 is where the LHC beam dump system is placed.

7. The betatron collimation system of the LHC, hosted in IR7, intercepts protons with large amplitudes of betatron oscillations. At the same time, it ensures that all debris that arises from the collisions between protons and collimators are also intercepted safely by secondary collimators to minimize energy deposition in the superconducting magnets.

8. Finally, the detector of the Large Hadron Collider beauty (LHCb) experiment is hosted in IR8, along with the injection point of the beam rotating counterclockwise.

At the center of each of the four detectors (ATLAS, CMS, LHCb, ALICE) there is an interaction point at which the particle bunches collide. The two particle beams collide at an angle in order to avoid collisions in places other than the interaction points. In order to put the particle trajectories such that they form an angle, dipole correctors are used in the Insertion Region around the corresponding interaction point.

A particularly important set of magnets in the LHC lattice are the Inner Triplet (IT) quadrupoles around the interaction points. Those are used in order to decrease the beam size at the interaction point and therefore increase the produced luminosity. The reduction of the beam size leads to an increase of the relative oscillation amplitude inside the IT quadrupole magnets. Moreover, the Inner Triplet quadrupoles have “common beam chambers” which means that the two beams are not isolated from each other and they can influence each other through the electromagnetic fields they produce. An overview of the layout at the right side of IR1 is visible in Fig. 1.5. The layout, which is identical to the one in IR5, is symmetric around the interaction point.

Chapter 2

Electron clouds

2.1 Overview of electron cloud buildup

The formation of electron clouds (e-clouds) is often observed in synchrotrons that are operating with closely spaced bunches of positively charged particles. This is the result of an exponential multiplication of electrons in the beam pipe driven by secondary electron emission and photo-emission from the surface of the beam pipe [30, 44, 45].

Primary electrons

The process of the e-cloud formation begins with the emission of the primary electrons. The two most dominant mechanisms for the production of primary electrons are the residual gas ionization and the photoemission due to synchrotron radiation. Residual gas ionization occurs when the beam particles ionize the molecules of the residual gas in the imperfect vacuum. At high beam energies, the photoemission due to synchrotron radiation is dominant primary production effect. Synchrotron radiation is emitted when a particle accelerates in a direction perpendicular to its direction. This happens mostly at bending magnets but any magnetic field causes transverse acceleration and therefore emission of synchrotron radiation. The energy spectrum of the emitted photons consisting the synchrotron radiation ranges from zero up to a "critical" energy equal to:

$$E_c = 3\frac{\hbar c \gamma_{\mathrm{rel}}^3}{2\rho}, \tag{2.1}$$

where $\hbar$ is the reduced Planck constant, c is the speed of the light, γ_{rel} is the relativistic gamma factor of the beam particles and ρ is the radius of the curvature of the trajectory.

If this energy is larger than the work function of the beam chamber's material, electrons can be emitted through the photoelectric effect. It is important to note that photons emitted through synchrotron radiation can also be reflected multiple times from the surface of the beam chamber and therefore impact on different spots. Because of this, even though the emission of the photons from the particle beam happens in a narrow cone that is tangential to particle beam direction, primary electrons can be emitted basically anywhere on the chamber's walls.

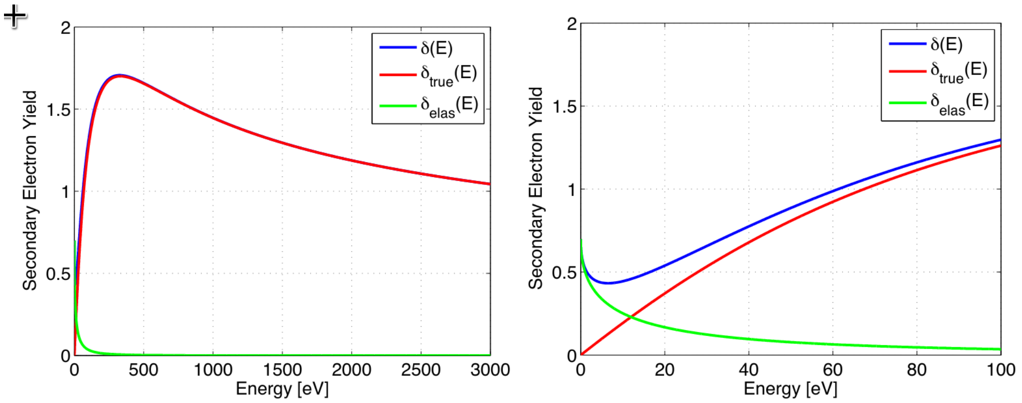

Figure 2.1: Secondary Emission Yield curve with $\delta_{\mathrm{max}} = 1.7$ for the elastic component (green), the secondary emission component (red) and their sum (blue). The right figure is a magnification of the left figure in the low energy region. Figure adapted from Ref. [17].

2.1.1 Secondary electrons

During the passage of a particle bunch, the primary electrons are accelerated by the beam's electromagnetic field. When the bunch has fully passed through, the electrons are typically moving towards the vacuum chamber's walls with energies that depend on the charge distribution of the particle bunch, which can reach a few keV. When an electron hits the wall, it can either get elastically scattered back, it can get absorbed by the wall, or it can induce the emission of more electrons in a process called secondary electron emission. The average number of electrons emitted is characterised by the Secondary Emission Yield (SEY). The modelling of the SEY is based mostly on laboratory measurements [46, 47, 48, 49, 50]. The SEY depends both on the energy and the angle of the impinging electron.

A typical SEY curve is presented in Fig. 2.1, where the component of elastic scattering $\delta_{\mathrm{el.}}$ (green), of secondary emission δ_{ts}(red) and of their sum δ (blue) are also shown. In the model usually used to characterize the beam chamber surface for CERN accelerators[48], the elastic component is parameterized by the function:

$$\delta_{\mathrm{el.}}(E) = R_0 \left(\frac{\sqrt{E} - \sqrt{E + E_0}}{\sqrt{E} + \sqrt{E + E_0}} \right)^2 , \tag{2.2}$$

where R_0 and E_0 are parameters of the model. For the LHC chambers, these parameters have been estimated as $R_0 = 0.7$ and $E_0 = 150\,\mathrm{eV}$ [48]. The component corresponding to the secondary emission is parameterized by

$$\delta_{\mathrm{ts}}(E) = \delta_{\mathrm{max}} \frac{s \dfrac{E}{E_{\mathrm{max}}}}{s - 1 + \left(\dfrac{E}{E_{\mathrm{max}}} \right)^s}, \tag{2.3}$$

where s is a shape parameter and E_{max} is the energy corresponding to the maximum of the SEY curve. For the LHC chambers, the parameters are estimated as $s = 1.35$

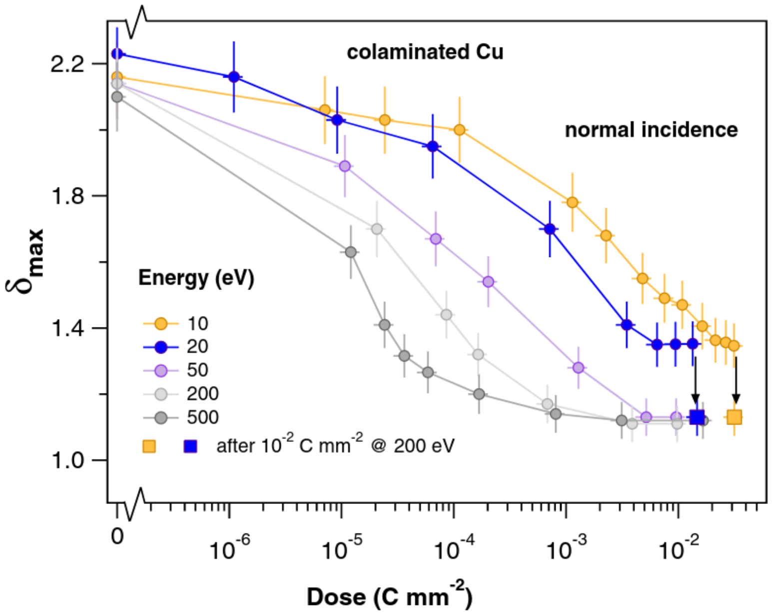

Figure 2.2: Maximum SEY as a function of the dose for different impinging electron energies at normal incidence on colaminated Cu of the LHC beam screen. Figure adapted from Ref. [18].

and $E_{\text{max}} = 332\,\text{eV}$. The parameter δ_{max} expresses the maximum SEY and is highly dependent on the properties of the chamber's walls as well as its history. In the next chapters, δ_{max} will be referred to as simply SEY. Further details on the modelling of the SEY can be found in Ref. [17].

2.1.2 Scrubbing — SEY reduction

Experimental studies have shown that the SEY of many materials decreases when the surface is exposed to electron irradiation[18]. This phenomenon is frequently called as "conditioning" or "scrubbing" and is the basis for mitigating electron cloud effects in the Large Hadron Collider[1]. An example of how the SEY evolves with the impinging electron dose can be seen in Fig. 2.2. The SEY can be strongly reduced by irradiation with electrons. Hence the e-cloud is a self-conditioning process in the sense that the electrons of the cloud impact the vacuum chamber surface gradually reducing the SEY and, in turn, the e-cloud generation.

In practice, dedicated "scrubbing runs" are scheduled to reduce e-cloud effects in the accelerator. The run consists in storing a particle beam that produces the maximum e-cloud that can be withstood by the accelerator in terms of beam stability and other machine constraints like acceptable vacuum pressure or cryogenic capacity. When the SEY has reduced sufficiently, a beam that generates a larger e-cloud can be injected and stored to continue the self-conditioning in a more efficient way. Typically, to increase the electron irradiation dose rate delivered by the e-cloud, it is possible to increase the number of circulating bunches.

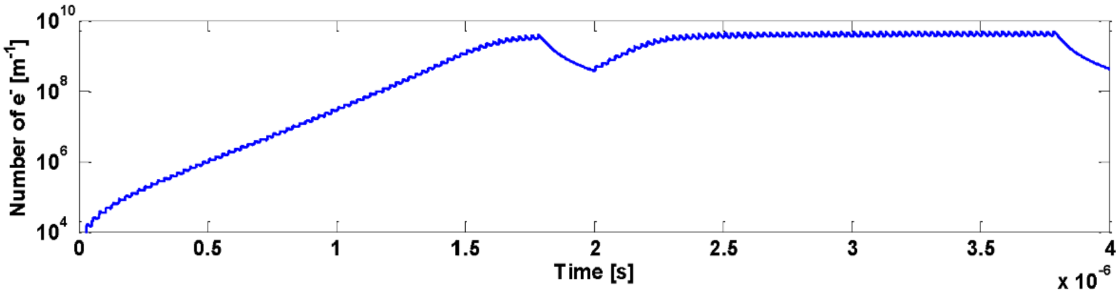

Figure 2.3: Number of electrons during an example of the electron cloud build-up. Figure adapted from Ref. [17].

2.1.3 Electron cloud buildup

The repeating passage of bunches can drive the buildup of the electron cloud. Each bunch generates a number of primary electrons and at the same time accelerates the existing electrons. After the passage of an individual bunch, the accelerated electrons hit the walls and according to their energy they induce the emission of more electrons. Until the passage of the next bunch, the electrons diffuse within the vacuum and get absorbed by the walls. If the ratio between the number of electrons after and before a bunch passage is larger than unity, then the total number of electrons increases exponentially and the buildup is said to follow the “multipacting” regime. If it is less than unity then it follows the “seed accumulation” regime where most electrons that are produced are primary electrons and there is a dynamic equilibrium between primary electron production and absorption. In the case of multipacting, the number of electrons will continue to increase until the space charge forces of the electrons themselves decelerate the electrons and a dynamic equilibrium is reached [51].

An example of an e-cloud buildup in the multipacting regime is visible in Fig. 2.3. Two trains, each of 72 bunches spaced at 25 ns are driving the buildup. During the passage of the first train, the density of electrons grows exponentially. Between the trains there is a gap of 450 ns, where the density of electrons drops by roughly an order of magnitude. During the passage of the second train ($t > 2$ µs), the density quickly grows to a steady state value and the dynamic equilibrium is reached.

2.1.4 Buildup in externally applied fields

The spatial profile of the electron density in the electron cloud depends heavily on the geometry of the beam chamber and on the magnetic field. In particular, the magnetic field plays a major role on the formation of the electron cloud. Typically these fields are designed to control high-energy particles for which the particle accelerator is designed. The electrons in the cloud however have a substantially smaller energy, and therefore perform small rapid cyclotron oscillations. The relation between the magnetic field and the cyclotron period and radius is illustrated in Fig. 2.4. The cyclotron radius is very small and the electrons are practically trapped on the magnetic field lines of the externally applied magnetic field.

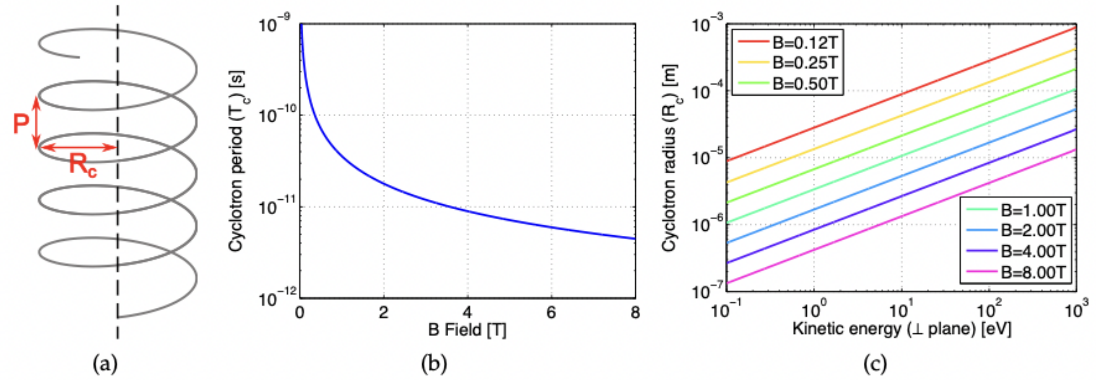

Figure 2.4: (a) Helicoidal trajectory of an electron moving in a uniform vertical magnetic field. (b) Cyclotron period as a function of the magnetic field. (c) Cyclotron radius as a function of the magnetic field and of kinetic energy associated to the motion in the plane orthogonal to the field lines. Figure adapted from Ref. [17].

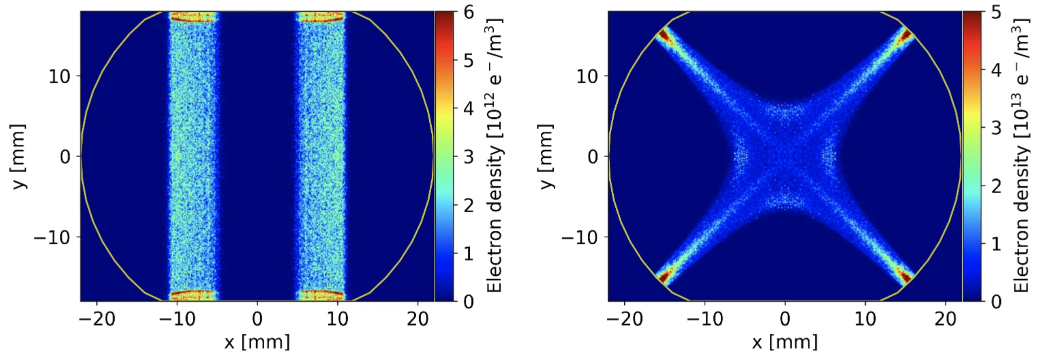

Figure 2.5: Simulated electron distribution in an LHC arc dipole (left) and arc quadrupole (right) at injection energy as seen right before the arrival of a bunch (from a Particle-in-Cell simulation). Figure adapted from Ref. [19].

Buildup in dipolar fields

In the LHC beam screens, the profile of the electron density in the cloud assumes two columns on either side of the beam location whose distance depends mainly on the intensity of the beam. An example of this is visible in the left plot of Fig. 2.5. Moreover, at moderate intensities (of $0.7 \cdot 10^{11}$ protons per bunch), a column of electrons appears at the location of the beam [20].

The projection of the electron density on the horizontal plane can be seen in Fig. 2.6 for different bunch intensities. Different colors correspond to different bunches inside the bunch train. As the bunch intensity increases, the two columns on the left and right of the beam location move further away from the beam location, while the peak density does not change significantly. Moreover, as the bunch intensity decreases, a middle column of large electron densities appears directly at the beam location.

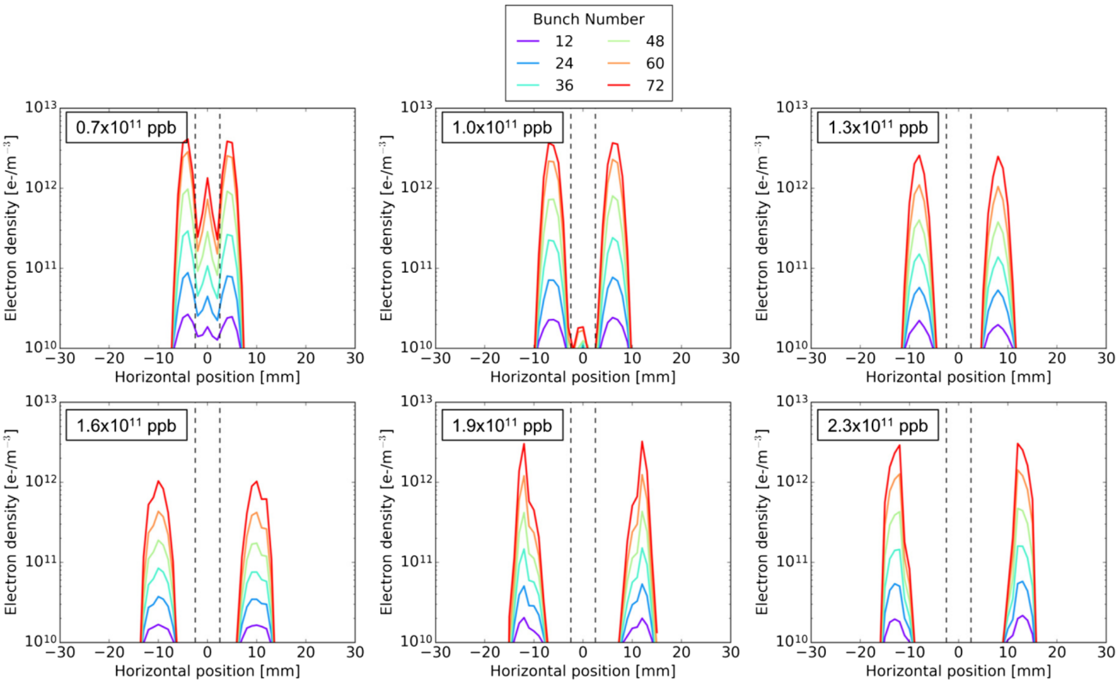

Figure 2.6: Horizontal electron density profile in a dipole magnet for different bunch intensities, and for different selected bunches along the train. The vertical dashed lines delimit a distance of 2.5 mm from the beam position. Figure adapted from Ref. [20].

Buildup in quadrupolar fields

The gradient of the magnetic field in high-order magnets (quadrupolar fields, sextupolar fields, and so on), favours the trapping of electrons through the magnetic bottle effect, frequently used to trap charged particles[52]. The magnetic trapping is often not sufficient to limit the multiplication of the electrons but is enough to limit the absorption of electrons inside the beam chamber walls. The magnetic field lines confine the electrons and in that way, the spatial density of electrons resembles that of the magnet's field lines. For this reason, high-order multipolar fields favour the appearance of increased electron densities at the origin of the field coordinates. An example of an electron distribution in one of the LHC arc quadrupoles at injection energy can be seen in the right plot of Fig. 2.5.

Dependence on bunch intensity

Simulations have predicted that the dependence of the heat load from e-cloud effects is not strictly proportional to the bunch intensity[19]. Instead, it was found in Ref. [19] that an interplay between the spectrum of the impacting electrons and the shape of the SEY curve can induce a non-monotonic dependence of the heat load on the bunch population. In particular simulations reveal that the induced heat load from e-cloud decreases at high bunch populations in quadrupolar magnetic fields (with the configuration of the LHC beam parameters and vacuum chamber).

2.2 Electrodynamics in the electron cloud

The formalism of the effect of an e-cloud on the trajectory of a proton is summarized in this section based on Ref. [53]. The equations of motion are developed by employing a thin-lens approximation for the effect of an electron distribution, in conjunction with the "smooth approximation", which essentially states that the beam particles traverse the e-cloud in a straight line along the longitudinal direction.

In the laboratory frame of reference for a single e-cloud, the electrons in a cloud will be distributed according to a charge distribution $\rho(x, y, s, t)$ and their motion will define current density $\boldsymbol{J}(x, y, s, t)$. In a lattice element, neglecting fringe fields and cavities with time-dependent electromagnetic fields, the electrons will be under the influence of magnetic fields, if any, which are independent of the position s. Moreover, the electromagnetic field of the charged beam as felt by the electrons will only produce transverse electromagnetic forces in the ultra-relativistic approximation. This implies that 1) the longitudinal component of the electron current density vanishes ($J_s = 0$), and 2) the evolution of the e-cloud follows the passage of the bunch and the fields of the e-clouds will be stationary when expressed with respect to the coordinate τ:

$$\tau = \frac{s}{\beta_0} - ct, \tag{2.4}$$

As such, the charge and current densities can be written as $\rho(x, y, \tau)$ and $\boldsymbol{J}(x, y, \tau)$, under the above approximations. Because of this dependence, it is convenient to move to the rest frame of a rigid bunch, one whose distribution does not change while crossing the e-cloud and moves straight along the longitudinal position s. The Lorentz transformation [34] that moves the coordinates from the laboratory frame to the rest frame of the rigid bunch is:

$$\begin{align} ct' &= \gamma_0 \left(ct - \beta_0 s\right), \tag{2.5}\\ x' &= x, \tag{2.6}\\ y' &= y, \tag{2.7}\\ s' &= \gamma_0 \left(s - \beta_0 ct\right) = \beta_0 \gamma_0 \tau. \tag{2.8} \end{align}$$

This transformation defines the charge ρ' and current $\boldsymbol{J'} = \left(J'_x, J'_y, J'_s\right)$ densities in the rest frame of the rigid bunch as:

$$\begin{align} c\rho' &= \gamma_0 \left(c\rho - \beta_0 J_s\right), \tag{2.9}\\ J'_x &= J_x, \tag{2.10}\\ J'_y &= J_y, \tag{2.11}\\ J'_s &= \gamma_0 \left(J_s - \beta_0 c\rho\right). \tag{2.12} \end{align}$$

Using the approximation that $J_s = 0$, Eqs. (2.9) and (2.12) become:

$$\begin{align} \rho' &= \gamma_0 \rho, \tag{2.13}\\ J'_s &= -\gamma_0 \beta_0 c\rho. \tag{2.14} \end{align}$$

The sources (ρ' and J'_s) of the electromagnetic fields are time-independent in this frame of reference and therefore the fields are also stationary. Choosing the Lorentz gauge, it follows from Maxwell's equations that for stationary fields:

$$\nabla'^2 \phi' = -\frac{\rho'}{\epsilon_0}, \tag{2.15}$$

$$\nabla'^2 A'_s = -\mu_0 J'_s = \mu_0 \beta_0 c \rho', \tag{2.16}$$

where ϵ_0 and μ_0 are the permittivity and permeability of free space, respectively, and with

$$\nabla'^2 = \frac{\partial^2}{\partial x'^2} + \frac{\partial^2}{\partial y'^2} + \frac{\partial^2}{\partial s'^2}. \tag{2.17}$$

By comparing Eqs. (2.15) and (2.16), it is clear that due to the absence of longitudinal currents, the potentials are related through:

$$A'_s = -\frac{\beta_0 \phi'}{c}. \tag{2.18}$$

The inverse transformation of the scalar ϕ and vector $\boldsymbol{A} = \left(A_x, A_y, A_s\right)$ potentials is:

$$\frac{\phi}{c} = \gamma_0 \left(\frac{\phi'}{c} + \beta_0 A'_s\right), \tag{2.19}$$

$$A_x = A'_x, \tag{2.20}$$

$$A_y = A'_y, \tag{2.21}$$

$$A_s = \gamma_0 \left(A'_s + \beta_0 c \phi\right). \tag{2.22}$$

Substituting Eq. (2.18) in Eqs. (2.19) and (2.22), it follows that:

$$\phi = \frac{\phi'}{\gamma_0}, \tag{2.23}$$

$$A_s = 0. \tag{2.24}$$

Additionally, from the definition of τ (see Eq. (2.4)) and from Eq. (2.8), the operator in Eq. (2.17) is rewritten as:

$$\nabla'^2 = \frac{\partial^2}{\partial x^2} + \frac{\partial^2}{\partial y^2} + \frac{1}{\beta_0^2 \gamma_0^2} \frac{\partial^2}{\partial \tau^2}. \tag{2.25}$$

The substitution of Eqs. (2.13), (2.23) and (2.25) in Eq. (2.15) leads to:

$$\frac{\partial^2 \phi}{\partial x^2} + \frac{\partial^2 \phi}{\partial y^2} + \frac{1}{\beta_0^2 \gamma_0^2} \frac{\partial^2 \phi}{\partial \tau^2} = -\frac{\rho}{\epsilon_0}. \tag{2.26}$$

The dynamics of e-clouds in the LHC manifest in scales of $\Delta x \sim 10^{-3}$ m, $\Delta y \sim 10^{-3}$ m, $\Delta \tau \sim 10^{-2}$ m. Moreover, the relativistic factor $\gamma_0 = 450$ for protons at injection energy of the LHC, makes the longitudinal derivative much smaller than the transverse ones by several orders of magnitude.

$$\frac{\partial^2 \phi}{\partial x^2}, \frac{\partial^2 \phi}{\partial y^2} \gg \frac{1}{\beta_0^2 \gamma_0^2} \frac{\partial^2 \phi}{\partial \tau^2}. \tag{2.27}$$

This justifies the approximation of neglecting the term with the second order derivative in τ and Eq. (2.26) becomes:

$$\frac{\partial^2\phi}{\partial x^2} + \frac{\partial^2\phi}{\partial y^2} = -\frac{\rho}{\epsilon_0}. \tag{2.28}$$

It should be reminded that both ϕ and ρ depend on the coordinate τ. The electrons will move according to the scalar potential of the e-cloud ϕ and the interaction with the proton beam. This will lead to a change of ρ with respect to the τ coordinate which will in turn lead to a change of ϕ with respect to τ.

2.2.1 The electron cloud map

In the previous subsection, all of the potentials in the rest frame of the rigid beam (K') have been related to the potentials in the laboratory frame K. The derivation of the e-cloud map is done on the rest frame of the rigid proton beam so as to take into account only the contribution from ϕ' since the particle in the rigid beam is approximated as if at rest.

In the laboratory frame, the beam particle has a constant speed in the longitudinal direction.

$$\frac{\Delta s}{\Delta t} = \beta_0 c. \tag{2.29}$$

Also in the laboratory frame, the e-cloud has a length equal to $\Delta s = L$. Therefore, the interaction of a beam particle with the e-cloud, from the moment it enters until the moment it exits, will last for $\Delta t = \frac{L}{\beta_0 c}$. With this information, the duration of the interaction in the frame K', according to Eq. (2.5), is equal to:

$$\Delta t' = \frac{L}{\beta_0\gamma_0 c}. \tag{2.30}$$

The change of momentum after the interaction in the frame K' is:

$$\Delta \boldsymbol{P'} = -q\int_0^{\Delta t'} \nabla'\phi' \mathrm{d}t', \tag{2.31}$$

or

$$\Delta \boldsymbol{P'} = -\frac{qL}{\beta_0 c}\nabla'\phi. \tag{2.32}$$

This vector equation is written as:

$$\Delta P'_x = -\frac{qL}{\beta_0 c}\frac{\partial\phi}{\partial x'}, \tag{2.33}$$

$$\Delta P'_y = -\frac{qL}{\beta_0 c}\frac{\partial\phi}{\partial y'}, \tag{2.34}$$

$$\Delta P'_s = -\frac{qL}{\beta_0 c}\frac{\partial\phi}{\partial s'}. \tag{2.35}$$

Since the Lorentz transformation does not affect the quantities x, y, P'_x, P'_y, Eqs. (2.33) and (2.34) give the transverse deflections after they are divided by the reference momentum P_0:

$$\Delta p_x = \frac{\Delta P_x}{P_0} = -\frac{qL}{\beta_0 P_0 c}\frac{\partial\phi}{\partial x}, \tag{2.36}$$

$$\Delta p_y = \frac{\Delta P_y}{P_0} = -\frac{qL}{\beta_0 P_0 c}\frac{\partial\phi}{\partial y}. \tag{2.37}$$

For the longitudinal part of the map Δp_τ, the change of energy in the laboratory frame is calculated. In the rest frame of the rigid beam, the energy E' of a particle is related to its momenta $\left(P'_x, P'_y, P'_s\right)$ as:

$$E' = \sqrt{m_0^2 c^4 + \left({P'_x}^2 + {P'_y}^2 + {P'_s}^2\right) c^2}. \tag{2.38}$$

Both before and after the interaction with the e-cloud, the momentum of the particle will be small with respect to its mass in this frame of reference and Eq. (2.38) can be approximated as:

$$E' = m_0 c^2 \left(1 + \frac{{P'_x}^2 + {P'_y}^2 + {P'_s}^2}{2 m_0^2 c^2}\right). \tag{2.39}$$

The Lorentz transformation defines the energy E in the laboratory frame with respect to the energy E' and the longitudinal momentum P'_s in the rest frame of the rigid beam as:

$$E = \gamma_0 \left(E' + \beta_0 c P'_s\right). \tag{2.40}$$

Substituting Eq. (2.39) in Eq. (2.40), the energy is written as:

$$E = \gamma_0 \left(m_0 c^2 \left(1 + \frac{{P'_x}^2 + {P'_y}^2 + {P'_s}^2}{2 m_0^2 c^2}\right) + \beta_0 c P'_s\right), \tag{2.41}$$

and neglecting terms which are of second order in the momentum, we obtain:

$$E = \gamma_0 \left(m_0 c^2 + \beta_0 c P'_s\right). \tag{2.42}$$

The energy change ΔE due to the interaction with the e-cloud is therefore equal to:

$$\Delta E = \gamma_0 \beta_0 c \Delta P'_s. \tag{2.43}$$

Using Eq. (2.35), the definition of τ and dividing both parts with $P_0 c$, the energy change becomes:

$$\frac{\Delta E}{P_0 c} = -\frac{qL}{\beta_0 c}\frac{\partial\phi}{\partial\tau}, \tag{2.44}$$

which is equal to the change in p_τ due to the interaction with the e-cloud:

$$\Delta p_\tau = -\frac{qL}{\beta_0 c}\frac{\partial\phi}{\partial\tau}. \tag{2.45}$$

Summarizing Eqs. (2.36), (2.36) and (2.45), the full map describing the interaction with an e-cloud which is described by the scalar potential ϕ is:

$$x \mapsto x, \tag{2.46}$$

$$p_x \mapsto p_x - \frac{qL}{\beta_0 c}\frac{\partial \phi}{\partial x}\left(x, y, \tau\right), \tag{2.47}$$

$$y \mapsto y, \tag{2.48}$$

$$p_y \mapsto p_y - \frac{qL}{\beta_0 c}\frac{\partial \phi}{\partial y}\left(x, y, \tau\right), \tag{2.49}$$

$$\tau \mapsto \tau, \tag{2.50}$$

$$p_\tau \mapsto p_\tau - \frac{qL}{\beta_0 c}\frac{\partial \phi}{\partial \tau}\left(x, y, \tau\right). \tag{2.51}$$

This map is generated by the Hamiltonian:

$$H = \frac{qL}{\beta_0 P_0 c}\phi\left(x, y, \tau\right)\delta\left(s - s_0\right), \tag{2.52}$$

and is therefore symplectic by construction.

2.3 E-clouds effects at the LHC

The electrons and the generated electromagnetic fields can affect the operation of an accelerator in several unwanted ways. The flux of electrons onto the walls of the vacuum chamber can cause [30]

1. A dynamic pressure rise, degrading the vacuum.
2. Heat deposition, raising the temperature of the affected device.
3. Interference with beam instrumentation leading to spurious signals.

The electromagnetic fields generated by the e-cloud can affect the beam dynamics leading to performance limitations in the accelerator. In particular, they can lead to:

1. A tune-shift that is bunch-by-bunch dependent [54].
2. A synchronous phase-shift along the bunch trains through the energy loss (of the beam particles) when interacting with the electrons[55].
3. Coherent beam instabilities causing to fast beam loss or emittance blow-up[20, 56].
4. Incoherent effects to cause slow beam loss or slow emittance growth[12, 45, 10, 7, 11].

In the LHC, the e-cloud results in strong coherent transverse instabilities, which need to be mitigated with the usage of a feedback system and by operating with large chromaticity and tune spread from octupole magnets[57, 58, 20, 56].

2.3.1 SEY measurements in the LHC

The SEY in the LHC has been estimated by comparing heat load measured during the operation of LHC and heat load simulated using the PyECLOUD software [59]. The estimation of SEY is described in Refs. [21, 60]. By simulating the heat load in the dipole magnets, the quadrupole magnets and the drift spaces in between, using the beam conditions during the measurements, the SEY that reproduces the measurements if found for each half-cell of the LHC individually. The estimated SEY per half-cell is shown in Figs. 2.7 and 2.8 for the different arcs and for measurements recorded during 2012 and during 2018.

A peculiar feature that is observed is that there are strong variations of the SEY across different half-cells. In fact, sectors 78, 81, 12 and 23 show a systematically larger SEY than sectors 34, 45, 56 and 67. The difference in SEY is attributed to the appearance of different oxides on the surface of the LHC beam screens [61]. However, the systematic difference of SEY between the different sectors is still under investigation at the time of writing.

2.4 Incoherent e-cloud effects

Even when instabilities are successfully controlled, the e-cloud can still induce significant beam degradation through incoherent effects, resulting in slow beam losses and transverse emittance growth. Notably, at the Large Hadron Collider (LHC) [1] e-clouds induce a significant beam lifetime degradation both at injection energy and in collision [62, 24, 22]. The modelling of such beam degradation is particularly difficult since these effects are the result of an interplay between the non-linear e-cloud forces and the non-linearities of the accelerator lattice. Furthermore, such effects are often visible only on very long time scales corresponding to several millions of beam revolutions. Therefore, numerical models and computer programs used for this purpose need to be at the same time sufficiently accurate to correctly describe the phenomena and sufficiently fast to allow the simulation of such long time scales.

Incoherent effects from e-cloud were addressed by different studies over the last two decades. Furman *et al.* [7] showed that e-clouds can cause a tune spread, distort the betatron functions and dispersion, as well as cause a synchro-betatron coupling. The incoherent tune shift was also studied by Romano *et al.* [8],as well as Petrov *et al.* [9]. Franchetti *et al.* [10] used simplified cloud distributions to express analytically the forces induced on the beam particles by the e-cloud. Such an approach is very convenient in terms of computation time but lacks the capability of accurately describing realistic e-cloud distributions, especially in the presence of magnetic field gradients. Ohmi and Oide [11] studied the incoherent emittance growth driven by e-cloud with self-consistent Particle-In-Cell simulations of the coupled dynamics between the e-cloud and the beam particles. Such an approach is extremely demanding in terms of computation time and ultimately does not allow the simulation of the long time scales required for the study of these effects in realistic configurations.

Incoherent modifications of the beam distribution driven by e-cloud effects are typically slow processes. Hence, it is reasonable to assume that over a relatively large

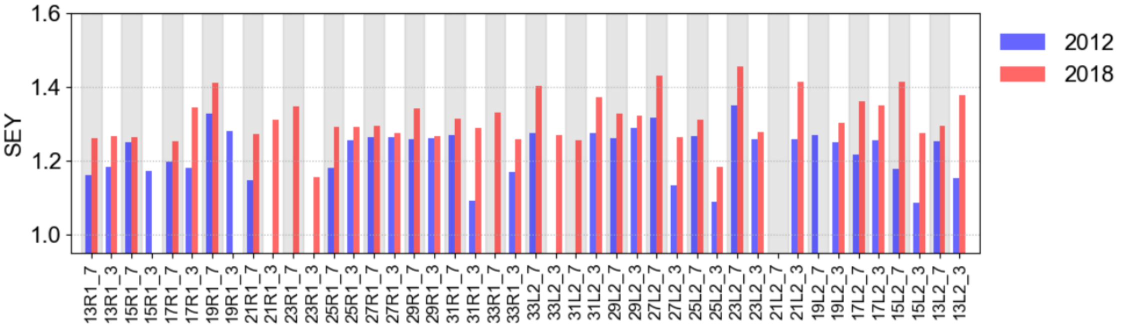

(a) Arc 12

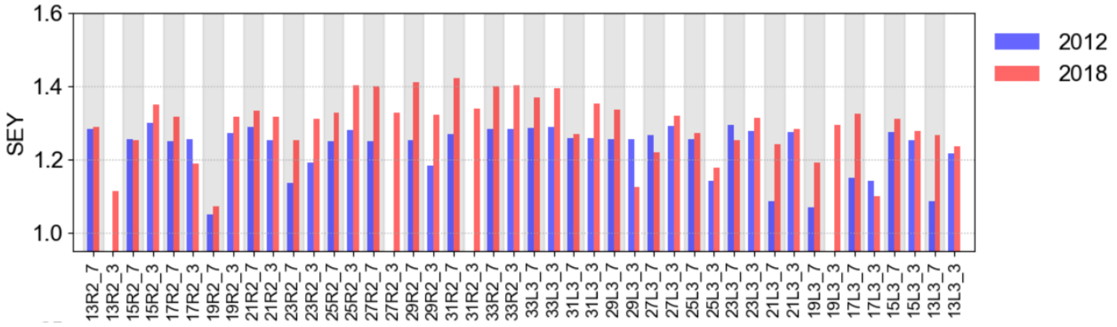

(b) Arc 23

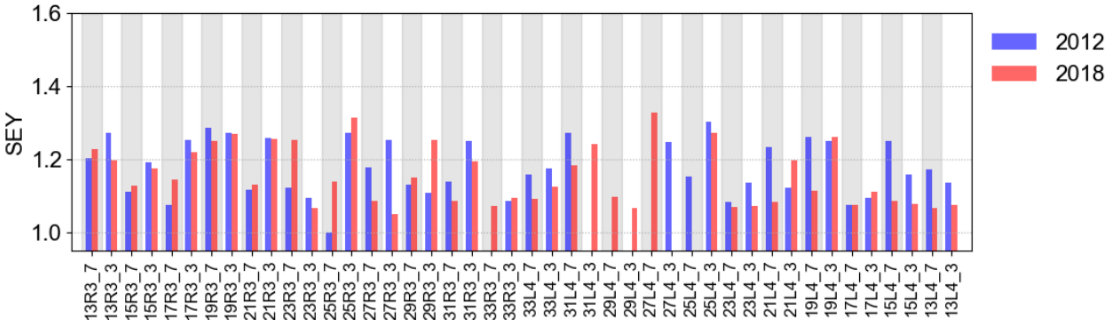

(c) Arc 34

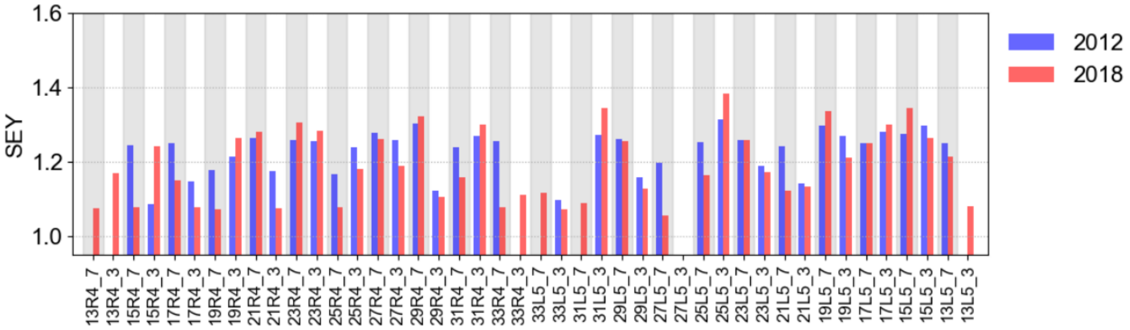

(d) Arc 45

Figure 2.7: Estimated SEY in the half-cells of the 12 (a), 23 (b), 34 (c) and 45 (d) LHC sectors in 2012 (blue) and 2018 (red). Figures adapted from Ref. [21].

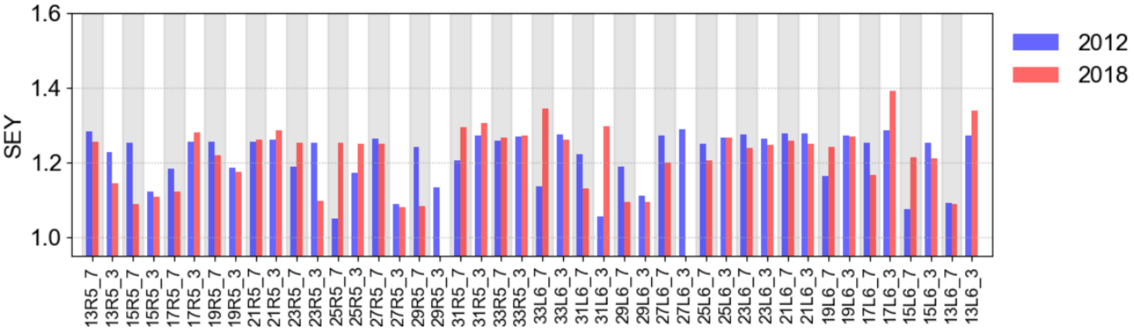

(a) Arc 56

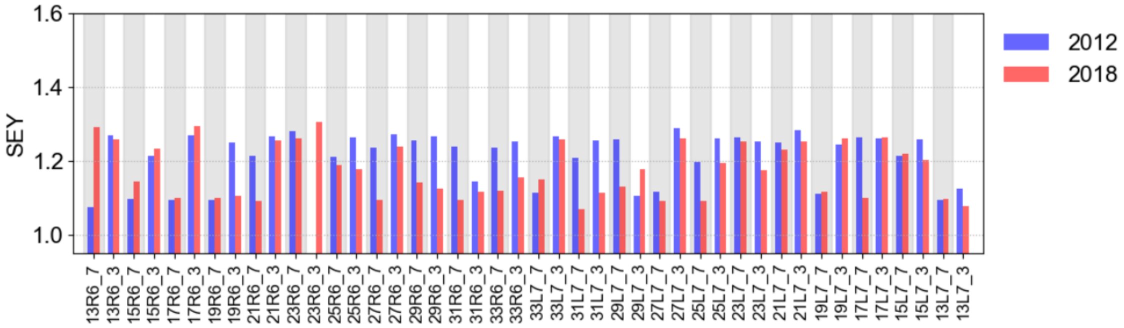

(b) Arc 67

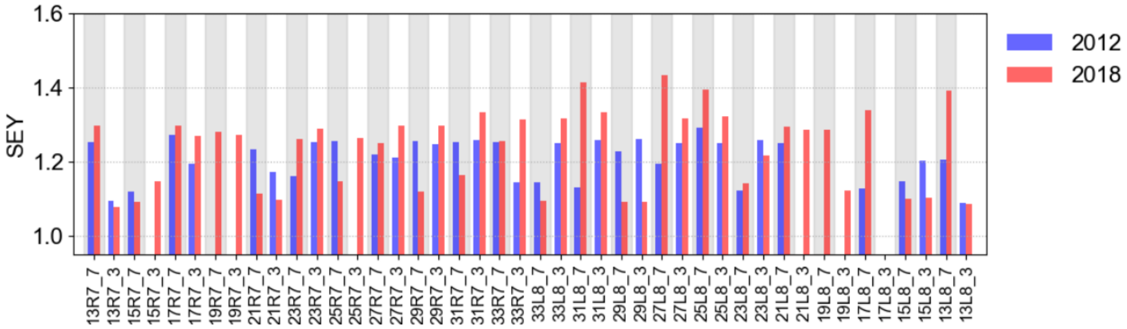

(c) Arc 78

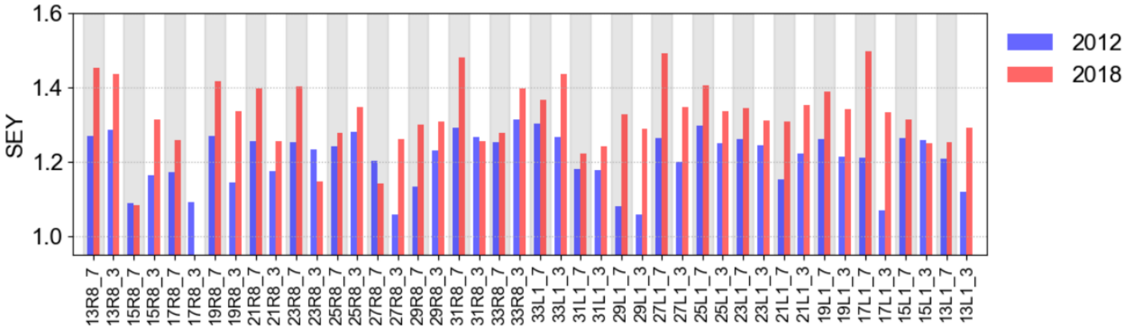

(d) Arc 81

Figure 2.8: Estimated SEY in the half-cells of the 56 (a), 67 (b), 78 (c) and 81 (d) LHC sectors in 2012 (blue) and 2018 (red). Figures adapted from Ref. [21].

number of turns the impact of the changes in the beam distribution on the e-cloud dynamics can be neglected. Based on this consideration, Benedetto *et al.* [12, 13] introduced the approach of pre-recording the e-cloud forces on a discrete grid and computing the forces on the beam particle location using an interpolation scheme. In this work the authors do not address the issue of the symplecticity of the simulated interaction. As will be discussed in more detail in Section 5.1.1, the usage of an interpolation scheme does not guarantee the preservation of the symplecticity of the particle interaction with the e-cloud. If the numerical model is not symplectic, artificial growth or damping can be introduced in the amplitude of the particle motion, leading to unacceptable modifications on observables of interest like beam lifetime and emittance evolution [14].

The e-cloud pinch

The dynamics of the e-cloud depends on a large set of parameters, including spacing between bunches, bunch charge, transverse beam sizes and bunch length. It also depends on properties of the accelerator, for example the magnetic field configuration, the geometry of the vacuum chamber and the material properties of the vacuum chamber's walls, in particular their Secondary Electron Yield (SEY). Figure 2.9 shows a typical evolution of the e-cloud charge density during the passage of a bunch in the absence of externally applied magnetic fields.

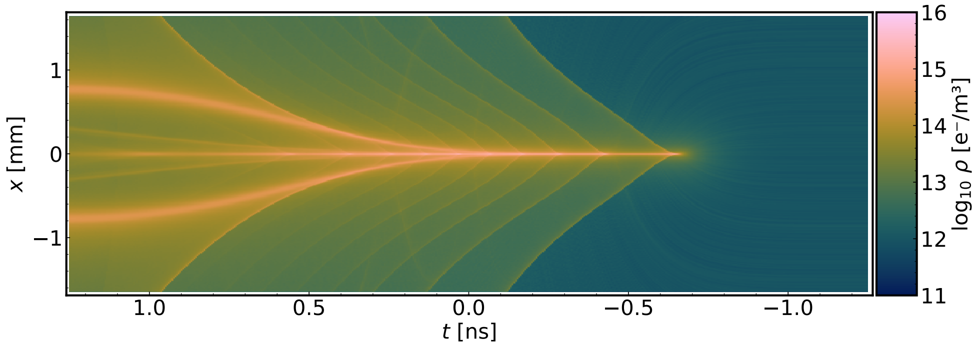

Figure 2.9: Time evolution of the $x = 0$ slice of the electron density distribution during an e-cloud pinch. The head of the bunch is at $t < 0$.

While the bunch passes through the cloud, the electron density increases significantly at the bunch location and complex structures appear in the density profile. This is commonly referred to as the e-cloud "pinch" [10, 63]. The field generated by such an evolving charge distribution has very specific features illustrated in Fig. 2.10. In the transverse plane, the field changes sign very abruptly within the core of the bunch, as shown in Fig. 2.10a. Moreover, strong oscillations of the fields are observed as a function of time as illustrated in Fig. 2.10b. It is evident that describing such a field behaviour with analytical expressions is practically unfeasible.

Furthermore, in the presence of a magnetic field the electrons are confined by the field lines and the electron dynamics can get even more complicated. Both the non-linear behavior of the transverse field distribution and its time-varying nature

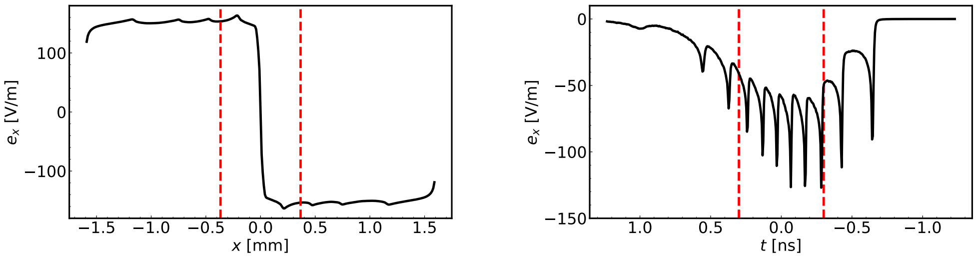

(a) (b)

Figure 2.10: (a) Horizontal field as a function of horizontal position x at $y = 0, t = 0$. (b) Horizontal field as a function of time t at $y = 0, x = 5$ µm.

have a strong impact on the dynamics of the beam particles that are subject to these fields. It is therefore important to correctly model these features when simulating the beam dynamics in the presence of the e-cloud.

Chapter 3

Bunch-by-bunch measurement of slow beam losses in the LHC

In 2018, during the LHC Run 2 [64] in 2018, a large fraction of the physics luminosity production was performed with a beam energy of 6.5 TeV, a bunch spacing of 25 ns and beta functions of 30 cm at the high luminosity interaction points. Because of the luminosity burn-off, the intensity of the two counter-rotating beams was gradually reducing during the fills. This allowed to gradually reduce the crossing angle between the two beams in order to maximize the integrated luminosity produced[65]. In this chapter, the available experimental observations are reviewed that allow disentangling the contributions to the observed beam degradation caused by the different collective effects, namely the beam-beam and the electron cloud effects. As it will be shown, e-cloud effects are the most significant contributors in the degradation of the beam lifetime. A bunch-by-bunch analysis of different specialized tests points to the fact that the e-cloud in the final focusing quadrupoles of the Inner Triplet (IT) assemblies is mostly responsible (see Sec. 1.4)

In the analysis, only the beam circulating in the clockwise direction(so called beam 1) is considered. The same features are observed in the beam circulating counter-clockwise (so called beam 2), but they are more pronounced in beam 1. The beam loss rate is calculated from the drop of intensity as measured by the Fast Beam Current Transformer, in intervals of five minutes. The losses of beam

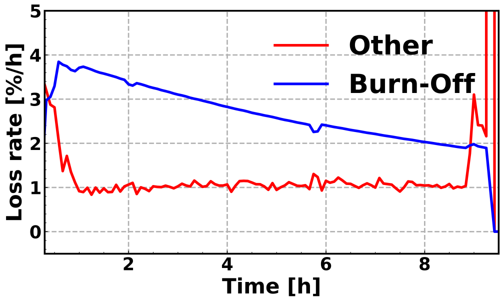

Figure 3.1: Total beam losses separated into luminosity burn-off and other sources, as a observed during a single typical LHC fill in 2018. Figure adapted from Ref. [22]
.

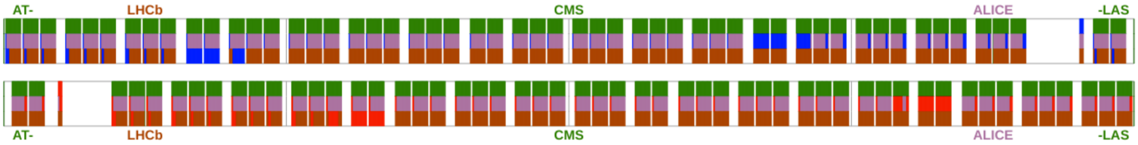

Figure 3.2: Typical BCMS filling scheme used during the LHC Run 2 in 2018. Figure adapted from Ref. [23].

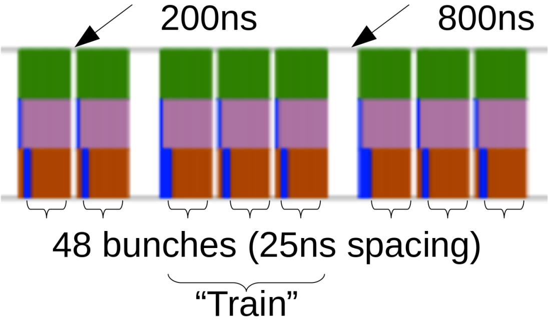

Figure 3.3: Magnification in a small region of Fig. 3.2.

1 are shown in Fig. 3.1 where they are split in two contributions. The blue line shows the contributions of burn-off, *i.e.* of protons lost because of inelastic proton-proton collisions. This burn-off is calculated by using the instantaneous luminosity L, provided by the ATLAS and CMS experiments. and is is equal to

$$\frac{dN}{dt} = L\ \sigma_{\text{inel}} \quad , \tag{3.1}$$

where L is the instantaneous luminosity [32] and σ_{inel} is the total inelastic cross section which is equal to 79.5 ± 1.8 mbarn at $\sqrt{s} = 13$ TeV [66]. The contribution to the instantaneous luminosity from the ALICE and LHCb experiments is considered negligible. Subtracting the burn-off contribution from the total loss rate, the losses due to other sources are obtained, visible in the red line of Fig. 3.1. While the contribution of burn-off decays with time due to the decaying intensity, the additional losses remain constant after a fast decrease during the first hour. One observes that the additional losses are comparable to the burn-off losses, especially towards the end of the fill. The analysis of the additional losses can help identify the sources that cause them.

3.1 Analysis strategy

Significant insight can be gained from the bunch-by-bunch analysis of the losses, allowing to attribute the losses to either single-bunch effects or effects that affect each bunch differently. The typical filling scheme used during Run 2 of the LHC is based on the Bunch Compression Merging and Splitting (BCMS) production scheme in the LHC injectors [67]. This is illustrated in Fig. 3.2 where each bar represents a bunch train for a total of 2556 bunches in each beam. Apart from 12 non-colliding bunches, the filling scheme consists of batches of 48 bunches, with a bunch spacing of 25 ns, produced in the Proton Synchrotron. A magnification on the filling scheme

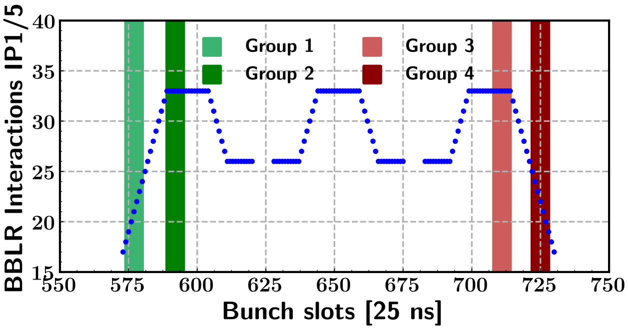

Figure 3.4: Number of BBLR interactions per high luminosity interaction point for each bunch in a train consisting of three batches. Figure adapted from Ref. [22].

is shown in Fig. 3.3. A train of two batches and two trains of three batches are shown. Each batch in a train is separated by 200 ns, necessary for the rise time of Super Proton Synchrotron injection kicker. The trains are separated by gaps of 800 ns, necessary for the rise time of the LHC injection kicker.

There are two main effects that can affect the losses of each bunch differently. The first one is the e-cloud, which builds up from the head of the train towards the tail of the train. The 200 ns gap between batches just barely reduces the electron density in the cloud but the 800 ns gap between the trains is enough that e-clouds almost completely decay. Depending the on the vacuum chamber, the SEY of its walls and the characteristics of the beam, the e-cloud may or may have not reached saturation. Additionally, the bunches will encounter Beam-Beam Long-Range (BBLR) interactions close to interaction points where they collide head-on with the other beam. The number of encounters depends on the bunch structure of the opposite beam. For a train of three batches, the number of BBLR encounters according to the position of the bunch in the train is plotted in Fig. 3.4. The number of BBLR interactions is symmetric with respect to the center of the train. The first and last bunches of the train exhibit the minimal amount BBLR interaction.

Using these signatures of bunch-by-bunch patterns, four groups of bunches are selected in order to disentangle the two effects, illustrated with the colored bands in Fig. 3.4. Their properties are the following:

Group 1: Bunches at the head of the leading batch of the train. These experience the minimal amount of BBLR interactions and small e-cloud densities.

Group 2: Bunches at the center of the leading batch of the train. These experience the maximal amount of BBLR interactions and small e-cloud densities.

Group 3: Bunches at the center of the trailing batch of the train. These experience the maximal amount of BBLR interactions and large e-cloud densities;

Group 4: Bunches at the tail of the trailing batch of the train. These experience the minimal amount of BBLR interactions and large e-cloud densities.

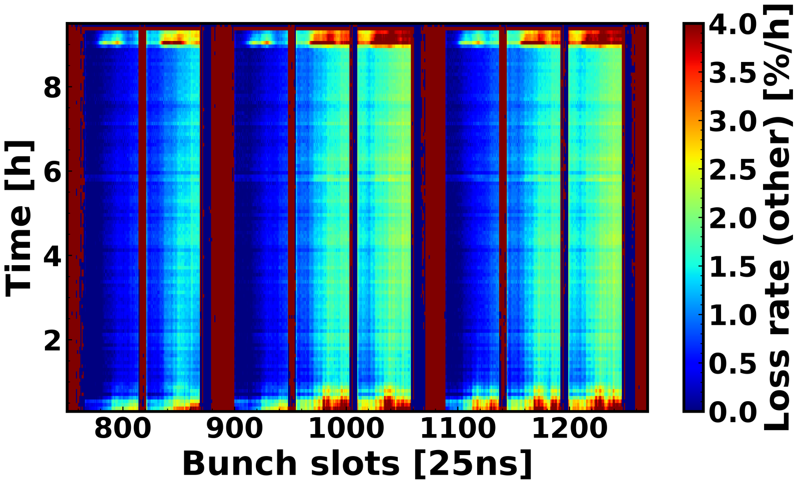

Figure 3.5: Bunch-by-bunch additional loss rate for three consecutive bunch train and its evolution with time, beginning from the onset of collisions in a typical LHC physics fill. The loss rate from luminosity burn-off has been subtracted. Figure adapted from Ref. [22].

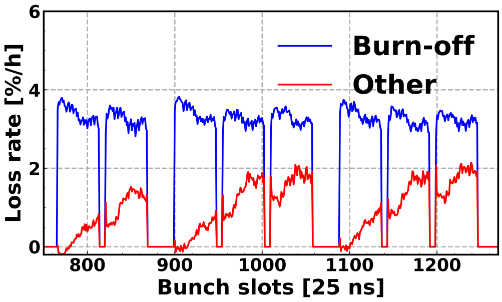

Figure 3.6: Bunch-by-bunch loss rates for three consecutive bunch train at time $t = 2$ hours since the onset of collisions in a typical LHC physics fill. The additional losses (red) are plotted alongside the losses due to burn-off (blue) subtracted. Figure adapted from Ref. [22].

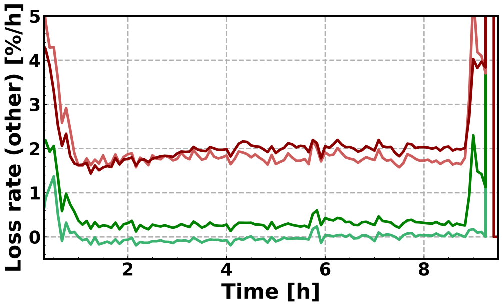

Figure 3.7: Additional loss rates for the four groups of bunches, as measured during a typical LHC physics fill. The losses are shown for group 1 (light green), group 2 (dark green), group 3 (light red), group 4 (dark red), defined in Fig. 3.4. Figure adapted from Ref. [22].

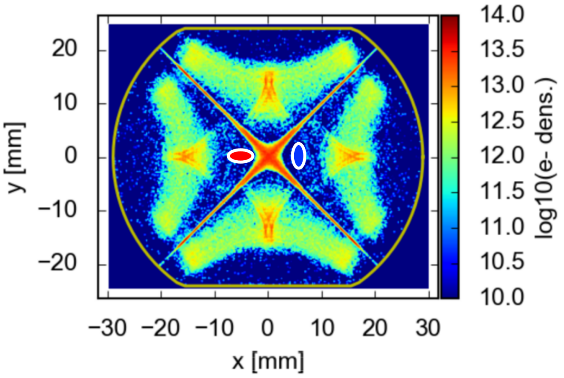

Figure 3.8: Snapshot of a simulated electron cloud distribution in a slice of an IT quadrupole magnet. The positions and size of the two beams is indicated by the blue and red ellipses. Figure adapted from Ref. [22].

3.2 Beam losses during collisions

Figure 3.5 shows the evolution of the bunch-by-bunch loss rate for bunches in three consecutive bunch trains, where the contribution of burn-off to the loss rate has been subtracted. The evolution is shown beginning from the moment when bunches are put into collision. A slice at time $t = 2$ hours of these losses is shown in Fig. 3.6. The additional loss rate exhibits a trend that is increasing from the leading bunches towards the trailing bunches of each train.

The additional loss rates are calculated for the four groups of bunches described in Sec. 3.1 and their evolution in time is shown in Fig. 3.7. For all groups of bunches, strong losses are observed at early times, *i.e.* right after the beams are put into collision, which then decay within an hour. In the following part of the fill, bunches belonging in group 1 show negligible losses, while for group 2 losses are small. Bunches in groups 3 and 4 show very similar loss rates This means that the number of BBLR interactions doesn't appear to have a significant effect on the beam lifetime. These facts indicate that the strongest source of losses is most likely e-cloud effects. It should be noted that it is expected that the BBLR interaction wouldn't significantly degrade the beam lifetime as the operational settings (crossing angle and betatron tunes) have been chosen in order to minimize the effect of the BBLR interactions.

Effect of crossing angle

During physics fills in the LHC Run 2, as the bunch intensity decreases (mostly due to the luminosity burn-off), so does the strength of the BBLR interactions. This increases the margin available in terms of single-particle stability and allows to reduce the crossing angle in order to maximize the produced luminosity [68]. Indeed such a strategy is adopted in the operation of the LHC and the crossing angle is gradually reduced from 320 µrad to 260 µrad.

The crossing angle between the beams is created through a closed orbit bump in the insertion regions. Reducing the crossing angle makes the closed orbit bump smaller, bringing the two beams closer to the center of the IT quadrupoles. A

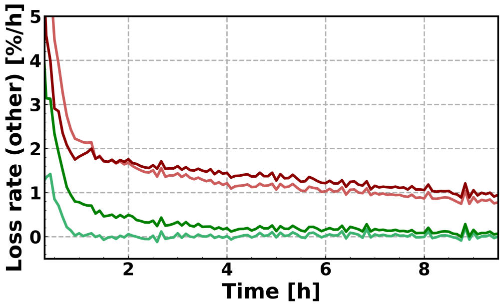

Figure 3.9: Additional loss rates for the four groups of bunches, as measured during a test LHC physics fill with a constant crossing angle. The losses are shown for group 1 (light green), group 2 (dark green), group 3 (light red), group 4 (dark red), defined in Fig. 3.4. Figure adapted from Ref. [22].

snapshot of the e-cloud in a slice of the IT can be seen in Fig. 3.8, where the beams are also illustrated with the red and blue solid ellipses. As is typical in a quadrupolar magnetic field, there is a large electron density concentrated in the center of the chamber and on the two diagonals passing through the four poles of the magnet. Therefore, a reduction of the crossing angle increases the effect both of the BBLR interactions and of the e-cloud in the insertion region around the high luminosity interaction points. Apart from the IT, the rest of the beam pipe in the common area is coated with a low-SEY material, completely suppressing the formation of e-cloud.

In order to investigate whether the change of crossing angle affects the beam loss rate, a special test fill is analyzed, where the crossing angle was kept constant at 320 µrad for the entire duration. The resulting loss rate for the same four groups of bunches is shown in Fig. 3.9. By comparing Figs. 3.7 and 3.9, it is clear that the loss rates reduce with time in all of the groups. Also for this fill, the fact that the loss rate is identical between bunches in group 3 and group 4 indicates that e-cloud effects are the most significant contributor to the degradation of the beam lifetime.

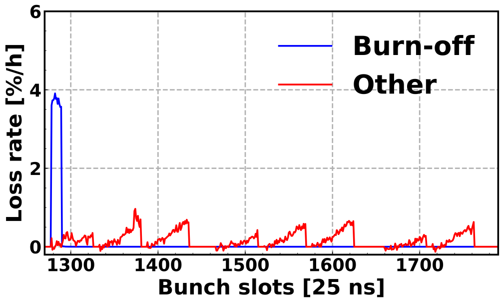

Figure 3.10: Bunch-by-bunch loss rates measured with a single circulating beam. A small train of 12 bunches is injected in the other beam as is visible by the blue line corresponding to the luminosity burn-off losses. Figure adapted from Ref. [22].

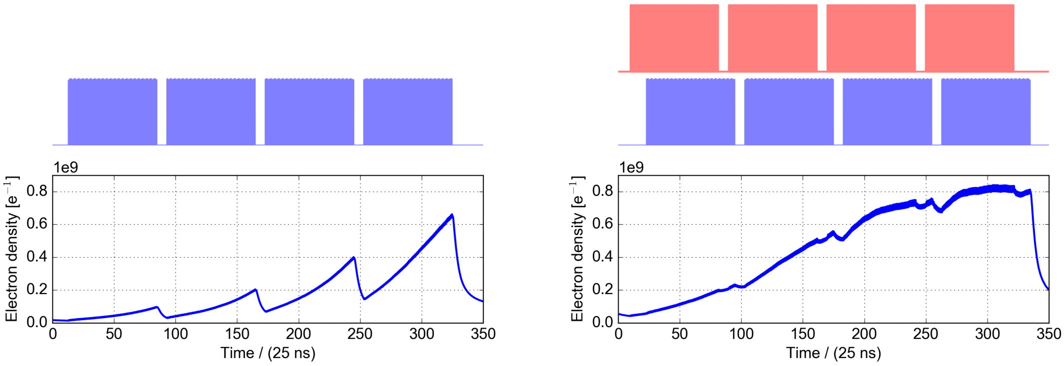

(a) (b)

Figure 3.11: Electron density as a function of time, simulated in a slice of an IT quadrupole magnet with one circulating beam (a) and two circulating beams (b). The bunch pattern is plotted on top of the figures for beam 1 (blue) and beam 2 (red). A train of 4 long batches of 72 bunches is simulated to also study the saturation of the electron density. Figure adapted from Ref. [22].

Single-beam losses

In an additional dedicated test the losses were recorded with trains that do not encounter the other beam, in the same configuration used for the typical physics fills. To precisely replicate the machine and beam configuration, a small train is present in beam 2 for technical reasons. The bunch-by-bunch loss rates that are measured during this experiment are shown in Fig. 3.10. By comparing Figs. 3.6 and 3.10, it is evident that the losses are significantly smaller, and show a different bunch-by-bunch pattern. In this configuration, the strong non-linear forces from the beam-beam interactions (either head-on or long-range) are absent. Moreover, the e-cloud density in the IT quadrupoles is expected to be reduced in the presence of a single circulating beam, when compared to the case where both beams are circulating [69]. Due to the large size of the vacuum chamber in the IT quadrupoles, a 200 ns gap between batches is enough to significantly limit the buildup of the e-cloud. However, the presence of an additional counter-rotating beam can sustain the electron density in the e-cloud during this 200 ns gap. Simulations of the e-cloud buildup in an IT quadrupole are illustrated in Fig. 3.11 for a single circulating beam (a) and two counter-rotating circulating beams (b). By comparing the e-cloud buildup of Fig. 3.11a to the bunch-by-bunch loss rate pattern of Fig. 3.10, and the e-cloud buildup of Fig. 3.11b to the bunch-by-bunch loss rate pattern of Fig. 3.6, the similarity is evident. Therefore, the e-cloud that forms in a common beam chamber under the influence of both beams is correlated to increased losses.

Different optics configuration

Another test that points to the e-cloud in the IT quadrupoles as the driving source behind the beam lifetime degradation was conducted during the validation of a special beam optics configuration to prepare for the LHC Run 3 [70, 71]. In the typical physics fill configuration, the horizontal and vertical betatron functions at the high luminosity interaction points were equal to $\beta^* = 30$ cm with a telescopic index $r = 2$. In the beam optics configuration used in this test, the betatron functions were equal to $\beta^* = 65$ cm with a larger telescopic index of $r = 3$. The telescopic index determines the amplification of the betatron functions in the strong sextupoles of the arcs left and right of the high luminosity interaction points. Because of the larger β^*, the maximum betatron function in the IT is significantly smaller, while because of the increased telescopic index, the betatron functions in the S12, S45, S56 and S81 LHC arcs are increased. The measured bunch-by-bunch loss rates are shown in Fig. 3.12. They are significantly lower compared to those in Fig. 3.6. This shows that the contribution of the e-cloud in the arcs to the beam lifetime degradation is negligible while the reduction in losses is explained by the fact that a reduced betatron function at the IT quadrupoles results in weaker effects from the e-cloud at those location.

3.3 Beam losses during the betatron squeeze

During the typical operation of the LHC, the betatron function at the interaction points is $\beta^* = 1$ m at the end of the energy ramp. Before the beams are brought into collision, β^* is a reduced to the value of 30 cm. This happens in a dedicated process called the *betatron squeeze*. The evolution of β^* during this process is illustrated in the top of Fig. 3.13. In the bottom of Fig. 3.13, the total loss rate, averaged over several fills, is shown for two fill categories, before and after the optimization of the beam lifetime. In order to optimize the beam lifetime, the betatron tune settings that are used during the betatron squeeze were changed from $(Q_x, Q_y) = (0.31, 0.32)$ to $(0.305, 0.315)$. The blue line in Fig. 3.13 shows the average loss rate for fills before the change of the set betatron tunes while the red line shows the average loss rate for those after.

The modification of the tune betatron settings was motivated by simulations of dynamic aperture through particle tracking. In these simulation studies, magnetic non-linearities and BBLR effects were included, but e-cloud effects were not. The simulations showed that a larger dynamic aperture can be obtained by lowering the

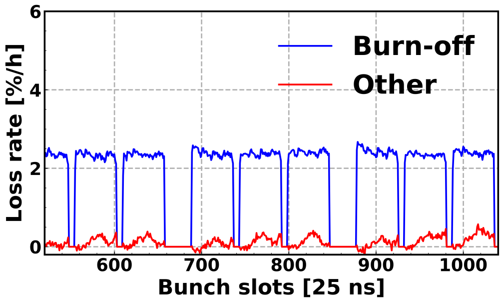

Figure 3.12: Bunch-by-bunch additional loss rates (red) and luminosity burn-off losses (blue) measured during a test with larger betatron functions in the arcs and smaller ones in the ITs. Figure adapted from Ref. [22].

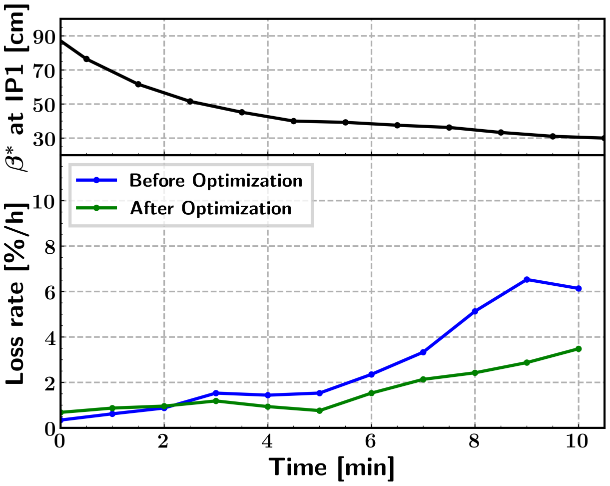

Figure 3.13: Top: evolution of β^* during the betatron squeeze. Bottom: Total beam loss rate measured during fills before (blue) and after (green) the optimization of the betatron tunes. Figure adapted from Ref. [24].

tunes. For coherent stability issues due to residual linear coupling in the transverse motion [72], the difference between the fractional horizontal and vertical betatron tunes was kept constant.

Bunch-by-bunch loss rates for two fills before and after the optimization can be seen in Fig. 3.15. A significant improvement is observed with respect to the total beam losses. Features of both BBLR interactions and e-cloud effects can be noticed. After the tune change, the pattern of the BBLR interaction disappears in the bunch-by-bunch loss rates. while the pattern of e-cloud remains unchanged. This is in line with the fact that simulations with only BBLR effects were used to optimize the lifetime.

A systematic analysis of these losses was carried out following the strategy of the four groups defined in the Sec. 3.1. The average loss rate is presented in Fig. 3.16 for bunches in group 1 (top left), bunches in group 2 (top right), bunches in group 3 (bottom left) and bunches in group 4 (bottom right). It is easy to notice that the bunches showing the best lifetime are those belonging in group 1, *i.e.* those with the minimum number of BBLR interaction and reduced e-cloud effects. Additionally, bunches in group 2 show a significantly better lifetime compared to bunches in group 3, even though they experience the same number of BBLR interactions. Moreover, after the optimization of the lifetime, bunches in group 3 and group 4 show similar losses. Finally the lifetime of bunches in group 3 and group 4 is always larger than the lifetime of bunches in group 1 and group 2.

Since the evolution of losses is correlated with the evolution of the β^* and equivalently of the betatron functions in the IT quadrupole magnets, these observations are consistent with the hypothesis that the e-cloud in the IT quadrupole magnets is the most significant source contributing to these losses. The fact that the change of betatron tunes for the optimization of the lifetime did not affect bunches in group 4,

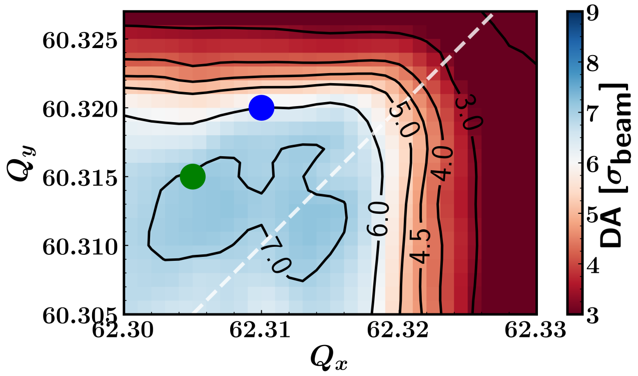

Figure 3.14: Dynamic aperture as a function of the set betatron tune settings in simulations at the end of the betatron squeeze with BBLR interactions. The dots represent tune settings used during operation before (blue) and after (green) the change of the tune settings. Figure adapted from Ref. [24].

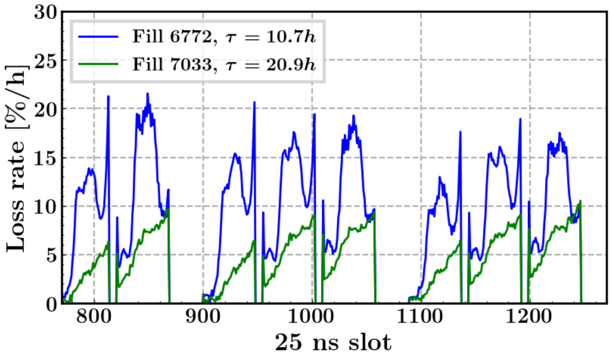

Figure 3.15: Bunch-by-bunch loss rates for three consecutive trains of bunches at $\beta^* = 33$ cm for a fill before the tune change (blue) and a fill after the tune change (green). Figure adapted from Ref. [24].

shows that the cause of the losses cannot be a coherent tune-shift along the trains.

3.4 Remarks

The analysis of bunch-by-bunch slow beam losses reveals that the e-cloud in IT quadrupole magnets is a strong source of non-linearities causing a degradation of slow beam losses. This is consistent with a large set of measurements at a proton reference energy of 6.5 TeV. For the High-Luminosity LHC upgrade, the beam screens of the ITs are planned to be coated with amorphous carbon (a-C) [73]. The amorphous carbon coating features a low SEY, which is expected to lead to a mitigation suppression of thee-cloud multipacting and buildup in the ITs.

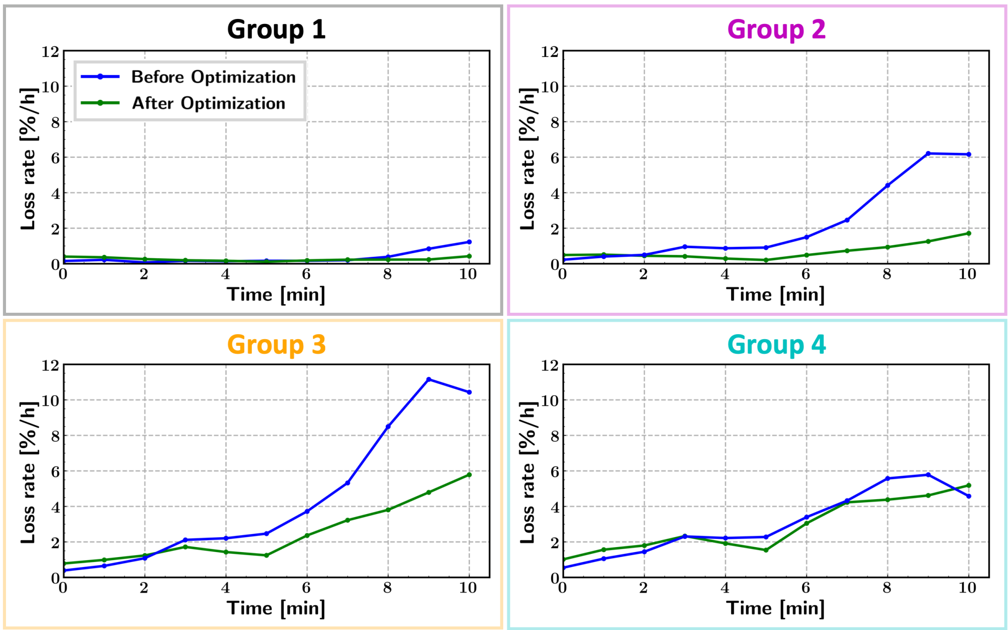

Figure 3.16: Measured loss rate for bunches belonging in the groups defined in Fig. 3.4, averaged over several fills before (blue) and after (green) the optimization of the beam lifetime. Figure adapted from Ref. [24].

Chapter 4

Long-term simulations of particle distributions for colliding beams in the LHC

From the analysis conducted in Chapter 3, it is clear that when looking at Figs. 3.7 and 3.9, there are strong additional losses at early times with respect to the onset of collisions for all of the bunches. These losses are thought to come from the introduction of the beam-beam head-on interaction between the two beams. The topic of this chapter is the usage of particle tracking simulations to compute the impact of incoherent effects on observable quantities like beam lifetime and emittance evolution.

4.1 Description of the simulation

In recent software development of particle tracking engines, SixTrackLib [74] was created in order to efficiently use Graphics Processing Units (GPU). In comparison to the few number of powerful cores that a typical Central Processing Unit (CPU) has, a GPU holds typically a few thousand, but slower, cores. The CPU cores can execute instructions independently of each other, while the GPU cores need to execute in relatively large groups the same instructions. Such architecture fits very well conveniently the requirements of tracking simulations in which multiple particles need to be propagated along the same lattice. An example of the time needed to track particles as a function of their number is shown in Fig. 4.1 for the case of using a typical single-threaded, single-core CPU (red) and GPU (blue). Naturally, on the single-threaded single-core CPU the computation time is simply proportional to the number of particles that are being simulated. On the GPU, instead, the computation time is constant with respect to the number of particles until the capacity of the GPU is reached. Then for a larger number of particles, the relation becomes again roughly proportional. It is import to note that, if only a very small number of particles needs to be tracked, then a CPU will have a shorter computation time than the GPU. On the other hand, the GPU offers a significant speedup when many thousands of particles need to be tracked concurrently.

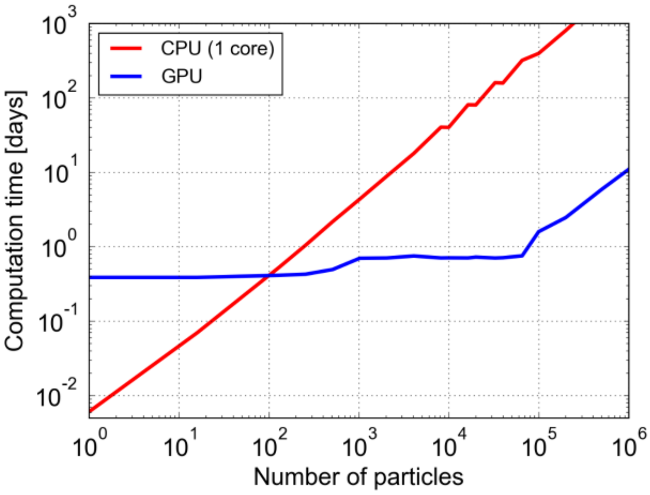

Figure 4.1: Total computation time as a function of the number of particles that are being simulated when using a single-core CPU core (red) and a GPU (blue).

Modelling of the beam-beam long range interactions

For the setup of the simulation, SixTrackLib parses the MAD-X [75] description of the LHC lattice and converts it to a sequence of elements used to propagate the particles' motion. The lattice is "thin", in order to numerically solve the equations of motion, in the sense that each element has been sliced to sequences of drifts (elements that change the position of the particle) and kicks (elements that change the momentum of the particle). The beam-beam interaction is applied using a weak-strong approximation where the simulated particles belong to a "weak" beam which is unable to influence the opposing "strong" beam. This approximation is appropriate to address the single-particle stability of individual particles when the particle distribution of the two beams changes very little over the simulated time. In this and the following subsection, a brief summary of the modelling used for the beam-beam interaction is presented from the literature [76, 77, 6, 78, 79].

For the beam-beam long range interaction, the length of the bunch is neglected. The Hamiltonian that describes this beam-beam interaction between bi-Gaussian beams is the following [77, 76]:

$$H = \frac{Nq}{P_0 c} U(x, y; \sigma_x, \sigma_y)\, \delta(s), \tag{4.1}$$

where N corresponds to the bunch intensity, q is the charge of the simulated particle in the weak beam, c is the speed of light and P_0 is the reference momentum of the particles in the weak beam. σ_x and σ_y are the r.m.s. horizontal and vertical beam sizes of the bi-Gaussian distribution, respectively. The scalar potential U is:

$$U(x, y; \sigma_x, \sigma_y) = -\frac{q_s}{4\pi\varepsilon_0} \int_0^\infty \frac{\exp\left(-\frac{x^2}{2\sigma_x^2+u} - \frac{y^2}{2\sigma_y^2+u}\right)}{\sqrt{2\sigma_x^2 + u}\sqrt{2\sigma_y^2 + u}} \mathrm{d}u, \tag{4.2}$$

where q_s is the charge of the particles in the strong beam and ε_0 is the permittivity of free space. factor. According to this Hamiltonian, the normalized canonical momenta of the particles change as:

$$p_x \mapsto p_x + \frac{Nq}{P_0 c} f_x(x, y; \sigma_x, \sigma_y), \tag{4.3}$$

$$p_y \mapsto p_y + \frac{Nq}{P_0 c} f_y(x, y; \sigma_x, \sigma_y), \tag{4.4}$$

where the forces f_x, f_y are equal to:

$$\begin{aligned} f_x = {} & \frac{e}{2\varepsilon_0 \sqrt{2\pi\left(\sigma_x^2 - \sigma_y^2\right)}} \times \\ & \times \ \mathrm{Im}\left[w\left(\frac{x + iy}{\sqrt{2\left(\sigma_x^2 - \sigma_y^2\right)}} \right) - \exp\left(-\frac{x^2}{2\sigma_x^2} - \frac{y^2}{2\sigma_y^2} \right) w\left(\frac{x\frac{\sigma_y}{\sigma_x} + iy\frac{\sigma_x}{\sigma_y}}{\sqrt{2\left(\sigma_x^2 - \sigma_y^2\right)}} \right) \right], \end{aligned} \tag{4.5}$$

$$\begin{aligned} f_y = {} & \frac{e}{2\varepsilon_0 \sqrt{2\pi\left(\sigma_x^2 - \sigma_y^2\right)}} \times \\ & \times \ \mathrm{Re}\left[w\left(\frac{x + iy}{\sqrt{2\left(\sigma_x^2 - \sigma_y^2\right)}} \right) - \exp\left(-\frac{x^2}{2\sigma_x^2} - \frac{y^2}{2\sigma_y^2} \right) w\left(\frac{x\frac{\sigma_y}{\sigma_x} + iy\frac{\sigma_x}{\sigma_y}}{\sqrt{2\left(\sigma_x^2 - \sigma_y^2\right)}} \right) \right], \end{aligned} \tag{4.6}$$

for elliptic beam with $\sigma_x > \sigma_y$ and with $w(z)$ being the Faddeeva function, defined as

$$w(z) = e^{-z^2}\left(1 + \frac{2i}{\sqrt{\pi}} \int_0^z e^{t^2} \mathrm{d}t\right). \tag{4.7}$$

For the special case of round beams with $\sigma_x = \sigma_y = \sigma$, the forces become

$$f_x = \frac{1}{2\pi\varepsilon_0}\left[1 - \exp\left(-\frac{x^2 + y^2}{2\sigma^2}\right)\right] \frac{x}{x^2 + y^2}, \tag{4.8}$$

$$f_y = \frac{1}{2\pi\varepsilon_0}\left[1 - \exp\left(-\frac{x^2 + y^2}{2\sigma^2}\right)\right] \frac{y}{x^2 + y^2}. \tag{4.9}$$

Modelling of the beam-beam head-on interaction

The beam-beam head-on interaction requires a significantly more detailed description. This is needed because 1) the collision point between a particle in the weak beam and the strong beam has a strong dependence on the coordinates of the particle (including τ) and 2) because the beam size in the collision point changes with the longitudinal position τ of the particle inside the weak beam. The dependence on τ also implies that the interaction will lead to an energy change (a change of p_τ). This interaction is modelled using the synchro-beam mapping described in Refs. [6, 78, 79]. The modelling is based on using a Lorentz-boosted reference frame where the weak and the strong beam are moving towards each other on a line. The boosted strong beam is then approximated as a finite number of thin slices. The collision point between a slice of the strong beam and the weak particle will differ from the interaction point. For each slice, the weak particle and the strong beam slice are propagated to their collision point where the transverse forces are applied. Due to the crossing angle, the forces (which are transverse to the strong beam) introduce an energy change (longitudinal force). Additionally, the energy change will have a component that is directly related to the gradient of the strong beam's potential with respect to the variable τ. For the final part of the interaction, the particle of the weak beam is drifted back to its original s coordinate and the inverse Lorentz-boost to recover the reference frame.

A brief summary of the beam-beam head-on interaction steps is presented here but details about its technical and numerical implementation can be found in Ref. [77]. The opposing beam is split into a finite number of slices. The interaction between a particle and a slice of the opposing beam can be calculated through the following steps:

1. Transform the coordinates of the particle with a Lorentz-boost to a frame of reference with no crossing angle.
2. Compute the particle coordinates at the point where it collides with the slice of the opposing beam.
3. Compute the transverse and longitudinal kicks from the slice based on the coordinates at the collision point.
4. Transform the kicks back to the original coordinates of the particle.
5. Transform the coordinates back to the original frame of reference with the inverse Lorentz-boost.
6. The process is repeated for each slice of the opposing beam.

It should be noted that transporting the slice (from the interaction point to the collision point) also changes its distribution. The slice and its beam distribution momenta are calculated at the collision point according to the optics functions of the accelerator.

Modelling of the LHC lattice

In this study, the LHC lattice is modeled including dipolar, quadrupolar, sextupolar and octupolar magnetic fields. Magnet imperfections and misalignment are not considered. The nominal parameters of a typical fill from the 2018 run are used, which are summarized in Table 4.1. It is noted that there is a strong sextupolar component in order to set the horizontal and the vertical chromaticity equal to 15. Moreover, a particularly strong octupolar component is needed, as the octupole magnets are powered with 500 A. Both of these settings are needed in operation to prevent coherent beam instabilities caused by electron cloud effects.

The effect of the beam-beam interaction has a non-linear nature. For small amplitudes of oscillation (of up to around one r.m.s. beam size), the interaction can be approximated with linear defocusing force. For moderate amplitudes (between one and five r.m.s. beam sizes), it becomes very non-linear while the effect of the beam-beam interaction vanishes as the amplitudes tend to infinity. However, because of the strong sextupolar and octupolar magnetic fields in the ring, the particle motion at large amplitudes becomes unstable. The combination of beam-beam interactions with the strong sextupolar and octupolar magnetic fields drives a

Table 4.1: Typical operational parameters of the LHC during Run 2 with beams in collision, used in the simulations.

Bunch population [p/bunch]	$1.25 \cdot 10^{11}$
Reference energy [GeV]	6500
R.m.s. bunch length [cm]	9
R.m.s. horizontal emittance (normalized) [µm]	2
R.m.s. vertical emittance (normalized) [µm]	2
Horizontal betatron tune	62.31
Vertical betatron tune	60.32
Synchrotron tune	$2 \cdot 10^{-3}$
Horizontal chromaticity	15
Vertical chromaticity	15
Octupole magnets' current [A]	500
Amplitude detuning coefficient [80], α_{xx} [µm^{-1}]	0.27
Amplitude detuning coefficient [80], α_{yy} [µm^{-1}]	0.28
Amplitude detuning coefficient [80], α_{xy} [µm^{-1}]	-0.19
RF voltage [MV]	12
Bunch spacing [ns]	25

significant decrease of the dynamic aperture. Dynamic aperture is a beam dynamics indicator which defines the extend of phase phase in which particles remain stable over a certain amount of time [81]. In the simulation, particles are considered lost when they escape from the aperture which is set to 1 m. This number is artificial and is typically set large enough so that the trajectory of the particle is stopped before it escapes to infinity. In post-processing of the simulation data, the value of the aperture, which is typically defined by the primary collimators in the LHC, is varied to investigate its effect.

4.2 Evolution of slow beam losses

Typically in the LHC, the longest simulations in terms of simulated beam time are those of dynamic aperture, where particles are being tracked typically for 10^6 turns to estimate the extent of the region of single-particle stability. Moreover, the number of particles needed to estimate dynamic aperture is relatively small (in the order of 100 particles). Finally, dynamic aperture is a powerful qualitative indicator of the non-linear beam dynamics but it can become difficult to relate to observable quantities like the rate of the slow beam loss. For this reason, taking advantage of the property of the GPU to be efficient when simulating tens of thousands of particles at the same time, the slow beam loss is simulated directly through the tracking of particle distributions.

Monte-Carlo integration

The intensity of a bunch $I(t)$ is, by definition, the number of particles at any moment t. By considering particles that exist at $t = 0$ and are lost[1] at a time $t = t_L$, the bunch can be written as:

$$I(t) = \sum_{i=1}^{N} S\left(t, t_L^{(i)}\right) , \tag{4.10}$$

where the i-th particle is lost at time $t_L^{(i)}$, N is the number of particles at $t = 0$ and S is the step function defined as:

$$S(t, t_L^{(i)}) = \begin{cases} 1 & \text{if} \quad t < t_L^{(i)} , \\ 0 & \text{if} \quad t \geq t_L^{(i)} . \end{cases} \tag{4.11}$$

Due to the large number of particles typically in a bunch at the LHC ($\sim 10^{11}$ protons), it is convenient, and a good approximation, to consider a continuous particle density distribution. The intensity can be then written as:

$$I(t) = \int_{\mathcal{V}_{6D}} S(t, t_L) \; P\left(x, p_x, y, p_y, \tau, p_\tau\right) \, \mathrm{d}x\mathrm{d}p_x\mathrm{d}y\mathrm{d}p_y\mathrm{d}\tau\mathrm{d}p_\tau , \tag{4.12}$$

where $t_L = t_L(x, p_x, y, p_y, \tau, p_\tau)$ is a function of all the canonical variables and the function $P(x, p_x, y, p_y, \tau, p_\tau)$ expresses the distribution of particles at time $t = 0$ normalized such that

$$I_0 = \int_{\mathcal{V}_{6D}} P\left(x, p_x, y, p_y, \tau, p_\tau\right) \, \mathrm{d}x\mathrm{d}p_x\mathrm{d}y\mathrm{d}p_y\mathrm{d}\tau\mathrm{d}p_\tau , \tag{4.13}$$

with I_0 being the initial bunch intensity. The integration is performed over the available 6D phase-space $\mathcal{V}_{6D}$. It is easier to define the distribution of particles in terms of linear normal form analysis of the accelerator one-turn map as described in Section 1.2. A change to the normalized phase space variables $(\hat{x}, \hat{p}_x, \hat{y}, \hat{p}_y, \hat{\tau}, \hat{p}_\tau)$ transforms Eq. (4.12) as:

$$I(t) = \int_{\mathcal{V}_{6D}} S(t, t_L) \; P\left(\hat{x}, \hat{p}_x, \hat{y}, \hat{p}_y, \hat{\tau}, \hat{p}_\tau\right) \, \mathrm{d}\hat{x}\mathrm{d}\hat{p}_x\mathrm{d}\hat{y}\mathrm{d}\hat{p}_y\mathrm{d}\hat{\tau}\mathrm{d}\hat{p}_\tau . \tag{4.14}$$

In a typical fill in the operation of the LHC, the majority of particles remain stable for timescales longer than the fill itself. It is therefore inefficient to count the remaining particles and, instead, the lost particles should be counted to define the loss rate directly. This can be realized by integrating the derivative of the intensity

---

[1] In the LHC, particles are lost when their oscillations can reach large amplitudes at which point they are intercepted by the collimators.

with respect to time, between times t_1 and t_2.

$$\Delta I\left(t_1, t_2\right) = -\int_{t_1}^{t_2} \frac{\mathrm{d}I}{dt'}\mathrm{d}t' \ , \tag{4.15}$$

$$= \int_{\mathcal{V}_{6D}} \left(-\int_{t_1}^{t_2} \frac{\mathrm{d}S(t', t_L)}{\mathrm{d}t'}\ \mathrm{d}t'\right) P\left(\hat{x}, \hat{p}_x, \hat{y}, \hat{p}_y, \hat{\tau}, \hat{p}_\tau\right)\ \mathrm{d}\hat{x}\mathrm{d}\hat{p}_x\mathrm{d}\hat{y}\mathrm{d}\hat{p}_y\mathrm{d}\hat{\tau}\mathrm{d}\hat{p}_\tau \ , \tag{4.16}$$

$$= \int_{\mathcal{V}_{6D}} \left(\int_{t_1}^{t_2} \delta(t' - t_L)\ \mathrm{d}t'\right) P\left(\hat{x}, \hat{p}_x, \hat{y}, \hat{p}_y, \hat{\tau}, \hat{p}_\tau\right)\ \mathrm{d}\hat{x}\mathrm{d}\hat{p}_x\mathrm{d}\hat{y}\mathrm{d}\hat{p}_y\mathrm{d}\hat{\tau}\mathrm{d}\hat{p}_\tau \ , \tag{4.17}$$

where the property of the Dirac delta function δ was used:

$$\delta(t - t_L) = -\frac{\mathrm{d}S(t, t_L)}{\mathrm{d}t} \ . \tag{4.18}$$

The integral of the δ function appearing in Eq. (4.17) defines the piecewise function:

$$K(t_L; t_1, t_2) = \int_{t_1}^{t_2} \delta(t' - t_L)\ \mathrm{d}t' \ , \tag{4.19}$$

$$K(t_L; t_1, t_2) = \begin{cases} 1 & \text{if} \quad t_1 < t_L < t_2 \ , \\ 0 & \text{otherwise} \ . \end{cases} \tag{4.20}$$

Substituting Eq. (4.20) into Eq. (4.17), the loss rate becomes

$$\Delta I\left(t_1, t_2\right) = \int_{\mathcal{V}_{6D}} K(t_L; t_1, t_2)\, P\left(\hat{x}, \hat{p}_x, \hat{y}, \hat{p}_y, \hat{\tau}, \hat{p}_\tau\right)\ \mathrm{d}\hat{x}\mathrm{d}\hat{p}_x\mathrm{d}\hat{y}\mathrm{d}\hat{p}_y\mathrm{d}\hat{\tau}\mathrm{d}\hat{p}_\tau \ . \tag{4.21}$$

Another approximation that can be made to simplify the equation is to factorize the initial particle distribution P into a transverse and a longitudinal one. The factorization is as follows:

$$P\left(\hat{x}, \hat{p}_x, \hat{y}, \hat{p}_y, \hat{\tau}, \hat{p}_\tau\right) = I_0 \cdot \rho\left(\hat{x}, \hat{p}_x, \hat{y}, \hat{p}_y\right) \cdot h\left(\hat{\tau}, \hat{p}_\tau\right) \ , \tag{4.22}$$

where I_0 is the initial bunch intensity, ρ is the transverse initial distribution, normalized to unity in the 4D transverse phase space and h is the longitudinal initial distribution, normalized to unity as well in the longitudinal phase space. Additionally, the longitudinal distribution can be approximated as unaffected by the transverse motion and the longitudinal variables $\hat{\tau}, \hat{p}_\tau$ can be transformed back to their canonical coordinates τ, p_τ:

$$h\left(\hat{\tau}, \hat{p}_\tau\right)\ \mathrm{d}\hat{\tau}, \mathrm{d}\hat{p}_\tau = h\left(\tau, p_\tau\right)\ \mathrm{d}\tau, \mathrm{d}p_\tau \ . \tag{4.23}$$

Another change of variable can be made to bring the system to action-angle coordinates as described in Sec. 1.3:

$$h\left(\tau, p_\tau\right)\ \mathrm{d}\tau, \mathrm{d}p_\tau = h\left(J_\tau, \phi_\tau\right)\ \mathrm{d}J_\tau, \mathrm{d}\phi_\tau \ . \tag{4.24}$$

A distribution that is matched in the longitudinal plane is one that will depend only on J_τ and therefore it follows that

$$h\left(\hat{\tau}, \hat{p}_\tau\right)\, \mathrm{d}\hat{\tau}, \mathrm{d}\hat{p}_\tau = h\left(J_\tau\right)\, \mathrm{d}J_\tau, \mathrm{d}\phi_\tau\ . \tag{4.25}$$

Substituting Eq. (4.22) and (4.25) into Eq. (4.21), separating the integrals in the transverse phase space volume $\mathcal{V}_{4D}$ and in the longitudinal phase space, the loss rate becomes

$$\Delta I\left(t_1, t_2\right) = \int_{\phi_\tau=0}^{2\pi} \int_{J_\tau=0}^{J_{\mathrm{ufp}}} \int_{\mathcal{V}_{4D}} K(t_L; t_1, t_2)\, I_0\, \rho\left(\hat{x}, \hat{p}_x, \hat{y}, \hat{p}_y\right)\ h(J_\tau) \mathrm{d}\hat{x}\mathrm{d}\hat{p}_x\mathrm{d}\hat{y}\mathrm{d}\hat{p}_y\mathrm{d}J_\tau\mathrm{d}\phi_\tau\ . \tag{4.26}$$

where J_{ufp} is the value of J_τ which corresponds to the unstable fixed point in the separatrix of the single-harmonic RF potential. Assuming that t_L does not depend on the initial angle ϕ_τ, Eq. (4.26) becomes

$$\frac{\Delta I\left(t_1, t_2\right)}{I_0} = 2\pi \int_{J_\tau=0}^{J_{\mathrm{ufp}}} \left(\int_{\mathcal{V}_{4D}} K(t_L; t_1, t_2)\, \rho\left(\hat{x}, \hat{p}_x, \hat{y}, \hat{p}_y\right)\ \mathrm{d}\hat{x}\mathrm{d}\hat{p}_x\mathrm{d}\hat{y}\mathrm{d}\hat{p}_y \right) h(J_\tau)\, \mathrm{d}J_\tau\ . \tag{4.27}$$

Here, t_L is a function of the variables $\hat{x}, \hat{p}_x, \hat{y}, \hat{p}_y, \hat{\tau}, \hat{p}_\tau$. The term in the parenthesis can be renamed as:

$$\frac{\Delta I\left(t_1, t_2; J_\tau\right)}{I_0} = \int_{\mathcal{V}_{4D}} K(t_L; t_1, t_2)\, \rho\left(\hat{x}, \hat{p}_x, \hat{y}, \hat{p}_y\right)\ \mathrm{d}\hat{x}\mathrm{d}\hat{p}_x\mathrm{d}\hat{y}\mathrm{d}\hat{p}_y\ , \tag{4.28}$$

and is equivalent to the loss rate computed for a transverse distribution ρ and a longitudinal distribution that is a δ function in the action variable of the longitudinal phase space. In this expression of the loss rate, J_τ is considered a parameter. The total loss rate, including the contribution of the longitudinal distribution is equal to

$$\frac{\Delta I\left(t_1, t_2\right)}{I_0} = 2\pi \int_{J_\tau=0}^{J_{\mathrm{ufp}}} \frac{\Delta I\left(t_1, t_2; J_\tau\right)}{I_0}\, h(J_\tau)\, \mathrm{d}J_\tau\ . \tag{4.29}$$

By bringing the equations in this form, the total loss rate can be calculated by discretizing J_τ and calculating $\Delta I\left(t_1, t_2; J_\tau\right)/I_0$ in each case. The integral in Eq. (4.28) is calculated by applying the Monte-Carlo integration technique [82, 83] by randomly sampling $\hat{x}, \hat{p}_x, \hat{y}, \hat{p}_y$ uniformly in a 4D hypersphere, each time for a specific value of the action J_τ. Each sample defines a particle with initial coordinates $x^{(i)}, p_x^{(i)}, y^{(i)}, p_y^{(i)}, \tau^{(i)}, p_\tau^{(i)}$ that is tracked with SixTrackLib through the model of the LHC lattice for $2 \cdot 10^7$ turns and the time that each particle is lost $t_L^{(i)}$ is calculated. By applying the Monte-Carlo integration technique, Eq. (4.28) is rewritten as:

$$\frac{\Delta I\left(t_1, t_2; J_\tau\right)}{I_0} \simeq \frac{V_{4D}}{N} \sum_{i=1}^{N} K\left(t_L^{(i)}; t_1, t_2\right) \cdot \rho\left(\hat{x}^{(i)}, \hat{p}_x^{(i)}, \hat{y}^{(i)}, \hat{p}_y^{(i)}\right)\ , \tag{4.30}$$

where N is the number of particles and V_{4D} is the volume of the hypersphere inside which the simulated particles were sampled. By considering only particles that were lost between t_1 and t_2, the Monte-Carlo estimator becomes

$$\frac{\Delta I\left(t_1, t_2; J_\tau\right)}{I_0} \simeq \frac{V_{4D}}{N} \sum_{j} \rho\left(\hat{x}^{(j)}, \hat{p}_x^{(j)}, \hat{y}^{(j)}, \hat{p}_y^{(j)}\right)\ , \tag{4.31}$$

with j such that

$$t_1 < t_L^{(j)} < t_2 \ . \tag{4.32}$$

The variance associated to this estimator is equal to:

$$V\left[\frac{\Delta I\left(t_1, t_2; J_\tau\right)}{I_0}\right] \simeq \frac{V_{4D}^2}{N}\left(\frac{1}{N}\sum_j \rho^2\left(\hat{x}^{(j)}, \hat{p}_x^{(j)}, \hat{y}^{(j)}, \hat{p}_y^{(j)}\right) - \left(\frac{1}{N}\sum_j \rho\left(\hat{x}^{(j)}, \hat{p}_x^{(j)}, \hat{y}^{(j)}, \hat{p}_y^{(j)}\right)\right)^2\right) \ . \tag{4.33}$$

This variance expresses the *degree of belief* in the estimation of the loss rate. According to Monte-Carlo theory, the degree of belief in the estimation of the loss rate is expressed by a Gaussian distribution whose mean value is equal to the estimator in Eq. (4.31) and whose variance is equal to the one in Eq. (4.33) [82, 83].

It is clear from Eq.(4.33) that the r.m.s. error (square root of variance) is proportional to the volume of integration V_{4D}. In this way, the discretization of J_τ has enabled the reduction of the error associated to Monte-Carlo integration. Moreover, this also allows the study of the loss rate as a function of the longitudinal action J_τ (or equivalently the longitudinal oscillation amplitude).

It is important to note that in this framework, the distributions ρ and h are defined at the post-processing of the simulated data and do not influence the tracking simulations themselves. This allows to study the dependence on the beam distributions without repeating the time-consuming simulations. Moreover, the aperture defined by the primary collimators can be also be varied during the post-processing of the simulated tracking data, allowing also to study the dependence of the loss rate on the aperture. Finally, what is left is to define the expressions to be used for the distributions ρ and h.

For the LHC, experimental measurements of the transverse beam profiles ρ show that their core can be described very well by Gaussian distributions. However, measurements of the tails of the beam profiles are more difficult. The available data based on destructive "beam scraping measurements" suggests that the tails of the profiles are slightly overpopulated with respect to a purely Gaussian distribution [84]. The loss rate is strongly related to the population of particles in the tails due to their large oscillation amplitude. In order to study the sensitivity of our results to the tail population, we use 4D q-Gaussian distributions in which the population of the tails is controlled by a q parameter [85, 86].:

$$\rho(\hat{x}, \hat{p}_x, \hat{y}, \hat{p}_y) \propto \left[1-(1-q)\left(\frac{\hat{x}^2+\hat{p}_x^2}{2\varepsilon_x}+\frac{\hat{y}^2+\hat{p}_y^2}{2\varepsilon_y}\right)\right]^{\dfrac{1}{1-q}} \ . \tag{4.34}$$

For $q = 1$, the distribution is a Gaussian distribution, for $q > 1$ the distribution has overpopulated tails, and for $q < 1$ the tails are underpopulated.

For the longitudinal case, three different distributions are considered in order to study their effect: 1) an exponential:

$$h_1(J_\tau) \propto \exp\left(-\frac{J_\tau}{\varepsilon_\tau}\right), \tag{4.35}$$

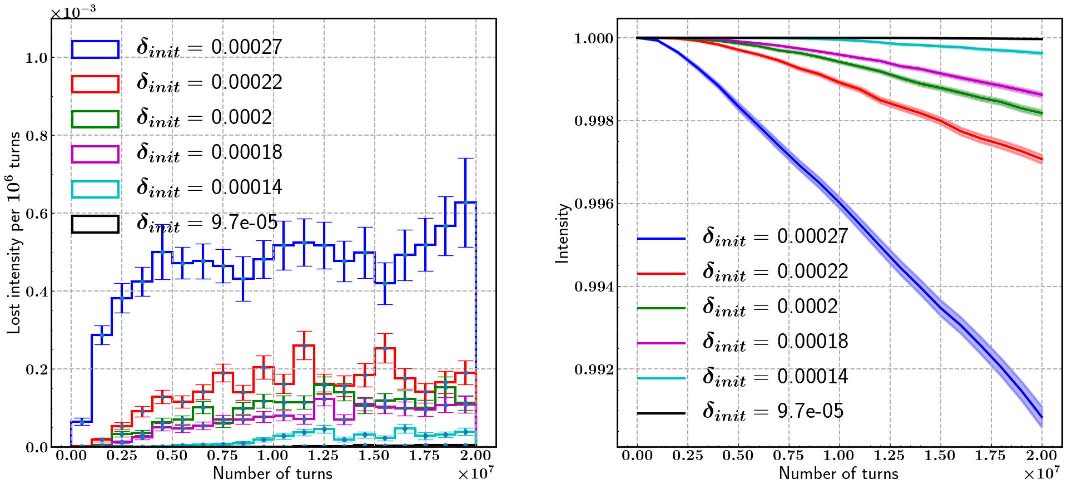

(a) (b)

Figure 4.2: Simulations of loss rate (a) and intensity (b) for Gaussian distributions as a function of time for different values of J_τ (max(p_τ)= δ_{init}).

2) a q-exponential with $q = 0.85$:

$$h_2(J_\tau) \propto \left[1 - (1-q)\left(\frac{J_\tau}{\varepsilon_\tau}\right)\right]^{\dfrac{1}{1-q}}, \tag{4.36}$$

3) a parabolic distribution in the action variable J_τ.

$$h_3(J_\tau) \propto \left[1 - \left(\frac{J_\tau}{\varepsilon_\tau}\right)\right]^2. \tag{4.37}$$

In each case, the parameter ε_τ is chosen in order to have the desired r.m.s. bunch length. It is easy to see that the parabolic distribution is a special case of the q-exponential with $q = 0.5$. In all of the cases, the parameters of the distributions are chosen such that the r.m.s. bunch length is kept constant.

Simulation results

By applying Eq. (4.31) on different sets of tracking simulations, each with a different initial longitudinal action J_τ and by assuming Gaussian distributions in transverse planes, the loss rate is shown in Fig. 4.2. It is evident that the loss rate increases for larger longitudinal actions.

By considering all of the simulations, the loss rate at the latest time interval is shown as a function of the longitudinal amplitude in Fig. 4.3, by using h_1 (red), h_2 (green), h_3 (blue) for the longitudinal distribution. It is apparent that the largest fraction of the lost particles are not located at the largest longitudinal amplitudes when considering the longitudinal distribution. This happens because the population of particles falls faster with respect to the longitudinal amplitude than the

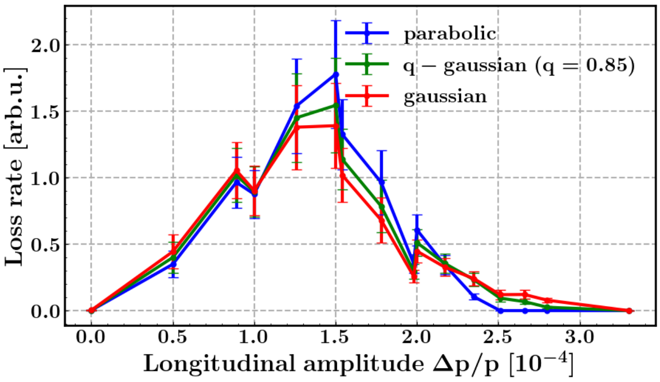

Figure 4.3: Simulations of loss rate for different values of J_τ ($\max(p_\tau) = \max(\Delta p/p)$).

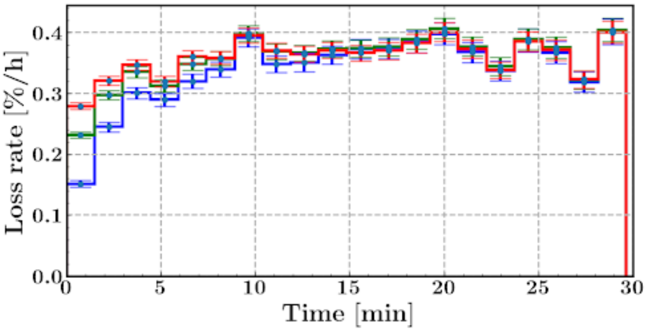

Figure 4.4: Simulations of the final loss rate as a function of time, considering the exponential distribution h_1 (red), the q-exponential distribution h_2 (green), and the parabolic h_3 distribution (blue).

loss rate increases. The final loss rate is equal to the integral of these functions. Although the choice of the distribution appears to affect the loss rate as a function of the longitudinal action, it increases in some regions while it decreases in some others. The total area under the curve appears to be affected only barely by the choice of distribution.

By integrating the loss rates appearing in Fig. 4.3 as in Eq. 4.29, the total loss rate as a function of time is calculated and shown in Fig. 4.4 for the different longitudinal distributions. The loss rates become approximately constant for late times ($t > 10$ min). Moreover, the choice of longitudinal distribution barely affects the loss rate, except at very early times ($t < 10$ min).

Another parameter that can influence the loss rate is the aperture limitation induced by the primary collimators in the LHC. The evolution of the final loss rate for different settings of the aperture (distance of the primary collimators in the LHC) is illustrated in Fig. 4.5. A slightly smaller aperture strongly increases the loss rate at early times, which then converges to a steady loss rate.

The strongest uncertainty of the loss rate arises from the uncertainty in the tails of the transverse distributions. The evolution of losses is presented in Fig. 4.6 for different values of the q. Larger q corresponds to a larger population in the tails of

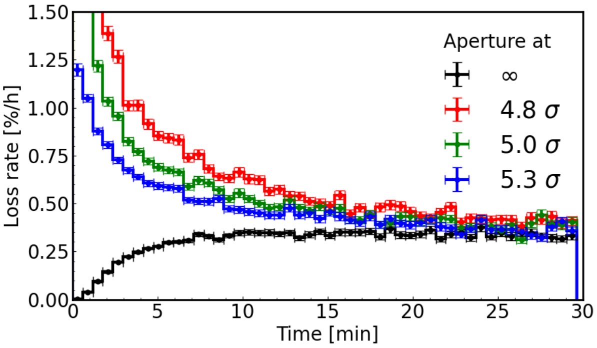

Figure 4.5: Simulations of the final loss rate as a function of time for an aperture set at infinity (black), 4.8σ (red), 5.0σ (green) and 5.3σ (blue). The beam size σ here refers to the nominal σ according to the design report [1], for normalized emittances of 3.5 µm.

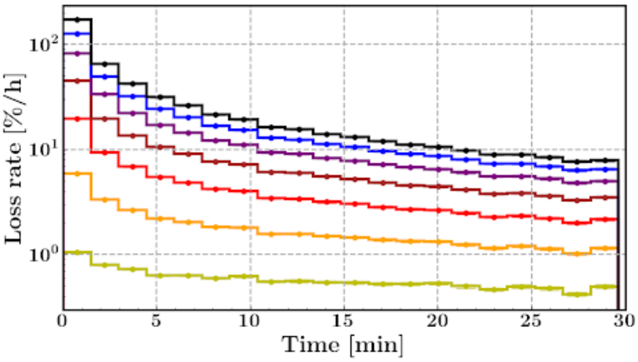

Figure 4.6: Simulations of the final loss rate as a function of time for the q parameter values: (gold) $q = 1.00$, (orange) $q = 1.05$, (red) $q = 1.10$, (brown) $q = 1.15$, (purple) $q = 1.20$, (blue) $q = 1.25$, (black) $q = 1.30$, controlling the population of particles at the tails of the transverse distributions.

the distribution and leads to larger loss rates.

4.3 Evolution of the transverse beam profiles

Additionally to the estimation of loss rate, the horizontal and vertical profiles can be estimated from the tracking simulations. From these profiles, the emittance can be calculated by fitting a Gaussian distribution on the core of the distribution. This is done in order to mimic the conditions under which the emittance measurement is done practically at the LHC. The horizontal and vertical profiles are shown in Fig. 4.7 at time $t = 0$ and at $t = 2 \cdot 10^7$ turns, assuming Gaussian initial transverse profiles. Figure 4.8 shows the profiles assuming a q-Gaussian initial transverse distribution with $q = 1.1$. By comparing the initial and final profiles it is easy to see that there is no significant change in the profiles. If the initial profiles are Gaussian, then they remain Gaussian. If the initial profiles have over-populated tails, then the tails are preserved throughout the simulated time interval.

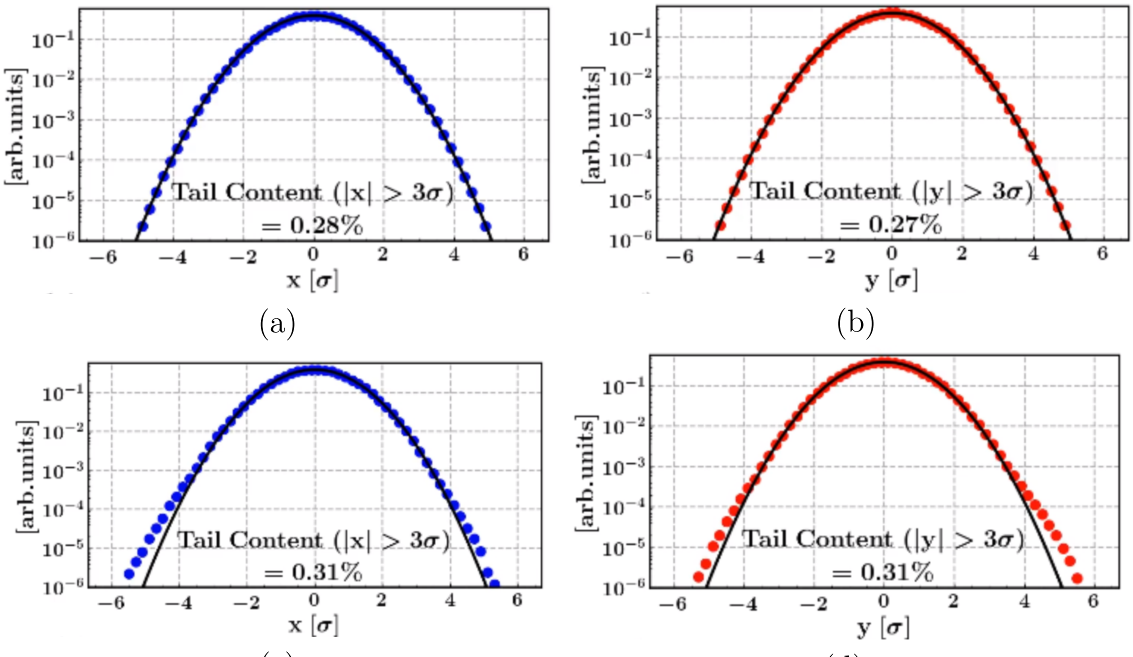

(a) (b)

(c) (d)

Figure 4.7: Simulations of the initial horizontal profile (a), initial vertical profile (b), final horizontal profile (c), final vertical profile (d). The value $q = 1.0$ was used for the initial distribution. The final profiles correspond to those at the end of the tracking simulations at $2 \cdot 10^7$ turns.

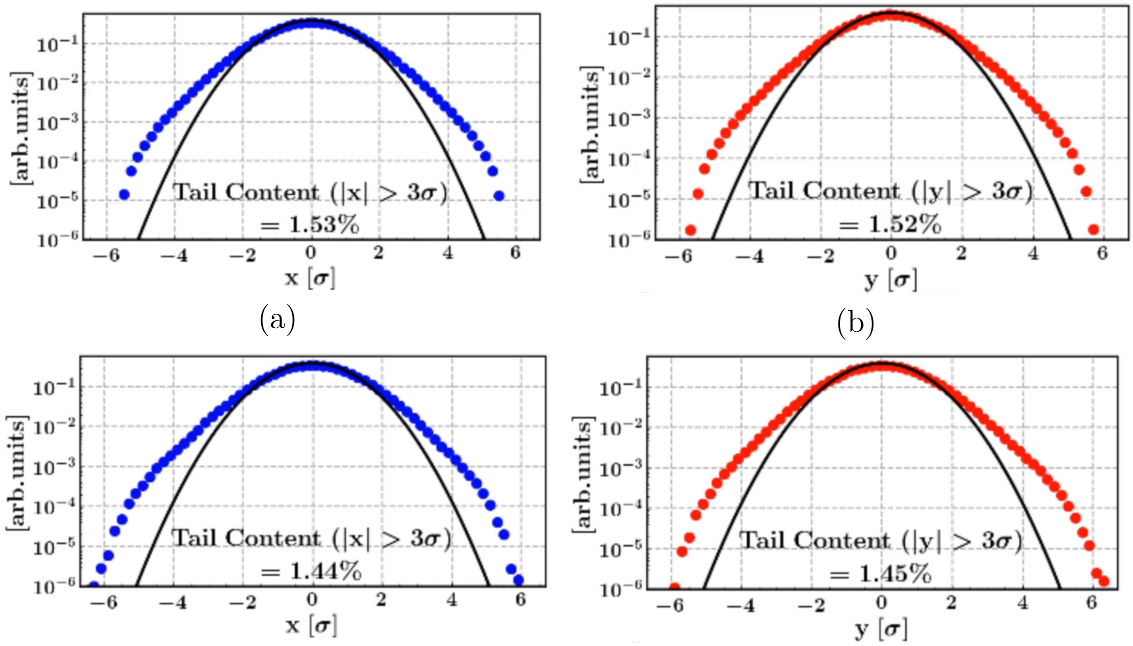

(a) (b)

(c) (d)

Figure 4.8: Simulations of the initial horizontal profile (a), initial vertical profile (b), final horizontal profile (c), final vertical profile (d). The value of $q = 1.1$ was used for the initial distribution. The final profiles correspond to those at the end of the tracking simulations at $2 \cdot 10^7$ turns.

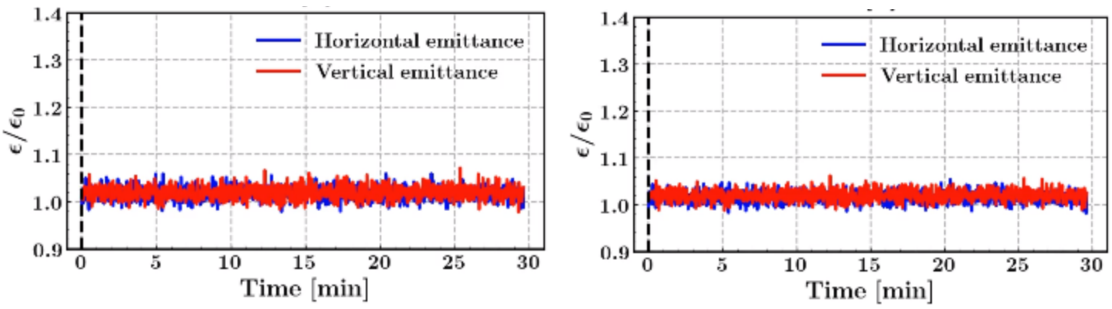

(a) (b)

Figure 4.9: Evolution of the horizontal (blue) and vertical (red) emittances for $q = 1$ (a) and $q = 1.1$ (b) in the initial transverse distributions.

The evolution of the horizontal (blue) and the vertical (red) emittances as estimated from these profiles are shown in Fig. 4.9 for $q = 1$ (a) and for $q = 1.1$ (b). As also deduced from the comparison of the initial and final profiles in the previous figures, the emittance stays practically constant over the whole simulated time.

Chapter 5

Simulations of incoherent electron cloud effects for the LHC at injection energy

5.1 Symplectic implementation of the e-cloud map

The forces that describe the effect of an e-cloud on a beam particle are conveniently calculated in the frame of the reference particle. In such a frame, the forces are proportional to the gradient of a scalar potential ϕ, which, for ultra-relativistic beams, can be calculated with good approximation by solving the 2D Poisson equation [53]:

$$\frac{\partial^2\phi\left(x,y,\tau\right)}{\partial x^2}+\frac{\partial^2\phi\left(x,y,\tau\right)}{\partial y^2}=-\frac{\rho\left(x,y,\tau\right)}{\varepsilon_0},\tag{5.1}$$

where ε_0 is the vacuum permittivity and $\rho\left(x,y,\tau\right)$ is the charge density of the e-cloud. Such an approximation is used in most simulation codes used for this purpose, for example PyECLOUD[59], POSINST[87], HEADTAIL[88], OPENECLOUD[89]. The integrated forces from the e-cloud in a small segment of the accelerator of length L, which is centered around the longitudinal position s_0, can be generated from the following Hamiltonian

$$H=\frac{qL}{\beta_0 P_0 c}\phi\left(x,y,\tau\right)\delta\left(s-s_0\right),\tag{5.2}$$

where β_0 is the ratio between the speed of the reference particle and the speed of light c, and P_0 is the total momentum of the reference particle. More details about the canonical conjugate variables used in this coordinate system can be found in

Section 1.1. The map obtained from this Hamiltonian is:

$$x \mapsto x, \tag{5.3}$$

$$p_x \mapsto p_x - \frac{qL}{\beta_0 P_0 c} e_x\left(x, y, \tau\right), \tag{5.4}$$

$$y \mapsto y, \tag{5.5}$$

$$p_y \mapsto p_y - \frac{qL}{\beta_0 P_0 c} e_y\left(x, y, \tau\right), \tag{5.6}$$

$$\tau \mapsto \tau, \tag{5.7}$$

$$p_\tau \mapsto p_\tau - \frac{qL}{\beta_0 P_0 c} e_\tau\left(x, y, \tau\right), \tag{5.8}$$

where

$$e_x = -\frac{\partial\phi}{\partial x}, \quad e_y = -\frac{\partial\phi}{\partial y}, \quad e_\tau = -\frac{\partial\phi}{\partial\tau}. \tag{5.9}$$

As discussed in Section 2.4, changes in the beam distribution driven by incoherent e-cloud effects are typically slow processes. Over a relatively large number of turns, the impact on the e-cloud dynamics from the modifications in the beam distribution can be neglected. Therefore, the e-cloud dynamics can be simulated once and , in a form of a “weak-strong approximation”, the corresponding potential can be stored to apply the e-cloud forces to the beam particles over multiple turns without repeating the time-consuming calculation of the potential. Moreover, following this approach, the same e-cloud forces can be applied in multiple locations of the accelerator where the beam size and the geometry of the chamber are the same. This is convenient especially in lattices with a strong degree of periodicity such as those of high energy accelerators. Furthermore, the resulting map does not exhibit turn-by-turn fluctuations from the limited number of macroparticles used to describe the electron distributions. This is particularly important as these fluctuations can lead to artificial modifications in the results and need to be controlled with special care.

5.1.1 Tricubic Interpolation

The standard tool for the simulation of the e-cloud dynamics is codes based on the Particle-In-Cell method. For this purpose, the PyECLOUD [59] code is used in LHC studies. It has been extensively benchmarked against experiments [60, 21] as well as other simulation codes [90]. PyECLOUD provides the charge density $\rho(x, y, \tau)$ and the scalar potential $\phi(x, y, \tau)$ on a regular three-dimensional grid with cell sizes $\Delta x, \Delta y, \Delta\tau$:

$$\phi^{ijk} = \phi(x_i, y_j, \tau_k), \tag{5.10}$$

$$\rho^{ijk} = \rho(x_i, y_j, \tau_k), \tag{5.11}$$

where $x_i = x_0 + i\Delta x$, $y_j = y_0 + j\Delta y$, $\tau_k = \tau_0 + k\Delta\tau$ and x_0, y_0, τ_0 define the position of the grid in the three-dimensional space. In PyECLOUD, the fields are calculated by solving Eq. (5.1) with a finite difference method, evaluating the gradient

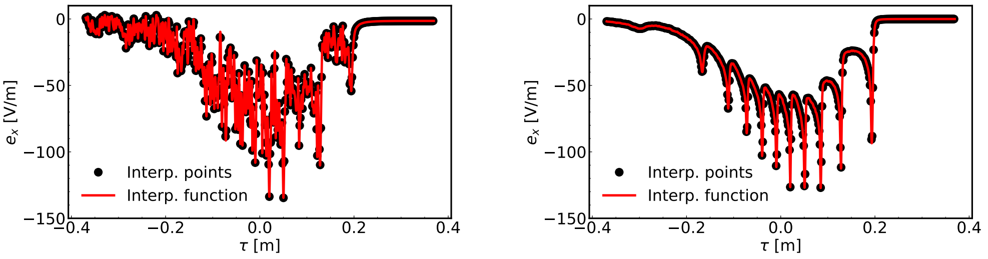

(a) (b)

Figure 5.1: Horizontal field of the e-cloud as a function of τ in a single simulation (a) and the average of 4000 simulations (b).

of the potential at the grid nodes with central differences and then using a linear interpolation scheme to get the field at the location of the electrons.

The field map obtained by such simulations with typical numerical settings exhibit significant macroparticle noise as visible in Fig. 5.1a. This does not affect the motion of electrons because it is largely dominated by the beam's field. However, it is not acceptable when evaluating its effect on the beam particles over many turns. As the potential table is computed and stored before starting the beam particle tracking simulations, such a problem can be effectively solved by simulating the dynamics of the e-cloud multiple times. Each simulation will have a different random seed in the generation of the initial electron distribution, and therefore averaging the resulting charge density and scalar potential will lead to a more accurate estimate of the charge density and scalar potential with less macroparticle noise. The result of such an averaging process over 4000 simulations is shown by the black points of Fig. 5.1b.

A map in the form given by Eqs. (5.3)-(5.8) is symplectic if the following conditions are verified:

$$\frac{\partial}{\partial x}\left(\frac{\partial \phi}{\partial y}\right) = \frac{\partial}{\partial y}\left(\frac{\partial \phi}{\partial x}\right), \tag{5.12}$$

$$\frac{\partial}{\partial x}\left(\frac{\partial \phi}{\partial \tau}\right) = \frac{\partial}{\partial \tau}\left(\frac{\partial \phi}{\partial x}\right), \tag{5.13}$$

$$\frac{\partial}{\partial y}\left(\frac{\partial \phi}{\partial \tau}\right) = \frac{\partial}{\partial \tau}\left(\frac{\partial \phi}{\partial y}\right). \tag{5.14}$$

If the potential ϕ is a smooth function, for example if it is an analytic function, these conditions are automatically satisfied. However, the potential ϕ^{ijk} from the PyECLOUD simulation is known only on a discrete grid. As such, an interpolation scheme needs to be used to obtain the potential or the field in an arbitrary point in space. The conventional interpolation scheme that is used in PIC simulations, is based on linear interpolation and finite differences for evaluation of the fields. This scheme does not preserve symplecticity of the map as it is shown in Appendix A.

The symplecticity condition will hold, however, if the derivatives are computed analytically from an interpolating function $\phi^{\text{int}}(x, y, \tau)$, which has continuous mixed derivatives:

$$\frac{\partial^2\phi^{\mathrm{int}}}{\partial x\partial y},\ \frac{\partial^2\phi^{\mathrm{int}}}{\partial x\partial \tau},\ \frac{\partial^2\phi^{\mathrm{int}}}{\partial y\partial \tau}. \tag{5.15}$$

Such a function could be created by fitting globally a high-order polynomial in three dimensions to the discrete samples ϕ^{ijk}. The order of such a polynomial would need to be prohibitively high to accurately reproduce complex features of typical e-cloud forces. For this reason, the usage of a local interpolation scheme is investigated that can preserve symplecticity.

Such a scheme can be realized by following the approach introduced by Lekien and Marsden [91], which consists in a a local tricubic interpolation scheme that is able to preserve the global continuity of the functions:

$$\phi^{\mathrm{int}}, \frac{\partial\phi^{\mathrm{int}}}{\partial x}, \frac{\partial\phi^{\mathrm{int}}}{\partial y}, \frac{\partial\phi^{\mathrm{int}}}{\partial \tau}, \frac{\partial^2\phi^{\mathrm{int}}}{\partial x\partial y}, \frac{\partial^2\phi^{\mathrm{int}}}{\partial y\partial \tau}, \frac{\partial^2\phi^{\mathrm{int}}}{\partial x\partial \tau}, \frac{\partial^3\phi^{\mathrm{int}}}{\partial x\partial y\partial \tau}. \tag{5.16}$$

Such a list of globally continuous quantities includes those in Eq. (5.15). Therefore the symplectic structure of the scheme is guaranteed. In such a scheme, the interpolating function is a piece-wise polynomial:

$$\phi^{\mathrm{int}}(x,y,\tau) = \sum_{i,j,k=0}^{3} a_{ijk}x^i y^j \tau^k, \tag{5.17}$$

where the coefficients a_{ijk} are different for each hexahedral cell of the grid and are calculated by imposing the quantities listed in Eq. (5.16) at the 8 nodes of the corresponding cell. By imposing these quantities on the 8 nodes of each hexahedral cell, all functions in Eq. (5.16) are shown to be globally continuous across the domain covered by the grid. Since the exact derivatives of the potential are not known for e-clouds, central differences are used to evaluate them from the discrete samples ϕ^{ijk}, for example:

$$\frac{\partial\phi^{ijk}}{\partial x} \approx \frac{\phi^{i+1,j,k} - \phi^{i-1,j,k}}{2\Delta x}. \tag{5.18}$$

5.1.2 Refinement of the potential

For a typical e-cloud distribution, a direct application of the scheme described in the previous section can lead to unacceptable artifacts on the interpolated forces. This is shown by the red line in Fig. 5.2. It is evident that the interpolating function is irregular. This is due to the fact that the derivatives

$$\frac{\partial e_x^{\mathrm{int}}}{\partial x} = -\frac{\partial^2\phi^{\mathrm{int}}}{\partial x^2},\ \frac{\partial e_y^{\mathrm{int}}}{\partial y} = -\frac{\partial^2\phi^{\mathrm{int}}}{\partial y^2},\ \frac{\partial e_\tau^{\mathrm{int}}}{\partial \tau} = -\frac{\partial^2\phi^{\mathrm{int}}}{\partial \tau^2}, \tag{5.19}$$

are not globally continuous and, in fact are discontinuous across the x, y, τ directions, respectively, as discussed in Ref. [91]. Expressions for the first derivative of e_x^{int} at

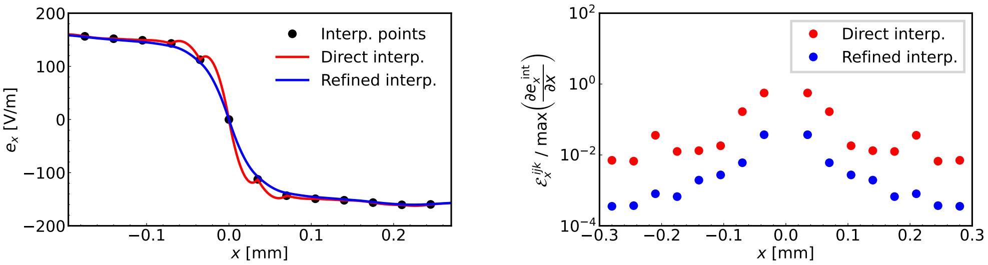

(a) (b)

Figure 5.2: (a) Horizontal forces from the e-cloud interaction as a function of the transverse coordinate x in the vicinity of the closed orbit of the beam for $x = 0, t = 0$. The (red) interpolating function obtained by the direct application of the tricubic method is shown alongside the (blue) result obtained with the refinement procedure. (b) Corresponding discontinuities on the first derivatives.

the grid points are derived in Ref. [91]

$$\left.\frac{\partial e_x^{\mathrm{int}}}{\partial x}\right|_{x\to x_i^+} = -6\frac{\phi^{i+1,j,k} - \phi^{i,j,k}}{\Delta x^2} - 2\frac{e_x^{i+1,j,k} + 2e_x^{i,j,k}}{\Delta x}, \tag{5.20}$$

$$\left.\frac{\partial e_x^{\mathrm{int}}}{\partial x}\right|_{x\to x_i^-} = -6\frac{\phi^{i-1,j,k} - \phi^{i,j,k}}{\Delta x^2} + 2\frac{e_x^{i-1,j,k} + 2e_x^{i,j,k}}{\Delta x}, \tag{5.21}$$

from which the discontinuity at the grid nodes can be computed as

$$\mathcal{E}_x^{ijk} = \left.\frac{\partial e_x^{\mathrm{int}}}{\partial x}\right|_{x\to x_i^+} - \left.\frac{\partial e_x^{\mathrm{int}}}{\partial x}\right|_{x\to x_i^-} = -6\frac{\phi^{i+1,j,k} - \phi^{i-1,j,k}}{\Delta x^2} - 2\frac{e_x^{i+1,j,k} + 4e_x^{i,j,k} + e_x^{i-1,j,k}}{\Delta x}. \tag{5.22}$$

Taking into account that e_x^{ijk} are evaluated by directly applying central differences (see Eq. (5.18)) on the discrete samples ϕ^{ijk}, it follows that:

$$\mathcal{E}_{x,\mathrm{direct}}^{ijk} = \frac{\phi^{i+2,j,k} - 2\phi^{i+1,j,k} + 2\phi^{i-1,j,k} - \phi^{i-2,j,k}}{\Delta x^2}. \tag{5.23}$$

By Taylor expanding $\phi(x, y, \tau)$ with respect to x around x_i, the discontinuity reads:

$$\mathcal{E}_{x,\mathrm{direct}}^{ijk} = -2\frac{\partial^3\phi}{\partial x^3}\left(x_i, y_j, \tau_k\right)\Delta x + O\left(\Delta x^3\right). \tag{5.24}$$

The expression shows that the discontinuity could be lowered by reducing the grid spacing Δx in the PIC simulations of the electron dynamics. However, when the grid spacing is reduced by a factor of h in all three dimensions, the number of macroparticles need to be increased by a h^3 factor so as to avoid the introduction of numerical noise. In a realistic e-cloud simulation, this approach quickly becomes restrictive both in terms of memory consumption and computation time.

It is important to note that the chosen Δx is sufficient to properly resolve the electron dynamics and the introduced forces on the grid. It is only at the interpolation stage that the artifact is introduced. Therefore, it is possible to leave Δx

unchanged in the PIC simulation and instead apply a refinement scheme directly on the result of such a simulation. Specifically, the resolution of ϕ can be increased locally by linearly interpolating ρ on a grid with spacing reduced by a factor of h

$$\Delta x_{\text{refined}} = \frac{\Delta x}{h}, \tag{5.25}$$

and solving once more the Poisson equation on this finer grid. This provides the potential in additional grid points, for example along the x direction of the cell with indices i, j, k:

$$\phi^{i,j,k}, \phi^{i+1/h,j,k}, \phi^{i+2/h,j,k}, \; \dots \; , \phi^{i+(h-1)/h,j,k}, \phi^{i+1,j,k}. \tag{5.26}$$

Working on such a refined grid allows for a more local estimate of all quantities in Eq. (5.16) on the grid nodes using central differences, for example:

$$\frac{\partial \phi^{ijk}}{\partial x} \approx h \frac{\phi^{i+1/h,j,k} - \phi^{i-1/h,j,k}}{2\Delta x}. \tag{5.27}$$

The memory required to store such quantities in all nodes of the finer grid scales with h^3. In practical cases, this strongly limits the choice of the factor h. To avoid this limitation, the quantities in Eq. (5.16) as obtained from the refined grid are stored only on the nodes of the original (coarse) grid, where they are used to apply the tricubic interpolation scheme. The quantities in the rest of the (fine) grid are discarded. The discontinuities introduced through this scheme can be evaluated by following the same approach as before, obtaining:

$$\begin{aligned} \mathcal{E}^{ijk}_{x,\text{refined}} = & -6 \frac{\phi^{i+1,j,k} - \phi^{i-1,j,k}}{\Delta x^2} + h \frac{-\phi^{i+1+1/h,j,k} + \phi^{i+1-1/h,j,k}}{\Delta x^2} \\ & + h \frac{-4\phi^{i+1/h,j,k} + 4\phi^{i-1/h,j,k} - \phi^{i-1+1/h,j,k} + \phi^{i-1-1/h,j,k}}{\Delta x^2}. \end{aligned} \tag{5.28}$$

Expanding $\phi(x, y, \tau)$ as a Taylor series with respect to x around x_i, the discontinuity becomes:

$$\mathcal{E}^{ijk}_{x,\text{refined}} = -2 \frac{\partial^3 \phi}{\partial x^3} \left(x_i, y_j, \tau_k\right) \frac{\Delta x}{h^2} + O\left(h^{-4} \Delta x^3\right). \tag{5.29}$$

The comparison of Eqs. (5.24) and (5.29) shows that the proposed refinement scheme is able to arbitrarily reduce the discontinuities while keeping the memory required to store the interpolation coefficients independent of the choice of h. The result obtained by applying such a scheme to the samples in Fig. 5.2a is shown by the blue line in the same figure. Evindently, the artifacts are practically suppressed. Figure 5.2b provides a quantitative comparison of the observed discontinuities, showing that the artifacts are reduced by an order of magnitude across the domain of the grid.

The importance of using this refinement scheme is visible in Fig. 5.3, where Poincaré plots of the non-linear motion of the beam particles over several turns are shown in the normalized phase space. The Poincaré plots were produced by tracking in the two degrees of freedom x, p_x through the successive applications of the e-cloud forces shown in Fig. 5.2 interleaved with a one-turn-map that is linear on the particle coordinates. The artifacts introduced by the direct interpolation method result into modifications of the particle dynamics, which are removed when using the refined interpolation method.

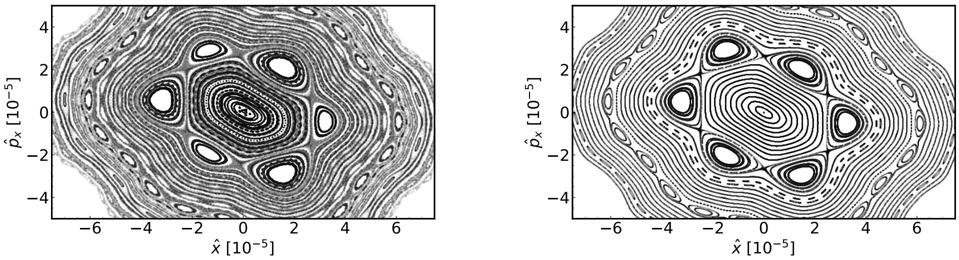

(a) (b)

Figure 5.3: Poincaré plot in normalized phase space with direct interpolation (a) and refined interpolation (b) of the e-cloud scalar potential.

5.2 Electron clouds in the LHC arcs

To illustrate the potential of the method presented in the previous sections, the case of the LHC is considered. In particular the simulations focus on the operation with protons at injection energy with the typical configuration used during the LHC Run 2. The main parameters defining the considered scenario are listed in Table 5.1. In this configuration, the effect of the beam-beam interaction is negligible and the optics do not have very large betatron functions around the interaction points, as opposed to when the beams are put in collision. The strongest non-linear effects apart from the e-cloud non-linear forces are due to the large current used to power the magnetic octupoles. This is necessary to introduce a sizable amplitude detuning in order to to mitigate coherent beam instabilities from e-cloud effects. The e-clouds in the LHC arcs only are considered, as they constitute the largest fraction of the ring circumference. Specifically, the model includes the effect of e-cloud developing in the main dipole magnets (MB) (~66% of the ring circumference) and the main quadrupole magnets (MQ) (~7% of the ring circumference). The e-cloud buildup and the electron dynamics are simulated with the PyECLOUD code [59]. More information on such a simulation model and its comparison against experimental data can be found in Refs. [21, 60].

Figure 5.4a shows the simulated electron distribution in an arc dipole magnet (MB) for the nominal bunch intensity of $1.2 \cdot 10^{11}$ p/bunch. It is characteristic of the e-cloud developing in the dipolar field of the LHC MB magnets that the two vertical stripes form on the left and on the right of the proton beam's closed orbit position [20]. For the nominal bunch intensity, such stripes are located far away from the beam location and the force exerted within the bunch is rather linear as shown in Fig. 5.4b. The situation is significantly different when considering a reduced bunch intensity, as is visible in Fig. 5.5a for $0.6 \cdot 10^{11}$ p/bunch. Here the electron stripes overlap with the beam distribution introducing significant non-linearities in the forces within the bunch, as shown in Fig. 5.5b.

In the main quadrupole magnets magnets (MQ), the e-cloud overlaps with the beam distribution independently of the considered bunch intensity and generate non-linearities in the forces within the bunch, as shown in Figs. 5.6 and 5.7 for the nominal and reduced bunch intensities, respectively.

Each arc of the LHC consists of 23 regular FODO cells each including 6 MB

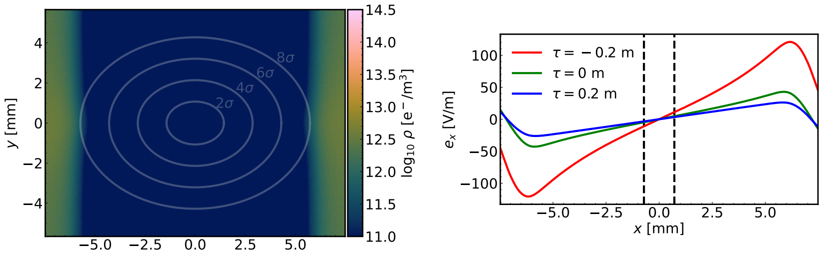

(a)

(b)

Figure 5.4: Snapshot of the e-cloud density in an MB magnet (a) and horizontal field in the plane $y = 0$ at different moments during the bunch passage (b) for the nominal bunch intensity of $1.2 \cdot 10^{11}$ p/bunch.

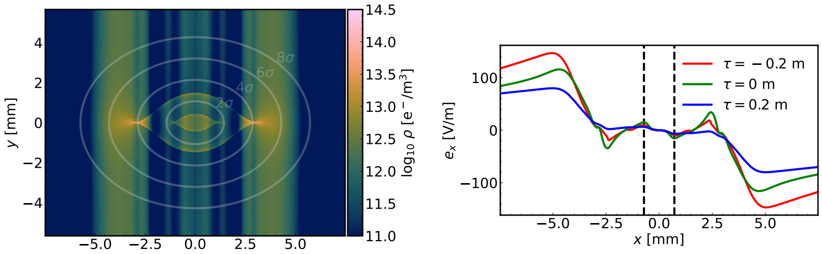

(a)

(b)

Figure 5.5: Snapshot of the e-cloud density in an MB magnet (a) and horizontal field in the plane $y = 0$ at different moments during the bunch passage (b) for the reduced bunch intensity of $0.6 \cdot 10^{11}$ p/bunch.

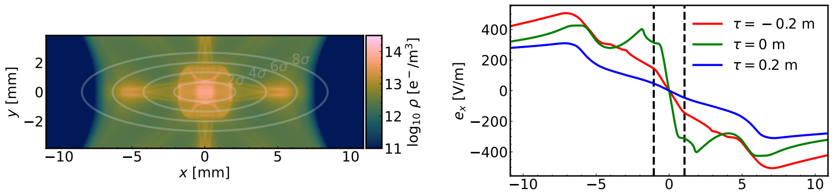

(a)

(b)

Figure 5.6: Snapshot of the e-cloud density in a focusing MQ magnet (a) and horizontal field in the plane $y = 0$ at different moments during the bunch passage (b) for the nominal bunch intensity of $1.2 \cdot 10^{11}$ p/bunch.

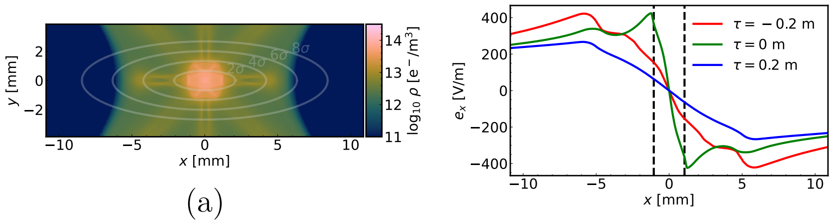

(a)

(b)

Figure 5.7: Snapshot of the e-cloud density in a focusing MQ magnet (a) and horizontal field in the plane $y = 0$ at different moments during the bunch passage (b) for the reduced bunch intensity of $0.6 \cdot 10^{11}$ p/bunch.

Table 5.1: Typical operational parameters of the LHC in Run 2 used in the simulations.

Bunch population [p/bunch]	$1.2 \cdot 10^{11}$
Reference energy [GeV]	450
R.m.s. bunch length [cm]	9
R.m.s. horizontal emittance (normalized) [µm]	2
R.m.s. vertical emittance (normalized) [µm]	2
Horizontal betatron tune	62.27
Vertical betatron tune	60.295
Synchrotron tune	$5.1 \cdot 10^{-3}$
Horizontal chromaticity	15
Vertical chromaticity	15
Octupole magnets' current [A]	40
Amplitude detuning coefficient [80], α_{xx} [µm^{-1}]	0.31
Amplitude detuning coefficient [80], α_{yy} [µm^{-1}]	0.32
Amplitude detuning coefficient [80], α_{xy} [µm^{-1}]	-0.22
RF voltage [MV]	6
Bunch spacing [ns]	25
MB magnet's length	14.3
MB magnet's field [T]	0.535
MQ magnet's length	3.1
MQ magnet's field gradient [T m^{-1}]	12.1
Primary collimators' set distance [σ]	7.5

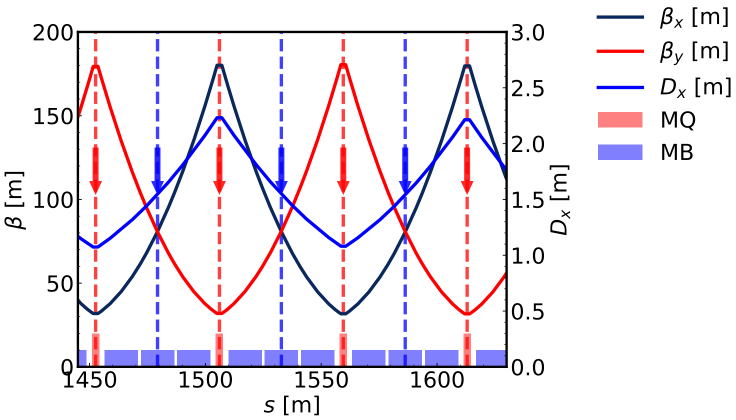

Figure 5.8: Betatron functions and horizontal dispersion in the FODO cells of the LHC arcs. The arrows indicate the places where the e-cloud interactions are applied.

magnets and two MQ magnets [1]. A small part of an arc is shown in Fig. 5.8 where the beta functions and the horizontal dispersion are plotted alongside an illustration of the position and extent of the main magnets.

The dynamics of the protons are simulated using the SixTrackLib code [74], where each element of the lattice is modelled with an appropriate number of thin lenses. To model the e-cloud, four e-cloud interactions are included in each cell, two modelling the e-cloud in the MB magnets and two modelling the e-cloud in the MQ magnets. Their locations are marked by the arrows in Fig. 5.8. In the simulation, particles are intercepted by the LHC primary collimators [1] which limit the amplitude of the betatron oscillations to 7.5 times the r.m.s. beam size. This is done in order to limit betatron oscillations to a domain where the e-cloud forces are defined.

A large number of turns needs to be simulated to study incoherent effects from e-clouds, which results in a significant computation time. For this reason, it is convenient to perform the simulations using GPUs instead of conventional CPUs, which is possible within the framework of the SixTrackLib code. For the simulations illustrated in the following sections, the usage of high-end GPUs provide a speedup in computation time of about 100 with respect to a single-thread simulation on a typical CPU.

5.3 Tracking simulations

5.3.1 Non-linear dynamics characterization

To characterize the single-particle stability in the presence of the different e-clouds, the DA [81] of the machine is evaluated through tracking simulations. As it is typical for LHC studies, the DA is defined as the normalized transverse oscillation amplitude above which particles are lost within 10^6 turns. The particles are initialized with an energy deviation of $p_\tau = 5.5 \cdot 10^{-4}$ (corresponding to around two thirds of an RF bucket height), in order to include effects from synchrotron oscillations in the

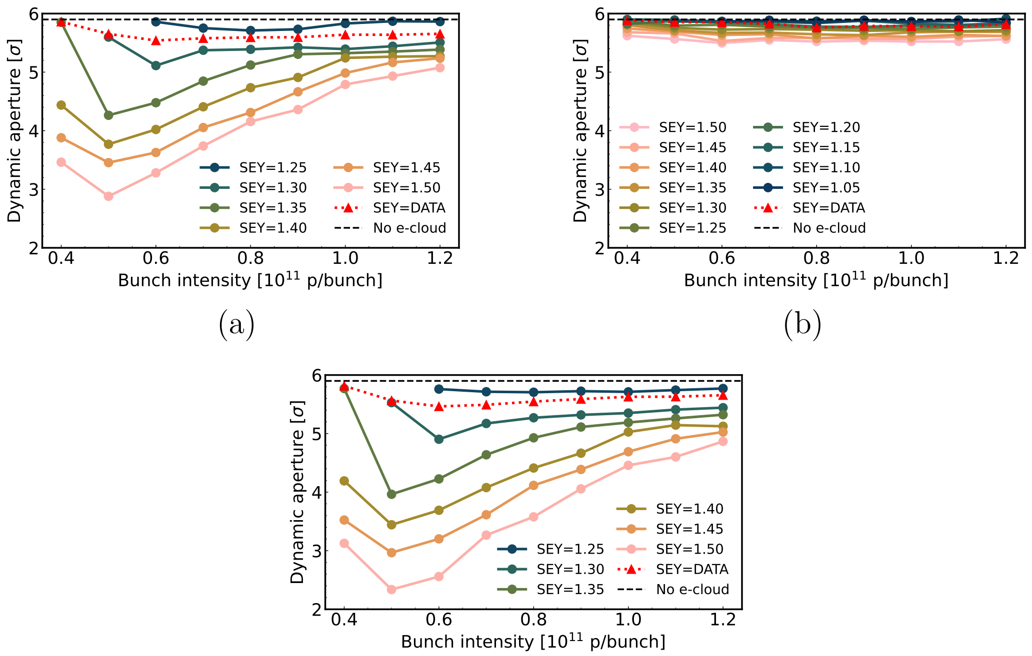

(a)

(b)

(c)

Figure 5.9: Dynamic aperture as a function of the bunch intensity and SEY with simulations including e-clouds in the MB magnets only (a), in the MQ magnets only (b) and in the MB and MQ magnets (c).

evaluation of DA.

Results are shown in Fig. 5.9 as a function of the bunch intensity and for different values of the SEY. The dashed black line marks the DA obtained in simulations without e-cloud effects.

Figure 5.9a shows the DA when only the e-cloud in the MB magnets is included in the simulations. Increasing the SEY makes the e-cloud stronger, which results in a decrease of the DA. The e-cloud in the MB magnets causes a degradation of the single-particle stability that is stronger for relatively low bunch intensities, for which the stripes in the electron distribution come closer together and overlap with the bunch resulting in stronger non-linear forces (see Fig. 5.5). For comparison, simulations approximating the actual SEY in the LHC dipole chambers were performed. In fact, the beam pipes in the different half-cells of the LHC arcs show different SEY as a result of different oxidation states of the surface [61]. The red dotted curve shows the DA computed with a special e-cloud potential which has been constructed by averaging over the potentials obtained from simulations performed with the appropriate SEY for each half-cell (as estimated through cryogenic heat-load measurements). The measurement and estimation of the SEY distribution is carried out and explained in Ref. [21].

Figure 5.9b shows the DA when only the e-cloud in the MQ magnets is included in the simulation. The effect of the e-cloud in the MQ magnets on the DA is significantly weaker compared to the case where only e-clouds in the MB magnets are included and there is a very small dependence on the bunch intensity. This

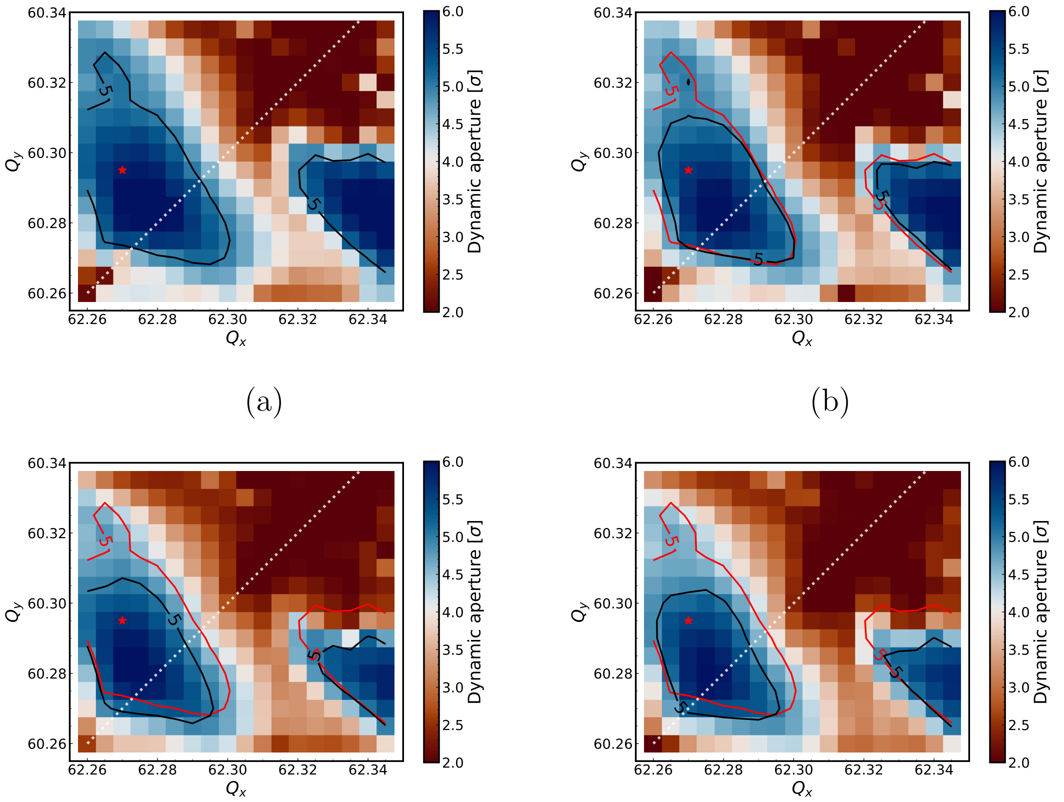

(a) (b)

(c) (d)

Figure 5.10: Dynamic aperture as a function of the horizontal and vertical betatron tunes in the absence of e-cloud (a) and with e-clouds in the MB magnets only (b), in the MQ magnets only (c), and in the MB and MQ magnets (d). The red marker corresponds to the working point set during operation. Contours of DA equal to 5σ are shown with the black lines while the red lines in (b), (c) and (d) report the contours obtained without e-cloud.

is in agreement from a qualitative comparison of the electron distributions for the different intensities, as illustrated for example in Figs. 5.7 and 5.6. The combined effect of e-clouds in both MB and MQ magnets is shown in Fig.5.9c.

The dependence of the DA on the betatron tune settings has also been studied through simulations. As shown in Fig. 5.10, the effect of the e-cloud reduces the region of the tune diagram available for operation, defined such that DA $> 5\sigma$. For coherent beam stability issues, a minimum difference of at least 0.01 is recommended in the fractional part of the tunes [72]. For this reason, the tune settings used in the operation of the LHC are set to $Q_x = 62.27$ and $Q_y = 60.295$, which is marked by the red star in Fig. 5.10.

Additional insight on the beam dynamics in the presence of e-cloud effects can be obtained through the Frequency Map Analysis (FMA) technique [92]. In this study, the FMA is realized by simulating a particle distribution that is uniform in the horizontal and vertical normalized amplitude space, which is tracked for $2 \cdot 10^4$ turns. The turn-by-turn positions are then used to estimate the betatron tunes in the

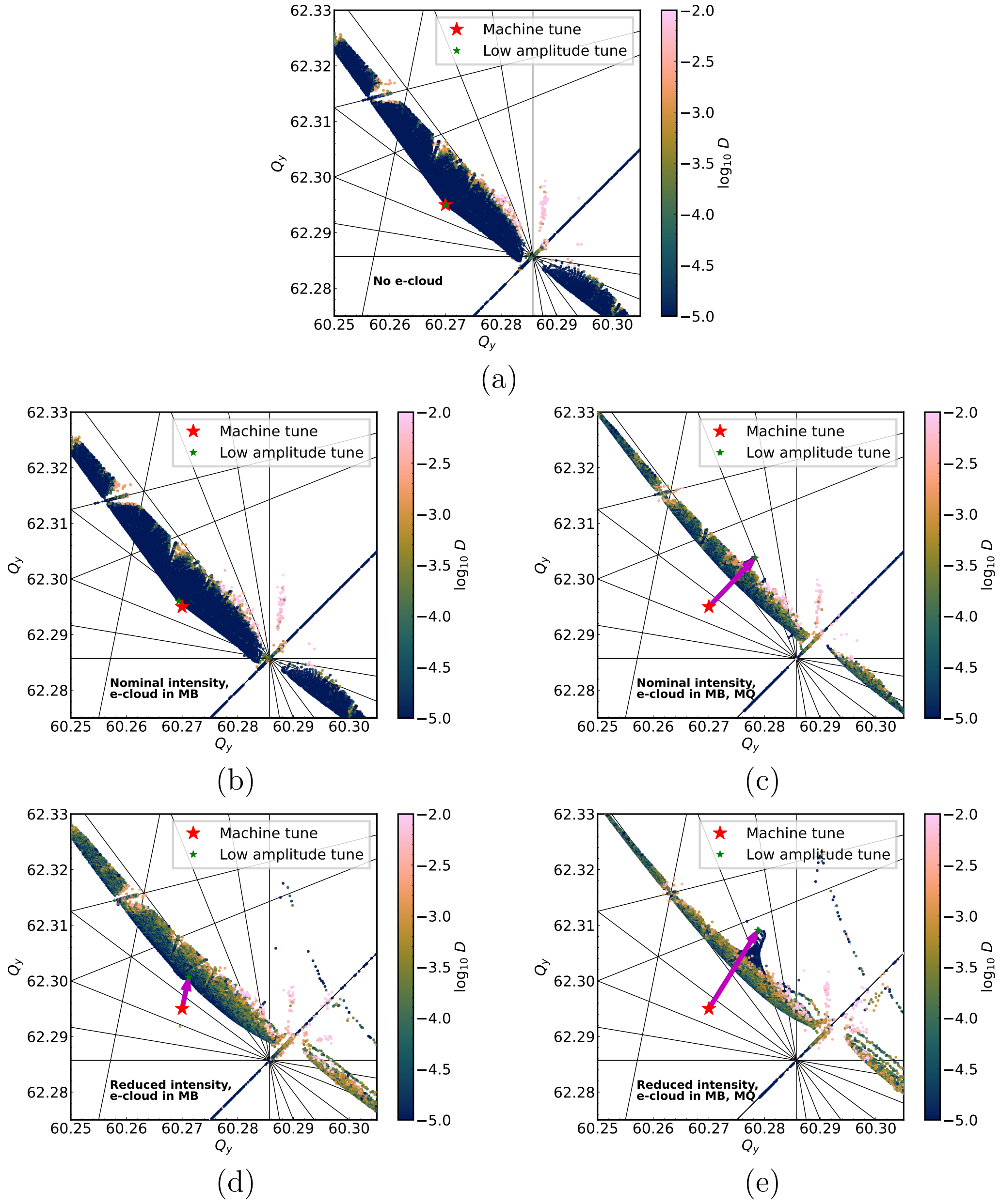

(a)

(b)

(c)

(d)

(e)

Figure 5.11: Frequency Map Analysis for on-momentum particles without e-clouds (a) and with e-clouds in the MB magnets at nominal intensity ($1.2 \cdot 10^{11}$ p/bunch) (b), in the MB and MQ magnets at nominal intensity (c), in the MB magnets at reduced intensity ($0.6 \cdot 10^{11}$ p/bunch) and in the MB and MQ magnets at reduced intensity (e). Transverse resonance lines up to order 7 are shown.

first 10^4 turns $(Q_{x,1}, Q_{y,1})$ and the last 10^4 turns $(Q_{x,2}, Q_{y,2})$. The numerical analysis of fundamental frequencies algorithm (NAFF) [93] is used for the identification of the tunes. The distance in the betatron tunes between the two time intervals defines a tune diffusion rate:

$$D = \sqrt{\left(Q_{x,2} - Q_{x,1}\right)^2 + \left(Q_{y,2} - Q_{y,1}\right)^2}. \tag{5.30}$$

The FMA simulations are carried out on-momentum, *i.e.* particles are initialized in the absence of synchrotron oscillations, as the estimation of the betatron tunes can become elusive in the presence of strong tune modulation effects [94]. The results of the FMA simulations are presented in Fig. 5.11 for the two bunch intensities. Figure 5.11a shows the FMA without e-cloud while Figs. 5.11b, d show the FMAs including only MB-type e-clouds and Figs. 5.11c, e show the FMAs with MB and MQ-type e-clouds. In all figures, the red marker indicates the betatron tune settings of the machine and the magenta marker shows the tune found for low-amplitude particles, as a result of the detuning forces from e-cloud effects.

For nominal intensity and e-clouds only in the MB magnets, there is no significant impact of the e-cloud on the on-momentum FMA, as observed when comparing Figs. 5.11a and b. When including the e-cloud in the MQ magnets, as presented in Fig. 5.11c, a much stronger low-amplitude tune-shift is observed, together with the excitation of several resonances as well as a significantly larger tune diffusion over the entire simulated particle distribution. The observations seem counter-intuitive when compared to the simulations of DA in Fig. 5.9, where it was observed that the effect of the e-cloud in the MB magnets was stronger than that of the e-cloud in the MQ magnets. This is caused by the fact that the losses from e-cloud are mostly driven from off-momentum particles, as will be discussed in Section 5.3.2, while only on-momentum particles are shown in Fig. 5.11. For this reason, these studies would strongly profit from the development in the future of advanced FMA techniques that would work robustly in the presence of strong tune modulations driven by synchrotron motion (recent attempts in this direction were made in Ref. [94]).

A similar analysis is presented in Figs. 5.11d, e for the reduced bunch intensity. In this case, an even stronger tune shift and resonance excitation are observed. These effects are visible even when the e-cloud is present only in the MB magnets, due to the increased electron density at the beam location (see Fig. 5.5) compared to the case with nominal bunch intensity.

5.3.2 Direct simulation of the beam evolution

Dynamic Aperture and FMA simulations provide important understanding on the non-linear beam dynamics. Nevertheless, it is usually difficult to use such results in order to infer observable quantities like beam lifetime and the evolution of the beam profile. Such effects, which at the LHC are visible only on very long timescales (in the order of several minutes), need to be studied with direct tracking simulations. For this purpose, we simulate 10^7 turns, corresponding to approximately 15 minutes of beam time.

The choice of the initial particle coordinates plays an important role in the simulation. One possibility would be to initialize the particles according to the

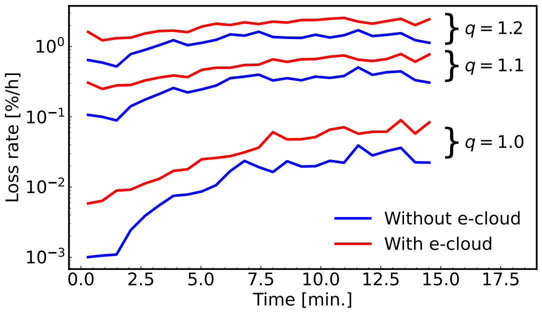

Figure 5.12: Loss rate as a function of time for three different values of the q parameter that defines the population of particles at large amplitudes. The red lines correspond to simulations with e-clouds in both MB and MQ magnets for nominal intensity and the blue lines to simulations without e-clouds. The loss rate is calculated over 30 seconds.

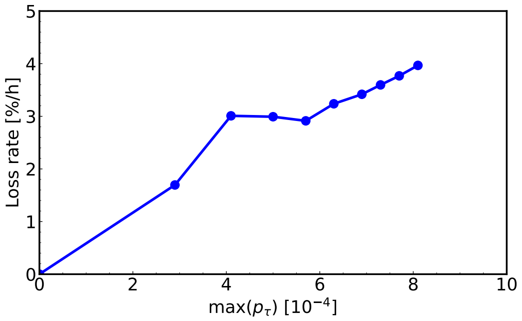

Figure 5.13: Average loss rate as a function of the synchrotron oscillation amplitude.

realistic beam distribution, for example a Gaussian distribution. However, such a choice is not optimal due to the fact that very few particles would be generated with large oscillation amplitudes, although it is especially such large-amplitude particles that determine observables like the beam lifetime.

Instead, it is convenient to generate particles randomly following a uniform distribution over the normalized transverse phase space $(\hat{x}, \hat{p}_x, \hat{y}, \hat{p}_y)$ and to repeat simulations for different synchrotron oscillation amplitudes in order to cover the entire 6D phase space. The distributions are matched to the optics by using the normalizing transformation $\mathcal{W}$ obtained by an eigenvector analysis of the linear 6D one-turn map as described in Sec. 1.2.

The loss rate and the evolution of the beam profile for the real non-uniform beam distribution can be calculated by assigning a weight to each particle according to the local phase density of the assumed particle distribution, following the procedure defined in Sec. 4.2. This approach has the advantage that the same tracking data can be used to estimate the evolution for different initial particle distributions extending over the same phase space area by simply changing the particle weights.

Experimental measurements of the transverse beam profiles in the LHC show that their core can be described very well with Gaussian distributions. However,

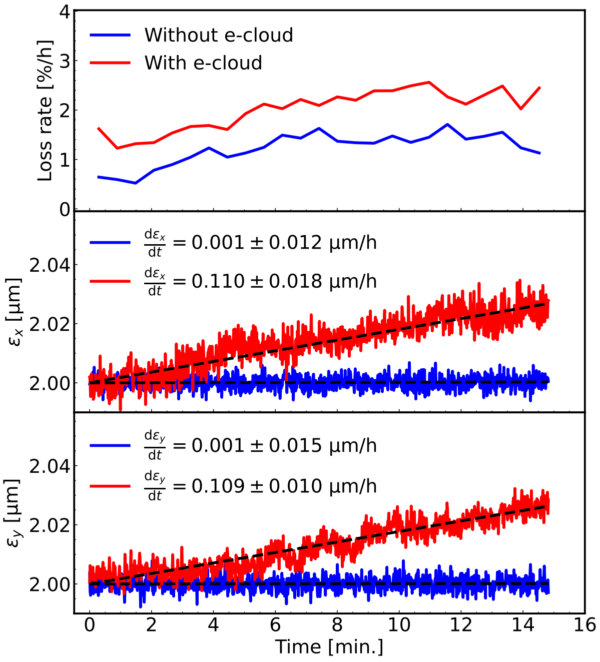

Figure 5.14: Long-term tracking simulation with particle distributions for the nominal intensity and SEY$_{\text{max}}$ based from measurements. The relative loss rate (top), the horizontal (middle) and the vertical emittance (bottom) are plotted as a function of time for simulations without e-clouds (blue) and with e-clouds in both the MB and MQ magnets (red). The black dashed lines correspond to linear fits.

measuring the tails of the beam profiles is more difficult. The available data suggests that the tails of the profiles are slightly overpopulated with respect to a purely Gaussian distribution [84]. The beam loss rate is directly related to the population of particles in the tails due to their large oscillation amplitude. As done in Chapter 4, in order to study the sensitivity of the results to the tail population, 4D q-Gaussian distributions are used. The population in the tails is controlled by the q parameter. For $q = 1$, the distribution is a Gaussian distribution, for $q > 1$ the distribution has overpopulated tails, and for $q < 1$ the tails are underpopulated [85, 86].

In the simulations, the longitudinal distribution is expressed as an exponential of the action variable of the single-harmonic RF potential, which is a realistic assumption based on profile measurements [95]. The parameters of the distribution are chosen such that the r.m.s. bunch length is equal to the one reported in Table 5.1.

Fig. 5.12 shows the evolution of the loss rate as a function of time without e-cloud (blue) and in the presence of e-cloud in both MB and MQ magnets (red). The evolution is illustrated for three different values of the parameter q of the transverse distribution. It is evident that the losses are very sensitive to the initial tail population.

It is interesting to observe the dependence of the losses on the synchrotron oscillation amplitude. This is shown in Fig. 5.13 where it is visible that losses are basically absent for on-momentum particles while they become larger as the oscillation amplitude increases.

Figure 5.14 shows the emittance evolution without e-cloud (blue) and in the presence of e-cloud in both MB and MQ magnets (red). The emittance is computed by fitting Gaussian functions on the projections of the weighted particle distributions. The fit is made on the core of the transverse distribution as done in measurements of the transverse emittance in the LHC. No emittance growth is found in the absence of e-cloud while a weak linear emittance growth is found in the simulations with e-cloud effects.

The simulations were repeated for different bunch intensities, considering e-cloud effects a) only in the MB magnets and b) in both MB and MQ magnets of the LHC arcs. All configurations, qualitatively, show the same features. With respect to the loss rate, a small increase is observed within the first 10 minutes while it becomes approximately constant in the last minutes of the simulated time interval. Concerning the emittance growth, if any, it is observed as linear across all configurations.

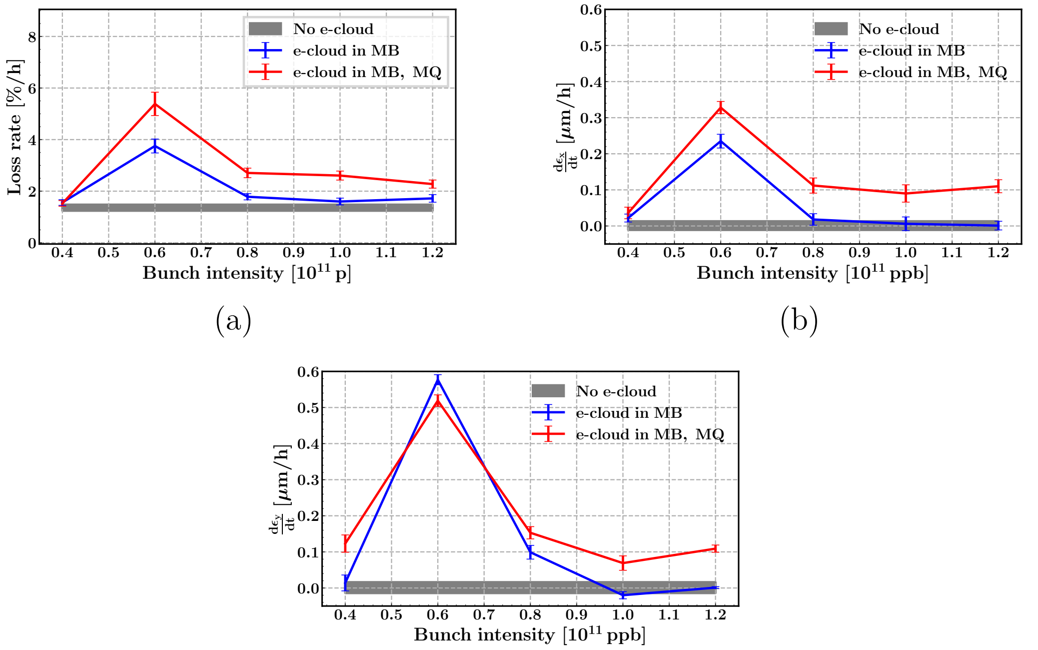

(a)

(b)

(c)

Figure 5.15: Simulations of loss rate (a), horizontal emittance growth rate (b) and vertical emittance growth rate (c) for different bunch intensities and (grey) without e-clouds, (blue) with MB-type e-clouds, (red) with MB and MQ-type e-clouds.

The summary of all configurations is illustrated in Fig. 5.15. Simulation results 1) with both MB and MQ-type e-clouds are shown in red, 2) with only MB-type e-clouds are shown in blue, while 3) the reference simulation without e-clouds is presented in gray. For the loss rate (Fig. 5.15a), the quoted number corresponds to the loss-rate within the five last minutes of the simulations. For the horizontal (Fig. 5.15b) and the vertical (Fig. 5.15c) emittance, the graphs present the slopes

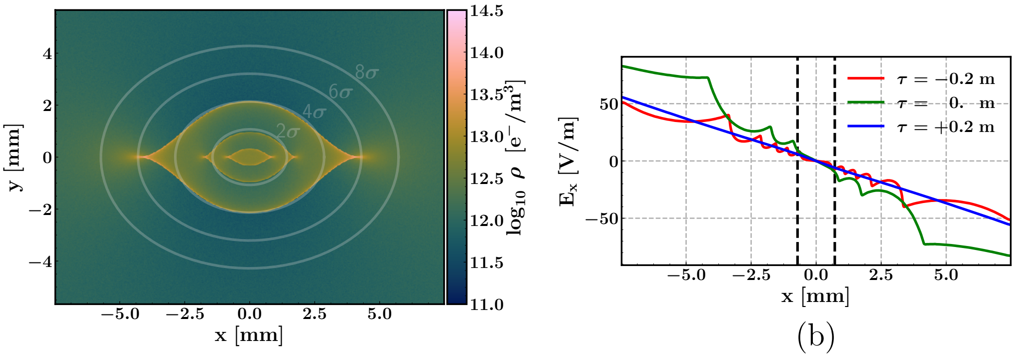

(b)

(a)

Figure 5.16: Electron cloud snapshots in MB magnets of (a) the charge density and (b) the horizontal field along $y = 0$ for a bunch intensity of $1.2 \cdot 10^{11}$ protons per bunch and a uniform initially distribution of electrons equal to 10^{12} e/m^3.

of the linear fits as in Fig. 5.14, *i.e.* the emittance growth rate.

Apart from the critical value of the bunch intensity at $0.6 \cdot 10^{11}$ p/b, the effect of the MB-type e-clouds on the loss rate is a small increase. The addition of the MQ-type e-cloud then increases the loss rate without an obvious dependence on the bunch intensity. Concerning the emittance growth, there is no emittance growth when including only the MB-type e-clouds except at the reduced bunch intensity of $0.6 \cdot 10^{11}$ p/b. Instead, at the nominal configuration of the LHC, it appears that the MQ-type e-clouds are the ones that contribute the most to the emittance growth. While the MQ-type e-clouds drive an emittance growth that is similar in the two transverse planes, the MB-type e-cloud has a stronger effect on the vertical emittance. Furthermore, the interplay between the MB-type and MQ-type e-cloud is not always straightforward since at the low bunch intensity of 0.6×10^{11} p/b, the emittance growth decreases when introducing the MQ-type e-cloud.

5.3.3 Additional uniform e-cloud

In the estimation of the SEY in the LHC half-cells, PyECLOUD was used to produce heat-load simulations which were compared to heat-load measurements. However, the heat-load in the dipole magnets is dominated by the electrons in the two large stripes, while the non-linear beam dynamics is mostly dominated by the density of electrons in the vicinity of the beam. While PyECLOUD can model and predict the heat-load at the LHC to a good extent, it is unknown whether it can accurately predict the density of electrons in the vicinity of the beam, due to the difficulty in measuring this density.

To probe the sensitivity to such densities, an additional e-cloud interaction is attached to the MB-type e-cloud interaction. For this interaction, the magnetic field of the MB magnet is used but the initial electron distribution is uniform in space and is a free parameter of the interaction. The evolution of the pinch that happens due to the interaction of the protons and the electrons is simulated normally. A

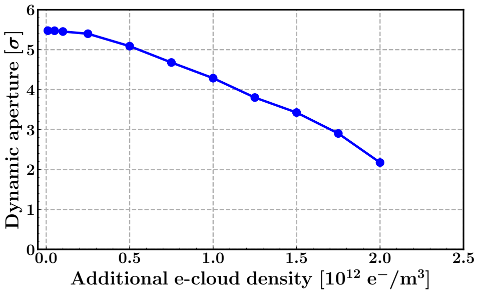

Figure 5.17: Dynamic aperture as a function of an additional initially electron density of the MB-type e-clouds, for a bunch intensity of $1.2 \cdot 10^{11}$ p/b.

snapshot of the charge density is illustrated in Fig. 5.16a while the horizontal field is plotted in Fig. 5.16b as a function of the horizontal position in the chamber for $y = 0$ and three different values of time: (red) $\tau = -0.2\,\mathrm{m}$, (green) $\tau = 0\,\mathrm{m}$, (blue) $\tau = 0.2\,\mathrm{m}$.

In this set of simulations the nominal operational parameters are used where the bunch intensity is equal to 1.2×10^{11} p/b. The dynamic aperture is scanned in Fig. 5.17 as a function of the electron density of the newly introduced interaction and a strong dependence is found on it. For reference, as can be seen in Fig. 5.4 a, the maximum of the initial electron density in the stripes of the MB-type e-cloud is equal to about $1.5 \cdot 10^{12}\, e^-/m^3$ while around the closed orbit the density is $< 0.1 \cdot 10^{12}\, e^-/m^3$. Figures 5.18a, 5.18b and 5.18c show the loss rate, the horizontal emittance growth rate and the vertical emittance growth rate, respectively, which are calculated through the tracking of particle distributions. As before, the simulations are carried out with only MB-type e-clouds (blue) as well as both MB-type and MQ-type e-clouds (red). Naturally, the beam quality worsens as the electron density becomes larger; the loss rate is larger and the emittance growth rate is also larger. Since in the newly introduced e-cloud interaction the magnetic field is the same as the one in the MB magnet, a behaviour that is qualitatively similar to the MB-type e-cloud is expected. Indeed, the vertical emittance growth is larger than the horizontal one.

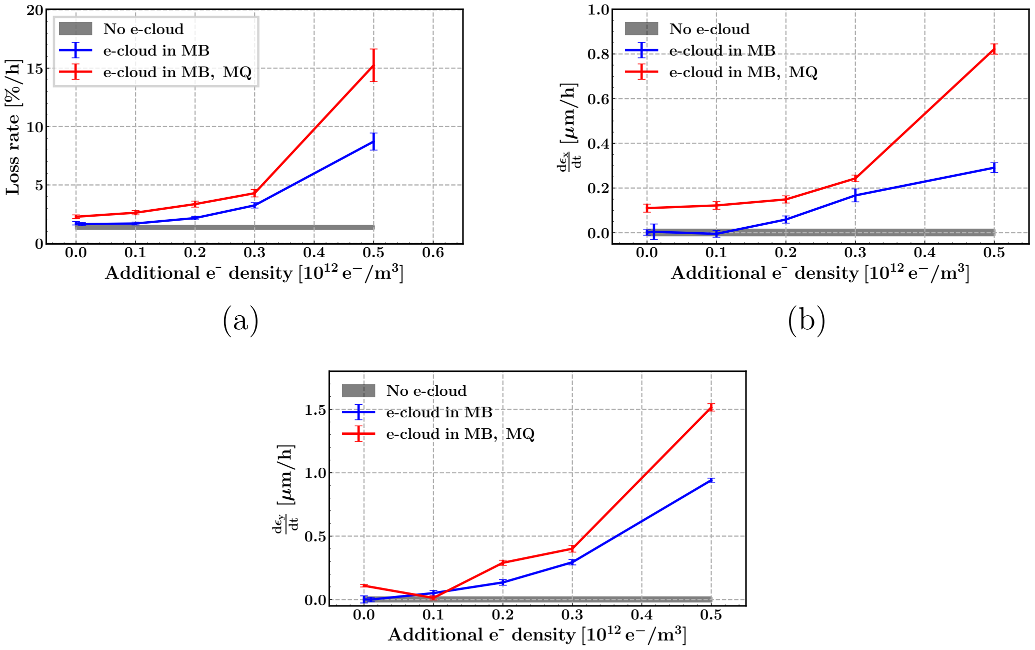

(a)

(b)

(c)

Figure 5.18: Simulations of relative loss rate (a), horizontal emittance growth (b) and vertical emittance growth (c) as a function of the additional initial electron densities in the MB-type e-clouds in simulations without e-clouds (gray), with MB-type e-clouds (blue), with MB and MQ-type e-clouds (red).

Part II

Phenomenological Model of the PICOSEC Micromegas detector

Chapter 6

The PICOSEC detector

6.1 Introduction

The PICOSEC Micromegas detection concept is realized by a two-stage Micromegas detector [96] coupled to a window that acts as a Cherenkov radiator, coated with a photocathode. The drift region of the detector is very small (~ 200 µm), which minimizes the probability of direct gas ionization as well as diffusion effects on the timing of the signal. The high electric field drives photoelectrons to undergo some pre-amplification in this drift region. The readout is a bulk Micromegas[97], consisting of a woven mesh and an anode plane that is separated by a gap of approximately 128 µm, mechanically defined by pillars. A relativistic charged particle that goes through the radiator window produces UV photons, which are simultaneously (with an RMS of less than 10 ps) converted into primary photoelectrons at the photocathode. These primary photoelectrons produce pre-amplification avalanches in the drift region (which hereafter will be referred to as the pre-amplification region). A fraction of these pre-amplification electrons manage to traverse through the mesh and enter the amplification region where they continue with the main amplification. The main detector components and a schematic representation of the microscopic processes producing the signal are visible in Fig. 6.1.

Electrons that arrive at the anode produce a fast signal component (with a rise time of approximately 0.5 ns) which is referred to as the electron-peak ("e-peak"). On the other hand, the movement of ions produced in the amplification gap generate a much slower (~ 100 ns) ion-tail component. This type of detector can reach high enough gain to detect single photoelectrons when operated with gas mixtures base on Ne or CF_4. The PICOSEC Micromegas detector (hereafter referred to as PICOSEC) has the potential to time Minimum Ionizing Particles (MIPs) with a precision below 25 ps[25]. A very good timing resolution in detecting single photons was also demonstrated through extensive tests with laser beams[26]. These laser beam data are also used for the calibrating the detector, and are referred to as "calibration data" in the following.

The PICOSEC approach to charged particle timing results in a significant improvement over the time resolution obtained when using a gaseous detector that is sensitive to ionization produced by charged particles traversing the gas volume. With multiple ionization and without the pre-amplification in the drift region, the

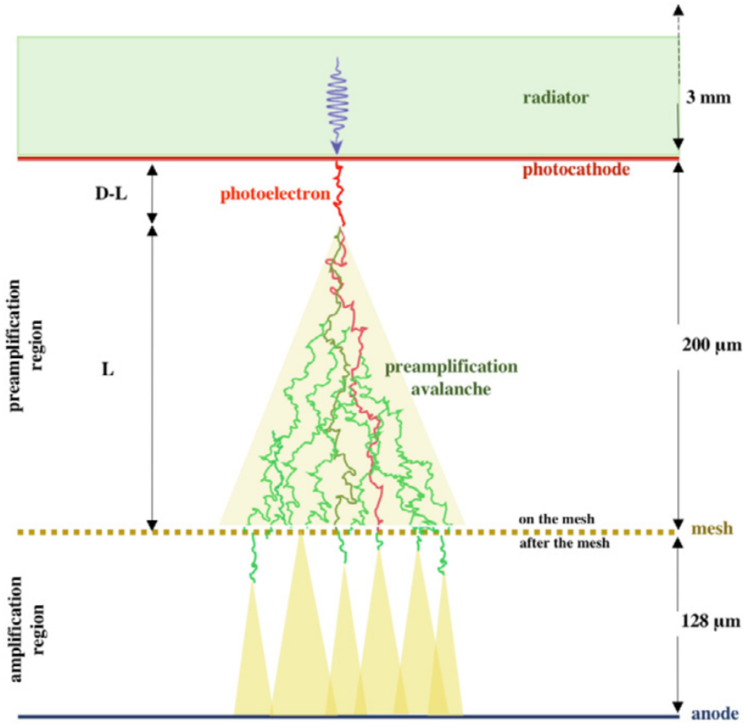

Figure 6.1: Illustration of the main PICOSEC detector components (dimensions are only indicative): the radiator of typical thickness ≈ 3 mm, the photocathode, the pre-amplification (drift) region of depth D (200 μm), the mesh, the amplification region (128 μm) and the anode. A photoelectron, after drifting for a distance $D - L$, produces a pre-amplification avalanche of length L, ending on the upper surface of the mesh (on the mesh). A fraction of the avalanche electrons traverse through to the lower surface of the mesh (after the mesh) and each produce avalanches in the amplification region. Figure adapted from Ref. [16].

timing resolution of a gaseous detector is of the order of a few nanoseconds[98]. With the above modifications to the typical Micromegas design, PICOSEC managed to achieve a far better precision in timing for two reasons. Firstly, the photoelectrons enter the drift region simultaneously. Secondly, the pre-amplification in the very thin drift region allows for the time-averaging of the electrons traversing through the mesh structure to arrive in the amplification region.

In this study, a full phenomenological description of the PICOSEC performance is given and a detailed model is provided that can be used for further optimization of this device to a mature and robust detector. With this model in hand, questions such as the following can be addressed:

1. What is the relative importance of the drift stage to the amplification stage in the time jitter of the PICOSEC Signal Arrival Time (SAT)?
2. How does the SAT that is generated by a single photoelectron depend on the fluctuating distance of where the avalanche is initiated in the drift region?
3. How does the time resolution depend on the properties of the gas mixture (that fills the detector) and on the voltage settings?

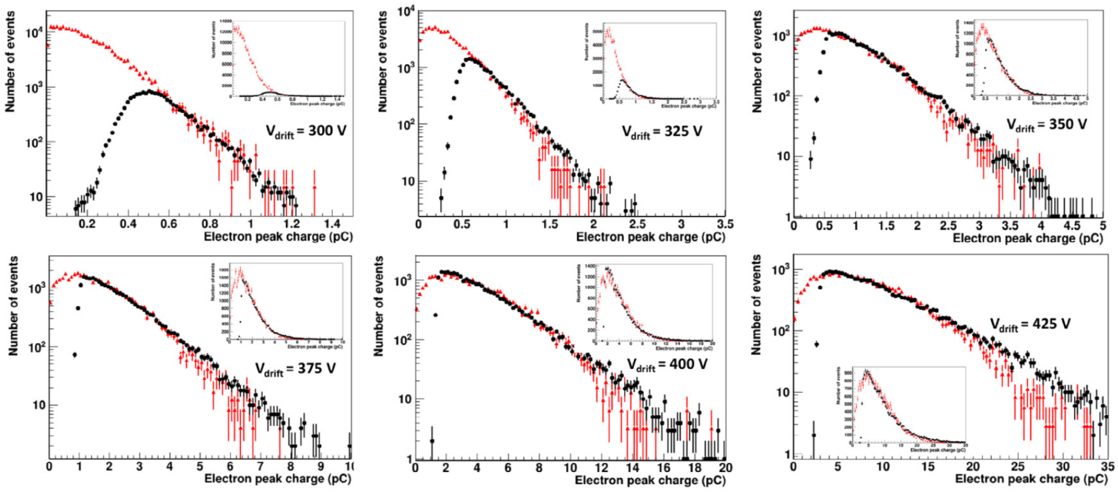

Figure 6.2: Distributions of the e-peak charge induced by a single photoelectron, for several drift voltage settings (300 V, 325 V, 350 V, 375 V, 400 V and 425 V). The black points represent calibration data published in Ref. [25] while the red triangles correspond to GARFIELD++ simulated PICOSEC e-peak waveforms treated the same way as the experimental data, as described in Ref. [26]. The data distributions are affected, at low e-peak charge values, by the amplitude threshold applied for data collection. Figure adapted from Ref. [16].

4. What is the effect of the transmission through the mesh structure on the time resolution?
5. Which is the optimal structure?

A detailed microscopic description of the physics principles underlying the PICOSEC detector is necessary to answer these questions.

The timing resolution of the PICOSEC detector depends on the drift and the anode operating voltages. During the tests with laser beams, where the anode voltage had to be high ($> 400\,\mathrm{V}$), it was observed that the timing resolution of detecting single photoelectrons is determined mostly by the drift field. Additionally, it was found the the SAT of the PICOSEC and the time resolution are functions of the size of the e-peak, *i.e.* the e-peak voltage amplitude or the respective e-peak charge. Their functional forms were shown to be practically the same for drift voltages in the range of 300 V to 425 V. It should be noted that these dependencies were found to not be systematic artifacts of the experimental timing technique[25, 26]. Instead they emerge from the physics determining the production of the signal.

Detailed simulations performed with the GARFIELD++[99] package, and including the simulation of the electronic response of the detector and the contribution from noise, were able to reproduce the observed PICOSEC performance characteristics when detecting single-photons[26]. By comparing the simulation predictions with the calibration data from the tests with laser beams, the Penning transfer rate (Ptr) [100] of the COMPASS gas could be estimated. The term “COMPASS gas” refers to the mixture 80% Ne, $10\%C_2H_6$, $10\%CF_4$, as is used by the COMPASS Collaboration. The Ptr for this gas mixture was estimated to be approximately 50%. The e-peak charge distribution of the simulated waveforms agrees well with

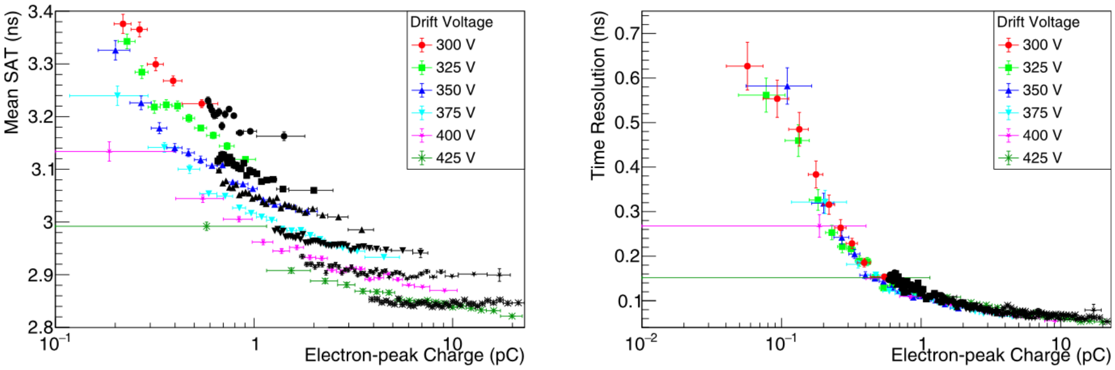

Figure 6.3: (left) Mean SAT as a function of the electron peak charge. (right) Time resolution as a function of the electron peak charge. In both figures black points represent experimental measurements[25] while colored symbols correspond to simulations[26]. The gas used is the COMPASS gas with an anode voltage of 450 V and for drift voltages of (red) 300 V, (light green) 325 V, (blue) 350 V, (cyan) 375 V, (magenta) 400 V and (dark green) 425 V. Figure adapted from Ref. [16].

the calibration data, as shown in Fig. 6.2. Moreover, in Fig. 6.3, the SAT and the timing resolution of the simulated waveforms depends on the e-peak size in exactly the same way that is found in the measurements.

The agreement between simulations and measurements is exploited in order to identify the microscopic physical variables that determine the observed timing characteristics. In particular, simulations with GARFIELD++ show that the number of pre-amplification electrons traversing the mesh, and therefore entering the amplification region to initiate avalanches, determine the size of the PICOSEC (a macroscopic and observable quantity) as is visible in the left plot of Fig. 6.4. The number of pre-amplification electrons traversing the mesh is a microscopic quantity and hereafter will be referred to as the "electron multiplicity after the mesh".

In the simulation, one has the ability, for each pre-amplification electron traversing the mesh to determine the time it enters the anode region, measured from the time instant of the photoelectron emission. The average times over all the pre-amplification electrons defines the microscopic variable that will be called "total-time after the mesh". This microscopic variable has the same properties as the measured SAT of the PICOSEC signal, which is defined at a constant fraction (20%) of the e-peak amplitude (as described in Ref. [25]). In the right plot of Fig.6.4, for simulated single photoelectron events with the same e-peak size, the RMS spread of the microscopic "total-time after the mesh" are found equal to the spread of the corresponding SAT, i.e. the macroscopic PICOSEC timing resolution. Moreover, it is visible in the middle plot of Fig. 6.4 that the mean value of the "total-time after the mesh" differs only by a constant time offset from the respective mean values of the PICOSEC SAT. This offset does not depend on the e-peak size and comes from the fact that the SAT also includes the propagation time of the amplification avalanches and the signal rise time up to the 20% of the e-peak amplitude.

After identifying the relevant microscopic variables that determine the timing characteristics of the PICOSEC detector, the detailed simulations are further used

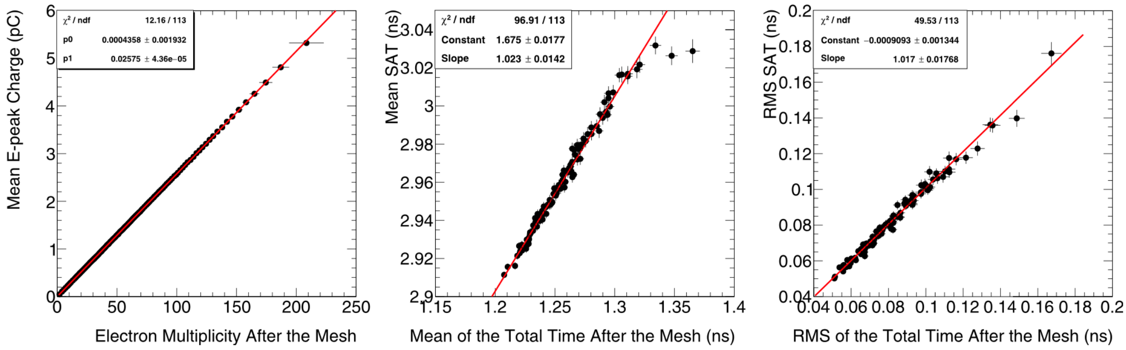

Figure 6.4: (left) The mean e-peak charge of simulated PICOSEC signals versus the respective "electron multiplicity after the mesh". The middle and right plots demonstrate that the macroscopically determined PICOSEC SAT has the same properties as the microscopic variable "total-time after the mesh", as described in the text. Figure adapted from Ref. [16].

in this work to study the evolution of the PICOSEC signal in terms of electron multiplicities and other important variables, like the primary photoelectron drift path and the length of the pre-amplification avalanches. Furthermore, to gain insight on the physical mechanism causing the dependence of the PICOSEC timing characteristics on the signal size and the weak influence of the mesh transparency on the timing resolution, a stochastic model is constructed. This model is based on a simple concept of "time-gain per interaction" and reproduces the PICOSEC timing characteristics as well as the simulations with the GARFIELD++ software. Moreover, the model offers a phenomenological interpretation to a number of peculiar statistical properties found in the GARFIELD++ results.

An overview of this chapter is given in Sec. 6.2 while the other sections contain a description of the stochastic modelling of all relevant processes and demonstrate the performance of the model.

6.2 Overview

In this work, the GARFIELD++ package (https://gitlab.cern.ch/garfield/garfieldpp, commit e018bcca, 8 May 2017), is used to describe microscopically the PICOSEC timing properties by simulating in detail the relevant processes. The statistical interpretation of the simulation leads to several observations which are counter-intuitive. For example:

- The primary photoelectron drift velocity seems to depend on Ptr (Penning transfer rate),
- The avalanche electrons drift faster than the primary photoelectron,
- The average speed of the avalanche as a whole is larger than the drift velocity of its constituent electrons,
- The longitudinal diffusion of the avalanche is almost independent of its length,
- The 25% transparency of the mesh has a very minor effect on the PICOSEC timing resolution.

Moreover, it is observed that the PICOSEC timing resolution is mainly determined by the drift path of the primary photoelectron. However, when expressing the timing resolution as a function of the number of electrons passing through the mesh (*i.e.* the e-peak size), the related photoelectron and avalanche contributions to the resolution were found heavily correlated.

To identify the main physical processes causing the observed behaviour, a simple phenomenological model is presented. The model is based on a simple mechanism of "time-gain per interaction" and it employs a statistical description of the avalanche evolution. It describes well the aforementioned phenomena in agreement with the GARFIELD++ simulation results, as demonstrated in the following sections.

The parameters of the model (*i.e.* drift velocities, ionization probabilities per unit length, multiplication and diffusion coefficients, mean value and variance of the "time-gain per interaction", average mesh transparency and longitudinal diffusion around the mesh, etc.) are commonly used statistical variables with values that depend on the PICOSEC gas filling and the operating voltage settings. The values of these parameters are estimated from the GARFIELD++ simulations for the COMPASS gas mixture, assuming several values of Ptr (Penning transfer rates: 0%, 50%, 100%), anode voltage fixed to 450 V, and various drift voltages: 300 V, 325 V, 350 V, 375 V, 400 V and 425 V. A compilation of these parameters can be found at the end of this chapter. The predictions of the model were compared with the GARFIELD++ results for all of the above operating conditions, which will be referred to as the "considered operating conditions". When the PICOSEC operating conditions are not explicitly stated, Ptr of 50% Ptr, anode voltage of 450 V and a drift voltage of 425 V are implied.

The model is based on the observation (see Ref. [101]) that an electron which is drifting in an homogeneous electric field and is undergoing only elastic scatterings, drifts along the field with less average velocity than an electron suffering energy losses through its interactions. In Sec. 6.3, this concept is quantified with a "time-gain per interaction". It is used to explain the different drift velocities between a photoelectron prior to ionization and of an avalanche electron. It also explains the apparent effect of the Ptr on drift velocities.

Sections 7.1 to 8.1 describe the modelling of the microscopic processes up until the mesh. At this point, the important microscopic variables are:

1. The number of pre-amplification electrons arriving on the mesh (electron multiplicity on the mesh),
2. The average of the arrival times of the individual pre-amplification electrons on the mesh (total time on the mesh).

The transfer of the pre-amplification through the mesh is modelled in Sec. 8.3.

In particular, the average avalanche velocity is a statistical outcome over several dynamical effects, including those that determine the growth of the avalanche. Section 7.1 investigates the properties of the GARFIELD++ simulated pre-amplification avalanches including the statistical distribution of the avalanche electron multiplicity before and after the mesh. The mean mesh transparency to pre-amplification electrons is observed to be constant and independent of the avalanche characteristics, for all of the considered operating conditions. This brings the implication that size of the signal is effectively determined by the "electron multiplicity on the mesh".

The simultaneous drift and growth of the pre-amplification avalanche is also modeled in Section 7.1 and the "avalanche transmission time", defined as the average of the arrival times of the pre-amplification avalanche electrons of the mesh, starting from the instant of the first ionization which initiated the avalanche, is expressed in terms of its length and its electron multiplicity. The model explains in quantitative terms the GARFIELD++ prediction that the avalanche, as a whole, moves faster than its constituent electrons.

In Sec. 7.2, by integrating properly the results of Sec. 7.1, the model quantifies the dependence of the "total time on the mesh" on the number of pre-amplification electrons.

The arrival times of the avalanche electrons on a plane are mutually correlated, due to the sharing of common parent electrons. This correlation is quantified in Sec. 8.1. Evaluating the avalanche contribution to the statistical spread of the "total time on the mesh", the model predicts that it is almost independent of the avalanche length. The longitudinal diffusion of the primary photoelectron, along its drift path prior to the first ionization, is the major factor that determines the PICOSEC timing resolution. However, due to the fact that the photoelectron drift path and the avalanche length sum up to the pre-amplification region, the timing resolution indirectly depends on the avalanche length.

Although the length of the avalanche is an important physical parameter, it is not an experimental observable. In Sec. 8.2, the statistical spread of the "total time on the mesh" is expressed as a function of the pre-amplification electron multiplicity by modelling the growth of the avalanche. The influence of the mesh on the PICOSEC timing properties is quantified in Sec. 8.3 in terms of the mesh transparency, the number of the pre-amplification electrons reaching the mesh and an extra time-spread term, due to the electrons drifting through the inhomogeneous electric field around the mesh.

Finally, the limitation of the model to describe accurately the PICOSEC timing characteristics in the case of very small electron multiplicities on the mesh are discussed in Sec. 9. There the model extension to predict the complete probability density function, which determines the timing properties of the PICOSEC signal, is presented.

6.3 Electron drift velocities and basic model assumptions

Electrons which are moving forward lose time when they are back-scattered elastically from gas molecules before the electric field or another collision brings their motion forward again, when compared to electrons that are losing energy from their interactions and are also profiting from longer mean-free paths at low energies due to a smaller scattering cross section (Ramsauer minimum). The fact that an electron gains in transmission time when it loses energy is used to explain the different drift velocities observed in the detailed simulations with GARFIELD++.

Let L be the length of a pre-amplification avalanche inside a pre-amplification region of depth D. Then, $D - L$ will be the corresponding drift length of the

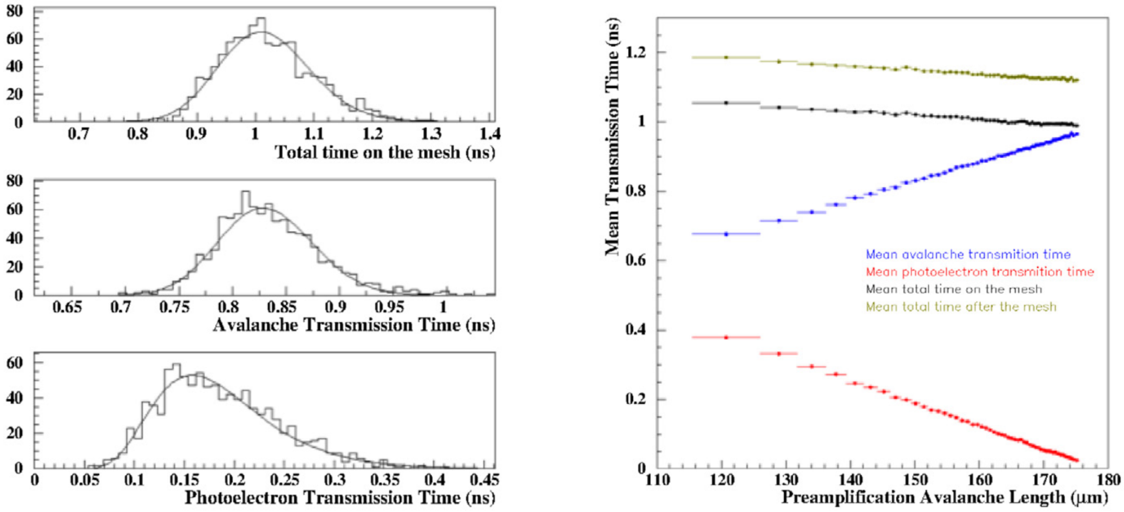

Figure 6.5: On the left, the plots show the distributions of the “total time on the mesh” (top), the “avalanche transmission time” (middle) and the “photoelectron transmission time” (bottom), in the case that the length of the simulated avalanche (L) is between 144.45 and 144.75 µm. The solid lines represent fits with the Wald distribution function. The right plot presents the mean values of the above times, as well as the mean of the “total time after the mesh”, versus the length of the respective pre-amplification avalanche. It is worth noticing that the total time after the mesh differs only by a constant time-offset from the respective total time on the mesh, at all considered avalanche lengths. Figure adapted from Ref. [16].

photoelectron before the first ionization that initiates the avalanche. Let $T_p(L)$ be the time taken from the emission of the photoelectron until the first ionization (hereafter referred to as “photoelectron transmission time” or just “photoelectron time”). Measured from the time instant of the first ionization, let $T(L)$ be the average time that the avalanche electrons take to reach the mesh (hereafter referred to as “avalanche transmission time” or just “avalanche time”). The “total-time on the mesh”, $T_{tot}(L)$ is equal to the sum of the photoelectron and avalanche transmission times, or $T_{tot}(L) = T_p(L) + T(L)$. All of these time-variables behave statistically as random variables and follow probability distributions that are well approximated by Inverse Gaussian (Wald) functions, as visible in the left plot of Fig. 6.5, using GARFIELD++ simulations. The simulations also show that the mean values of the above time distributions depend linearly on the avalanche length, as is shown in the right plot of Fig. 6.5. The mean value of the time $T_{ea}(x)$, which is the time than a single avalanche electron takes to cover a distance x along the drift field, was also found to depend linearly on x. The slopes of the above linear dependencies define the inverse of the respective drift velocities.

Hereafter, V_p stands for the “photoelectron drift velocity”, V_a is the “avalanche drift velocity” and V_{ea} denotes the “drift velocity of an avalanche electron”, assuming that all electrons in the avalanche drift with the same velocity. The above drift velocities have been estimated and are compiled in Tab. C.1, for three different Ptr (Penning transfer rate) values and using the default voltage settings, while they are presented in Tab. C.8 for only 50% Ptr, 450 V anode voltage but several drift voltage

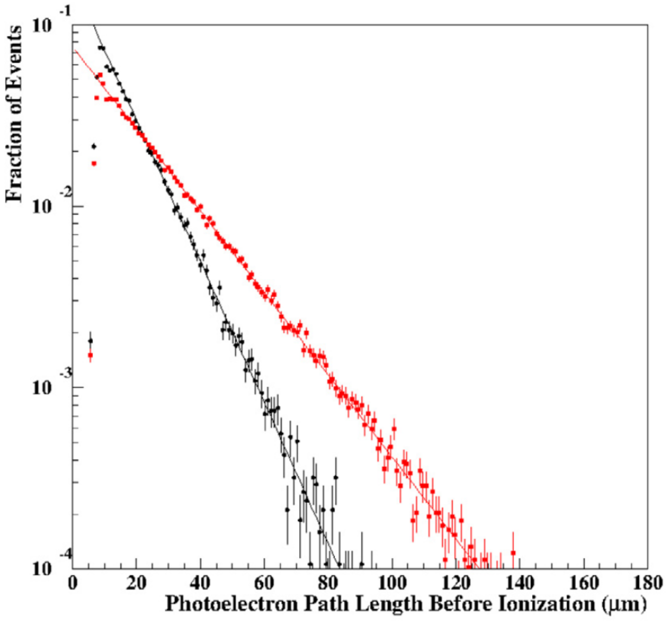

Figure 6.6: Distributions of the photoelectron drift path length, before the initiation of the avalanche, produced by GARFIELD++ simulations with 425 V drift voltage and Ptr equal to 100% (black circles) and 0% (red squares). The solid lines represent the results of exponential fits. Figure adapted from Ref. [16].

settings. The V_p, V_a and ${}_{ea}$ values are estimated with linear fits to the $T_p(L)$ versus L, $T(L)$ versus L and $T_{ea}(x)$ versus x dependencies, respectively, as resulted from the GARFIELD++ simulations. The linear fits show small non-zero constant terms which are attributed to the fact that the stochastic description of the electron drift and the avalanche development starts to be valid only after a statistical equilibrium is reached. All of the above drift velocities increase with the drift voltage. However, the photoelectron drift velocity is smaller than the drift velocity of the avalanche as whole. Furthermore, as a function of Ptr, the photoelectron drift velocity decreases, the drift velocity of the avalanche as a whole increases, while the drift velocity of a single electron in the avalanche remains constant.

The model presented here attributes the different values for the above drift velocities to time-gains per inelastic interactions. The frequency of these interactions is related to the probability per unit length that an electron provides enough energy for the production of a new, free electron in the gas (either by direct or by indirect ionization). The probability per unit length (which is the first Townsend coefficient, hereafter denoted by “a”), is estimated by an exponential fit to the distribution of the photoelectron longitudinal drift path length, up to the point of the ionization that initiates the avalanches. Example of these fits are visible in Fig. 6.6. Values of the first Townsend coefficient a, estimated with GARFIELD++ simulations for different Ptr and drift voltage settings are compiled in Tabs. C.2 and C.8.

The ionization probability per unit length depends on the Ptr value, r, as $a(r) = a(0) + r \cdot \beta$, where $\beta = a(1) - a(0)$ is the increase of the ionization probability per unit length due to the Penning transfer effect for a 100% transfer rate. The values of the first Townsend coefficients in Tab. C.2 show indeed a linear dependence on

r and a linear fit estimates: $a(0) = 0.0519 \pm 0.0003$ µm^{-1} and $\beta = 0.0366 \pm 0.0007$ µm^{-1}.

An electron that is drifting in a noble gas mixture loses energy with probability β per unit length, due to the excitation of the atoms, independently of the Ptr. When the first ionization occurs though, there is a probability of $fracr \cdot \beta a(0) + r \cdot \beta$ that the ionization was a result of the Penning transfer effect.

Considering a photoelectron, before the first ionization, that drifts for a distance Δx in a time interval of Δt, it will undergo on average $(1-r)\cdot\beta\cdot\Delta x$ inelastic collisions, exciting noble atoms and providing enough energy for the indirect ionization though without such an ionization taking place. If the photoelectron does not lose energy this way, it would drift with a velocity V_0. However, assuming that the photoelectron gains on average a time τ after each such energy loss, the following relation holds:

$$\Delta t = \frac{\Delta x}{V_0} - (1-r) \cdot \beta \cdot \tau \cdot \Delta x, \tag{6.1}$$

or

$$\frac{1}{V_{eff}(r)} = \frac{\Delta t}{\Delta x} = \frac{\Delta x}{V_0} - (1-r) \cdot \beta \cdot \tau, \tag{6.2}$$

where $V_{eff}(r)$ is the observed effective drift velocity for Ptr equal to r. It is clear that for $r = 1$, $V_0 = V_{eff}(1)$. Equation (6.2) shows that by increasing the Ptr value, the effective velocity of the photoelectron decreases, in accordance with the GARFIELD++ results. Indeed, Eq. (6.2) fits the drift velocities of Tab. C.1, resulting in an estimate of $V_0 = 142.6 \pm 0.6$ µm/ns and a value for the mean time-gain per interaction of $\tau = 17.9 \cdot 10^{-3} \pm 1.2 \cdot 10^{-3}$ ns.

After the photoelectron initiates the avalanche, its effective drift velocity is determined by the time-gain every time it loses energy, either due to the excitation of the noble atoms or due to their direct ionization. However, the energy loss effect on the drift velocity cannot be dependent on whether the excitation of the noble atom results in a subsequent ionization through the Penning transfer effect. Therefore, it can be expected that the drift velocity of an avalanche electron will not be dependent on the Ptr value. This is confirmed with the GARFIELD++ simulations, as shown in Tab. C.1.

By definition, a photoelectron doesn't undergo interactions that produces new electrons before initiating the avalanche. An avalanche electron undergoes the same number of such interactions per unit length but also ionizes directly atoms and molecules. Following the argument that more frequent energy losses results in larger drift velocities, it is expected that electrons in an avalanche drift faster than the photoelectron before the first ionization. This is true for any Ptr value and is in agreement with the GARFIELD++ simulation results reported in Tab. C.1.

The drift velocity of the avalanche as a whole is determined by a combination of the "time-gain per interaction" and the electron multiplication processes that occur during the evolution of the avalanche. These effects are described in the following Section.

Chapter 7

Modelling of the electron transmission times

7.1 Drift of the pre-amplification avalanche

Following the assumptions of the model, every time an electron in the avalanche ionizes, it gains a time ξ_I relative to an electron that undergoes only elastic scattering. Any new electron that is produced by ionization starts with low energy. At the start of the new electron's path, it suffers from a smaller delay due to elastic back-scattering compared to its parent. For this reason, the model assumes that such a newly produced electron will advance in time by ρ_I, relative to its parent. The parameters ξ_I and ρ_I should follow a joint probability distribution determined by the physical process of ionization and the respective properties of interacting molecules. As discussed in Sec. 6.3, the collective effect of time-gains ξ_I is a change in the drift velocity from V_p, which is the photoelectron drift velocity before ionization, to an effective drift velocity V_{ea}, which is the drift velocity of an ionizing electron in the avalanche. By taking V_{ea} to be the drift velocity of any electron in the avalanche, the effect of the energy loss on the drift of the parent electron is taken into account. However, the time-gain ρ_I of a newly produced electron is assumed to follow a distribution with a mean value equal to ρ and a variance equal to w^2. After that moment, this new electron will drift with a velocity V_{ea}, as any other electron in the avalanche. Notice that this way, the model approximates the time gains of the parent and daughter electrons as uncorrelated variables.

Considering an avalanche that has been developed up to a length of $x - \Delta x$, the number of electrons reaching the plane at $x - \Delta x$ will be equal to $n(x - \Delta x)$. Let Δn be the number of electrons that are produced by ionization in the next development step which is of length Δx. Without loss of generality, the production of the new electrons (visible in red in Fig. 7.1) is assumed to take place on the plane at $x - \Delta x$.

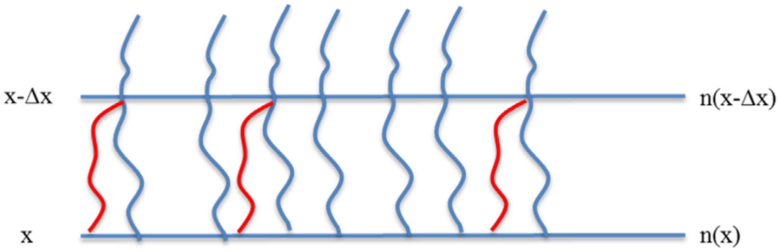

Figure 7.1: Schematic representation of the change in the electron multiplicity in two stages of the avalanche evolution, depicted as a plane at $x-\Delta x$ and a plane at x. Figure adapted from Ref. [16].

The average arrival time of the $n(x)$ electrons at plane x can be written as:

$$\begin{aligned}
T_0(x,n(x)) &= \frac{1}{n(x)}\sum_{k=1}^{n(x)} t_k(x) && (7.1)\\
&= \frac{1}{n(x)}\left[\sum_{k=1}^{n(x-\Delta x)} \left(t_k(x-\Delta x)+\Delta t_k\right) + \sum_{j=1}^{\Delta n}\left(t_j^f(x-\Delta x)+\Delta\tau_j\right)\right] && (7.2)\\
&= \frac{1}{n(x)}\left[\sum_{k=1}^{n(x-\Delta x)} t_k(x-\Delta x) + \sum_{j=1}^{\Delta n} t_j^f(x-\Delta x) + \sum_{k=1}^{n(x-\Delta x)}\Delta t_k + \sum_{j=1}^{\Delta n}\Delta\tau_j\right], && (7.3)
\end{aligned}$$

where all the times are with respect to the instant of the first ionization that initiated the avalanche. The times $t_k(x)$ and $t_k(x-\Delta x)$ refer to the time when the k-th electron reachs the planes on x and $x-\Delta x$, respectively. The time that the parent electorn of the j-th newly produced electron reaches the plane on $x-\Delta x$ is $t_j^f(x-\Delta x)$. Obviously, $t_j^f(x-\Delta x)$ is one of the $t_k(x-\Delta x)$, with $k=1,2,3,\ldots,n(x-\Delta x)$. The time spent by the k-th electron that arrived at $x-\Delta x$ to reach the plane at x is Δt_k and $\Delta\tau_j$ is the time that is spent by the j-th electron (produced at $x-\Delta x$) to arrive at the plane on x.

A newly produced electron gains a certain time, ρ_i, with $i=1,2,\ldots,\Delta n$, relative to the parent electron. Therefore, $\Delta\tau_j$ can be written as $\Delta t_j^f-\rho_j$. The set

$$\left\{t_1^f(x-\Delta x),t_2^f(x-\Delta x),t_3^f(x-\Delta x),\ldots,t_{\Delta n}^f(x-\Delta x)\right\}, \quad (7.4)$$

can be any Δn-sized subset of

$$\left\{t_1(x-\Delta x),t_2(x-\Delta x),t_3(x-\Delta x),\ldots,t_{n(x-\Delta x)}^f(x-\Delta x)\right\}. \quad (7.5)$$

For this reason, any of the $n(x-\Delta x)$ electrons has the same probability, $\Delta n/n(x-\Delta x)$, to produce a new electron. Moreover, any of the Δt_j^f, for $j=1,2,3,\ldots,\Delta n$, coincides with one of Δt_k, for $k=1,2,3,\ldots,n(x-\Delta x)$. Consequently, averaging Eq. (7.5) over all the possible configurations of Δn newly produced electrons, it follows that:

$$T_1\left(x, n(x)\right) \equiv \langle T_0\left(x, n(x)\right)\rangle_{\Delta n} \tag{7.6}$$

$$= \frac{1}{n(x-\Delta x)} \sum_{k=1}^{n(x-\Delta x)} t_k(x-\Delta x) + \frac{1}{n(x-\Delta x)} \sum_{k=1}^{n(x-\Delta x)} \Delta t_k - \frac{1}{n(x)} \sum_{j=1}^{\Delta n} \rho_j . \tag{7.7}$$

Additionally, by averaging Eq. (7.7) over the possible values of Δt_k, the mean time that the avalanche drifts in order to reach a plane on x is:

$$T\left(x, n(x)\right) \equiv \langle T_1\left(x, n(x)\right)\rangle_{\Delta t}\, , \tag{7.8}$$

or

$$T\left(x, n(x)\right) = T\left(x-\Delta x, n(x-\Delta x)\right) + \langle \Delta t_k\rangle - \frac{\Delta n}{n(x)}\rho, \tag{7.9}$$

where $T\left(x-\Delta x, n(x-\Delta x)\right) = \frac{1}{n(x-\Delta x)} \sum_{k=1}^{n(x-\Delta x)} t_k(x-\Delta x)$ and $\rho = \langle\rho\rangle$ is the mean value of the time-gain.

Finally, the definition $V_{ea} = \langle \Delta x/\Delta t_k\rangle$ can be used after taking the limit for an infinitesimal Δx and integrating up to an avalanche length L in order to obtain:

$$dT\left(x, n(x)\right) = \frac{dx}{V_{ea}} - \frac{dn}{n(x)}\rho, \tag{7.10}$$

or

$$T\left(L, N_L\right) = \frac{L}{V_{ea}} - \rho\cdot\ln\left(N_L\right) + C, \tag{7.11}$$

where N_L is the number of the avalanche electrons reaching a plane on L and C is an integration constant which is approximated also independent of L. The reason for this approximation will be discussed later in this Section. Equation (7.11) predicts that the avalanche transmission time depends on the drift length L linearly, as is the case for each individual electrons of the avalanche, but it also depends logarithmically on the electron multiplicity of the avalanche. The quantity $\Delta T(N_L) = T(L, N_L) - L/V_{ea}$ however does not depend explicitly on the length of the avalanche. For this reason, the average residual time $\langle \Delta T(N_L)\rangle_L$, over all avalanches with N_L electrons arriving on the mesh, depends only on N_L. If $G(L|N_L)dL$ is the conditional probability of an avalanche with N_L electrons arriving on the mesh to have an avalanche length in the region $[L, L+dL]$, then the average residual time is written as:

$$\langle \Delta T(N_L)\rangle_L = \int_0^\infty \left[-\rho\cdot\ln\left(N_L\right) + C\right]\cdot G\left(L|N_L\right)\mathrm{d}L, \tag{7.12}$$

or

$$\langle \Delta T(N_L)\rangle_L = -\rho\cdot\ln\left(N_L\right) + C. \tag{7.13}$$

Equation (7.13) expresses the mean deviation of the avalanche transmission time to the time that would be expected in case the drift velocity of the avalanche is equal to the drift velocity of its constituent electron. Simulations with GARFIELD++ show that this mean time-deviation is described well for all considered operating

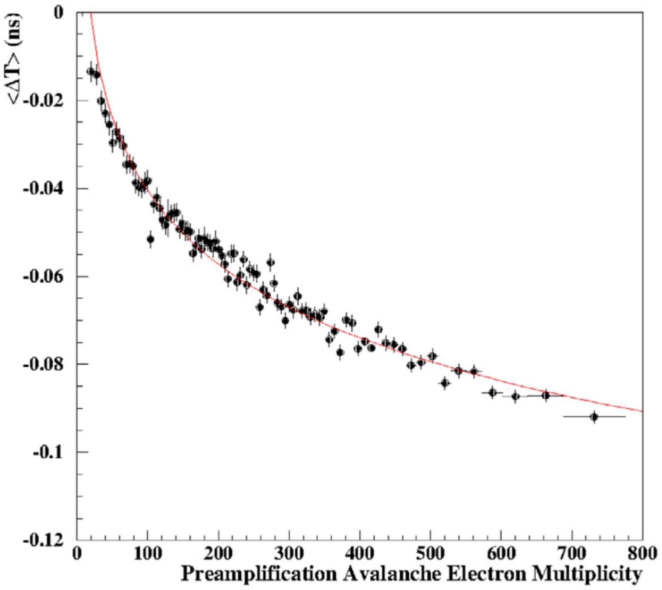

Figure 7.2: Mean deviation ($\langle \Delta T \rangle$) of the avalanche transmission time from the naively expected time (see text) versus the respective avalanche multiplicity of electrons. The points represent results of GARFIELD++ simulations, assuming 50% Ptr, anode voltage 450 V and drift voltage 375 V. The line represents a fit using Eq. (7.13). Figure adapted from Ref. [16].

parameters by the logarithmic expression of Eq. (7.13), as is visible in Fig. 7.2. The mean value of the time-gain ρ and the constant term C were estimated by fitting results of GARFIELD++ simulations with the expression of Eq. (7.13). The estimation for the above parameters are compiled in Tabs. C.3 and C.8 for various Ptr values and drift voltages, respectively.

At the beginning of their path, newly produced electrons would gain in average the same time independently of their production mechanism, *i.e.* through direct ionization or Penning transfer. Therefore, the estimated values of the parameter ρ shouldn't depend on the Ptr value. This was confirmed by fitting GARFIELD++ simulation results (see Tab. C.3). Furthermore, as the newly produced electrons accelerate and reach equilibrium faster at higher (rather than at lower) drift fields, it is to be expected that the time-gain parameter, ρ, should decrease as the drift voltage increases. This is in agreement with the estimated values presented in Tab. C.8.

Equation (7.11) was derived by treating the simultaneous drift and growth of the avalanche differentially. Consequently, the integration constant, C, depends on a minimum avalanche length, after which the growth of the mean avalanche electron multiplicity can be described with a differential treatment. This minimum avalanche length depends on the avalanche electron multiplication, which in turn depends on the Ptr and the drift voltage, as can be observed in Tabs. C.3 and C.8.

The drift velocity of the avalanche can be determined by expressing the mean avalanche transmission time, $\langle T(L) \rangle$, as a function of the avalanche length, L. This can be achieved by averaging Eq. (7.11) over all the possible values of the electron

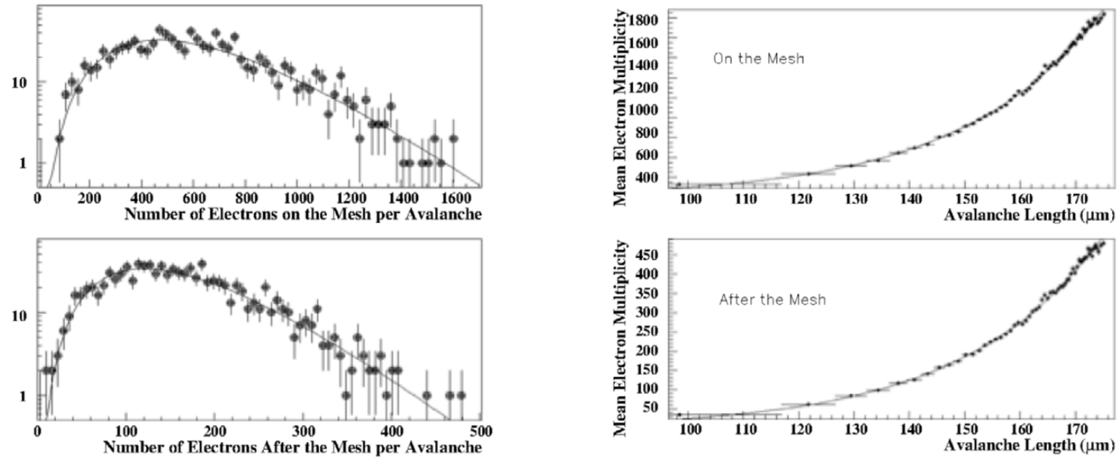

Figure 7.3: The points represent GARFIELD++ simulation results. (top-left) Distribution of the number of electrons arriving on the mesh, produced in avalanches with a length between 144.45 and 144.75 µm. The solid line represents a Gamma distribution function fitted to the simulation results. (top-right) The mean value of the avalanche electron multiplicity on the mesh versus the length of the respective avalanche. The solid line represents exponential fit to the simulation results, as described in the text. For the sake of completeness, GARFIELD++ simulation results, related to the electron multiplicity after the mesh, are also presented in the bottom-row plots. Figure adapted from Ref. [16].

multiplicity in the avalanche:

$$\langle T(L) \rangle = \int_0^\infty T\left(L, N_L\right) \cdot \Pi(N_L'|L) \mathrm{d}N_L', \tag{7.14}$$

where $\Pi(L|N_L)$ expresses the conditional probability density function of observing that N_L number of electrons are produced in an avalanche that has length L.

By using GARFIELD++ simulations, $\Pi(N_L|L)$ can be well approximated using the Gamma distribution function $P\left(N_L; q(L), \theta\right)$, where $q(L)$ is the mean value and θ is the shape parameter of the Gamma distribution. The success of this approximation can be observed in the top-left plot of Fig. 7.3.

Even though the shape parameter is found to be independent of the length of the avalanche, the mean value depends exponentially on the it, *i.e.* $q(L; a_{eff}) = 2 \cdot e^{a_{eff} L}$, as shown in in the right plot of Fig. 7.3. The exponential slope a_{eff}, which will be hereafter called “multiplication factor”, is the probability per unit length for the production of a new electron. The values of a_{eff} and θ have been estimated using the GARFIELD++ simulations with different values of Ptr and drift voltage and are compiled in Tabs. C.4, C.5 and C.8.

It can be observed that the electron multiplicity after the mesh also follows a Gamma distribution function with the same θ shape parameter as the respective distribution of the electron multiplicity on the mesh, as is demonstrated in the left-bottom plot of Fig. 7.3 (see also Tab. C.5).

The mean electron multiplicity after the mesh is also found to depend exponentially on the avalanche length, as it is shown in the bottom-right plot of Fig. 7.3.

Furthermore, the exponential slope is found to be equal to the multiplication factor, a_{eff} which implies that the transparency of the mesh does not depend on the length of the avalanche length. Moreover, it is deduced from GARFIELD++ simulations for all considered operating conditions, that the mean electron multiplicity after the mesh is consistently 25% of the number of the avalanche electrons arriving on the mesh, (see Tables C.4and C.8). Taking into account that the PICOSEC e-peak signal size was found (see Fig. 6.4) to depend linearly on the electron multiplicity after the mesh, the constant mesh transparency implies that the observed signal size is practically determined by the electron multiplicity on the mesh.

After expressing the term $\Pi(N_L|L)$ of Eq. (7.14) as a Gamma distribution function, $P\left(N_L; q(L) = 2e^{a_{eff}L}, \theta\right)$, and substituting $T(L, N_L)$ from Eq. (7.11), the average time that it takes for an avalanche to drift along a length L, for any number of electrons N_L follows:

$$\langle T(L) \rangle = \frac{L}{V_{ea}} - \rho \cdot \int_0^\infty \ln\left(N_L\right) P\left(N_L; q(L) = 2e^{a_{eff}L}, \theta\right) \mathrm{d}N_L + C. \tag{7.15}$$

By using the properties of the Gamma distribution function, Eq. (7.15) can be written as:

$$\langle T(L) \rangle = L \cdot \left[\frac{1}{V_{ea}} - \rho \cdot a_{eff}\right] + \left[-\rho \ln(2) + C + \rho \ln(\theta + 1) - \rho\psi(\theta + 1)\right], \tag{7.16}$$

where $\psi(x)$ is the digamma function.

Equation (7.16) relates linearly the mean value of the avalanche transmission time to the avalanche length. It can be easily verified by using numerical values for the model parameters (ρ, θ, a_{eff}, C from Sec. C) that the constant term,

$$\left[-\rho \ln(2) + C + \rho \ln(\theta + 1) - \rho\psi(\theta + 1)\right], \tag{7.17}$$

takes very small values for all of the considered drift voltages and Ptr values. For this reason, the effective avalanche drift velocity is determined by the inverse of the term $\left[\frac{1}{V_{ea}} - \rho \cdot a_{eff}\right]$. Both ρ and a_{eff} are positive parameters and therefore the model predicts that as the avalanche as a whole drifts with a higher velocity than any of its constituent electrons, as was also observed in the GARFIELD++ simulations. Moreover, the GARFIELD++ simulations are found to agree well with the model predictions of Eq. (7.16), visible in Fig. 7.4. The agreement holds for all of the considered operating conditions.

7.2 Transmission times vs the electron multiplicity of the avalanche

In Sec. 6.1 it was shown that the total time after the mesh determines the PICOSEC signal arrival time (SAT). Nevertheless, as will be discussed in detail in Sec 8.3, the total time after the mesh differs from the respective total time on the mesh by only a constant interval, which does not depend on electron multiplicities and drift lengths. Moreover, in Sec. 7.1 it was shown that the mean electron multiplicity

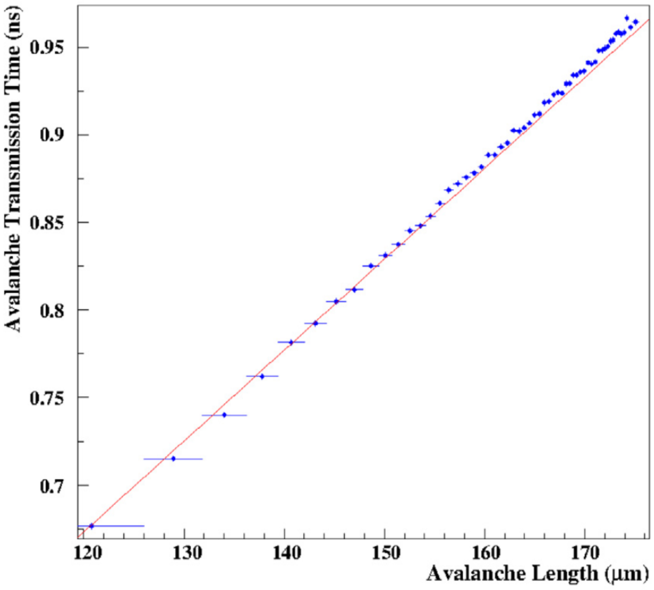

Figure 7.4: The average time needed by an avalanche, of a certain length, to arrive on the mesh (the avalanche transmission time) as a function of the length of the avalanche. The points are GARFIELD++ simulation results for 50% Ptr and a drift voltage of 425 V. The solid line represents the model prediction, expressed by Eq. (7.16). Figure adapted from Ref. [16].

after the mesh, which is the variables that determines the signal size, is a constant fraction (25%) of the electron multiplicity on the mesh. Therefore, the expression of the mean total time as a function of the electron multiplicity on the mesh, by properly integrating Eq. (7.11), should provide the microscopic description of the PICOSEC SAT dependence on the signal size (visible in Fig. 6.3).

By using Bayes' theorem, the conditional p.d.f., $G(L|N)$, that an avalanche with N electrons reaching the mesh has a length in the region $[L, L+\mathrm{d}L]$, can be written as:

$$G(L|N) = \frac{p(N|L)R(L)}{p(N)}. \tag{7.18}$$

Here, $R(L)$ is p.d.f of an avalanche to have length equal to L, $p(N|L)$ is the conditional p.d.f that an avalanche produced N electrons, if it has a length equal to L. The normalized term $p(N)$ is defined as:

$$p(N) = \int_{x_1}^{x_2} p(N|L)R(L)\mathrm{d}L, \tag{7.19}$$

and expresses the p.d.f. that an avalanche has N electrons reaching the mesh, and any length in the region $x_1 \leq L \leq x_2$. The lower integration limit x_1 is equal to 0. However, the maximum avalanche length x_2 is not equal to D because, as is observed in the simulations with GARFIELD++, the initial photoelectron needs to travel a minimum distance before it gains enough energy to initiate an avalanche. Naturally, this distance depends on the drift voltage, as shown in the values compiled in Tab. C.8.

In this model, $p(N|L)$ is being approximated by the Gamma distribution function $P\left(N_L; q(L) = 2e^{a_{eff}L}, \theta\right)$, as discussed in Sec. 7.1. The p.d.f. $R(L)$ can be expressed in terms of the first Townsend coefficient a as:

$$R(L) = R(L;a) = a\frac{exp\left[a \cdot L\right]}{exp\left[a \cdot x_2\right] - exp\left[a \cdot x_1\right]}. \tag{7.20}$$

The conditional p.d.f then becomes:

$$G(L|N) = \frac{P\left(N_L; q(L) = 2e^{a_{eff}L}, \theta\right) R(L;a)}{\int_{x_1}^{x_2} P\left(N_L; q(L) = 2e^{a_{eff}L}, \theta\right) R(L;a)\mathrm{d}L}. \tag{7.21}$$

Using Eq. (7.11), the average transmission time, $\langle T(N)\rangle = \int_{x_1}^{x_2} T(N,L)G(L|N)\mathrm{d}L$ follows:

$$\langle T(N)\rangle = \frac{\langle L(N)\rangle}{V_{ea}} - \rho \ln N + C, \tag{7.22}$$

where $\langle L(N)\rangle = \int_{x_1}^{x_2} L \cdot G(L|N)\mathrm{d}L$ is the average length of avalanches that result in N electrons on the mesh.

As in Sec. 6.3, the mean transmission time of the photoelectron before it ionizes depends on its drift path $D - L$:

$$T_p(L) = \frac{D - L}{V_p} + d_{off}, \tag{7.23}$$

where the d_{off} constant term comes from the fact that the drift velocity is a statistical quantity which characterizes the drift of an electron only after it has undergone enough scattering to be described statistically. The mean transmission time of the photoelectron from its emission until the first ionization that creates an avalanche with N electrons on the mesh is:

$$\left\langle T_p(N)\right\rangle = \int_{x_1}^{x_2} T_p(L)G(L|N)\mathrm{d}L, \tag{7.24}$$

or

$$\left\langle T_p(N)\right\rangle = \frac{D - \langle L(N)\rangle}{V_p} + d_{off}. \tag{7.25}$$

The total time taken for all the electron to reach the mesh, $\langle T_{tot}(N)\rangle$, will be the sum of the two terms given in Eqs. (7.22) and (7.25):

$$\langle T_{tot}(N)\rangle = \left\langle T_p(N)\right\rangle + \langle T(N)\rangle, \tag{7.26}$$

or

$$\langle T_{tot}(N)\rangle = \langle L(N)\rangle \left[\frac{1}{V_{ea}} - \frac{1}{V_p}\right] - \rho \ln N + \left[\frac{D}{V_p} + C + d_{off}\right]. \tag{7.27}$$

The third term in the right hand side of Eq. (7.27) represents the total time on the mesh in absence of any “time-gain” caused by the interactions. In such a case the SAT should be constant ($\approx D/V_p$), determined only by the photoelectron drift velocity (V_p) and should not depend on the signal size. However, due to time-gains because of inelastic interactions, the avalanche electrons drift faster than the

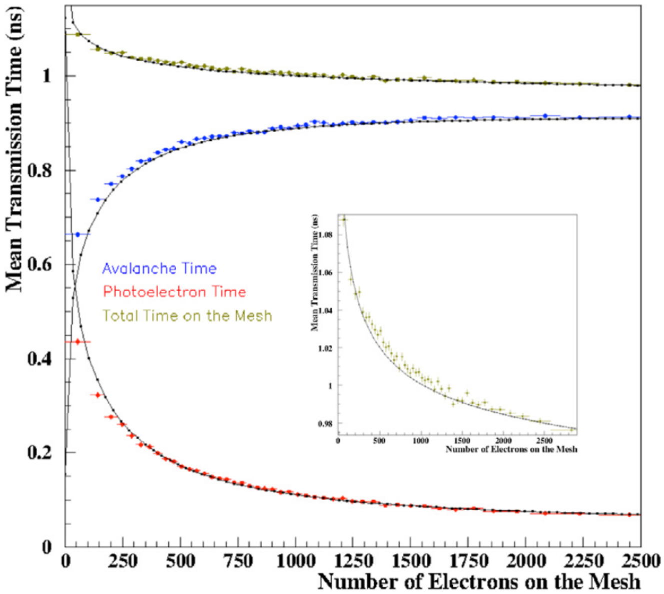

Figure 7.5: The points represent GARFIELD++ simulation results related to the mean transmission times versus the respective multiplicity of the avalanche electrons arriving on the mesh, for 50% Ptr; 425 V and 450 V drift and anode voltages respectively: (red) the transmission time of the photoelectron before the first ionization, (blue) the transmission time of the avalanche from its beginning until the mesh and (golden) the transmission time of the whole process, from the photoelectron emission until the avalanche reaches the mesh. The solid lines represent the predictions of Eqs. (7.22), (7.25), (7.27), respectively. The inset plot details the dependence of the total time on the mesh on the number of electrons arriving on the mesh. Figure adapted from Ref. [16].

photoelectron. Therefore, the first term corresponds to the total time gain by a collection of electrons drifting with V_{ea} relative to a photoelectron drifting the same distance. Finally, the second term represents an extra time gain, since each newly produced electron in the avalanche gains on average a time ρ relative to its parent. Considering that the average avalanche length is a positive and increasing function of N, both of the above time gain terms increase in absolute value as N increases. Equivalently, Eq. (7.27) predicts that, due to the time gain concepts employed by our model, large size PICOSEC signals should arrive earlier than smaller pulses, which is in accordance with both the experimental observations and the GARFIELD++ simulation results.

The model predicts, as shown in Fig. 7.5, that the photoelectron (Eq. (7.25)), the avalanche (Eq. (7.22)), and the total (Eq. (7.27)) transmission times and their dependence on the electron multiplicity on the mesh are agreeing with the GARFIELD++ simulation results. Furthermore, using the appropriate values to the model parameters, *e.g.* from Tab. C.8, the model can successfully reproduce the respective GARFIELD++ results for all of the considered operating conditions of PICOSEC.

Chapter 8

Modelling of the timing resolution

8.1 Timing resolution versus the length of the avalanche

As it was shown in Fig. 6.4, the timing resolution of the PICOSEC signal is determined by the spread of the total-time after the mesh. However, the processes occurring in the pre-amplification region influence the statistical SAT fluctuations in a much stronger way than the passage of the pre-amplification electrons through the mesh, as discussed in Sec.8.3. This section focuses on describing stochastically the spread of the total-time on the mesh as a function of the avalanche length. The longitudinal diffusion of the primary photoelectron and the spread of the avalanche transmission time are the sources of this spread. The latter emerges as the combination of:

1. The individual avalanche electrons diffusion,
2. the electron multiplicity increase as the avalanche grows and
3. the statistical correlation between the drift times of the individual electrons.

It should be noted that the avalanche length (L or its residual $D - L$) is the natural parameter to express the photoelectron diffusion, as well as the avalanche growth and the correlation between its electrons.

In GARFIELD++ simulations the variance of the photoelectron transmission time $V\left[T_p(L)\right]$, and the variance of the drift time of an avalanche electron $V\left[T_{ea}(x)\right]$ depend linearly on the respective drift lengths:

$$V\left[T_p(L)\right] = (D - L) \cdot \sigma_p^2 + \Phi, \tag{8.1}$$

and

$$V\left[T_{ea}(L)\right] = \sigma_0^2 \cdot x + \phi. \tag{8.2}$$

The slopes (σ_p^2, σ_0^2) and the constant terms (Φ, ϕ) in the above relations are evaluated with linear fits to the GARFIELD++ simulation results. In which case simulation results refer to the variances of the respective time distributions, estimated with fits to Wald distributions, as discussed in Sec. 6.3 (see Fig. 6.5). Estimated values of these parameters, for all of the considered PICOSEC operating conditions, are compiled in Tabs. C.6-C.8.

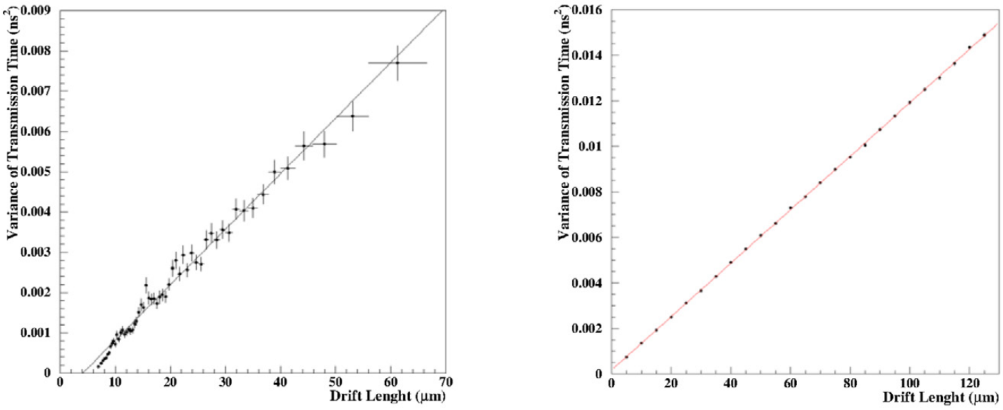

Figure 8.1: The points represent GARFIELD++ simulation results. (left) The variance of the photoelectron transmission time at the point of the first ionization versus the respective drift length. (right) The variance of the time taken by an avalanche electron to drift a certain length versus the respective length. The solid curves represent linear fits to the points. Figure adapted from Ref. [16].

Across all estimations, the variable $\boldsymbol{\Phi}$ is found to take negative values. This is due to the fact that the photoelectron motion at its initial part has not yet reached statistical equilibrium, as can be seen in the left plot of Fig. 8.1. On the other hand, only positive values were found for ϕ, as it is shown in the right plot of Fig. 8.1. A positive ϕ value implies that an avalanche electron inherits some time spread before it starts drifting which is, however, consistent with the phenomenological model advocated in this study. Indeed, all the terms expressing time-gains in this model behave as random variables, with variances contributing to the variance of the respective drift times. For this reason, the constant term ϕ corresponds to the variance of the time that is gained by the first avalanche electron when it initiates the avalanche. Nevertheless, the contribution of the constant term, ϕ, in Eq. (8.2) is much smaller than the part which is proportional to the drift length and it will be ignored in the following. It should be noted that according to GARFIELD++ simulations, across all voltage settings considered in this study, the vast majority of the avalanches have lengths greater than 100 μm, even in the case of 0% Ptr. For a 100 μm long avalanche, the time variance of an avalanche electron that arrives on the mesh, is more than 70 times larger than the contribution of the constant term ϕ.

For an avalanche of length L that is initiated by a photoelectron after drifting a length $D - L$, the avalanche time $T(L)$ and the photoelectron time $T_p(L)$ are statistically uncorrelated. Consequently, the total time on the mesh $T_{tot}(L)$ and its variance $V\left[T_{tot}(L)\right]$ are written as:

$$T_{tot}(L) = T_p(L) + T(L), \tag{8.3}$$

$$V\left[T_{tot}(L)\right] = V\left[T_p(L)\right] + V\left[T(L)\right], \tag{8.4}$$

where $V\left[T_p(L)\right]$ can be calculated from Eq. (8.1).

The term $V\left[T(L)\right]$ will be evaluated by considering the evolution of the avalanche between two planes, one on $x-\Delta x$ and one on x, as presented in Sec. 6.3 and illustrated in Fig. 7.1. The average of the electron arrival times at a plane on x, expressed by Eq. (7.5), is factorized as the sum of five terms (A, B, C, D and E), as follows:

$$T_0\left(x, n(x)\right) =$$
$$= \frac{1}{n(x)}\left[\underbrace{\sum_{k=1}^{n(x-\Delta x)} t_k(x-\Delta x)}_{A} + \underbrace{\sum_{j=1}^{\Delta n} t_j^f(x-\Delta x)}_{B} + \underbrace{\sum_{k=1}^{n(x-\Delta x)} \Delta t_k}_{C} + \underbrace{\sum_{j=1}^{\Delta n} \Delta t_j^f}_{D} + \underbrace{\sum_{j=1}^{\Delta n} \rho_j}_{E}\right] \quad (8.5)$$

As in Sec. 6.3, the model treats the times Δt_k (with $k = 1, 2, 3, ..., n(x-\Delta x)$) as mutually uncorrelated variables as well as independent of the history of pre-existing electrons. It should be recalled that the time $\Delta\tau$, taken by the newly produced electrons to drift between the planes on $x-\Delta x$ and on x, is the difference between the two random variables: $\Delta\tau_j = \Delta t_j^f - \rho_j$, with $j = 1, 2, \ldots, \Delta n$. The first variable ($\Delta t_j^f$) has the same statistical properties as the times Δt_k of the pre-existing electrons. The time-gains acquired by the new electrons, ρ_j, are mutually uncorrelated and are also uncorrelated with any of the Δt_k times.

As is done in Sec. 6.3, the model assigns a probability $\Delta n/n(x-\Delta x)$ to each of the pre-existing electrons at the plane on $x-\Delta x$ to ionize and produce a new electron. With these assumptions, the terms B and D of Eq. (8.5) become:

$$B_1 = \left\langle \sum_{j=1}^{\Delta n} t_j^f\left(x-\Delta x\right) \right\rangle_{\Delta n} = \frac{\Delta n}{n(x-\Delta x)} \sum_{k=1}^{n(x-\Delta x)} t_k(x-\Delta x), \quad (8.6)$$

and

$$D_1 = \left\langle \sum_{j=1}^{\Delta n} \Delta t_j^f \right\rangle_{\Delta n} = \frac{\Delta n}{n(x-\Delta x)} \sum_{k=1}^{n(x-\Delta x)} \Delta t_k. \quad (8.7)$$

By considering the relations mentioned previously between individual drift times and time-gains, the covariances $cov\left[A, B_1\right]$ and $cov\left[A, B_1\right]$ have non-zero contributions to the total time spread. All other term combinations have covariances equal to zero. Therefore, the variance of $T_1\left(x, n(x-\Delta x)\right) = \langle T_0(x, n(x))\rangle_{\Delta n}$ is written:

$$V\left[T_1\left(x, n(x-\Delta x)\right)\right] = \frac{1}{n^2(x)}\left(V[A] + V[B] + V[C] + V[D] + V[E] + \right.$$
$$\left. + 2cov\left[A, B_1\right] + 2cov\left[A, D_1\right]\right), \quad (8.8)$$

where

$$\begin{aligned} V\left[A\right] = &\sum_{k=1}^{n(x-\Delta x)} \underbrace{\left(E\left[t_k^2(x-\Delta x)\right] - E^2\left[t_k(x-\Delta x)\right]\right)}_{\sigma_k^2(x-\Delta x)} \\ &+ \sum_{k=1}^{n(x-\Delta x)} \sum_{l=1,k\neq l}^{n(x-\Delta x)} \underbrace{\left(E\left[t_k(x-\Delta x)t_l(x-\Delta x)\right] - E\left[t_k(x-\Delta x)\right] E\left[t_l(x-\Delta x)\right]\right)}_{c_{kl}}, \end{aligned} \tag{8.9}$$

or

$$V\left[A\right] = \sum_{k=1}^{n(x-\Delta x)} \sigma_k^2(x-\Delta x) + \sum_{k=1}^{n(x-\Delta x)} \sum_{l=1,k\neq l}^{n(x-\Delta x)} c_{kl}. \tag{8.10}$$

The variance of B_1 is:

$$V\left[B_1\right] = \left(\frac{\Delta n}{n(x-\Delta x)}\right)^2 \cdot \left(\sum_{k=1}^{n(x-\Delta x)} \sigma_k^2(x-\Delta x) + \sum_{k=1}^{n(x-\Delta x)} \sum_{l=1,k\neq l}^{n(x-\Delta x)} c_{kl}\right), \tag{8.11}$$

or

$$V\left[B_1\right] = \left(\frac{\Delta n}{n(x-\Delta x)}\right)^2 \cdot V\left[A\right], \tag{8.12}$$

The variance of C is:

$$V\left[C\right] = \sum_{k=1}^{n(x-\Delta x)} \underbrace{\left(E\left[(\Delta t_k)^2\right] - E^2\left[\Delta t_k\right]\right)}_{\delta_k^2} = \sum_{k=1}^{n(x-\Delta x)} \delta_k^2. \tag{8.13}$$

The variance of D_1 is:

$$V\left[D_1\right] = \left(\frac{\Delta n}{n(x-\Delta x)}\right)^2 \sum_{k=1}^{n(x-\Delta x)} \delta_k^2 = \left(\frac{\Delta n}{n(x-\Delta x)}\right)^2 V\left[C\right]. \tag{8.14}$$

The variance of E is:

$$V\left[E\right] = \sum_{j=1}^{\Delta n} \underbrace{\left(E\left[\left(\rho_j\right)^2\right] - E^2\left[\rho_j\right]\right)}_{d_j^2} = \sum_{j=1}^{\Delta n} d_j^2. \tag{8.15}$$

Similarly, the covariance terms can be written as:

$$cov\left[A, B_1\right] = \frac{\Delta n}{n(x-\Delta x)} V\left[A\right] \tag{8.16}$$

$$cov\left[C, D_1\right] = \frac{\Delta n}{n(x-\Delta x)} V\left[C\right] \tag{8.17}$$

By substituting Eqs. 8.10 through (8.17) in Eq. (8.8), the variance takes the expression:

$$V\left[T_1\left(x, n(x)\right)\right] = \frac{1}{n^2\left(x-\Delta x\right)}\left(\sum_{k=1}^{n(x-\Delta x)} \sigma_k^2(x-\Delta x) + \sum_{k=1}^{n(x-\Delta x)} \sum_{l=1,k\neq l}^{n(x-\Delta x)} c_{kl}\right) + \frac{1}{n^2(x-\Delta x)} \sum_{k=1}^{n(x-\Delta x)} \delta_k^2 + \frac{1}{n^2(x)} \sum_{j=1}^{\Delta n} d_j^2. \quad (8.18)$$

After taking into account the fact that all of Δt_k will follow the same distribution with variance δ^2 proportional to the drift distance Δx, *i.e* $\delta^2 - \sigma_0^2 \cdot \Delta x$, as well as that the time-gains ρ_j, with $j = 1, 2, 3, \ldots, \Delta n$, follow a distribution whose variance is equal to w^2, the last two terms of Eq. (8.18) can be written as:

$$\frac{1}{n^2(x-\Delta x)} \sum_{k=1}^{n(x-\Delta x)} \delta_k^2 = \frac{\sigma_0^2 \cdot \Delta x}{n(x-\Delta x)}, \quad (8.19)$$

and

$$\frac{1}{n^2(x)} \sum_{j=1}^{\Delta n} d_j^2 = \frac{\Delta n}{n^2(x)} w^2 \quad (8.20)$$

Furthermore, the total avalanche time variance on the plane $x - \Delta x$ is equal to:

$$V\left[T_1\left(x-\Delta x, n(x-\Delta x)\right)\right] = \frac{1}{n^2(x-\Delta x)}\left(\sum_{k=1}^{n(x-\Delta x)} \sigma_k^2(x-\Delta x) + \sum_{k=1}^{n(x-\Delta x)} \sum_{l=1,l\neq k}^{n(x-\Delta x)} c_{kl}\right) \quad (8.21)$$

By substituting Eqs.(8.19), (8.20), (8.21), as well as the approximation

$$n^2(x) \simeq n(x) \cdot n(x-\Delta x), \quad (8.22)$$

into Eq. (8.18), one gets:

$$V\left[T_1\left(x, n(x)\right)\right] - V\left[T_1\left(x-\Delta x, n(x-\Delta x)\right)\right] \simeq \frac{\sigma_0^2 \cdot \Delta x}{n(x-\Delta x)} - w^2\left(\frac{1}{n(x)} - \frac{1}{n(x-\Delta x)}\right), \quad (8.23)$$

that expresses the increase in the variance of the avalanche time as the avalanche grows from $x - \Delta x$ to x, given that $n(x-\Delta x)$ electrons arrived on the first plane while Δn more electrons arrived on the second.

The variance of all avalanches evolving up to length x can be obtained by averaged Eq. (8.23) over all possible values of Δn and $n(x-\Delta x)$. In particular:

$$\frac{\left\langle V\left[T_1\left(x, n(x)\right)\right] - V\left[T_1\left(x-\Delta x, n(x-\Delta x)\right)\right]\right\rangle_{n,\Delta n}}{\Delta x} = \\ = \sigma_0^2 \left\langle \frac{1}{n(x-\Delta x)} \right\rangle_{n,\Delta n} - \frac{w^2}{\Delta x}\left\langle \frac{1}{n(x)} - \frac{1}{n(x-\Delta x)} \right\rangle_{n,\Delta n}. \quad (8.24)$$

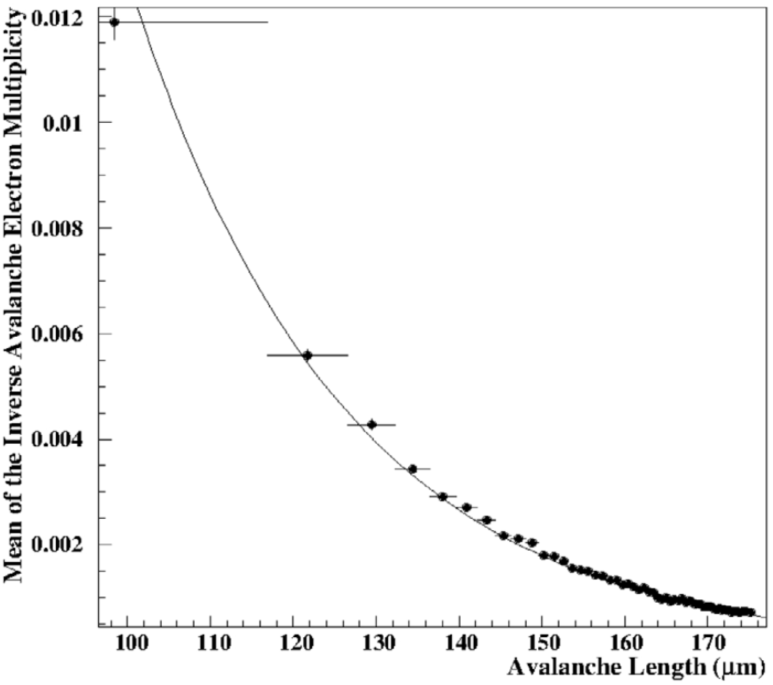

Figure 8.2: The points represent the mean value of the inverse avalanche-electron multiplicity for simulated avalanches of a certain length. The GARFIELD++ simulation package has been used, assuming 50% Ptr, a drift voltage of 425 V and anode voltage of 450 V. The solid curve represents graphically Eq. (8.25) with the proper values for the physical parameters, from Tab. C.8. Figure adapted from Ref. [16].

By assuming again that $n(x)$ follow the Gamma distribution function, the mean value of the inverse multiplicity, $1/n(x)$, is given by:

$$\left\langle \frac{1}{n(x)} \right\rangle_n = \frac{\theta+1}{2\theta} exp\left[-a_{eff}\cdot x\right], \tag{8.25}$$

which is in perfect agreement with the results from GARFIELD++ simulations, visible in Fig. 8.2

By substituting Eq. (8.25) into Eq. (8.24), differential increase of the variance of the avalanche transmission time is written as:

$$\begin{aligned}\frac{\langle V\left[T_1(x)\right] - V\left[T_1(x-\Delta x)\right]\rangle}{\Delta x} &= \\ &= \sigma_0^2 \frac{\theta+1}{2\theta} exp\left[-a_{eff}\cdot x\right] exp\left[a_{eff}\cdot \Delta x\right] \\ &\quad - \frac{w^2}{\Delta x}\frac{\theta+1}{2\theta} exp\left[-a_{eff}\cdot x\right]\cdot\left(1 - exp\left[a_{eff}\cdot\Delta x\right]\right).\end{aligned} \tag{8.26}$$

The right hand side of Eq. (8.26) can be expanded with respect to Δx, keeping only up to first order terms and letting Δx go to zero. The differential equation then that expresses the evolution of the variance of the avalanche transmission time is:

$$\frac{\mathrm{d}\left[T(x)\right]}{\mathrm{d}x} = \frac{\theta+1}{2\theta}\exp\left[-a_{eff}\cdot x\right]\cdot\left(\sigma_0^2 + w^2 a_{eff}\right). \tag{8.27}$$

By integrating up to an avalanche length of L, the variance of the avalanche transmission time for length L is found:

$$V\left[T(L)\right] = \frac{\theta+1}{2\theta}\left(\sigma_0^2 + w^2 a_{eff}\right)\frac{1-\exp\left[-a_{eff}\cdot L\right]}{a_{eff}}. \tag{8.28}$$

Consequently, the variance of the total time on the mesh according to Eq. (8.4) is written as:

$$V\left[T_{tot}(L)\right] = V\left[T(L)\right] + V\left[T_p(L)\right], \tag{8.29}$$

or

$$V\left[T_{tot}(L)\right] = \frac{\theta+1}{2\theta}\left(\sigma_0^2 + w^2 a_{eff}\right)\frac{1-\exp\left[-a_{eff}\cdot L\right]}{a_{eff}} + (D-L)\cdot\sigma_p^2 + \Phi. \tag{8.30}$$

This expression is expected to describe the GARFIELD++ simulations for photoelectrons that have drift lengths long enough in order to guarantee statistical equilibrium (typically $(D-L) > 10$ μm).

The time spreads that the model predicts and are expressed by Eqs. (8.1), (8.28) and (8.30), are presented in Fig. 8.3 and shown to be in excellent agreement with the simulation results. The same good agreement is found for all values of Ptr and drift voltages considered in this work.

Even though the mean value of the time-gain parameter ρ has been evaluated from GARFIELD++ simulations (see Fig. 7.2), there is no similar and straightforward way to estimate the value of its variance ($w^2 = V\left[\rho\right]$). As an alternative, the double lines in Fig. 8.3 represent the predictions of Eqs. (8.28) and (8.30) for $w = 0$ and $w = \rho$, that is either assuming that the time-gain per newly produced electron is a constant or that it follows a very broad physical distribution that has an RMS equal to 100% of its mean value. Clearly, even by imposing a 100% spread on ρ, only a small change is induced to the model predictions.

As indicated in Fig. 8.3, signals that are produced by long avalanches achieve good resolution because they are associated with photoelectrons that drift for short distances, and therefore suffer small longitudinal diffusion. The model predicts that the contribution of short avalanches to the timing resolution depends on their length. However, as the avalanche length grows, the variance of the avalanche time reaches a plateau. At the operational parameter settings considered in this study, the vast majority of the GARFIELD++ simulated avalanches in the PICOSEC pre-amplification region are too long to reveal the increase of the avalanche time spread. In order to check the model prediction in detail, special GARFIELD++ simulations of shorter pre-amplification avalanches were performed. Two groups of such simulation results are also shown, as bright green points in the same Figure. This demonstrates the success of the model in predicting the avalanche time spread at all avalanche lengths. Nevertheless, the predicted spread of the photoelectron time seems to deviate from the GARFIELD++ points at very large avalanche lengths (or equivalently short photoelectron drift paths), due to the inadequacy of Eq. (8.1) to describe the photoelectron longitudinal diffusion at the beginning of its drift path, *i.e.* before it has reached statistical equilibrium through multiple scatterings with the gas. As mentioned, this small deviation appears only in the region of very large avalanche lengths, where the timing resolution is practically determined solely by the avalanche time spread.

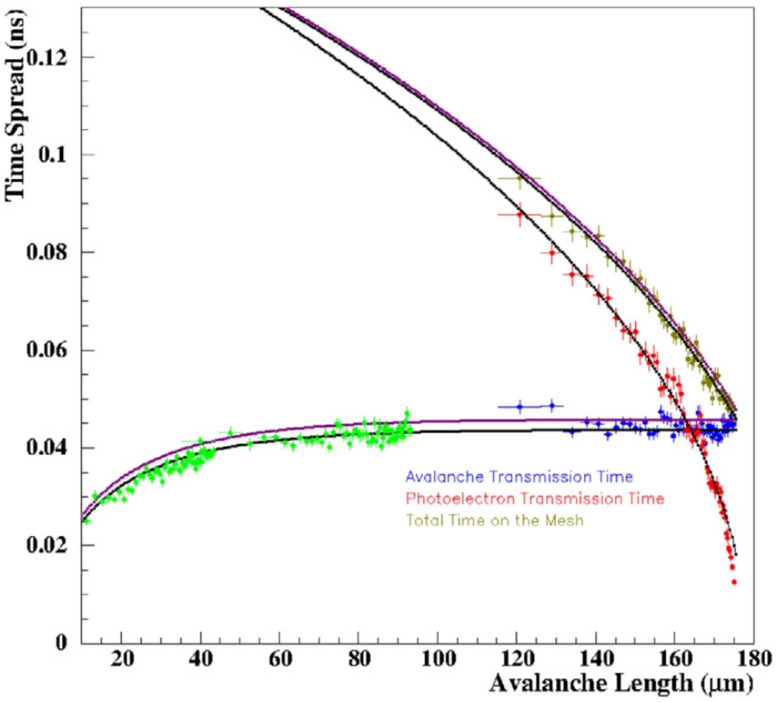

Figure 8.3: The points show results of GARFIELD++ simulations assuming 50% Ptr, 425 V drift and 450 V anode voltages, versus the respective length of the avalanche. The golden points depict the spread of the total time on the mesh. The red and blue (plus bright green) points represent spreads of the primary photoelectron time and of the avalanche time, respectively. The corresponding model predictions, for the two w values discussed in the text, are presented as solid lines. Figure adapted from Ref. [16].

8.2 Timing resolution versus electron multiplicity on the mesh

The results of GARFIELD++ simulations have shown that the electron multiplicity on the mesh determines the PICOSEC signal size (see Sec. 6.1and 7.1). In order to get insight on the dependence of the timing resolution on the signal amplitude, the effects of the photoelectron drift and the pre-amplification avalanche development are written as functions of the electron multiplicity on the mesh. The effect of the passage of avalanche electrons through the mesh on the timing resolution, which is much weaker, is discussed in Sec. 8.3.

The variance of the avalanche transmission time can be evaluated as a function of the electron multiplicity on the mesh, N_L, by averaging Eq. (8.23) over $n(x)$ under the condition that at $x = L$, the observed number of electrons reaching the mesh is equal to $n(L) = N_L$. The conditional p.d.f., $\Pi\left(n(x)|n(L) = N_L\right)$, that an avalanche has $n(x)$ electrons at a distance x from the point of first ionization, and N_L electrons at a distance L (with $L > x$) is given by:

$$\Pi\left(n(x)|n(L) = N_L\right) = \frac{\Pi\left(n(L) = N_L|n(x)\right) \cdot \Pi\left(n(x)\right)}{\Pi\left(n(L) = N_L\right)}. \tag{8.31}$$

The term $\Pi\left(n(x)\right)$ denotes the p.d.f. that an avalanche consists of $n(x)$ at a plane x. This p.d.f. is approximated by the Gamma distribution function (see Fig. 7.3), *i.e.*

$$\Pi\left(n(x)\right) = P\left(n(x); q = 2e^{a_{eff}\cdot x}, \theta\right). \tag{8.32}$$

The other term in the numerator of Eq. 8.31, $\Pi\left(n(L) = N_L | n(x)\right)$, is the conditional p.d.f. that an avalanche has N_L electrons at a plane on L, given that it has $n(x)$ electrons at a plane on x. By assuming that each of the $n(x)$ electrons will initiate an avalanche, independent of the other initiated avalanches, there will be $n(x)$ statistically identical and independent avalanches reaching the plane on L, each with a length of $L - x$. In that case, $\Pi\left(n(L) = N_L | n(x)\right)$ can be approximated by the convolution of $n(x)$ Gamma distributions. This results in the expression:

$$\Pi\left(n(L) = N_L | n(x)\right) = \overbrace{P_1(n) \otimes P_1(n) \otimes \cdots \otimes P_1(n)}^{n(x)\ \text{times}}, \tag{8.33}$$

or

$$\Pi\left(n(L) = N_L | n(x)\right) =$$
$$\frac{1}{q(L-x)} \frac{(\theta+1)^{n(x)(\theta+1)}}{\Gamma\left(n(x)\cdot(\theta+1)\right)} \cdot \left(\frac{N_L}{q(L-x)}\right)^{n(x)(\theta+1)-1} \cdot \exp\left[-\left(\theta+1\right)\frac{N_L}{q\left(L-x\right)}\right], \tag{8.34}$$

where $q(L-x)$ is the mean number of electrons of a single avalanche with length $L - x$. The mean value of the above p.d.f. is equal to $n(x) \cdot q(L-x)$ while its variance is equal to $n(x) \cdot \frac{q^2(L-x)}{\theta+1}$. One drawback in expressing $\Pi\left(n(L) = N_L | n(x)\right)$ with Eq. (8.34) is that $n(x)$ should be treated as an integer number while N_L is a real number. Alternatively, the Central Limit Theorem can invoked and a Gaussian distribution can be used in the case that $n(x)$ is a large number:

$$\Pi\left(n(L) = N_L | n(x)\right) = \frac{1}{\sqrt{2\pi \cdot n(x) \cdot \sigma^2(L-x)}} \exp\left[-\frac{\left(n(x)\cdot q(L-x) - N_L\right)^2}{2 \cdot n(x) \cdot \sigma^2(L-x)}\right], \tag{8.35}$$

where $\sigma^2(L-x)$ is the variance in the number of electrons of a single avalanche of length $L - x$. The p.d.f. that is expressed by Eq. (8.35) is strictly valid only in the case that $n(x)$ is an integer parameter. However, in order to simplify the numerical calculations, $n(x)$ is treated as if it is a continuous variable.

The normalizing term that appears in the denominator of Eq. (8.31) is defined as:

$$\Pi\left(n(L) = N_L\right) = \sum_{n=0}^{\infty} \Pi\left(n(L) = N_L | n\right) \cdot \Pi\left(n\right), \tag{8.36}$$

or

$$\Pi\left(n(L) = N_L\right) \simeq \int_0^{\infty} \Pi\left(n(L) = N_L | n(x)\right) \cdot \Pi\left(n(x)\right) \mathrm{d}n(x). \tag{8.37}$$

Having determined the functional form $\Pi\left(n(x) | n(L) = N_L\right)$, it is straightforward to properly average Eq. (8.23) by imposing the condition that the electron multiplicity at an avalanche length L is equal to N_L. By using the following definitions:

$$\langle V(x) \rangle_{n(L)=N_L} \equiv \int_0^{\infty} V\left[T_1\left(x, n(x)\right)\right] \cdot P\left(n(x) | n(L) = N_L\right) \mathrm{d}n(x), \tag{8.38}$$

$$\begin{aligned}&\langle V(x-\Delta x)\rangle_{n(L)=N_L} \equiv \\ &\qquad \int_0^{\infty} V\left[T_1\left(x-\Delta x, n(x-\Delta x)\right)\right] \cdot P\left(n(x-\Delta x) | n(L)=N_L\right) \mathrm{d}n(x-\Delta x),\end{aligned} \tag{8.39}$$

$$\left\langle \frac{1}{n(x)} \right\rangle_{n(L)=N_L} \equiv \int_0^{\infty} \frac{1}{n(x)} \cdot P\left(n(x) | n(L)=N_L\right) \mathrm{d}n(x), \tag{8.40}$$

along with Eq. (8.23), the average increase of the avalanche transmission time variance between planes $x-\Delta x$ and x, and under the condition that the electron multiplicity was equal to N_L at $x=L$, is expressed as:

$$\begin{aligned}&\langle V(x)\rangle_{n(L)=N_L} - \langle V(x-\Delta x)\rangle_{n(L)=N_L} = \\ &\qquad \sigma_0^2 \cdot \Delta x \left\langle \frac{1}{n(x-\Delta x)} \right\rangle_{n(L)=N_L} - w^2 \left(\left\langle \frac{1}{n(x)} \right\rangle_{n(L)=N_L} - \left\langle \frac{1}{n(x)} \right\rangle_{n(L)=N_L} \right).\end{aligned} \tag{8.41}$$

It should be noticed that the imposed condition, that $n(L)=N_L$, forces the averages, $\langle 1/n(x)\rangle_{n(L)=N_L}$ and $\langle V(x)\rangle_{n(L)=N_L}$, to become functions also of N_L. Hereafter, terms symbolized as $\langle \bullet(x)\rangle_{n(L)=N_L}$ have to be considered as functions of both x and N_L. A recursive summation of Eq. (8.41), starting from $x=L$ and stopping at $x=0$ in steps of Δx results in:

$$\begin{aligned}&\langle V(x)\rangle_{n(L)=N_L} - \langle V(0)\rangle_{n(L)=N_L} = \\ &\sigma_0^2 \cdot \Delta x \sum_{i=1}^{L/\Delta x} \left\langle \frac{1}{n(L-i\cdot\Delta x)} \right\rangle_{n(L)=N_L} - w^2 \left(\left\langle \frac{1}{n(L)} \right\rangle_{n(L)=N_L} - \left\langle \frac{1}{n(0)} \right\rangle_{n(L)=N_L} \right).\end{aligned} \tag{8.42}$$

By taking the limit as $\Delta x \to 0$, and using that:

$$\langle V(0)\rangle_{n(L)=N_L} = 0, \tag{8.43}$$

$$\left\langle \frac{1}{n(0)} \right\rangle_{n(L)=N_L} = \frac{1}{2}, \tag{8.44}$$

$$\left\langle \frac{1}{n(L)} \right\rangle_{n(L)=N_L} = \frac{1}{N_L}, \tag{8.45}$$

then Eq. (8.42) is written as:

$$\langle V(L)\rangle_{n(L)=N_L} = \sigma_0^2 \cdot \int_0^{L} \left\langle \frac{1}{n(x)} \right\rangle_{n(L)=N_L} \mathrm{d}x - w^2 \left(\frac{1}{N_L} - \frac{1}{2} \right), \tag{8.46}$$

expressing this way the variance of the avalanche time, when the electron multiplicity on the mesh is equal to N_L and given that the length of the avalanche is equal to L. The first term in Eq. (8.46) is a double integral which can be easily evaluated with numerical integration, for any L and N_L. It can be evaluated using Eq. (8.40) with the definition expressed by either Eq. (8.35) or Eq. (8.37), and setting appropriate values to the relevant model parameters (σ_0, θ, a_{eff}) from Tab. C.8.

To express the variance of the avalanche transmission time as a function of only the electron multiplicity on the mesh, N, Eq. (8.46) should be integrated considering the contribution of any avalanche, of any length L, which produces N electrons arriving on the mesh ($N = N_L$). Each such contribution should be weighted by the likelihood that such an avalanche is produced, which is given by the p.d.f. $G(L|N)$ defined by Eq. (7.21).

Considering a sample of avalanches with N electrons on the mesh, which comprises many (infinite) sets, each set consisting of avalanches with a certain length, L, with a population proportional to $G(L|N)$. The mean avalanche transmission time in a set is $T(N, L)$ and the respective variance is $\langle V(L)\rangle_{n(L)=N_L}$. In the hypothetical case that all the above subsets had the same mean avalanche time, the time variance of the whole sample would be given by the weighted sum of the respective variances of the subsets. On the other hand, due to the fact that the mean avalanche time varies among the sets, the variance of the avalanche time considering all avalanches in the sample should be evaluated according to Eq. (D.6) (see Sec. D). Therefore, the variance of the avalanche time, $V\left[T(N)\right]$, when the number of electrons on the mesh is N, is expressed as:

$$\begin{aligned} V\left[T(N)\right] = &\int_{x_1}^{x_2} \langle V(L)\rangle_{n(L)=N} \cdot G\left(N|L\right) \mathrm{d}L \\ &+ \int_{x_1}^{x_2} T^2(N, L) \cdot G\left(N|L\right) \mathrm{d}L - \left[\int_{x_1}^{x_2} T(N, L) \cdot G\left(N|L\right) \mathrm{d}L\right]^2 . \end{aligned} \tag{8.47}$$

Physically, the variance of the photoelectron time $V\left[T_p(L)\right]$, depends only on the drift length it takes, $D - L$, as expressed by Eq. (8.1). However, because the photoelectron drift length is the residual of the avalanche length, which determines the mean multiplicity of the avalanche electrons, the variance of the photoelectron time depends indirectly on the electron multiplicity on the mesh, N.

By weighting Eqs. (7.23) and Eq. (8.1) with $G(L|N)$, integrating over the length of the avalanche and applying Eq. (D.6), the variance of the photoelectron time becomes:

$$\begin{aligned} V\left[T_p(N)\right] = &\int_{x_1}^{x_2} V\left[T_p(L)\right] \cdot G\left(N|L\right) \mathrm{d}L \\ &+ \int_{x_1}^{x_2} T_p^2(L) \cdot G\left(N|L\right) \mathrm{d}L - \left[\int_{x_1}^{x_2} T_p(L) \cdot G\left(N|L\right) \mathrm{d}L\right]^2 . \end{aligned} \tag{8.48}$$

Finally, the variance of the total on the mesh can be expressed by applying Eq. (D.6) once more:

$$\begin{aligned} V\left[T_{tot}(N)\right] = &\int_{x_1}^{x_2} \left[V\left[T_p(L)\right] + \langle V(L)\rangle_{n(L)=N}\right] \cdot G(L|N)\mathrm{d}L \\ &+ \int_{x_1}^{x_2} \left[T(N, L) + T_p^2(L)\right] \cdot G\left(N|L\right) \mathrm{d}L - \left[\int_{x_1}^{x_2} \left[T(N, L) + T_p(L)\right] \cdot G\left(N|L\right) \mathrm{d}L\right]^2 . \end{aligned} \tag{8.49}$$

It is easy to see that the sum of Eq. (8.47) and Eq. (8.48) are not equal to Eq. (8.49). This would be so only the photoelectron and avalanche contributions to the total time, expressed as functions of the electron multiplicity on the mesh would be uncorrelated. This correlation is visible also in the GARFIELD++ simulations as illustrated in Fig. 8.4 and it is due to the fact that the same number of pre-amplification electrons arriving on the mesh can be produced by avalanches of different lengths.

The predictions of Eqs. (8.47)-(8.49) are in good agreement with the corresponding GARFIELD++ simulation results, visible in Fig. 8.4. Furthermore, the model reproduces successfully the related GARFIELD++ simulation results at all operational conditions considered in this study. For small values of electron multiplicity on the mesh, the time spread predicted by our model is systematically smaller than the related GARFIELD++ simulation results. This underestimation comes from the inadequacy of the p.d.f.'s that have been employed in this model to approximate the avalanche statistical properties at its very beginning (*i.e.* at small avalanche length and low electron multiplicity). This is discussed in Sec. 9.

8.3 Effects related to electrons traversing the mesh

The transport of the pre-amplification electrons through the mesh reduces their multiplicity by a factor of four that is independent of the avalanche length and of the electron multiplicity on the mesh (see Fig. 7.3 and the related comments in Sec. 7.1). This has been shown by GARFIELD++ simulations for all PICOSEC operation conditions considered in this study. As expected the passage of the electrons through the mesh adds a delay to the signal arrival time. Simulations show that the added delay depends only on the applied drift voltage, is independent of the pre-amplification avalanche length and of the electron multiplicity on the mesh. This is illustrated in Fig. 8.5. However, the spread of the total time after the mesh is found to increase relative to the spread of the total time on the mesh, *i.e.* the process of electrons traversing the mesh deteriorates the PICOSEC timing resolution. This effect depends on the applied drift field, as well as on the avalanche characteristics, illustrated in Figs. 8.6 and 8.7. Although the mesh transparency (≈ 25%) is found to be independent to the considered drift voltages, this reduction of the number of electrons influences the timing resolution in a way that depends on the drift voltage. This fact signifies the importance of the correlation between the individual arrival times of the pre-amplification electrons (on and after the mesh) in determining the mesh effect on the timing resolution.

Consider a pre-amplification avalanche of length L with N electrons arriving on the mesh, and let T_{tot} be the total transmission time on the mesh and let $V\left[T_{tot}\right]$ be the variance of it. Then,

$$T_{tot}(L,N) = T(L,N) + T_p(L) = \frac{1}{N}\sum_{k=1}^{N} t_k + T_p(L), \tag{8.50}$$

where T_p is the transmission time of the photoelectron that depends only on its drift length $(D - L)$ as in Eq. (7.23). The times t_k, with $k = 1, 2, \ldots, N$, correspond to

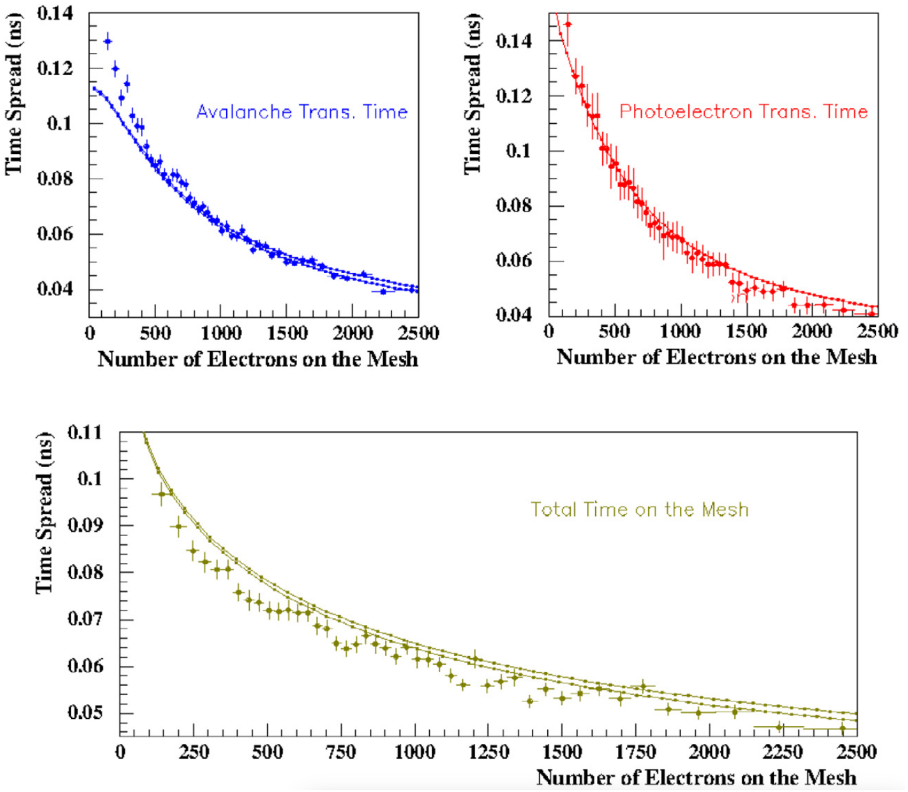

Figure 8.4: The points represent the transmission time spread as has been evaluated using GARFIELD++ simulations, with 50% Penning Transfer Rate, 425 V drift and 450 V anode voltage. The double lines present model predictions for $w = 0$ and $w = \rho$ as discussed in Sec. 8.1. The top-left (blue), the top-right (red) and the bottom (golden) plots show the avalanche time spread, the photoelectron time spread and the spread of the total time on the mesh, respectively, as functions of the number of pre-amplification electrons arriving on the mesh. Figure adapted from Ref. [16].

the pre-amplification electrons' arrival times on the mesh, starting from the time of the first ionization. The avalanche transmission, and therefore the total time on the mesh, is a function of both L and N, as expressed in Eq. (7.11).

The transmission time of the photoelectron is uncorrelated with every transmission time of the electrons in the avalanches. Consequently, the variance $V\left[T_{tot}\right]$ is written as:

$$V\left[T_{tot}(L,N)\right] = V\left[\frac{1}{N}\sum_{k=1}^{N} t_k\right] + V\left[T_p(L)\right]. \tag{8.51}$$

According to Eq. (8.1), the time variance of the photoelectron at the point of first ionization can be replaced to write the variance as:

$$V\left[T_{tot}(L,N)\right] = V\left[\frac{1}{N}\sum_{k=1}^{N} t_k\right] + \sigma_p^2 \cdot (D-L) + \Phi. \tag{8.52}$$

As discussed in Sec. 7.2, the arrival times (on the mesh) of the pre-amplification electrons in the avalanche are heavily correlated. The first term in Eq. (8.52) can

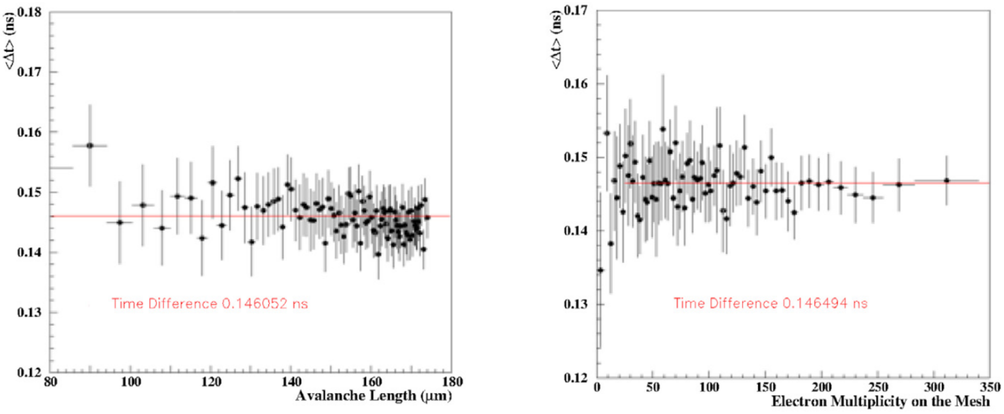

Figure 8.5: The points represent GARFIELD++ simulation results, assuming 50% Ptr, 450 V and 350 V drift and anode voltage, respectively. The time to pass through the mesh (*i.e.* $\langle \Delta t \rangle$ is the difference between the total time after the mesh and the total time on the mesh) is shown versus the respective avalanche length (left plot) and the electron multiplicity on the mesh (right plot). The solid curves represent fits by a constant function. Figure adapted from Ref. [16].

be written analytically as:

$$V\left[\frac{1}{N}\sum_{k=1}^{N} t_k\right] = \frac{\sigma_0^2 \cdot L}{N} + \frac{1}{N^2}\sum_{i=1}^{N}\sum_{j=1, j\neq i}^{N} C_{ij}, \tag{8.53}$$

where σ_0^2 is defined in Sec. 7.2 as the variance per unit length of a single electron in the avalanche, while C_{ij} expresses the covariance between the arrival times of the i-th and j-th electrons.

The production of new electrons while traversing the mesh is ignored. If M is the number of electrons entering the amplification region, then T_m is the total arrival time after passing the mesh (*i.e.* the average of the M arrival times on a plane just after the mesh), which is written as:

$$T_m(L, N) = \frac{1}{M}\sum_{k=1}^{M} t_k + \frac{1}{M}\sum_{k=1}^{M} \Delta t_k + T_p(L), \tag{8.54}$$

where Δt_k is the extra time that is required by the k-th electron to arrive at the plane just after the mesh.

The passage of an electron through the mesh is determined by the position of its impact point on the mesh. Therefore, if the same avalanche is shifted parallel to its longitudinal axis, a different subset of the N arriving electrons will pass through the mesh. This can be considered equivalent to giving the same probability, M/N, to each of the N arriving electrons to pass through the mesh. Using this argument, Eq. (8.54) becomes:

$$T_m(L, N) = \frac{1}{M}\frac{M}{N}\sum_{k=1}^{N} t_k + \frac{1}{M}\frac{M}{N}\sum_{k=1}^{N} \Delta t_k + T_p(L), \tag{8.55}$$

or using Eq. (8.50),

$$T_m(L,N) = T_{tot}(L,N) + \langle \Delta t \rangle \,, \tag{8.56}$$

where Δt is the mean time required by an electron to pass through the mesh. Equation (8.56) predicts that the total arrival time after the mesh is equal to the total arrival time on the mesh but delayed by a constant time, which is not dependent on the characteristics of the avalanche, as is observed in the GARFIELD++ simulations. Naturally, $\langle \Delta t \rangle$, which is the drift time of an electron traversing the mesh, depends on the electric field around the mesh.

The terms $\frac{1}{M}\sum_{k=1}^{M} t_k$, $\frac{1}{M}\sum_{k=1}^{M} \Delta t_k$ and T_p in Eq. (8.54) are uncorrelated with each other. Consequently, the variance of the total time after the mesh is written:

$$V\left[T_m(L,N)\right] = V\left[\frac{1}{M}\sum_{k=1}^{M} t_k\right] + V\left[\frac{1}{M}\sum_{k=1}^{M} \Delta t_k\right] + V\left[T_p(L)\right]. \tag{8.57}$$

The first term in Eq. (8.57) can be expressed analogously to Eq. (8.53):

$$V\left[\frac{1}{M}\sum_{k=1}^{M} t_k\right] = \frac{\sigma_0^2 \cdot L}{M} + \frac{1}{M^2}\sum_{i=1}^{M}\sum_{j=1,j\neq i}^{M} C_{ij}, \tag{8.58}$$

where is the covariance C_{ij} is defined in Eq. (8.53).

Equation (8.58) can be simplified by employing the argument that any of the pre-amplification electrons has the same probability to traverse the mesh. Moreover, the $\sum_{i=1}^{M}\sum_{j=1,j\neq i}^{M} C_{ij}$ term in Eq. (8.58) comprises in $M(M-1)$ C_{ij} terms, while the corresponding term in Eq. (8.53) consists of $N(N-1)$ C_{ij} terms. Using this, Eq. (8.58) is rewritten:

$$V\left[\frac{1}{M}\sum_{k=1}^{M} t_k\right] = \frac{\sigma_0^2 \cdot L}{M} + \frac{1}{M^2}\frac{M(M-1)}{N(N-1)}\sum_{i=1}^{N}\sum_{j=1,j\neq i}^{N} C_{ij}, \tag{8.59}$$

which can be approximated as

$$V\left[\frac{1}{M}\sum_{k=1}^{M} t_k\right] \simeq \frac{\sigma_0^2 \cdot L}{M} + \frac{1}{N^2}\sum_{i=1}^{N}\sum_{j=1,j\neq i}^{N} C_{ij}. \tag{8.60}$$

The Δt_k times are mutually uncorrelated and therefore the second term of Eq. (8.57) can be expressed as:

$$V\left[\frac{1}{M}\sum_{k=1}^{M} \Delta t_k\right] = \frac{\delta^2}{M}, \tag{8.61}$$

where δ^2 is the variance of the time taken by an electron to pass through the mesh. Equations (8.60) and (8.61) can be substituted in Eq. (8.57). Then, the variance of the total time after the mesh is written as:

$$V\left[T_m(L,N)\right] = \frac{\sigma_0^2 \cdot L}{M} + \frac{1}{N^2}\sum_{i=1}^{N}\sum_{j=1,j\neq i}^{N} C_{ij} + \frac{\delta^2}{M} + V\left[T_p(L)\right]. \tag{8.62}$$

Equation (8.53) can be then used to eliminate the double sum of the covariances. Consequently, the variance is now expressed as:

$$V\left[T_m(L,N)\right] = \sigma_0^2 \cdot L\left(\frac{1}{M} - \frac{1}{N}\right) + \frac{\delta^2}{M} + V\left[T_{tot}(L,N)\right]. \tag{8.63}$$

The average ratio M/N corresponds to the transparency of the mesh, tr, which is independent of the operating conditions for the cases studied in this work. Using the mesh transparency, M can be eliminated to simplify Eq. (8.63) to:

$$V\left[T_m(L,N)\right] = \frac{1}{N}\left[\sigma_0^2 \cdot L\left(\frac{1}{tr} - 1\right) + \frac{\delta^2}{tr}\right] + V\left[T_{tot}(L,N)\right]. \tag{8.64}$$

The increase in the total time variance, $V\left[T_m(L,N)\right] - V\left[T_{tot}(L,N)\right]$, is predicted by Eq. (8.64) to depend on the electron multiplicity N, on the electron transparency of the mesh tr and on the length of the avalanche L. As before, Eq. (8.64) can be averaged over all possible N, following the procedure that is described in Sec. 8.1, so that the variance of the total time after the mesh is expressed as a function of the avalanche length as:

$$\begin{aligned} V\left[T_m(L)\right] = \left\langle V\left[T_m(L,N)\right]\right\rangle_N = \\ \frac{\theta+1}{2\theta}\exp\left[-a_{eff}L\right] \cdot \left[\sigma_0^2 \cdot L\left(\frac{1}{tr} - 1\right) + \frac{\delta^2}{tr}\right] + V\left[T_{tot}(L)\right]. \end{aligned} \tag{8.65}$$

where the property of the Gamma distribution has been used:

$$\left\langle \frac{1}{N}\right\rangle = \frac{\theta+1}{\theta\langle N\rangle} = \frac{\theta+1}{2\theta}\exp\left[-a_{eff} \cdot L\right]. \tag{8.66}$$

The last term in Eq. (8.65), $V\left[T_{tot}(L)\right]$, is given by Eq. (8.30). The mesh contribution to the total time variance which determines the PICOSEC timing resolution is given in terms of the avalanche length as:

$$\begin{aligned} \Delta V(L) = V\left[T_m(L)\right] - V\left[T_{tot}(L)\right] = \\ \frac{\theta+1}{2\theta}\exp\left[-a_{eff}L\right] \cdot \left[\sigma_0^2 \cdot L\left(\frac{1}{tr} - 1\right) + \frac{\delta^2}{tr}\right]. \end{aligned} \tag{8.67}$$

The variance of the total time after the mesh can also be written as a function of the electron multiplicity on the mesh. By properly averaging Eq. (8.64) over all possible avalanche lengths, it follows that:

$$\begin{aligned} V\left[T_m(N)\right] = \left\langle V\left[T_m(L,N)\right]\right\rangle_L = \\ \frac{1}{N}\left[\sigma_0^2 \cdot \langle L(N)\rangle\left(\frac{1}{tr} - 1\right) + \frac{\delta^2}{tr}\right] + V\left[T_{tot}(N)\right]. \end{aligned} \tag{8.68}$$

The last term, $V\left[T_{tot}(N)\right]$, is given by Eq. (8.49), while the average avalanche length $\langle L(N)\rangle$ is defined in Sec. 7.1. The contribution of the mesh to the PICOSEC timing resolution as a function of the electron multiplicity N is then:

$$\Delta V(N) = V\left[T_m(N)\right] - V\left[T_{tot}(N)\right] = \frac{1}{N}\left[\sigma_0^2 \cdot \langle L(N)\rangle\left(\frac{1}{tr} - 1\right) + \frac{\delta^2}{tr}\right]. \tag{8.69}$$

Equations (8.68) and (8.69) can be easily reformulated as functions of the number of the electrons that pass through the mesh, M, by making use of the transformation $M = tr \cdot N$. It is recalled that the PICOSEC e-peak amplitude was found proportional to M [26] (see also Fig. 6.4).

In the above description of the electron transport through the mesh, two sources contribute to the increase of the time variance:

- An extra time spread due to the electron drift in the inhomogeneous electric field around the mesh,
- and the statistical effect caused by the depletion of mutually-correlated avalanche electrons.

The first contribution is expressed by the term proportional to δ^2 in Eq. (8.64) or equivalently in Eqs. (8.67) and (8.69). The time-spread δ depends on the PICOSEC operational conditions and it is treated as an input parameter in this model. Values of δ, which are evaluated using GARFIELD++ simulations, assuming several drift voltages, are compiled in Table A.8, where they are observed to exhibit a decreasing functional dependence on the drift voltage. It is important though to note that the terms proportional to δ^2 contributing to the increase of the time variance (*e.g.* in Eqs. (8.64), (8.67) and (8.69)) are much weaker than the other terms, which are related to statistical correlations.

Due to the correlation terms, the variance of the total-time after the mesh (*e.g.* in Eq. (8.63)) is not proportional to the variance of the total time on the mesh. The mesh adds to the variance a term which is almost proportional to $L \cdot \exp\left[-a_{eff}L\right]$ when expressed as a function of L (see Eq. (8.67)), or almost proportional to $\langle L(N) \rangle / N$ (see Eq. (8.69)) when it is expressed as a function of N. As the drift voltage increases, the electron multiplication factor, a_{eff} increases and both of the above terms decrease for all L and N. Therefore, the influence of the mesh on the timing resolution becomes weaker as the drift field increases, as is demonstrated by the GARFIELD++ simulations.

The model agrees well with the GARFIELD++ simulations in describing the quantitatively the effect of the mesh on the timing resolution, for all of the PICOSEC operating conditions that have been considered in this work, as demonstrated in Fig. 8.6 and 8.7.

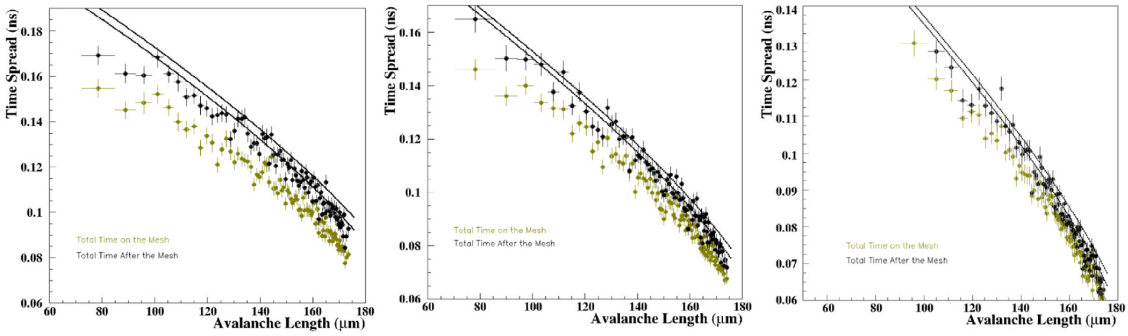

Figure 8.6: The points represent GARFIELD++ simulation results concerning the spread of the total time on the mesh (golden points) and the spread of the total time after the mesh (black points) versus the avalanche length. The solid lines represent predictions based on Eq. (63). The double lines indicate the systematic uncertainty due to the value of the *w* parameter, discussed in Sec. 8.1. The voltage settings considered in these comparisons are: 450 V at the anode and drift voltage of 325 V (left plot), 350 V (center plot), and 400 V (right plot). Figure adapted from Ref. [16].

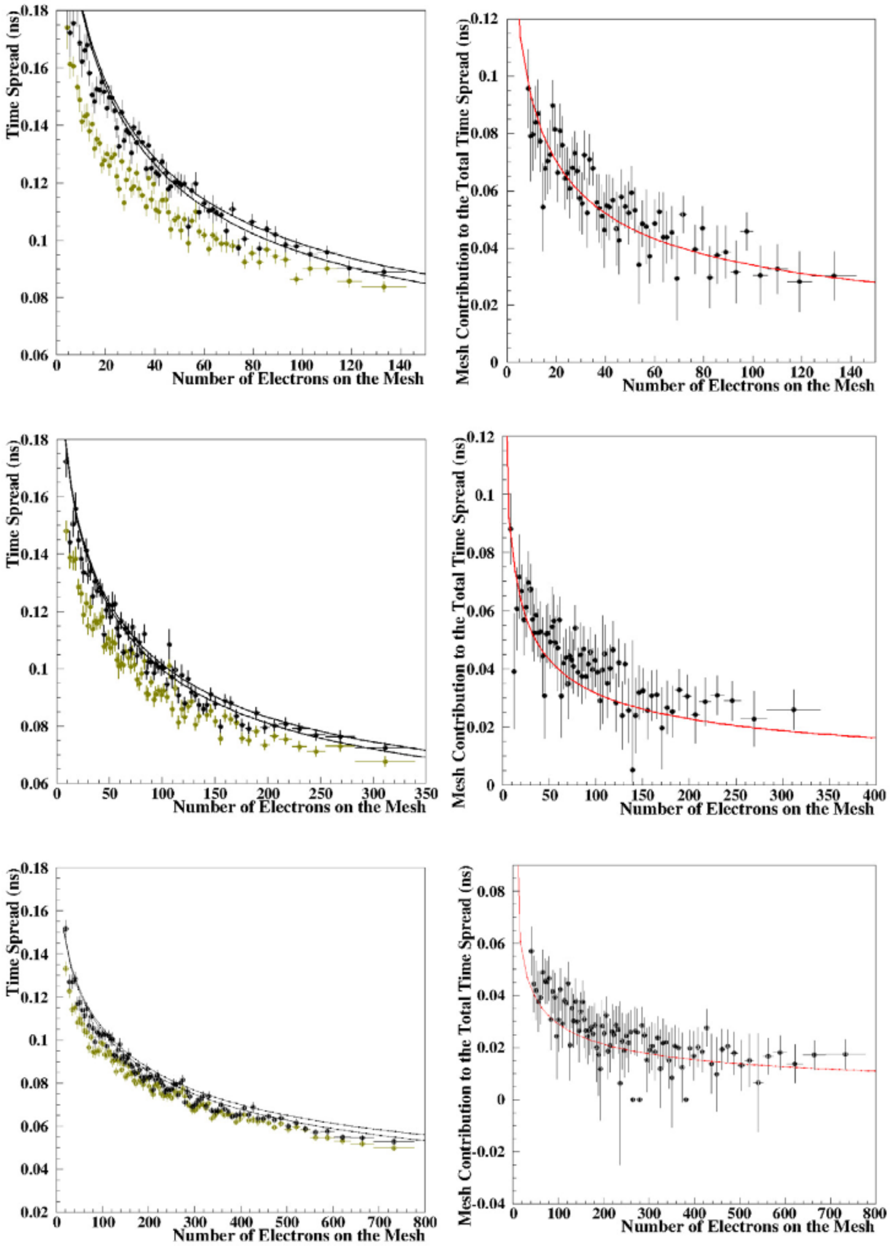

Figure 8.7: The points represent GARFIELD++ simulation results. The left column plots show the spread of the total time on the mesh (golden points) and after the mesh (black points) versus the electron multiplicity on the mesh. The right column plots display the mesh contribution (*i.e.* the square root of the difference between the variance of the total time after and on the mesh) versus the electron multiplicity on the mesh. The solid lines represent predictions of Eqs. (8.68) and (8.69). The double lines represent the systematic uncertainty due to the unknown value of the w model-parameter. The voltage settings considered in these comparisons are 450 V at the anode and drift voltages of 325 V (top row), 350 V (middle row), and 400 V (bottom row). Figure adapted from Ref. [16].

Chapter 9

Modelling the distributions of the transmission time

A weak but systematic deviation of the model predictions from the GARFIELD++ results has been noticed at low electron multiplicities on the mesh. As shown in Figs. 7.5 and 8.4, the model predictions of the mean value and the spread of avalanche time deviate from the GARFIELD++ points at avalanche electron multiplicities less than 300, for 50% Ptr, 425 V drift and 450 V anode voltages. As mentioned already, such deviations result from the inadequacy of the employed probability density functions to describe accurately the statistical properties of the avalanche at its very beginning (small avalanche length, low electron multiplicity). For example, the model predictions of both the mean value and the variance of the avalanche time, *i.e.* Eqs. (7.22) and (8.47), utilize the function $G(L|N)$. This conditional p.d.f., defined in Sec. 7.1 by Eq. (7.21), expresses the distribution of the length of an avalanche given that the avalanche electron multiplicity is equal to N. Predictions of Eq. (7.21) are compared to the respective distributions produced by GARFIELD++, in Fig. 9.1. It is clear that Eq. (7.21) approximates poorly the GARFIELD++ distributions at low N, though succeeds in describing the detailed simulation results for higher values of electron multiplicities. Consequently, the predictions of Eqs. (7.22) and (8.47) suffer from the poor performance of $G(L|N)$ to describe the GARFIELD++ results at low electron multiplicities.

On the other hand, PICOSEC data are collected with non-zero experimental amplitude thresholds for practical reasons. The data points shown in Fig. 6.3, in comparison with the results based on simulated PICOSEC pulses, were collected [25] with thresholds corresponding to e-peak charge greater than 3−4 pC, which translate (for 425 V drift and 450 V anode voltages, and 50% Ptr) to 400 – 500 electron multiplicity on the mesh. At this region of pre-amplification electron multiplicities, the model predictions are in good agreement with the results of GARFIELD++ simulations, as shown in Figs. 7.5 and 8.4.

Up to this point, the model has been used to provide information on the mean value and the variance (*i.e.* to evaluate the first and second moments) of transmission time distributions. However, it can also be used for more general statistical predictions, *e.g.* to predict the complete probability density functions of the above time variables. For example, Fig. 9.2 shows the distributions, produced by

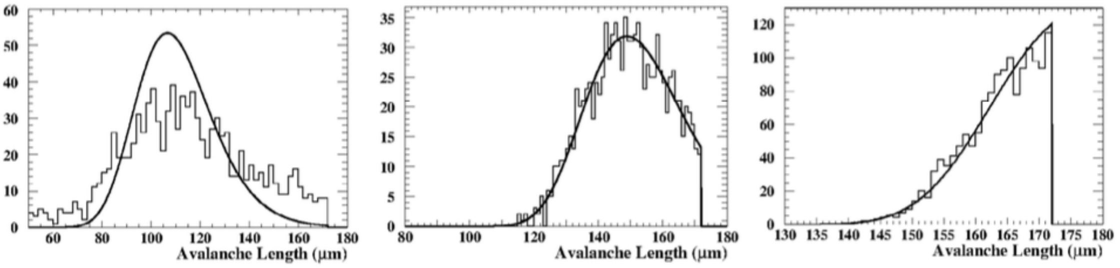

Figure 9.1: Distributions of the avalanche length, produced by GARFIELD++ simulations (assuming 50% Ptr, 425 V and 450 V drift and anode voltage, respectively) in the case that the multiplicity of pre-amplification electrons is less than 120 (left plot), between 400 and 440 (center plot) and 1230 and 1300 (right plot). The solid lines represent the related predictions of the distribution function $G(L|N)$ defined by Eq. (7.21). Figure adapted from Ref. [16].

GARFIELD++ simulations (black points), of the photoelectron, the avalanche and the total time (on and after the mesh), without selecting the avalanche length or the electron multiplicity on the mesh. The apparent left-right asymmetry and the long tails in these distributions are partially caused by the dependence of the mean transmission times on the length of the avalanche (or equivalently, on the length of the photoelectron drift path, before the first ionization). Nevertheless, the dependence of the variances on the length of the avalanche also contributes to the apparent asymmetry and the tails. In order to predict the functional form of the above asymmetric distributions, the model is complemented with the extra assumption that the related transmission times, corresponding to a certain avalanche length, follow an Inverse Gaussian distribution (Wald) function, which is expressed as:

$$f(x;\mu,\lambda) = \left(\frac{\lambda}{2\pi x^3}\right)^{1/2} \exp\left[-\frac{\lambda(x-\mu)^2}{2\mu^2 x}\right], \qquad (9.1)$$

where the parameter μ is the mean value and the shape parameter λ is related to the variance of the distribution as $V[x] = \mu^3/\lambda$. Generally, the convolution of two Wald distributions is not a Wald distribution. Consequently, even if the photoelectron and avalanche transmission times are described by Wald distributions, it is not necessary that the total times will be distributed according to the same functional form. However, GARFIELD++ simulation results indicate, see also Fig. 6.5, that the distributions of the total times, on and after the mesh, are well approximated by Wald functions.

Hereafter, the model assumes that the statistical properties of the photoelectron transmission time, T_p, and the avalanche transmission time, T, can be well described by Wald distributions as follows. The photoelectron transmission time follows the p.d.f.:

$$f\left(T_p;\mu_p(L),\lambda_p(L)\right) = \left(\frac{\lambda_p(L)}{2\pi T_p^3}\right)^{1/2} \cdot \exp\left[\frac{-\lambda_p(L)\left(T_p-\mu_p(L)\right)^2}{2\mu_p^2(L)\cdot T_p}\right], \qquad (9.2)$$

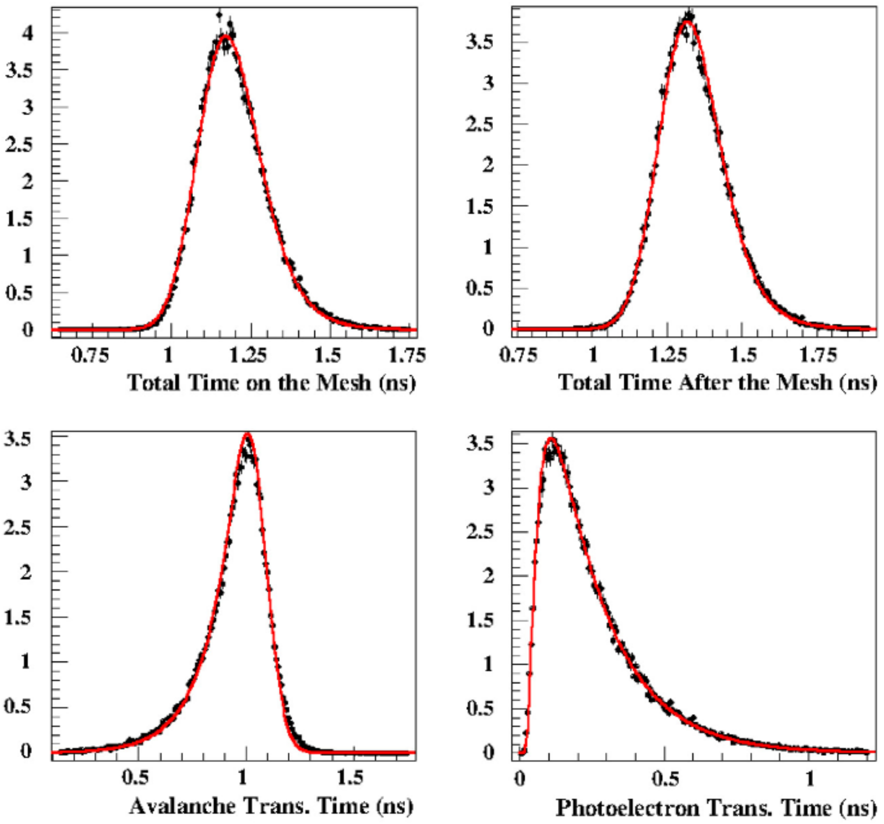

Figure 9.2: Transmission time distributions for all events at 350 V and 450 V drift and anode voltage respectively and 50% Ptr: (top left) Total time on the mesh, (top right) total time after the mesh, (bottom left) avalanche transmission time and (bottom right) photoelectron transmission time. The points are results of GARFIELD++ simulations while the red lines correspond to the respective model predictions, as described in the text. Figure adapted from Ref. [16].

while the avalanche transmission time follows the p.d.f.:

$$f\left(T;\mu(L),\lambda(L)\right)=\left(\frac{\lambda(L)}{2\pi T^3}\right)^{1/2}\cdot\exp\left[\frac{-\lambda(L)\,(T-\mu(L))^2}{2\mu^2(L)\cdot T}\right], \tag{9.3}$$

where according to Eq. (7.23):

$$\mu_p(L)=\frac{D_L}{V_p}+d_{off}, \tag{9.4}$$

and according to Eq. (8.1),

$$\lambda_p(L)=\frac{\mu_p^3(L)}{(D-L)\cdot\sigma_p^2+\Phi}. \tag{9.5}$$

Similarly for the parameters of the p.d.f. describing the avalanche transmission time,

$$\mu(L)=\langle T(L)\rangle\,, \tag{9.6}$$

where $\langle T(L)\rangle$ is given by Eq. (7.16). The shape parameter is defined by:

$$\lambda(L) = \frac{\mu^3(L)}{V\left[T(L)\right]}, \tag{9.7}$$

with $V\left[T(L)\right]$ given by Eq. (8.28).

Using the p.d.f. to observe an avalanche length L, $R(L;a)$, (defined in Eq. (7.20)) for the distributions of T_p and T for any value of L can be written as:

$$F_p(T_p) = \int_{x_1}^{x_2} f_p(T_p;\mu_p(L),\lambda_p(L)) \cdot R(L;a)\mathrm{d}L, \tag{9.8}$$

$$F(T) = \int_{x_1}^{x_2} f(T;\mu(L),\lambda(L)) \cdot R(L;a)\mathrm{d}L, \tag{9.9}$$

The solid lines in the bottom plots of Fig. 9.2 correspond to the predictions expressed by the aforementioned p.d.f. of Eqs. (9.8) and (9.9). The model predictions are in excellent agreement with the GARFIELD++ simulations. Similarly, it is assumed that the total time distributions on and after the mesh (T_{tot} and T_m) for a certain avalanche length L, can be approximated by Wald distributions:

$$f\left(T_{tot};\mu_{tot}(L),\lambda_{tot}(L)\right) = \left(\frac{\lambda_{tot}(L)}{2\pi T_{tot}^3}\right)^{1/2} \cdot \exp\left[\frac{-\lambda_{tot}(L)\left(T_{tot}-\mu_{tot}(L)\right)^2}{2\mu_{tot}^2(L)\cdot T_{tot}}\right], \tag{9.10}$$

$$f\left(T_m;\mu_m(L),\lambda_m(L)\right) = \left(\frac{\lambda_m(L)}{2\pi T_m^3}\right)^{1/2} \cdot \exp\left[\frac{-\lambda_m(L)\left(T_m-\mu_m(L)\right)^2}{2\mu_m^2(L)\cdot T_m}\right], \tag{9.11}$$

where according to Eqs. (7.16) and (7.23):

$$\mu_{tot}(L) = \frac{D_L}{V_p} + d_{off} + \langle T(L)\rangle, \tag{9.12}$$

and according to Eq. (8.30):

$$\lambda_{tot}(L) = \frac{\mu_{tot}^3(L)}{V\left[T_{tot}(L)\right]}. \tag{9.13}$$

Furthermore, according to Eq. (8.56):

$$\mu_m(L) = \mu_{tot} + \langle\Delta t\rangle, \tag{9.14}$$

and

$$\lambda_m(L) = \frac{\mu_m^3}{V\left[T_m(L)\right]}, \tag{9.15}$$

where $V\left[T_m(L)\right]$ is defined in Eq. (8.65).

The predictions of Eqs. (9.10) and (9.11) are visible in the top plots of Fig. 9.2, which are also in excellent agreement with the GARFIELD++ simulation results. In addition it has been verified that the model can describe successfully the transmission time distributions at all drift voltage settings considered in this study.

Conclusion

An analysis of the slow beam losses on a bunch-by-bunch basis have revealed that incoherent collective effects coming from beam-beam interactions and electron clouds are the main sources of slow beam losses at the LHC. In particular, the introduction of the beam-beam head-on interaction when the beams are put into collision causes a sharp temporary increase in the slow beam losses which decays within the next hour. Bunches at the tail of bunch trains seem to systematically suffer from a degraded beam lifetime. This has been attributed to electron cloud effects in the insertion regions around the interaction points 1 and 5. This is consistent with a significant electron density in the Inner Triplet quadrupoles which is also greatly enhanced by the presence of the two beams in the same vacuum chamber.

Tracking simulations have been used in order to predict the degradation from such incoherent collective effects. Due to the recent advances in software development of tracking simulation tools, GPUs could be utilized to gain a significant boost in computation speed, where particles are being tracked in parallel across the LHC lattice and including the relevant collective effects (beam-beam interactions or electron cloud effects). A first attempt in using particle tracking simulations was to reproduce the behaviour in the slow beam losses when the two beams are put into collision. The study showed that, through the increase of computational power, observable quantities such as the slow beam loss rate and the emittance growth could be simulated with particle tracking on realistic timescales, in the order of several minutes, up to half an hour. Moreover, the behaviour of the slow beam losses due to the introduction of the beam-beam head-on interaction was successfully reproduced in the simulations. An important limitation in the quantitative prediction of the slow beam losses was found to be the uncertainties in the population of the tails of the beam profiles, for which there exists no accurate and systematic measurement.

A major step forward was made in the simulations of incoherent electron cloud effects. Measurements of the slow beam losses as well as of emittance growth have revealed that the magnitude of these effects are small enough to allow the usage of the weak-strong approximation. Furthermore, the use of GPUs is found to be the perfect computational environment to perform simulations because of their massively parallel architecture with a relatively large memory (when compared to the available memory in a typical single-core CPU node of a computing cluster). The relatively large memory is required due to the big memory footprint (in the order of several GB) of the fieldmap describing an electron cloud interaction. The required memory is so large because the dynamics of the electrons inside an electron cloud distribution gives rise to complex time-dependent electromagnetic fields. An analytical approximation of these fields becomes increasingly difficult, especially in the presence of magnetic field gradients. Consequently, Particle-In-Cell simulations are employed to find these time-dependent electromagnetic fields on a discrete grid.

The fact that the fields are known only on a discrete grid requires special care if the beam dynamics are to be simulated in their presence. The Hamiltonian structure of proton beam dynamics suggests that the use of symplectic maps can greatly increase the accuracy in numerically solving the equations of motion for protons travelling in the LHC lattice. For this purpose, a method was developed that employs a tricubic interpolation scheme on the discrete points of the electron cloud fields, in order to preserve the symplectic structure of the map describing the electron cloud interaction. The method includes a refinement scheme that is able to effectively suppress artifacts introduced during the interpolation stage.

Using the developed method, particle tracking simulations were performed for protons at injection energy in the LHC lattice, under the influence of incoherent electron cloud effects in the arcs. The results showed that non-linear beam dynamics indicators like dynamic aperture and frequency map analysis can be significantly impacted by the effect of the electron cloud. Moreover, a degradation was observed in the beam lifetime though a quantitative prediction was once more limited by the uncertainty in the tails of the beam profiles. On the other hand, simulations showed an incoherent emittance growth of the same order of magnitude as the one observed in previous measurements reported in the literature. This is the first time that detailed simulations of incoherent electron cloud effects have been performed in the presence of the non-linear model of the LHC lattice, for long and observable timescales, and in the presence of multiple sources of electron clouds, *i.e.* electron clouds forming in dipolar and in quadrupolar magnetic fields.

These studies are of increasing relevance due to the increased concern from electron clouds in the LHC. In each of the Long Shutdown maintenance, the secondary emission yield of the vacuum chamber is being observed to undergo irreversible degradation. A larger secondary emission yield results in stronger electron clouds which can quickly result in a decrease of the dynamic aperture. Moreover, stronger electron clouds require stronger lattice non-linearities (chromaticity and amplitude detuning) in order to control coherent beam instabilities caused by the electron cloud themselves. These stronger non-linearities can degrade even more the dynamic aperture. During this study, electron clouds in the Inner Triplet quadrupoles have been identified as the main source of significant degradation of the beam lifetime during physics operation of the LHC. In the context of the High-Luminosity LHC upgrade, the Inner Triplet quadrupoles are planned to be replaced. The beam screens of the new inner triplet quadrupoles will to be coated with amorphous carbon in order to limit the formation of electron clouds.

In the context of modelling the timing characteristics of the PICOSEC Micromegas detector, this work employs the comparison of experimental data with detailed simulations, based on the GARFIELD++ software, and complemented with a statistical description of the electronic signal formation, to identify the microscopic quantities that determine the PICOSEC timing characteristics. Subsequently, a stochastic model is developed that describes the properties of the above quantities, offering a phenomenological, microscopic interpretation of the observed timing properties of the detector. The model is based on:

1. The fact that an electron drifting in a gas under the influence of an homogeneous electric field achieves higher drift velocity when, in addition to elastic scattering, undergoes inelastic interactions,
2. The assumption that a newly produced electron through ionization acquires a certain time-gain relative to its parent and subsequently drifts with the same velocity as the parent electron

The input parameters, compiled in Tab C.8, are commonly used statistical variables, with the exception of the time-gain parameter ρ that has been introduced here, and they have been evaluated by analyzing GARFIELD++ simulation results. The quantitative predictions of the model have been compared extensively with the related GARFIELD++ simulation results and found to be in excellent agreement at all operating PICOSEC conditions considered in this study, demonstrating the success of this stochastic interpretation. As demonstrated through this work, the developed model is very successful in providing insights for the major microscopic mechanisms, which determine the timing characteristics of the detector, and in explaining coherently the unexpected behavior of microscopic quantities, which have already been observed in GARFIELD++ simulations. Due to the very good agreement of the model predictions with GARFIELD++, the formulae developed here can be used as a tool for fast predictions, provided that the values of the model input parameters, *i.e.* the parameters shown in Tab. C.8, are known for the considered operating conditions. This limits the application of the developed model as a stand-alone tool. However, having available sets of input parameter values for certain operational settings, it is possible to derive empirical parametrizations of the input parameters, which can be used to provide input to the model for a broader region of operational settings covered by the above parameterization.

Appendix A

Symplecticity of maps based on linear interpolation

Typically in PIC codes, the scalar potential ϕ is calculated on a regular grid and its derivatives are approximated with central differences:

$$e_x^{(i,j)} = -\frac{\partial \phi}{\partial x}^{(i,j)} = -\frac{\phi^{(i+1,j)} - \phi^{(i-1,j)}}{2\Delta x}, \tag{A.1}$$

$$e_y^{(i,j)} = -\frac{\partial \phi}{\partial y}^{(i,j)} = -\frac{\phi^{(i,j+1)} - \phi^{(i,j-1)}}{2\Delta y}, \tag{A.2}$$

where $\Delta x, \Delta y$ are the distances between the grid nodes and i, j are the indices of the grid cells. The map of the interaction would then have the following form:

$$x \mapsto x, \tag{A.3}$$

$$p_x \mapsto p_x + A\, e_x(x, y), \tag{A.4}$$

$$y \mapsto y, \tag{A.5}$$

$$p_y \mapsto p_y + A\, e_y(x, y), \tag{A.6}$$

where A is a constant. The normalized fields $e_x(x, y), e_y(x, y)$ are interpolated linearly and independently of each other in order to obtain their values at an arbitrary point in the continuous space. In this case, the interpolating function is explicitly written as:

$$e_{x,y}(x, y) = a_{x,y}^{(i,j)} + b_{x,y}^{(i,j)} \frac{x - x^{(i,j)}}{\Delta x} + c_{x,y}^{(i,j)} \frac{y - y^{(i,j)}}{\Delta y} + d_{x,y}^{(i,j)} \frac{(x - x^{(i)})(y - y^{(j)})}{\Delta x \Delta y}, \tag{A.7}$$

where $a_{x,y}^{(i,j)}, b_{x,y}^{(i,j)}, c_{x,y}^{(i,j)}, d_{x,y}^{(i,j)}$ are given by:

$$a_{x,y}^{(i,j)} = e_{x,y}^{(i,j)}, \tag{A.8}$$

$$b_{x,y}^{(i,j)} = -e_{x,y}^{(i,j)} + e_{x,y}^{(i+1,j)}, \tag{A.9}$$

$$c_{x,y}^{(i,j)} = -e_{x,y}^{(i,j)} + e_{x,y}^{(i,j+1)}, \tag{A.10}$$

$$d_{x,y}^{(i,j)} = e_{x,y}^{(i,j)} - e_{x,y}^{(i,j+1)} - e_{x,y}^{(i+1,j)} + e_{x,y}^{(i+1,j+1)}, \tag{A.11}$$

and $x^{(i,j)}$, $y^{(i,j)}$ are the $x^{(i)}$ and $y^{(j)}$ coordinates of the neighbouring grid node. The Jacobian matrix J of the map in Eqs. (A.3)-(A.6) is equal to:

$$\mathbf{J} = \begin{pmatrix} 1 & 0 & 0 & 0 \\ A\partial_x e_x & 1 & A\partial_y e_x & 0 \\ 0 & 0 & 1 & 0 \\ A\partial_x e_y & 0 & A\partial_y e_y & 1 \end{pmatrix}, \tag{A.12}$$

where we have used $\partial_x \equiv \frac{\partial}{\partial x}$ to ease notation. The map is symplectic if the following condition is satisfied[14]:

$$\mathbf{J}\,\mathbf{S}\,\mathbf{J}^T = \mathbf{S}, \tag{A.13}$$

where $\mathbf{S}$ is the antisymmetric matrix:

$$\mathbf{S} = \begin{pmatrix} 0 & 1 & 0 & 0 \\ -1 & 0 & 0 & 0 \\ 0 & 0 & 0 & 1 \\ 0 & 0 & -1 & 0 \end{pmatrix}. \tag{A.14}$$

Combining Eqs. (A.12), (A.13) and (A.14), the following matrix equation follows:

$$\begin{pmatrix} 0 & 1 & 0 & 0 \\ -1 & 0 & 0 & A\left(\partial_y e_x - \partial_x e_y\right) \\ 0 & 0 & 0 & 1 \\ 0 & A\left(\partial_x e_y - \partial_y e_x\right) & -1 & 0 \end{pmatrix} = \begin{pmatrix} 0 & 1 & 0 & 0 \\ -1 & 0 & 0 & 0 \\ 0 & 0 & 0 & 1 \\ 0 & 0 & -1 & 0 \end{pmatrix}, \tag{A.15}$$

from where it can be observed that the symplectic condition of Eq. (A.13) is equivalent to the following condition on the derivatives:

$$\frac{\partial e_y}{\partial x} - \frac{\partial e_x}{\partial y} = 0. \tag{A.16}$$

Combining Eqs. (A.7) and (A.16), the condition of symplecticity becomes:

$$\frac{b_y^{(i,j)}}{\Delta x} + \frac{d_y^{(i,j)}}{\Delta x \Delta y}\left(y - y^{(j)}\right) - \frac{c_x^{(i,j)}}{\Delta y} - \frac{d_x^{(i,j)}}{\Delta x \Delta y}\left(x - x^{(i)}\right) = 0. \tag{A.17}$$

This equality must be true for any value of $x, y, x^{(i)}, y^{(j)}$, which requires that

$$\frac{b_y^{(i,j)}}{\Delta x} - \frac{c_x^{(i,j)}}{\Delta y} = 0, \tag{A.18}$$

$$d_y^{(i,j)} = 0, \tag{A.19}$$

$$d_x^{(i,j)} = 0. \tag{A.20}$$

By substituting the coefficients of Eqs. (A.9), (A.10), (A.11) and the fields of Eqs. (A.1) and (A.2), it can be noticed that the symplecticity condition holds in every point of the domain if the following relations hold for the discrete samples of the scalar potential:

$$\phi^{(i,j+1)} - \phi^{(i,j-1)} - \phi^{(i+1,j+1)} + \phi^{(i+1,j-1)} - \phi^{(i+1,j)} + \phi^{(i-1,j)} + \phi^{(i+1,j+1)} - \phi^{(i-1,j+1)} = 0, \tag{A.21}$$

$$-\phi^{(i+1,j)} + \phi^{(i-1,j)} + \phi^{(i+2,j)} - \phi^{(i,j)} + \phi^{(i+1,j+1)} - \phi^{(i-1,j+1)} - \phi^{(i+2,j+1)} + \phi^{(i,j+1)} = 0, \tag{A.22}$$

$$-\phi^{(i,j+1)} + \phi^{(i,j-1)} + \phi^{(i,j+2)} - \phi^{(i,j)} + \phi^{(i+1,j+1)} - \phi^{(i+1,j-1)} - \phi^{(i+1,j+2)} + \phi^{(i+1,j)} = 0. \tag{A.23}$$

Such relations are not automatically satisfied for a potential obtained from the discretized Poisson equation, which means that the map obtained with the scheme that is defined in Eqs. (A.1)-(A.11) is in general not symplectic.

To illustrate the implication of using such a non-symplectic map in tracking simulations, we apply it to numerically solve the dynamical system described by the following Hamiltonian:

$$H = \frac{p_1^2}{2} + \frac{p_2^2}{2} + e^{q_1-q_2}. \tag{A.24}$$

This Hamiltonian has a non-linear potential that cannot be represented exactly by polynomial interpolating functions and is completely integrable. In addition to the Hamiltonian, the system conserves the following quantities (integrals of motion)[15]:

$$J_1 = (p_1 - p_2)^2 + 4e^{q_1-q_2}, \tag{A.25}$$

$$I_1 = \frac{p_1 - p_2 + \sqrt{J_1}}{p_1 - p_2 - \sqrt{J_1}} \exp\left(\sqrt{J_1}\,\frac{q_1 + q_2}{p_1 + p_2}\right). \tag{A.26}$$

The numerical integration scheme is constructed by splitting the Hamiltonian into its kinetic (H_K) and potential (ϕ) terms:

$$H_k(p_1, p_2) = \frac{p_1^2}{2} + \frac{p_1^2}{2}, \tag{A.27}$$

$$\phi(q_1, q_2) = e^{q_1-q_2}. \tag{A.28}$$

The system is then integrated by applying Hamilton's equations to the two terms of the Hamiltonian separately. The scheme is constructed by arranging the solutions in the “drift-kick-drift” form:

$$q_1 \mapsto q_1 + \frac{\Delta t}{2} p_1, \tag{A.29}$$

$$q_2 \mapsto q_2 + \frac{\Delta t}{2} p_2, \tag{A.30}$$

$$p_1 \mapsto p_1 - \Delta t \,\frac{\partial \phi}{\partial q_1}(q_1, q_2)\,, \tag{A.31}$$

$$p_2 \mapsto p_2 - \Delta t \,\frac{\partial \phi}{\partial q_2}(q_1, q_2)\,, \tag{A.32}$$

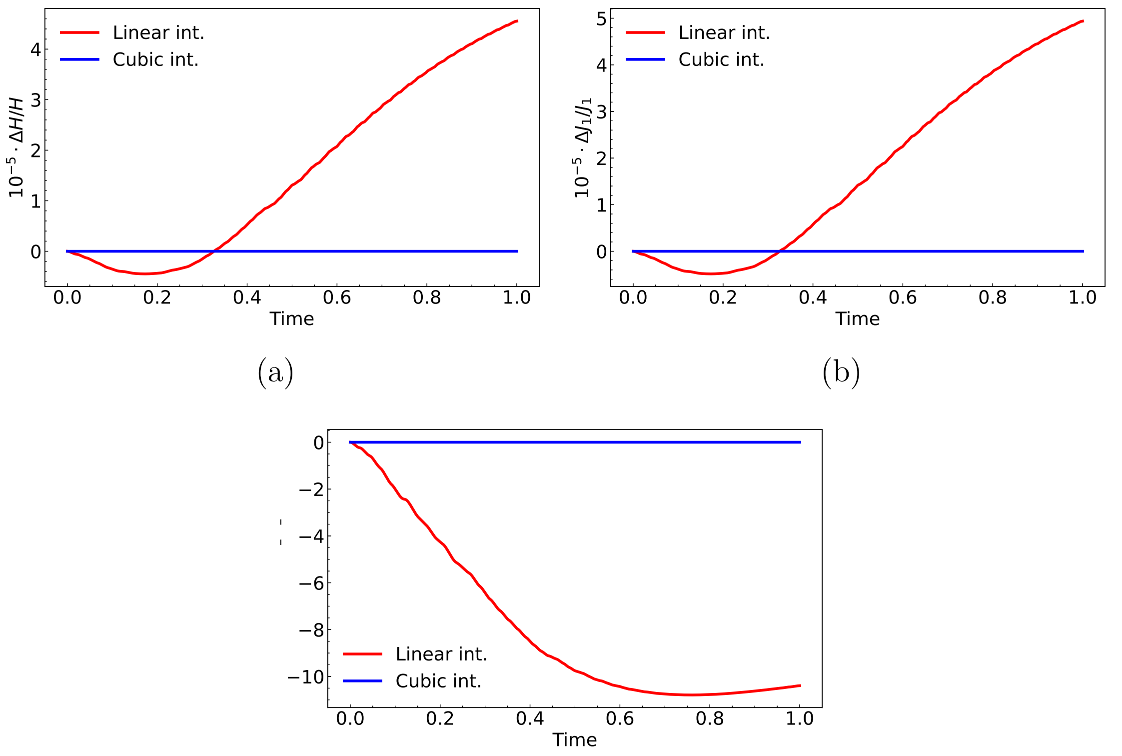

(a)

(b)

(c)

Figure A.1: Evolution of the error in the integrals of motion with time, using the two interpolation schemes. The error is quoted as a relative absolute difference with respect to the exact value of the integral of motion. The initial conditions used are $q_1 = 0.5,\ p_1 = 1,\ q_2 = -0.5,\ p_2 = 0$ with a time-step $\Delta t = 10^{-6}$.

$$q_1 \mapsto q_1 + \frac{\Delta t}{2} p_1, \tag{A.33}$$

$$q_2 \mapsto q_2 + \frac{\Delta t}{2} p_2, \tag{A.34}$$

We compare the performance of two different interpolation schemes in computing the derivatives of the potential in Eqs. (A.31) and (A.32). In particular we consider: 1) a linear interpolation scheme on the derivatives $\partial\phi/\partial q_1$, $\partial\phi/\partial q_2$ and 2) a cubic interpolation scheme on ϕ, as described in Sec. 5.1.1, but in two dimensions. For both interpolation schemes the parameters used were the same — a regular two-dimensional interpolation grid of 201 × 201 nodes with a distance of 0.02 between grid node in both dimensions. The error made on the integrals of motion with respect to time for the different integrals of motion is plotted in Fig. A.1. The red lines correspond to the simulations using the linear interpolation while the blue lines to when the cubic interpolation scheme is used.

It is clear that for the same grid spacing the performance of the linear interpolation scheme is worse. The linear interpolation scheme performs much worse in conserving the integrals of motion, which are shown to grow with time. This is expected as the map produced by this scheme is not symplectic. On the other hand, the scheme based on the cubic interpolation performs much better, with no observable growth in the integrals of motion.

Appendix B

Convergence studies of the electron cloud non-linear beam dynamics

B.1 Numerical convergence with MB-type e-clouds

In the discussion regarding the numerical implementation of the e-cloud interactions and its inclusion in the lattice model of the LHC, it is clear that the final result will depend on a number of technical parameters. Those are:

- The transverse and longitudinal distance between points in the grid used in the e-cloud buildup simulation.
- The transverse and longitudinal distance between points in the auxiliary grid used in the refinement of the scalar potential for the minimization of the interpolation artifacts.
- The number of simulations used to average out the macroparticle noise.
- The number of interactions place on the lattice of the LHC.

The dynamic aperture was computed when individually scanning them in order to ensure that the simulations are numerically converged. The configuration of the simulation one with the reduced intensity, $\mathrm{SEY}_{\mathrm{max}}$= 1.3 and only MB-type e-clouds. The results are summarized in Fig. B.1 where the dynamic aperture is plotted with respect to the longitudinal (a) and transverse (b) distance between grid points used in the e-cloud buildup simulations, the longitudinal (c) and transverse (d) distance between grid points used in the auxiliary grid for the refinement of the scalar potential, (e) the number of half-cells in which the interactions were placed on the LHC lattice, (f) the number of buildup simulations that were averaged for the reduction of the macroparticle noise and (g) the number of interactions place per half-cell. The dashed line in the figures represents the value used in the rest of the simulations. When varying the number of interactions, their strength was scaled in order to keep the sum of their strengths constant.

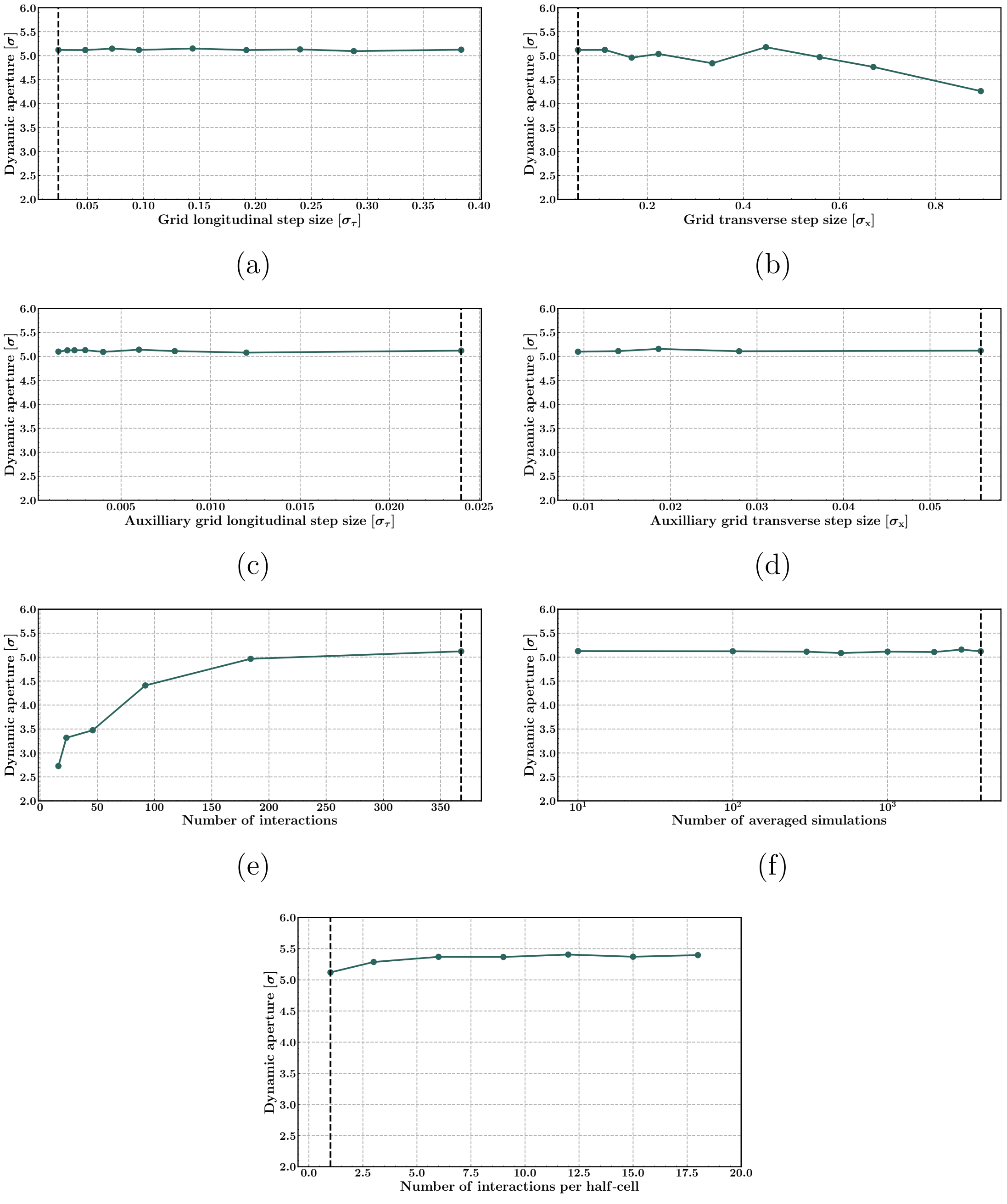

(a) (b)

(c) (d)

(e) (f)

(g)

Figure B.1: Convergence results showing the dynamic aperture as a function of the numerical parameter for MB-type e-clouds at reduced intensity and SEY= 1.3.

B.2 Numerical convergence with MQ-type e-clouds

A similar convergence study is carried out with only MQ-type e-cloud interactions. The same parameters are varied and the dynamic aperture is computed. In this configuration the bunch intensity is set to nominal intensity and $\mathrm{SEY}_{\mathrm{max}} = 1.3$. In order to have a sizeable effect on the dynamic aperture, the strength of the interaction was set to be 4 times larger. As in Sec. B.1, the results are summarized in Fig. B.2 where the dynamic aperture is plotted with respect to the longitudinal (a) and transverse (b) distance between grid points used in the e-cloud buildup simulations, the longitudinal (c) and transverse (d) distance between grid points used in the auxiliary grid for the refinement of the scalar potential, (e) the number of interactions placed on the LHC lattice and (f) the number of buildup simulations that were averaged for the reduction of the macroparticle noise. The dashed line in the figures represents the value used in the rest of the simulations and when varying the number of interactions, their strength was scaled in order to keep the sum of their strengths constant.

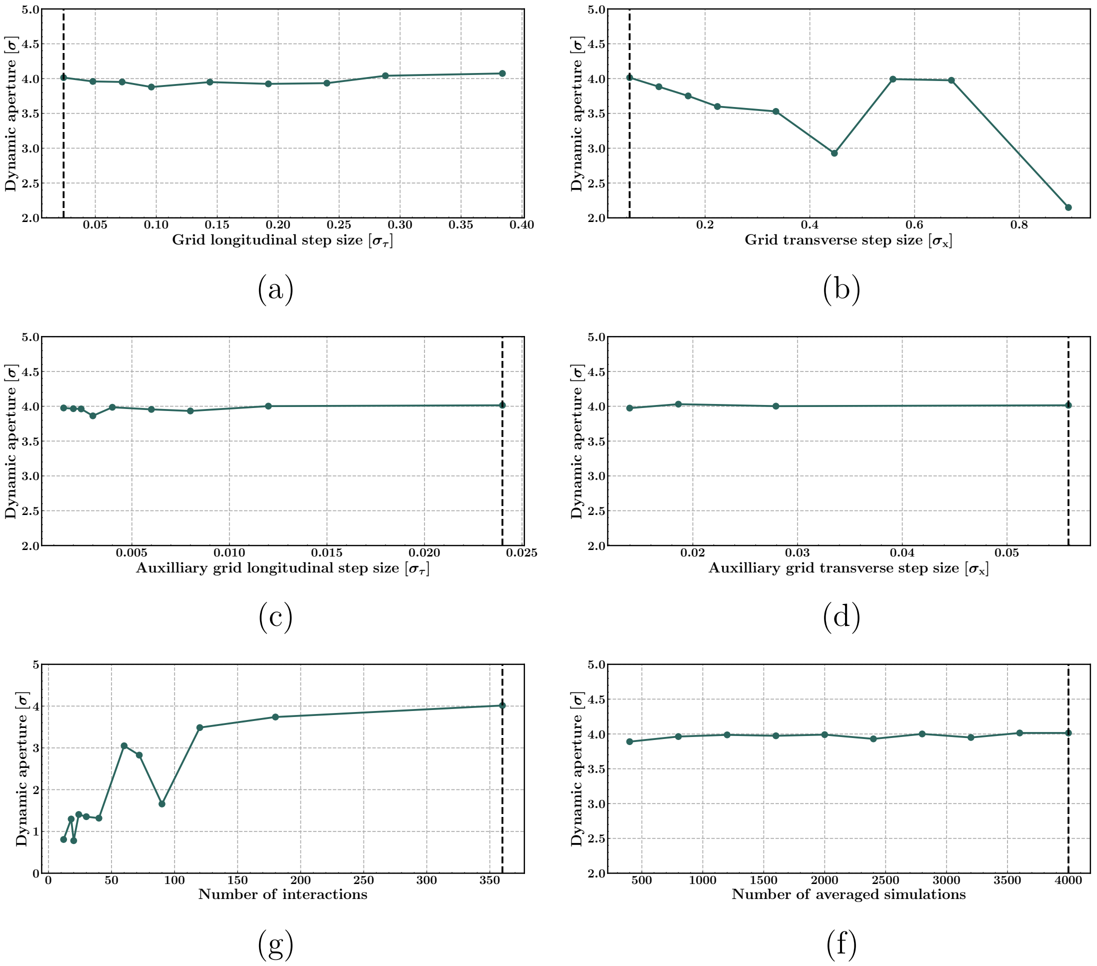

(a) (b)

(c) (d)

(g) (f)

Figure B.2: Convergence results showing the dynamic aperture as a function of the numerical parameter for MQ-type e-clouds at nominal intensity and SEY= 1.3.

Appendix C

PICOSEC model parameter tables

See Tabs C.1 to C.8.

Table C.1: The values of: the photoelectron drift velocity V_p, the avalanche drift velocity V_a and the drift velocity V_{ea}, of an avalanche-electron, for three different values of Ptr and default high voltage settings.

	Ptr 0%	Ptr 50%	Ptr 100%
Photoelectron drift velocity [$\mu m/ns$]	156.8 ± 0.4	150.5 ± 0.8	142.2 ± 1.0
Avalanche drift velocity [$\mu m/ns$]	181.4 ± 0.5	184.8 ± 0.8	188.2 ± 0.9
Avalanche-electron drift velocity [$\mu m/ns$]	169.9 ± 0.2	170.4 ± 0.2	170.0 ± 0.2

Table C.2: The first Townsend coefficient, estimated from GARFIELD++ simulations, for different Ptr values and the default drift voltage settings. Table adapted from Ref. [16]

	Ptr 0%	Ptr 50%	Ptr 100%
First Townsend coef. [μm^{-1}]	0.0520 ± 0.0003	0.0695 ± 0.0005	0.0893 ± 0.0008

Table C.3: Mean values of the time-gain ρ and values of the constant term C (see Eq. (7.13)), estimated for three Ptr values and the default drift voltage settings. Table adapted from Ref. [16]

	Ptr 0%	Ptr 50%	Ptr 100%
Mean time-gain, ρ [$10^{-3}ns$]	17.40 ± 0.3	17.25 ± 0.42	17.72 ± 0.48
Time constant, C [$10^{-3}ns$]	53.50 ± 3.0	60.00 ± 4.00	68.00 ± 5.00

Table C.4: The exponential slopes and the constant terms that determine the number of electrons on and after the mesh, as estimated by GARFIELD++ simulations. (top) The exponential slope a given as a function of the avalanche length (L) by the expression $q(L; a_{eff}) = q_0 \cdot e^{a_{eff}L}$, where the constant term (q_0) is set to $q_0 = 2$, because the avalanche starts with two electrons. (bottom) The number of electrons passing through the mesh, is also expressed exponentially as a function of L. The passage through the mesh does not affect the exponential slope. However the constant term is found to be $\simeq 0.5$, which translates to ~ 25% mesh transparency. Table adapted from Ref. [16]

Number of electrons on the mesh			
	Ptr 0%	Ptr 50%	Ptr 100%
Constant term	2 (fixed)	2 (fixed)	2 (fixed)
Multiplication coef., a_{eff} $[10^{-3}\mu m^{-1}]$	32.47 ± 0.01	39.12 ± 0.01	45.30 ± 0.02
Number of electrons after the mesh			
	Ptr 0%	Ptr 50%	Ptr 100%
Constant term	0.53 ± 0.01	0.50 ± 0.02	0.57 ± 0.02
Exponential slope, $[10^{-3}\mu m^{-1}]$	32.80 ± 0.3	39.40 ± 0.2	45.00 ± 0.2

Table C.5: Ratio of the RMS over the mean value of the number of electrons in any given avalanche length. Notice that this ratio equals to $\left(1/(1+\theta)^{1/2}\right)$, where θ is the parameter of the Gamma distribution function. Table adapted from Ref. [16]

	Ptr 0%	Ptr 50%	Ptr 100%
On the mesh	0.510 ± 0.005	0.464 ± 0.005	0.422 ± 0.005
After the mesh	0.530 ± 0.010	0.475 ± 0.005	0.430 ± 0.005

Table C.6: Diffusion properties of the avalanche electron. Table adapted from Ref. [16]

	Ptr 0%	Ptr 50%	Ptr 100%
Time variance per unit length $[10^{-5}\ ns^2/\mu m]$	11.65 ± 0.05	11.75 ± 0.05	11.67 ± 0.05
Constant term $[10^{-5}\ ns^2]$	16.55 ± 1.50	16.78 ± 1.62	17.03 ± 0.80

Table C.7: Diffusion properties of a photoelectron before it initiates an avalanche. Table adapted from Ref. [16]

	Ptr 0%	Ptr 50%	Ptr 100%
Time variance per unit length $[10^{-5}\ ns^2/\mu m]$	13.27 ± 0.3	13.80 ± 0.3	13.30 ± 0.6
Constant term $[10^{-5}\ ns^2]$	-47.27 ± 6.8	-56.22 ± 6.8	-67.64 ± 13.4

Table C.8: Parameter values used in the model. Table adapted from Ref. [16]

Penning transfer rate	50%				
Anode voltage	450 V				
Drift voltage	325 V	350 V	375 V	400 V	425 V
a $[10^{-2}\ \mu m^{-1}]$	3.607 ± 0.018	4.400 ± 0.020	5.208 ± 0.027	6.069 ± 0.027	6.950 ± 0.032
a_{eff} $[10^{-2}\ \mu m^{-1}]$	2.215 ± 0.001	2.629 ± 0.001	3.055 ± 0.001	3.484 ± 0.001	3.912 ± 0.001
θ	2.698 ± 0.142	2.906 ± 0.154	3.037 ± 0.162	3.313 ± 0.179	3.645 ± 0.191
V_{ea}^{-1} $[10^{-3}\ ns/\mu m]$	7.311 ± 0.003	6.877 ± 0.003	6.509 ± 0.002	6.173 ± 0.002	5.866 ± 0.004
V_p^{-1} $[10^{-3}\ ns/\mu m]$	8.065 ± 0.026	7.678 ± 0.026	7.266 ± 0.028	6.923 ± 0.028	6.643 ± 0.031
d_{off} $[10^{-2}\ ns]$	-3.831 ± 0.084	-3.437 ± 0.082	-2.883 ± 0.075	-2.678 ± 0.068	-2.364 ± 0.079
ρ $[10^{-2}\ ns]$	3.570 ± 0.054	2.919 ± 0.027	2.489 ± 0.030	2.185 ± 0.028	1.725 ± 0.045
C $[10^{-2}\ ns]$	7.555 ± 0.218	7.511 ± 0.117	7.668 ± 0.166	7.778 ± 0.196	7.001 ± 0.516
σ_p^2 $[10^{-4}\ ns^2/\mu m]$	2.137 ± 0.054	1.908 ± 0.046	1.662 ± 0.073	1.554 ± 0.050	1.380 ± 0.063
Φ $[10^{-4}\ ns^2]$	-9.967 ± 2.417	-7.936 ± 1.395	-6.400 ± 1.650	-7.525 ± 1.343	-5.622 ± 1.284
σ_0^2 $[10^{-4}\ ns^2/\mu m]$	2.094 ± 0.005	1.778 ± 0.003	1.543 ± 0.004	1.341 ± 0.003	1.175 ± 0.004
tr	0.244 ± 0.009	0.248 ± 0.044	0.238 ± 0.011	0.251 ± 0.009	0.247 ± 0.009
δ $[10^{-2}\ ns^2]$	7.217 ± 0.034	6.871 ± 0.032	6.607 ± 0.031	6.305 ± 0.030	5.938 ± 0.040
Δt_{mesh} $[10^{-1}\ ns]$	1.521 ± 0.005	1.455 ± 0.005	1.400 ± 0.004	1.344 ± 0.003	1.303 ± 0.004
Control parameters					
x_1 $[\mu m]$	0	0	0	0	0
x_2 $[\mu m]$	164	167	174	174	172
w/ρ	1	1	1	1	1
D $[\mu m]$	182	182	182	182	182
N_{max}	350	500	1250	1750	3500

Appendix D

Variance of a variable dependent on another variable

Let $y(L)$ be a measurement (random variable) of a physical variable Y, which depends on another physical variable, L, as $Y = f(L)$. Also, let the statistical properties of y depend on L such that

$$\langle y(L) \rangle = \int_{\Omega_y} y \cdot H(y, L) \mathrm{d}y = f(L), \tag{D.1}$$

and

$$\left\langle y^2(L) \right\rangle - \langle y(L) \rangle^2 = \int_{\Omega_y} [y - \langle y(L) \rangle]^2 \cdot H(y, L) \mathrm{d}y = u(l), \tag{D.2}$$

where Ω_y describes the set of all possible values of y and $H(y, L)$ is the p.d.f. describing the measurement process. Because the p.d.f. $H(y, L)$ depends on the physical variable L, the mean value and the variance will also depend on L. Moreover, let the physical variable L be distributed according to $g(L)$. In an experiment where several measurements y of the physical variable Y are performed, but in which there is no way to know the value of L, the mean and variance can be expressed in terms of $f(L)$, $u(L)$ and $g(L)$. The p.d.f. $h(y)$ that describes the outcome of a measurement y without knowing L is:

$$h(y) = \int_{\Omega_L} H(y, L) \cdot g(L) \mathrm{d}L, \tag{D.3}$$

where Ω_L stands for the set of all possible values of L. The mean value of the measurements y, for any possible L is:

$$\langle y \rangle = \int_{\Omega_y} \int_{\Omega_L} y \cdot H(y, L) \cdot g(L) \mathrm{d}L \mathrm{d}y = \int_{\Omega_L} f(L) \cdot g(L) \mathrm{d}L. \tag{D.4}$$

The second moment of y can be written the same way as:

$$\left\langle y^2 \right\rangle = \int_{\Omega_y} \int_{\Omega_L} y^2 \cdot H(y, L) \cdot g(L) \mathrm{d}L \mathrm{d}y = \int_{\Omega_L} \left[u(L) + f^2(L)\right] \cdot g(L) \mathrm{d}L. \tag{D.5}$$

where $u(L)$ is given by Eq. (D.2). Equations (D.4) and (D.5) can be combined to give the variance of y for any possible value of L:

$$
\begin{aligned}
V[y] &= \left\langle y^2 \right\rangle - \langle y \rangle^2 = \\
&\int_{\Omega_L} \left[u(L) + f^2(L) \right] \cdot g(L) \mathrm{d}L - \left[\int_{\Omega_L} f(L) \cdot g(L) \mathrm{d}L \right]^2 = \\
&\int_{\Omega_L} u(L) \cdot g(L) \mathrm{d}L + \left\{ \int_{\Omega_L} f^2(L) \cdot g(L) \mathrm{d}L - \left[\int_{\Omega_L} f(L) \cdot g(L) \mathrm{d}L \right]^2 \right\}, \qquad \text{(D.6)}
\end{aligned}
$$

where the first term expresses the proper averaging of the variances of y. The fact that the mean value of y depends on L, introduces the second term. This term expresses the variance of $f(L)$, when L is distributed with a p.d.f. of $g(L)$.

Bibliography

[1] O. S. Brüning, P. Collier, P. Lebrun, S. Myers, R. Ostojic, J. Poole, and P. Proudlock, *LHC Design Report.* CERN Yellow Reports: Monographs, Geneva: CERN, 2004.

[2] The ATLAS Collaboration, "The ATLAS Experiment at the CERN Large Hadron Collider," *Journal of Instrumentation*, vol. 3, p. S08003, aug 2008.

[3] The ALICE Collaboration, "The ALICE experiment at the CERN LHC," *Journal of Instrumentation*, vol. 3, p. S08002, aug 2008.

[4] The CMS Collaboration, "The CMS experiment at the CERN LHC," *Journal of Instrumentation*, vol. 3, p. S08004, aug 2008.

[5] The LHCb Collaboration, "The LHCb Detector at the LHC," *Journal of Instrumentation*, vol. 3, p. S08005, aug 2008.

[6] K. Hirata, H. W. Moshammer, and F. Ruggiero, "A symplectic beam-beam interaction with energy change," *Part. Accel.*, vol. 40, pp. 205–228, Sep 1992. https://cds.cern.ch/record/243013/.

[7] M. A. Furman and A. A. Zholents, "Incoherent effects driven by the electron cloud," in *Proceedings of the 1999 Particle Accelerator Conference, New York, NY, U.S.A.*, 1999.

[8] A. Romano, G. Iadarola, K. Li, and G. Rumolo, "Macroparticle Simulation Studies of the LHC Beam Dynamics in the Presence of Electron Cloud," in *Proc. of International Particle Accelerator Conference (IPAC'17), Copenhagen, Denmark, 14-19 May, 2017*, pp. 2081–2084, May 2017.

[9] F. Petrov, O. Boine-Frankenheim, and O. Haas, "Interaction of relativistic short proton bunches with space charge limited electron clouds," *Phys. Rev. ST Accel. Beams*, vol. 17, p. 121001, Dec. 2014.

[10] G. Franchetti, I. Hofmann, W. Fischer, and F. Zimmermann, "Incoherent effect of space charge and electron cloud," *Phys. Rev. ST Accel. Beams*, vol. 12, p. 124401, Dec. 2009.

[11] K. Ohmi and K. Oide, "Chaos and emittance growth due to nonlinear interactions in a circular accelerator," *Phys. Rev. ST Accel. Beams*, vol. 10, p. 014401, Jan 2007.

[12] E. Benedetto, G. Franchetti, and F. Zimmermann, "Incoherent Effects of Electron Clouds in Proton Storage Rings," *Phys. Rev. Lett.*, vol. 97, p. 034801, July 2006.

[13] E. Benedetto, *Emittance growth induced by electron cloud in proton storage rings.* PhD thesis, Politecnico di Torino, Turin, Italy, 2006.

[14] A. Wolski, *Beam Dynamics in High Energy Particle Accelerators.* IMPERIAL COLLEGE PRESS, 2014.

[15] M. A. Agrotis, P. A. Damianou, and C. Sophocleous, "The toda lattice is super-integrable," *Physica A: Statistical Mechanics and its Applications*, vol. 365, no. 1, pp. 235–243, 2006. Fundamental Problems of Modern Statistical Mechanics.

[16] J. Bortfeldt *et al.*, "Modeling the timing characteristics of the picosec micromegas detector," *Nuclear Instruments and Methods in Physics Research Section A: Accelerators, Spectrometers, Detectors and Associated Equipment*, vol. 993, p. 165049, 2021.

[17] G. Iadarola, *Electron cloud studies for CERN particle accelerators and simulation code development.* PhD thesis, Universitá degli Studi di Napoli Federico II, Naples, Italy, 2014. CERN-THESIS-2014-047.

[18] R. Cimino, M. Commisso, D. R. Grosso, T. Demma, V. Baglin, R. Flammini, and R. Larciprete, "Nature of the decrease of the secondary-electron yield by electron bombardment and its energy dependence," *Phys. Rev. Lett.*, vol. 109, p. 064801, Aug 2012.

[19] G. Skripka, G. Iadarola, L. Mether, and G. Rumolo, "Non-monotonic dependence of heat loads induced by electron cloud on bunch population at the lhc," *The European Physical Journal Plus*, vol. 137, jul 2022.

[20] A. Romano, O. Boine-Frankenheim, X. Buffat, G. Iadarola, and G. Rumolo, "Electron cloud buildup driving spontaneous vertical instabilities of stored beams in the Large Hadron Collider," *Phys. Rev. Accel. Beams*, vol. 21, p. 061002, June 2018.

[21] G. Iadarola, G. Skripka, *et al.*, "Beam-induced heat loads on the LHC arc beam screens with different beam and machine configurations: experiments and comparison against simulations," Dec. 2019. CERN-ACC-NOTE-2019-0057.

[22] K. Paraschou and G. Iadarola, "Incoherent electron cloud effects in the Large Hadron Collider," in *Vol. 9 (2020): Proceedings of the ICFA mini-Workshop on Mitigation of Coherent Beam Instabilities in Particle Accelerators, Zermatt, Switzerland, 23–27 September 2019*, pp. 249–249, Dec. 2020.

[23] "LHC Programme Coordination." http://lpc.web.cern.ch/.

[24] K. Paraschou, G. Iadarola, N. Karastathis, S. Kostoglou, Y. Papaphilippou, and L. Sabato, “Analysis on Bunch-by-Bunch Beam Losses at 6.5 TeV in the Large Hadron Collider,” in *Proc. 10^{th} International Particle Accelerator Conference (IPAC’19), Melbourne, Australia, 19-24 May 2019*, pp. 500–503, Jun. 2019.

[25] J. Bortfeldt *et al.*, “Picosec: Charged particle timing at sub-25 picosecond precision with a micromegas based detector,” *Nuclear Instruments and Methods in Physics Research Section A: Accelerators, Spectrometers, Detectors and Associated Equipment*, vol. 903, pp. 317–325, 2018.

[26] K. Paraschou, “Study of the picosec micromegas detector with test beam data and phenomenological modelling of its response,” 2018. Master Thesis, arXiv:2010.13535, https://doi.org/10.26262/heal.auth.ir.297707.

[27] M. Ferrario, M. Migliorati, and L. Palumbo, “Space Charge Effects,” 2014. 26 pages, contribution to the CAS - CERN Accelerator School: Advanced Accelerator Physics Course, Trondheim, Norway, 18-29 Aug 2013.

[28] W. Herr and T. Pieloni, “Beam-Beam Effects,” 2014. 29 pages, contribution to the CAS - CERN Accelerator School: Advanced Accelerator Physics Course, Trondheim, Norway, 18-29 Aug 2013.

[29] G. Rumolo, “Beam Instabilities,” 2014. Comments: 21 pages, contribution to the CAS - CERN Accelerator School: Advanced Accelerator Physics Course, Trondheim, Norway, 18-29 Aug 2013.

[30] F. Zimmermann, “Electron cloud effects in accelerators,” in *Vol. 7 (2020): ECLOUD’18 : Proceedings of the Joint INFN-CERN-ARIES Workshop on Electron-Cloud Effects, 3–7 June 2018, La Biodola, Isola d’Elba, Italy*, 2020.

[31] A. Chao, *Physics of Collective Beam Instabilities in High Energy Accelerators*. Wiley Series in Beam Physics and Accelerator Technology, Wiley, 1993.

[32] W. Herr and B. Muratori, “Concept of luminosity,” 2021. http://dx.doi.org/10.5170/CERN-2006-002.361.

[33] H. Goldstein, C. Poole, and J. Safko, *Classical Mechanics*. Addison Wesley, 1980.

[34] J. D. Jackson, *Classical Electrodynamics*. WILEY, 1998.

[35] A. Chao, “Lecture notes on topics in accelerator physics,” 2002. SLAC-PUB-9574.

[36] H. Yoshida, “Construction of higher order symplectic integrators,” *Physics Letters A*, vol. 150, no. 5, pp. 262–268, 1990.

[37] E. Forest and R. D. Ruth, “Fourth-order symplectic integration,” *Physica D: Nonlinear Phenomena*, vol. 43, no. 1, pp. 105–117, 1990.

[38] K. Skoufaris, J. Laskar, Y. Papaphilippou, and C. Skokos, “Application of high order symplectic integration methods with forward integration steps in beam dynamics,” *Phys. Rev. Accel. Beams*, vol. 25, p. 034001, Mar 2022.

[39] G. Ripken and F. Schmidt, “A symplectic six—dimensional thin-lens formalism for tracking.” CERN-SL-95-12. https://cds.cern.ch/record/281283.

[40] K. Heinemann, G. Ripken, and F. Schmidt, “Construction of nonlinear symplectic six-dimensional thin-lens maps by exponentiation.” DESY 95-189. https://doi.org/10.48550/arXiv.acc-phys/9510005.

[41] M. Berz, *Modern map methods in particle beam physics*, vol. 108. Academic Press, 1999.

[42] W. W. MacKay, “Comment on Healy’s symplectification algorithm,” in *Proceedings of EPAC 2006, Edinburgh, Scotland*, 2006.

[43] A. J. Brizard, “Jacobi zeta function and action-angle coordinates for the pendulum,” *Communications in Nonlinear Science and Numerical Simulation*, vol. 18, no. 3, pp. 511–518, 2013.

[44] R. Cimino and T. Demma, “Electron cloud in accelerators,” *International Journal of Modern Physics A*, vol. 29, no. 17, p. 1430023, 2014.

[45] G. Iadarola and G. Rumolo, “Electron Cloud Effects,” in *ICFA Mini-Workshop on Impedances and Beam Instabilities in Particle Accelerators, 18 - 22 Sep 2017, Benevento, Italy: Proceedings* (V. Brancolini, G. Rumolo, M. Masullo, and S. Petracca, eds.), pp. 49–56, 2018.

[46] B. Henrist and *et al.*, “Secondary electron emission data for the simulation of electron cloud,” in *Mini Workshop on Electron Cloud Simulations for Proton and Positron Beams, CERN, Geneva, Switzerland, 2002*, 2002.

[47] V. Baglin and *et al.*, “A summary of main experimental results concerning the secondary electron emission of copper,” in *LHC Project Report 472, 2002*, 2002.

[48] R. Cimino, I. R. Collins, M. A. Furman, M. Pivi, F. Ruggiero, G. Rumolo, and F. Zimmermann, “Can low-energy electrons affect high-energy physics accelerators?,” *Phys. Rev. Lett.*, vol. 93, p. 014801, Jun 2004.

[49] R. Cimino and I. Collins, “Vacuum chamber surface electronic properties influencing electron cloud phenomena,” in *Applied Surface Science, 2004*, 2004.

[50] A. Kuzucan and *et al.*, “Secondary electron yield on cryogenic surfaces as a function of physisorbed gases,” in *Proceedings of the IPAC11 International Particle Accelerator Conference, San Sebastian, Spain, 2011*, 2011.

[51] G. Iadarola, “A simplified analytical model for the electron cloud build-up process,” 2021.

[52] M. G. Billing, J. Conway, E. E. Cowan, J. A. Crittenden, W. Hartung, J. Lanzoni, Y. Li, C. S. Shill, J. P. Sikora, and K. G. Sonnad, "Measurement of electron trapping in the cornell electron storage ring," *Phys. Rev. ST Accel. Beams*, vol. 18, p. 041001, Apr 2015.

[53] G. Iadarola, "Modelling the interaction of a relativistic beam particle with an electron cloud," Aug. 2019. CERN-ACC-NOTE-2019-0033.

[54] K. Ohmi, S. Heifets, and F. Zimmermann, "Study of coherent tune shift caused by electron cloud in positron storage rings," in *2nd Asian Particle Accelerator Conference (APAC '01)*, p. WEP056, 12 2001.

[55] J. F. Esteban Müller, P. Baudrenghien, T. Mastoridis, E. Shaposhnikova, and D. Valuch, "High-accuracy diagnostic tool for electron cloud observation in the lhc based on synchronous phase measurements," *Phys. Rev. ST Accel. Beams*, vol. 18, p. 112801, Nov 2015.

[56] G. Iadarola, L. Mether, N. Mounet, and L. Sabato, "Linearized method for the study of transverse instabilities driven by electron clouds," *Phys. Rev. Accel. Beams*, vol. 23, p. 081002, Aug 2020.

[57] K. Ohmi and F. Zimmermann, "Head-tail instability caused by electron clouds in positron storage rings," *Phys. Rev. Lett.*, vol. 85, pp. 3821–3824, Oct 2000.

[58] G. Rumolo and F. Zimmermann, "Electron cloud simulations: beam instabilities and wakefields," *Phys. Rev. ST Accel. Beams*, vol. 5, p. 121002, Dec 2002.

[59] G. Iadarola, E. Belli, K. Li, L. Mether, A. Romano, and G. Rumolo, "Evolution of Python Tools for the Simulation of Electron Cloud Effects," in *Proc. of International Particle Accelerator Conference (IPAC'17), Copenhagen, Denmark, 14-19 May, 2017*, pp. 3803–3806, May 2017.

[60] G. Skripka, P. Dijkstal, G. Iadarola, L. Mether, G. Rumolo, and E. Wulff, "Comparison of Electron Cloud Build-Up Simulations Against Heat Load Measurements for the LHC Arcs With Different Beam Configurations," in *Proc. 10th International Particle Accelerator Conference (IPAC'19), Melbourne, Australia, 19-24 May 2019*, pp. 3232–3235, Jun. 2019.

[61] V. Petit, M. Taborelli, D. A. Zanin, M. Himmerlich, H. Neupert, P. Chiggiato, and G. Iadarola, "Beam-induced surface modifications as a critical source of heat loads in the Large Hadron Collider," *Commun Phys*, vol. 4, pp. 1–10, Aug. 2021.

[62] G. Iadarola, B. Bradu, L. Mether, K. Paraschou, V. Petit, G. Rumolo, L. Sabato, G. Skripka, M. Taborelli, and L. Tavian, "Progress in Mastering Electron Clouds at the Large Hadron Collider," in *Proc. IPAC'21*, no. 12 in International Particle Accelerator Conference, pp. 1273–1278, JACoW Publishing, Geneva, Switzerland, 08 2021. https://doi.org/10.18429/JACoW-IPAC2021-TUXA03.

[63] E. Benedetto and F. Zimmermann, “Analysis of the electron pinch during a bunch passage,” in *Proc. 31st Advanced ICFA Beam Dynamics Workshop on Electron-Cloud Effects (ECLOUD’04), Napa, USA, 19-24 April 2004*, pp. 81–87, 2005.

[64] J. Wenninger, “Operation and configuration of the LHC in run 2.” CERN-ACC-NOTE-2019-0007. https://cds.cern.ch/record/2668326/.

[65] B. Salvachua, “Overview of proton-proton physics during run 2,” in *Proceedings of the 2019 Evian Workshop on LHC Beam Operations*, pp. 7–14, 2019.

[66] G. Antchev, P. Aspell, I. Atanassov, *et al.*, “First measurement of elastic, inelastic and total cross-section at $\sqrt{s} = 13$ tev by totem and overview of cross-section data at lhc energies,” *Eur. Phys. J. C*, vol. 79, Feb 2019. https://doi.org/10.1140/epjc/s10052-019-6567-0/.

[67] H. Damerau *et al.*, “RF Manipulations for Special LHC-Type Beams in the CERN PS,” in *Proc. 9th International Particle Accelerator Conference (IPAC’18), Vancouver, BC, Canada, April 29-May 4, 2018*, pp. 1971–1974, June 2018. https://doi.org/10.18429/JACoW-IPAC2018-WEPAF063.

[68] N. Karastathis, K. Fuchsberger, M. Hostettler, Y. Papaphilippou, and D. Pellegrini, “Crossing Angle Anti-Leveling at the LHC in 2017,” in *Proc. 9th International Particle Accelerator Conference (IPAC’18), Vancouver, BC, Canada, April 29-May 4, 2018*, pp. 184–187, June 2018. https://doi.org/10.18429/JACoW-IPAC2018-MOPMF040/.

[69] G. Srkipka and G. Iadarola, “Electron cloud build-up in two-beam regions for HL-LHC, heat load and vacuum aspects,” in *Vol. 7 (2020): ECLOUD’18 : Proceedings of the Joint INFN-CERN-ARIES Workshop on Electron-Cloud Effects, 3–7 June 2018, La Biodola, Isola d’Elba, Italy*, 2020.

[70] S. Fartoukh, “Achromatic telescopic squeezing scheme and application to the lhc and its luminosity upgrade,” *Phys. Rev. ST Accel. Beams*, vol. 16, p. 111002, Nov 2013.

[71] S. Fartoukh *et al.*, “Combined ramp and telescopic squeeze,” Aug. 2020. CERN-ACC-2020-0028.

[72] L. R. Carver, X. Buffat, K. Li, E. Métral, and M. Schenk, “Transverse beam instabilities in the presence of linear coupling in the large hadron collider,” *Phys. Rev. Accel. Beams*, vol. 21, p. 044401, Apr 2018.

[73] O. Aberle *et al.*, *High-Luminosity Large Hadron Collider (HL-LHC): Technical design report.* CERN Yellow Reports: Monographs, Geneva: CERN, Dec. 2020. https://doi.org/10.23731/CYRM-2020-0010.

[74] M. Schwinzerl, H. Bartosik, R. D. Maria, G. Iadarola, A. Oeftiger, and K. Paraschou, “Optimising and Extending a Single-Particle Tracking Library

for High Parallel Performance," in *Proc. 12^{th} International Particle Accelerator Conference (IPAC'21), Campinas, SP, Brazil, 24-28 May 2021*, pp. 4146–4149, 08 2021. https://doi.org/10.18429/JACoW-IPAC2021-THPAB190.

[75] L. Deniau *et al.*, "MAD-X." http://cern.ch/madx.

[76] W. Herr, "Beam-beam interactions," 2006. http://dx.doi.org/10.5170/CERN-2006-002.379/.

[77] G. Iadarola, R. De Maria, and Y. Papaphilippou, "6D beam-beam interaction step-by-step," Feb. 2018. CERN-ACC-NOTE-2018-0023.

[78] K. Hirata, "Analysis of beam-beam interactions with a large crossing angle," *Phys. Rev. Lett.*, vol. 74, pp. 2228–2231, Mar 1995. https://doi.org/10.1103/PhysRevLett.74.2228/.

[79] L. H. A. Leunissen, G. Ripken, and F. Schmidt, "6D Beam-Beam Kick including Coupled Motion," Feb 2000. LHC-Project-Report-369. https://cds.cern.ch/record/425950/.

[80] N. Mounet, *The LHC Transverse Coupled-Bunch Instability.* PhD thesis, EPFL, Lausanne, Switzerland, 2012.

[81] M. Giovannozzi, "Dynamic aperture for single-particle motion: Overview of theoretical background, numerical predictions and experimental results," *AIP Conference Proceedings*, vol. 693, no. 1, pp. 26–31, 2003.

[82] F. James, *Statistical Methods in Experimental Physics.* WORLD SCIENTIFIC, 2nd ed., 2006. https://doi.org/10.1142/6096/.

[83] F. James, "Monte carlo theory and practice," *Reports on Progress in Physics*, vol. 43, pp. 1145–1189, sep 1980.

[84] A. Gorzawski, R. Appleby, M. Giovannozzi, A. Mereghetti, D. Mirarchi, S. Redaelli, B. Salvachua, G. Stancari, G. Valentino, and J. Wagner, "Probing LHC halo dynamics using collimator loss rates at 6.5 TeV," *Phys. Rev. Accel. Beams*, vol. 23, p. 044802, Apr. 2020.

[85] E. M. F. Curado and C. Tsallis, "Generalized statistical mechanics: connection with thermodynamics," *Journal of Physics A: Mathematical and General*, vol. 25, pp. 1019–1019, feb 1992.

[86] S. Papadopoulou, F. Antoniou, T. Argyropoulos, M. Hostettler, Y. Papaphilippou, and G. Trad, "Impact of non-gaussian beam profiles in the performance of hadron colliders," *Phys. Rev. Accel. Beams*, vol. 23, p. 101004, Oct 2020.

[87] M. Pivi and M. A. Furman, "POSINST." https://oraweb.cern.ch/pls/hhh/code_website.disp_code?code_name=POSINST.

[88] F. Zimmermann and G. Rumolo, "HEADTAIL." https://oraweb.cern.ch/pls/hhh/code_website.disp_code?code_name=HEADTAIL.

[89] “openECLOUD.” https://github.com/openecloud/openecloud.

[90] E. Wulff and G. Iadarola, “Implementation and benchmarking of the Furman-Pivi model for the Secondary Electron Emission in the PyECLOUD simulation code,” July 2019. CERN-ACC-NOTE-2019-0029.

[91] F. Lekien and J. Marsden, “Tricubic interpolation in three dimensions,” *Int. J. Numer. Meth. Engng*, vol. 63, pp. 455–471, May 2005.

[92] Y. Papaphilippou, “Detecting chaos in particle accelerators through the frequency map analysis method,” *Chaos*, vol. 24, p. 024412, June 2014.

[93] J. Laskar, C. Froeschlé, and A. Celletti, “The measure of chaos by the numerical analysis of the fundamental frequencies. application to the standard mapping,” *Physica D: Nonlinear Phenomena*, vol. 56, no. 2, pp. 253–269, 1992.

[94] S. Kostoglou, H. Bartosik, Y. Papaphilippou, G. Sterbini, and N. Triantafyllou, “Tune modulation effects for colliding beams in the high luminosity large hadron collider,” *Phys. Rev. Accel. Beams*, vol. 23, p. 121001, Dec 2020.

[95] J. F. Esteban Müller, *Longitudinal intensity effects in the CERN Large Hadron Collider.* PhD thesis, EPFL, Lausanne, Switzerland, 2016.

[96] Y. Giomataris, P. Rebourgeard, J. Robert, and G. Charpak, “Micromegas: a high-granularity position-sensitive gaseous detector for high particle-flux environments,” *Nuclear Instruments and Methods in Physics Research Section A: Accelerators, Spectrometers, Detectors and Associated Equipment*, vol. 376, no. 1, pp. 29–35, 1996.

[97] I. Giomataris, R. De Oliveira, S. Andriamonje, S. Aune, G. Charpak, P. Colas, G. Fanourakis, E. Ferrer, A. Giganon, P. Rebourgeard, and P. Salin, “Micromegas in a bulk,” *Nuclear Instruments and Methods in Physics Research Section A: Accelerators, Spectrometers, Detectors and Associated Equipment*, vol. 560, no. 2, pp. 405–408, 2006.

[98] F. Sauli, “Principles of operation of multiwire proportional and drift chambers,” 1977. CERN-77-09, http://dx.doi.org/10.5170/CERN-1977-009.

[99] H. Schindler and R. Veenhof, “Garfield++ simulation of tracking detectors.” https://garfieldpp.web.cern.ch/garfieldpp/.

[100] Ö. Şahin, İ. Tapan, E. N. Özmutlu, and R. Veenhof, “Penning transfer in argon-based gas mixtures,” *Journal of Instrumentation*, vol. 5, p. P05002, may 2010.

[101] L. Colli and U. Facchini, “Drift velocity of electrons in argon,” *Review of Scientific Instruments*, vol. 23, no. 1, pp. 39–42, 1952.